



3 1293 01020 6088

This is to certify that the

dissertation entitled

**STABILITY AND DYNAMICS  
OF  
LOW-DIMENSIONAL SYSTEMS**

presented by

**SEONG GON KIM**

has been accepted towards fulfillment  
of the requirements for

**PhD** degree in **Physics**

**P.M. Duxbury**

Major professor

Date **November 16, 1994**



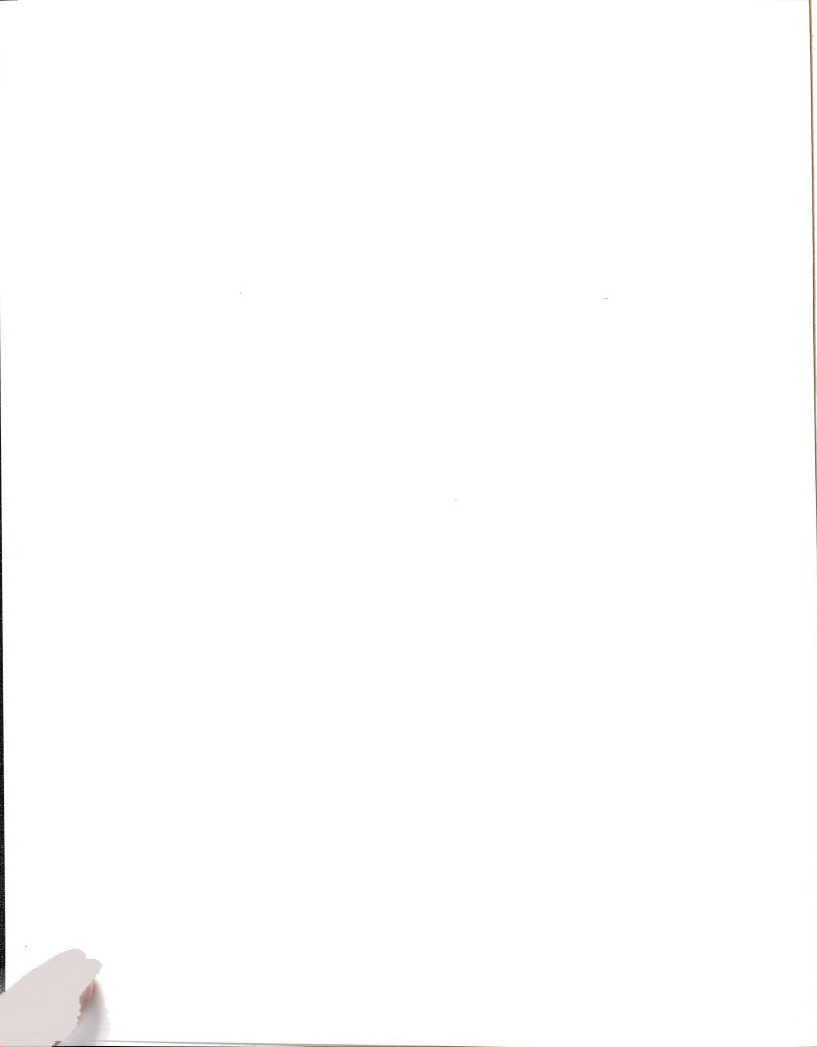
**LIBRARY**  
**Michigan State**  
**University**

**PLACE IN RETURN BOX** to remove this checkout from your record.  
**TO AVOID FINES** return on or before date due.

DATE DUE	DATE DUE	DATE DUE
_____	_____	_____
_____	_____	_____
_____	_____	_____
_____	_____	_____
_____	_____	_____
_____	_____	_____
_____	_____	_____

**MSU Is An Affirmative Action/Equal Opportunity Institution**

c:\circ\datedue.pm3-p.1



STABILITY AND DYNAMICS  
OF  
LOW-DIMENSIONAL SYSTEMS

By

Seong Gon Kim

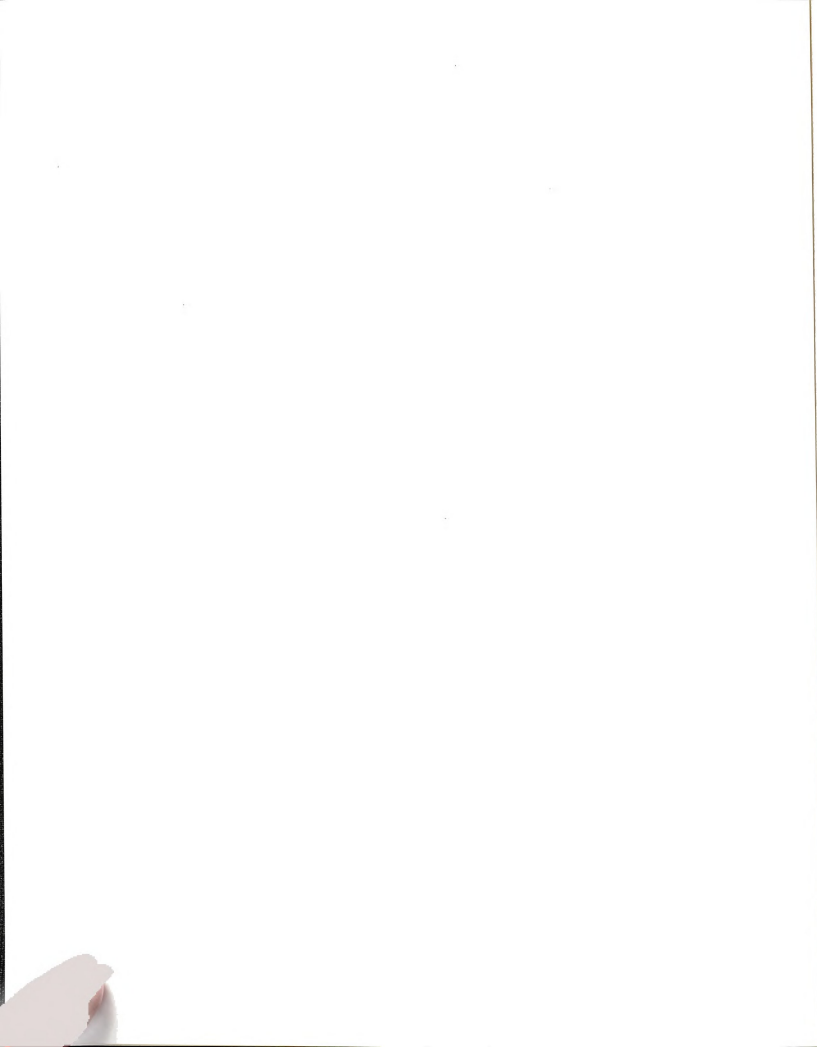
A DISSERTATION

Submitted to  
Michigan State University  
in partial fulfillment of the requirements  
for the Degree of

DOCTOR OF PHILOSOPHY

Department of Physics and Astronomy

1994



# ABSTRACT

## STABILITY AND DYNAMICS OF LOW-DIMENSIONAL SYSTEMS

By

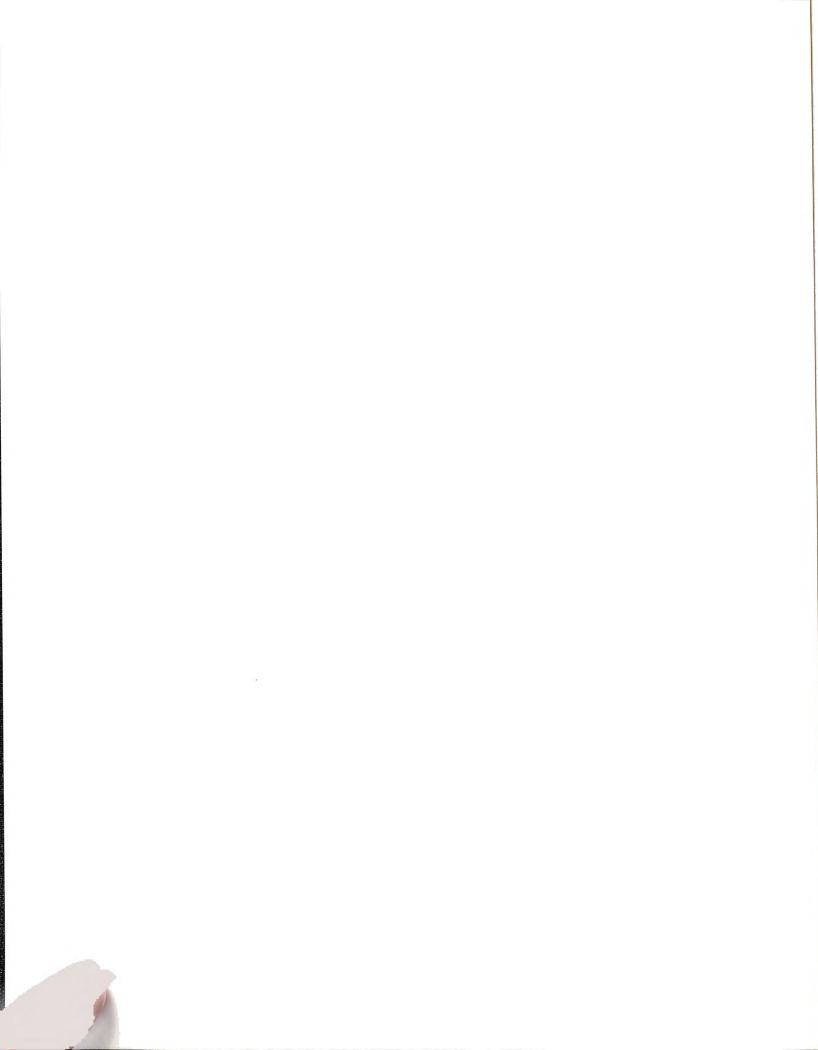
Seong Gon Kim

Understanding the structure and dynamics of physical systems has been one of the major tasks of condensed matter physics. In this thesis, I study this issue on four different physical systems: A superconductor connected to an external current source, random networks under tensile stress, carbon fullerenes in contact with an external heat bath and ferrofluid particles subject to an external field or heat source.

The critical current density of the superconductor depends on the distribution of its current density. For superconductors with defects, the critical current density will depend on how these defects enhance the local current densities. The numerical simulation results as well as analytic predictions on the dependence of critical current density on the geometry of the defects is presented.

The mechanical response of materials can be modeled by networks of nodes and bonds. Tuning the energy functional of the bond deformation, I analyze the

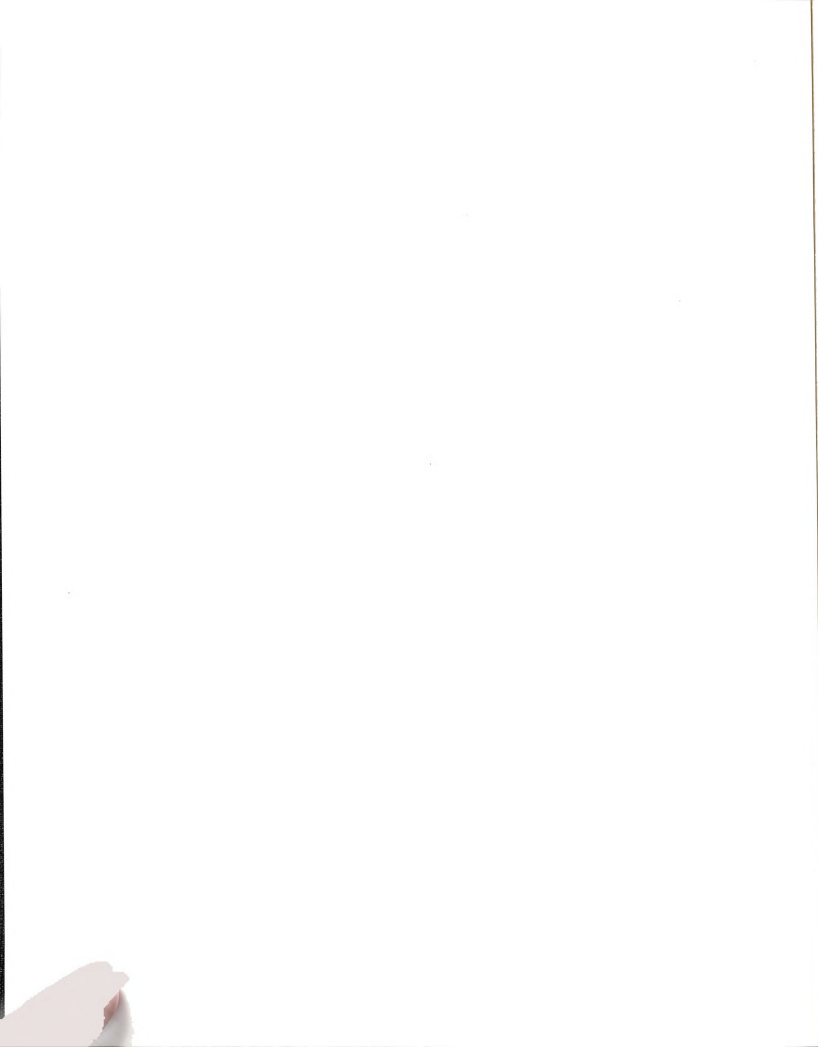




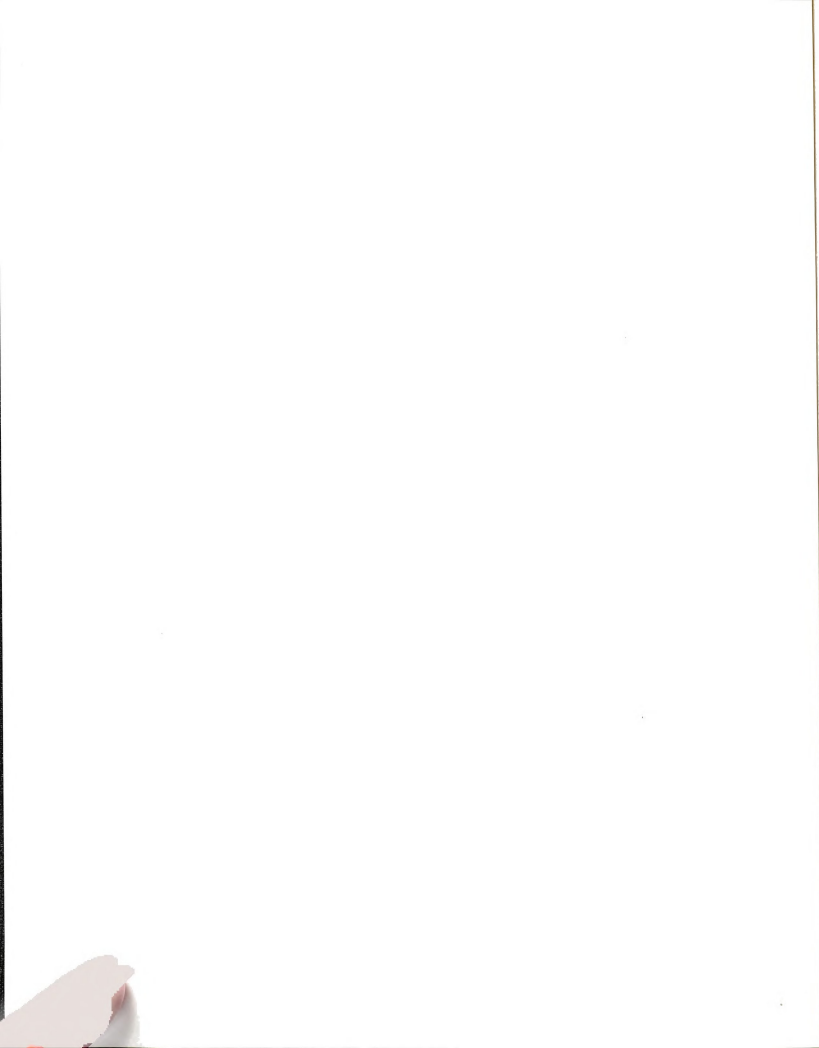
strength of the system and simulate the fracture process. A scaling theory is also presented.

Carbon is one of the most favored elements of scientists because of the many remarkable properties it possesses. Discovery of carbon fullerenes spurred even more interest in carbon clusters. I studied the thermal disintegration of fullerenes within the framework of tight-binding molecular dynamics. Not only the melting temperature but also many intermediate structures including a previously unknown "pretzel" phase have been identified.

A ferrofluid is a magnetic colloid made of magnetite particles suspended in a liquid, usually a petroleum oil. When a magnetic field is applied, they form well defined structures. Our study indicates that these particles show interesting structures even in zero-field. We also find that the ring structure is very stable and it should be observed in carefully controlled experiments.



*To my dear wife*  
*Jinwon*  
*and my precious children*  
*Danbee, Mara and Barunie*





# ACKNOWLEDGEMENTS

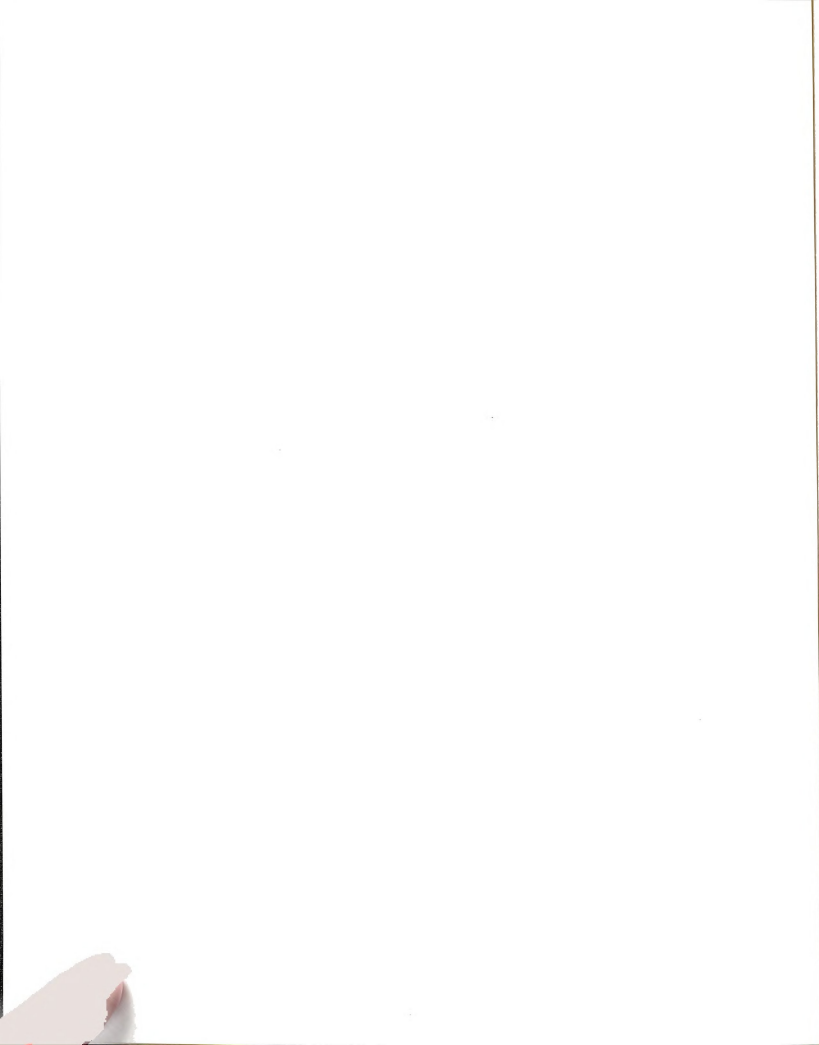
I thank God for all the blessings He has stored for me and my family.

I would like to express my deep gratitude to my thesis advisors Professor Phillip M. Duxbury and Professor David Tománek for their constant support, their physical insights and for sharing with me their enthusiasm for physics. I especially thank Dr. Duxbury for his generosity and pure concerns for my successful career to allow me to work with Dr. Tománek during his sabbatical leave. It was my great honor and privilege to be an apprentice to such great teachers. During the years of my learning to become a physicist myself, they have guided me with confidence and love through the ups and downs of research. Their continual search for simple and fundamental answers even in complex problems will always be my guiding light.

I am also grateful to Professors S.D. Mahanti, W. Pratt, W. Repko, D. Stump and W. Bauer for serving on my guidance committee. I would like to thank Mrs. Janet King and Stephanie Holland for making my life in this department so much simpler and enjoyable. The help from Mr. Ron Winsauer and Dr. George Perkins in solving the computational problems also weighs greatly.

I wish to thank Professor J. Hetherington and Dr. Philippe Jund for their numerous discussions, comments and help for the completion of the last chapter.

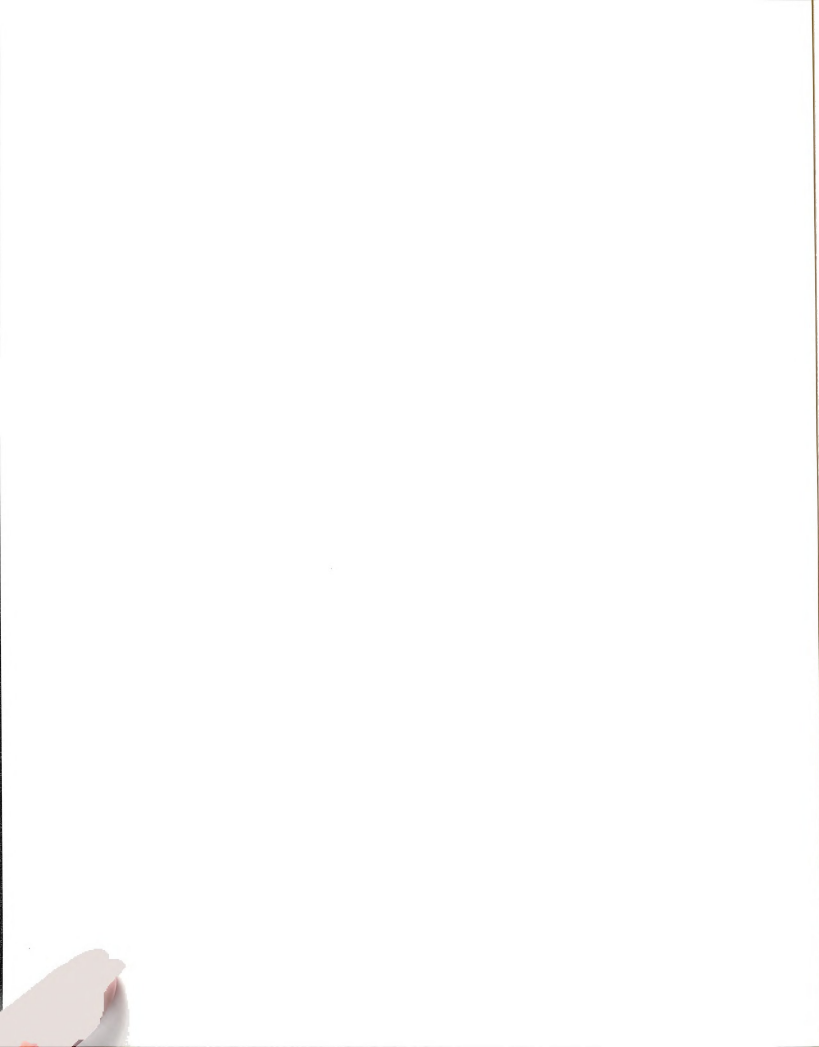
My deepest gratitude, however, can not go to anyone but to my dear wife Jinwon and my precious three children, Danbee, Mara and Barunie. They have been my strength, hope and the reason for completing this work. I sincerely desire



that someday I can pay back even a tiny fraction of the countless sacrifices they have made for me.

I also want to thank to all of my friends in this departments who made the life in East Lansing so much more enjoyable and pleasant. My final thank goes to Profs. W. Repko and W. Hartmann for keeping me in shape and recharging my strength with weekend tennis workouts.

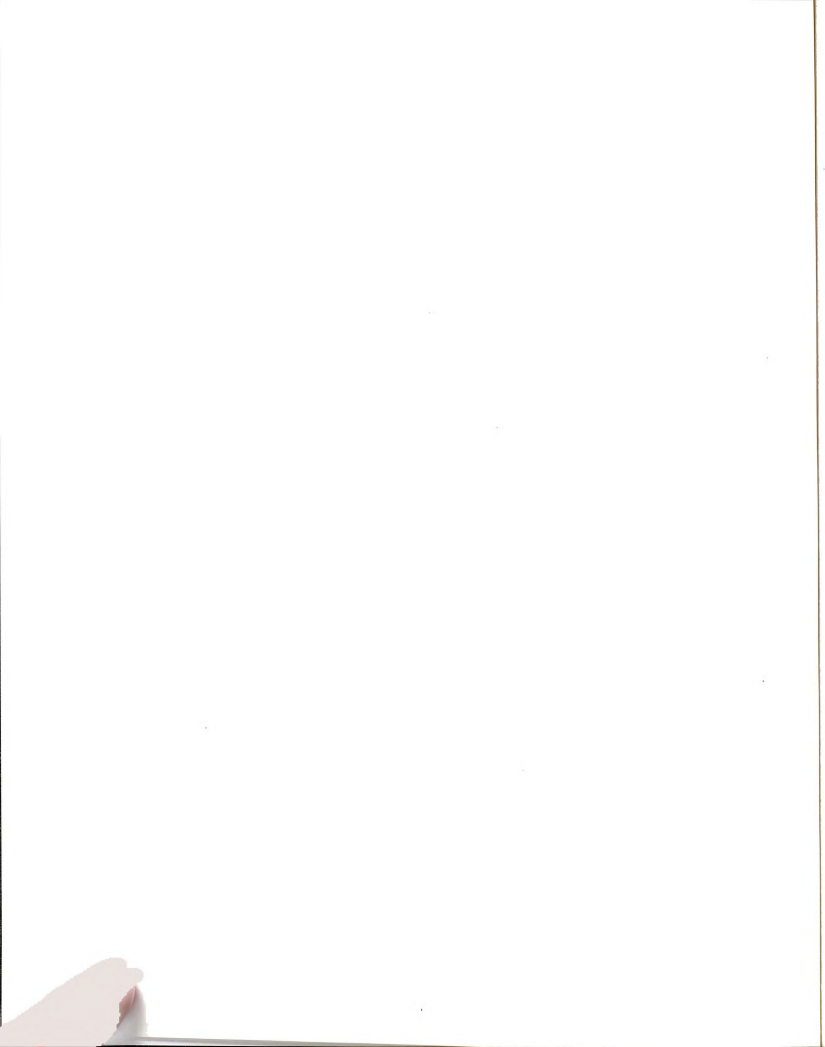
Financial support from the Natural Science Foundation and the Center for Fundamental Materials Research of MSU without which this thesis could not have been, is also greatly acknowledged.



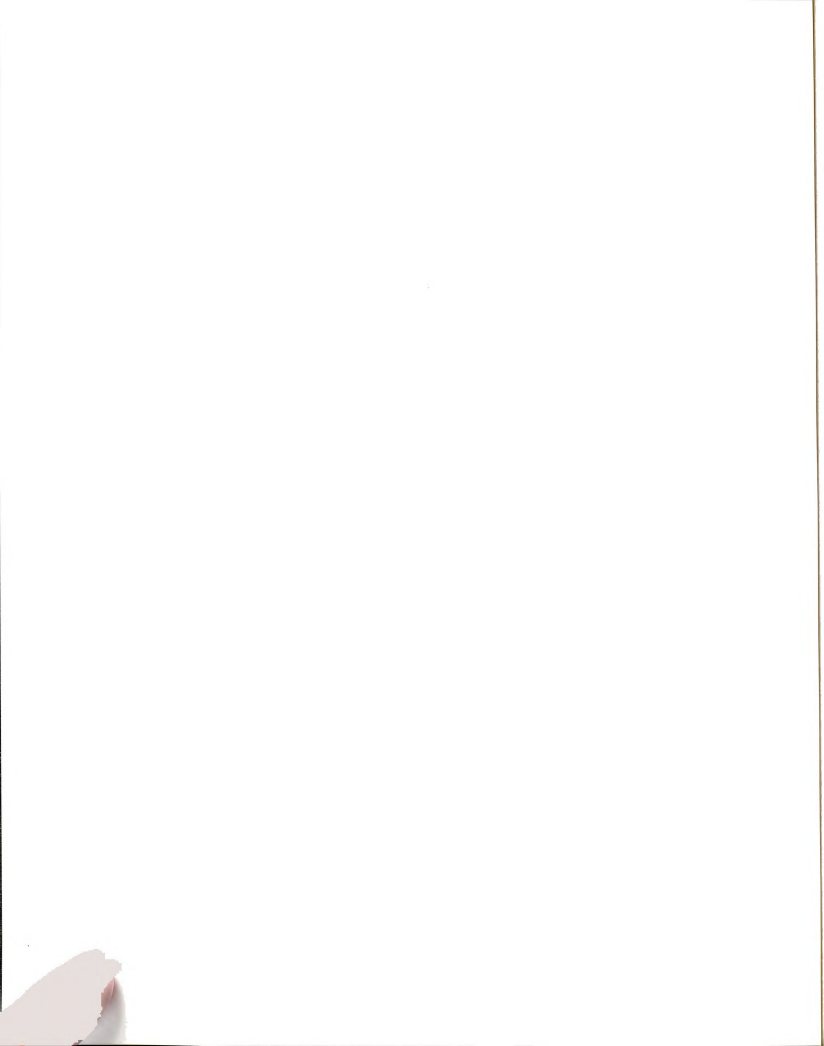
# Contents

<b>Abstract</b> . . . . .	<b>i</b>
<b>Acknowledgments</b> . . . . .	<b>iv</b>
<b>LIST OF TABLES</b>	<b>ix</b>
<b>LIST OF FIGURES</b>	<b>xii</b>
<b>1 Introduction</b>	<b>1</b>
1.1 Cracks and critical current . . . . .	3
1.2 Elasticity and fracture of disordered networks . . . . .	5
1.3 Melting of carbon fullerenes . . . . .	6
1.4 Stability of Magnetic Dipole Structures in Ferrofluids . . . . .	8
<b>2 Cracks and critical current</b>	<b>11</b>
2.1 Introduction . . . . .	12
2.2 Supercurrent enhancement at a crack tip . . . . .	13
2.2.1 The Model . . . . .	13
2.2.2 Exact solution as $a/\lambda \rightarrow 0$ . . . . .	18

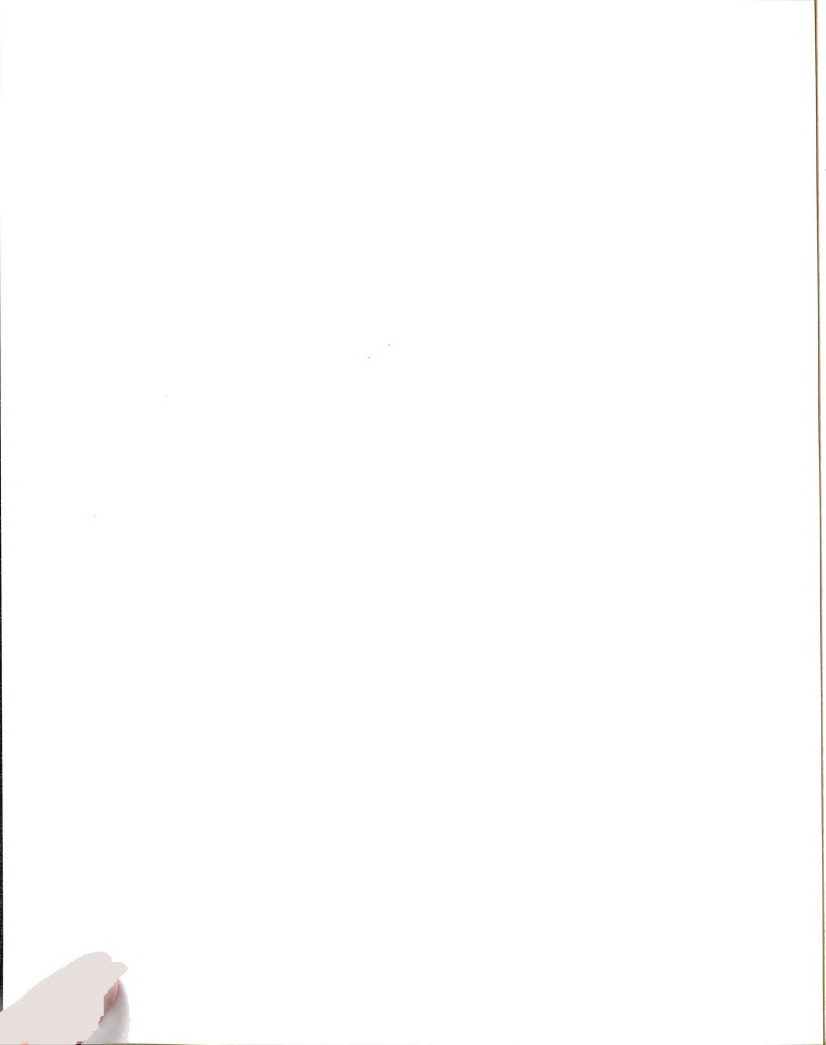




2.2.3	Saturation Effect as $a/\lambda \rightarrow \infty$ . . . . .	22
2.3	Numerical Simulation . . . . .	25
2.4	The Effects of a Crack on Critical Current . . . . .	32
2.4.1	The critical state model . . . . .	32
2.4.2	Hotspot theory . . . . .	34
2.5	Conclusions . . . . .	37
<b>3</b>	<b>Elasticity and fracture of disordered networks</b>	<b>40</b>
3.1	Introduction . . . . .	40
3.2	Central force networks . . . . .	42
3.2.1	Effective medium theory for elasticity . . . . .	43
3.2.2	Numerical simulation of damage and fracture . . . . .	45
3.3	Scaling theory of tensile fracture stress . . . . .	48
3.4	Bond Bending Networks . . . . .	57
3.4.1	Background . . . . .	57
3.4.2	Simulations of honeycomb networks . . . . .	60
3.5	Conclusions . . . . .	69
<b>4</b>	<b>Melting of carbon fullerenes</b>	<b>71</b>
4.1	Introduction . . . . .	71
4.2	The tight-binding potential for carbon . . . . .	76
4.3	The recursion method . . . . .	84



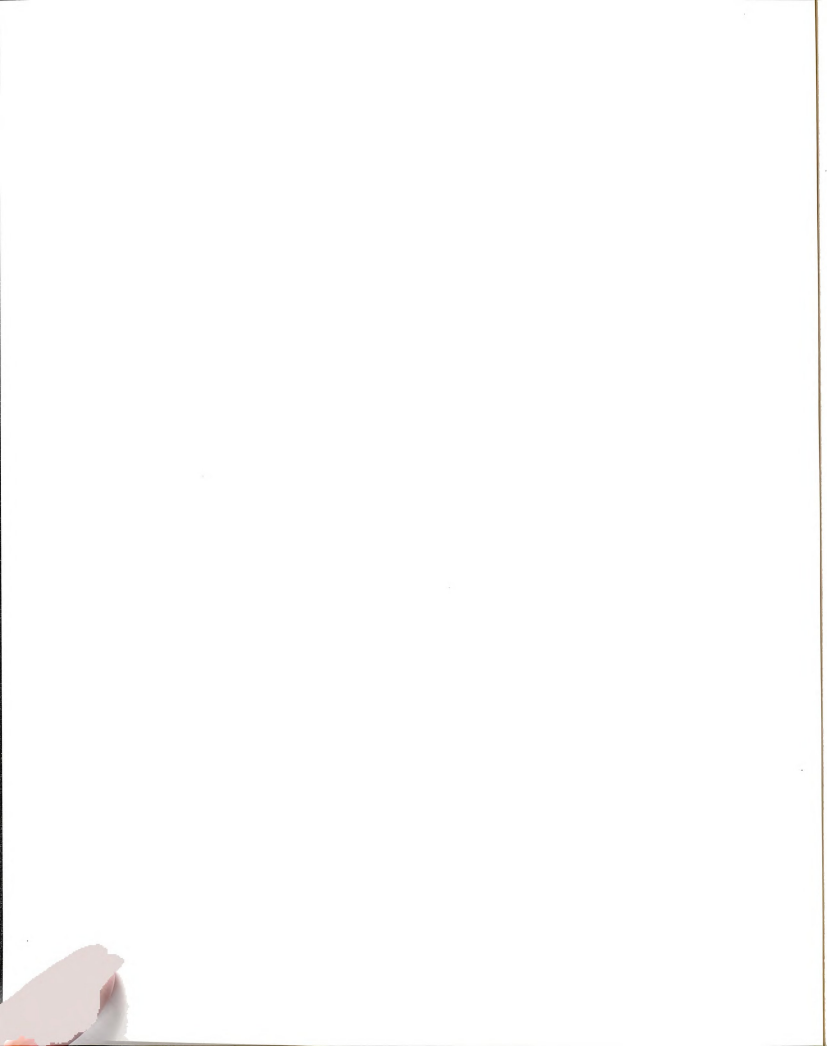
4.4	Molecular dynamics . . . . .	89
4.5	Simulation and Results . . . . .	94
4.6	Conclusions . . . . .	110
<b>5</b>	<b>Stability of Magnetic Dipole Structures in Ferrofluids</b>	<b>111</b>
5.1	Introduction . . . . .	111
5.2	Modeling of the ferrofluid . . . . .	114
5.3	Molecular dynamics of spherical tops . . . . .	122
5.4	Quaternion molecular dynamics . . . . .	126
5.5	Rings and chains . . . . .	133
5.6	Molecular dynamics study . . . . .	143
5.7	Ongoing work . . . . .	147
5.8	Conclusions . . . . .	152





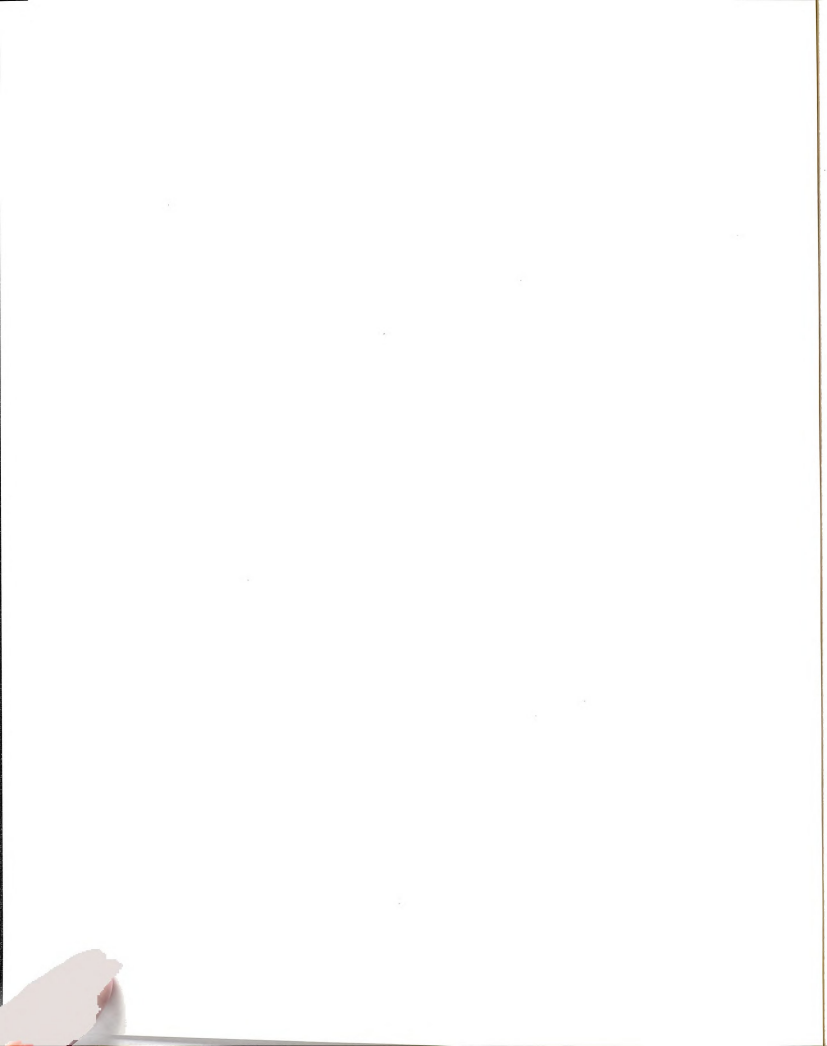
# List of Tables

4.1	Parameters for the band structure energy . . . . .	80
4.2	Parameters for the repulsive energy . . . . .	83
5.1	Units and conversion factors of physical quantities related to ferrofluids. . . . .	119
5.2	Physical parameters used in ferrofluid study. . . . .	120

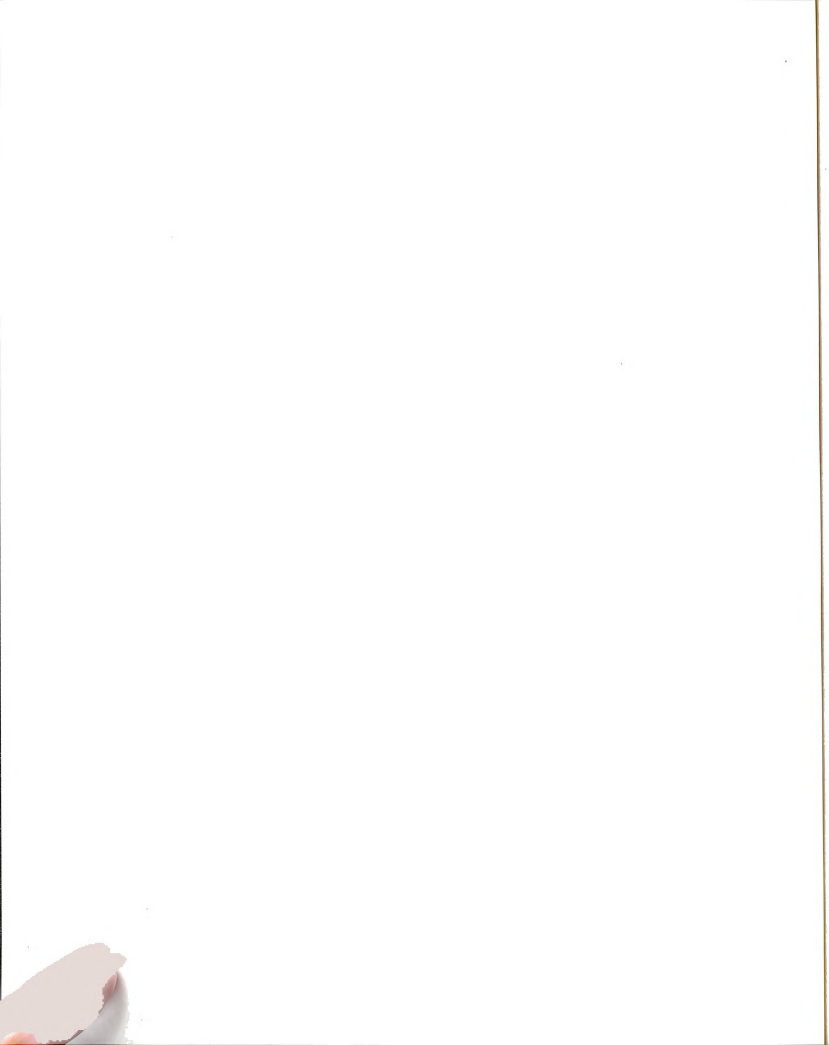


# List of Figures

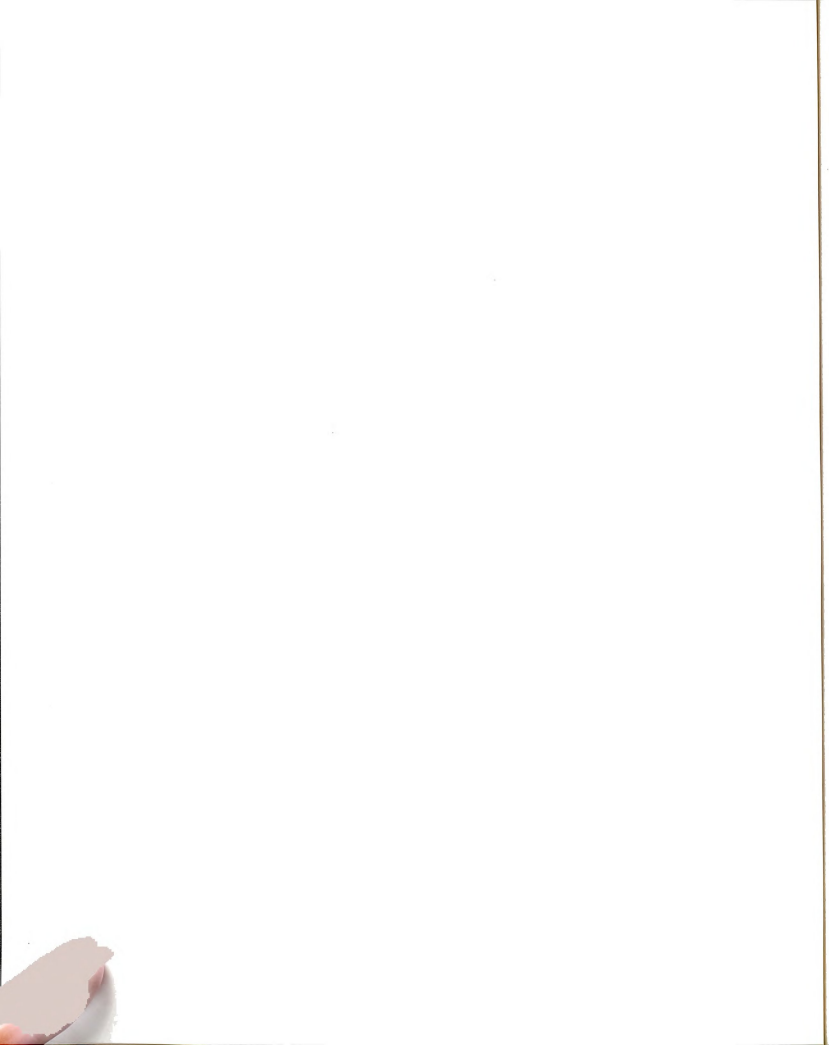
2.1	A superconductor with elliptic defect. . . . .	15
2.2	Elliptic coordinates. . . . .	17
2.3	The magnitude of current density near the crack tip. . . . .	20
2.4	A superconducting lattice with line defect. . . . .	26
2.5	The profile of the magnetic field near a crack. . . . .	28
2.6	The profile of the magnitude of the current density near a crack. .	29
2.7	The current at the crack tip as function of crack size. . . . .	30
2.8	The saturation current at the crack tip. . . . .	31
2.9	The Bean model (schematic). . . . .	33
3.1	The stress-strain behavior of a single spring. . . . .	46
3.2	The stress-strain behavior of a 50x50 triangular network. . . . .	47
3.3	The fracture evolution (early stage) . . . . .	49
3.4	Intermediate configuration. . . . .	50
3.5	The final fracture configuration. . . . .	51
3.6	The Young's modulus and tensile fracture stress . . . . .	54



3.7	Test of scaling of $\sigma_b(f)$ . . . . .	55
3.8	$C_{11}$ and $\mu$ for a honeycomb tube. . . . .	61
3.9	The stress-strain curve for honeycomb tube. . . . .	62
3.10	The initial configuration of tensile fracture of a hexagonal lattice .	64
3.11	The final path of tensile fracture of a hexagonal lattice . . . . .	65
3.12	The response of a graphite sheet containing a crack-like defect cluster.	66
3.13	The average fracture stress as a function of void volume fraction .	67
4.1	Carbon fullerenes. . . . .	72
4.2	Comparison of recursion method <i>vs.</i> conventional tight-binding method. . . . .	90
4.3	Temperature dependence of the total energy $E$ <i>per atom</i> for the $C_{60}$ fullerene. . . . .	96
4.4	Specific heat $c_V(T)$ <i>per atom</i> of $C_{20}$ , $C_{60}$ and $C_{240}$ . . . . .	97
4.5	"Snap shots" illustrating the geometry of a $C_{60}$ cluster at temper- atures corresponding to the different "phases". . . . .	99
4.6	Atomic binding energy distribution in a $C_{60}$ cluster at temperatures characteristic of the different "phases". . . . .	100
4.7	Bond length distribution in a $C_{60}$ cluster at temperatures charac- teristic of the different "phases". . . . .	102
4.8	Bond angle distribution in a $C_{60}$ cluster at temperatures character- istic of the different "phases". . . . .	103



4.9	Mass spectrum in a $C_{60}$ molecule at temperatures characteristic of the different "phases". . . . .	104
4.10	The entropy $S$ per atom for the $C_{60}$ fullerene and the metastable $C_{60}$ chain. . . . .	108
5.1	Soft-core potential for a ferrofluid particle. . . . .	117
5.2	Two dipoles on $x$ -axis. . . . .	121
5.3	Definition of Euler angles. . . . .	123
5.4	A chain and ring of 10 magnetic dipoles. . . . .	134
5.5	Energy of a chain and a ring of 10 magnetic dipoles in the absence of external field. . . . .	135
5.6	A vector representation of a ring of 10 magnetic dipoles. . . . .	137
5.7	Rings of 20 magnetic dipoles in the external field. . . . .	140
5.8	Energy of a chain and a ring of 10 magnetic dipoles in the external field. . . . .	141
5.9	Lower critical field for magnetic dipole rings. . . . .	144
5.10	Upper critical field for magnetic dipole rings. . . . .	145
5.11	Energy barrier $E^*$ of ferrofluid rings. . . . .	148
5.12	Estimation of melting temperature $T_M^*$ of ferrofluid rings. . . . .	149
5.13	Aggregation of 64 magnetic dipoles. . . . .	151



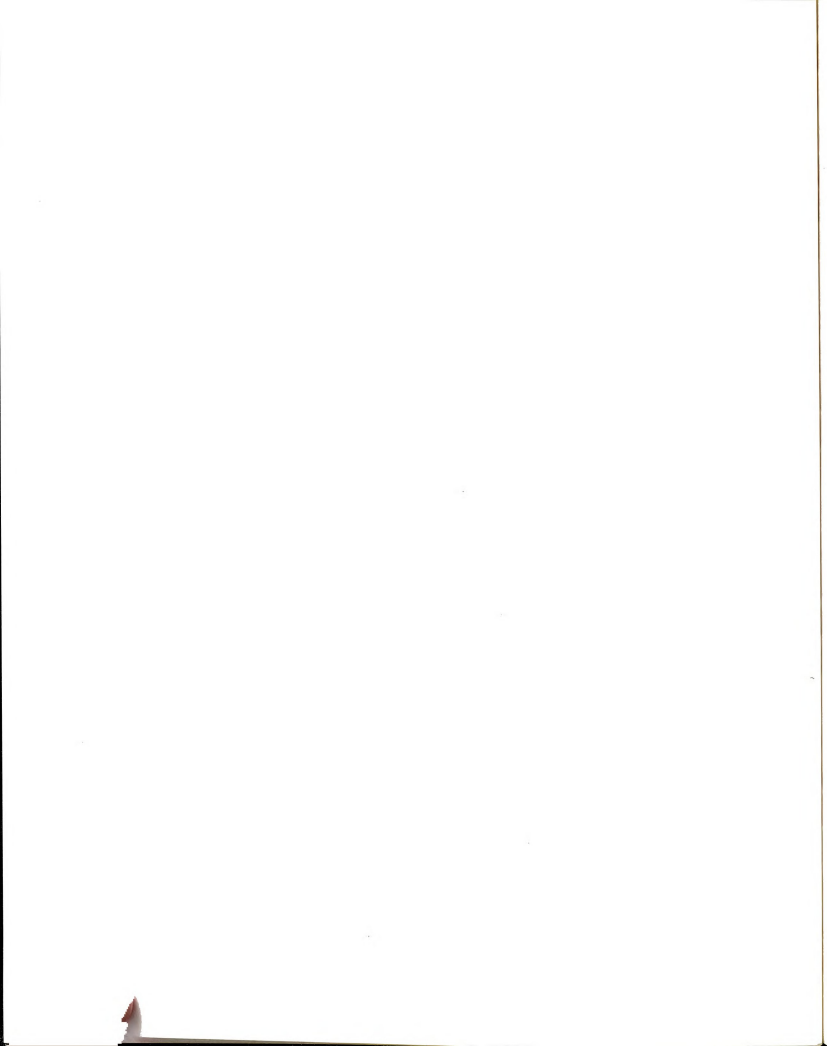


# Chapter 1

## Introduction

The major task of theoretical physics is to understand the fundamental laws which govern nature, use them to explain observed phenomena and predict the properties of new physical systems. The subjects of interest for theoretical condensed matter physics are electronic, magnetic, structural and dynamical properties of solids and liquids. The most fundamental technique to address most of these problems from first principles is the *ab initio* Density Functional Theory (DFT) [Lund83] in the Local Density Approximation (LDA) [Hohe64, Kohn65], which has been shown to describe the ground state properties of solids with high accuracy.

The heavy computational requirement associated with *ab initio* methods such as the LDA, however, limits the range of its applicability to relatively small systems with a high symmetry. In order to describe the dynamical behavior of large systems with low symmetry or disordered systems, we need to use somewhat less demanding approximation schemes. In this thesis, I use the Tight-Binding (TB) method, or parameterized Linear Combination of Atomic Orbitals (LCAO) formalism to study the dynamics and stability of carbon fullerenes. TB method conveniently parametrizes *ab initio* LDA results for structures as different as  $C_2$ ,

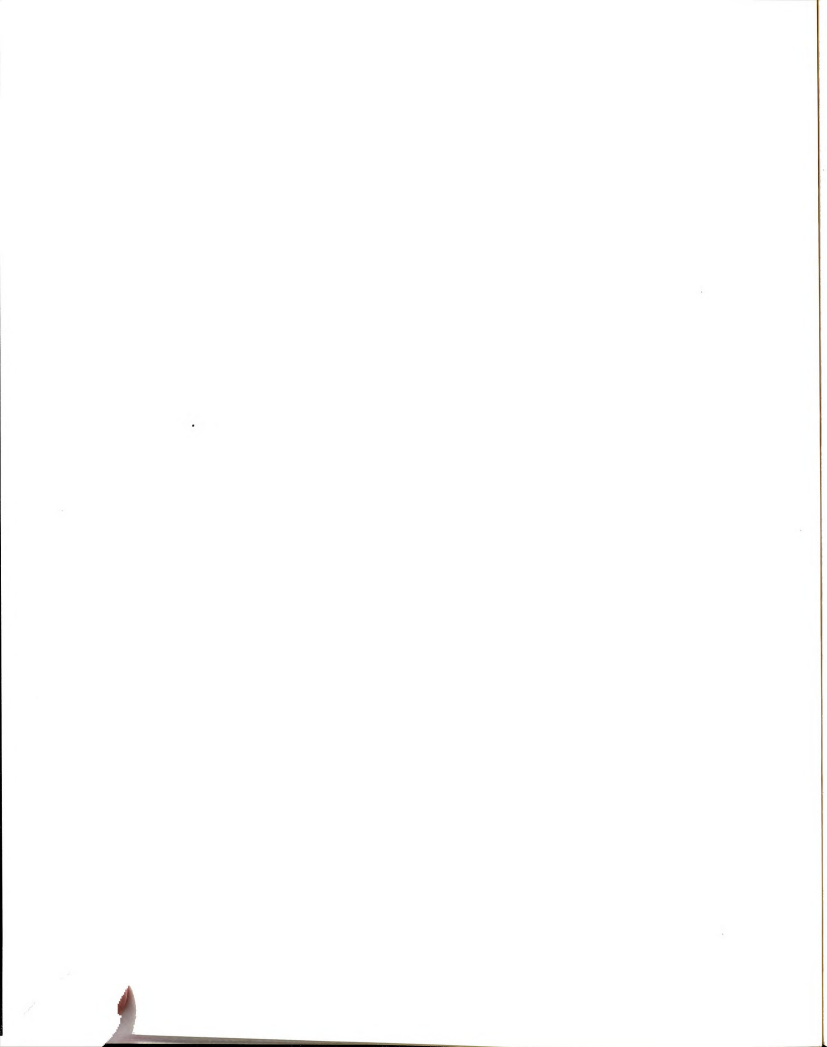


carbon chains, graphite, and diamond [Toma91].

This method is much more efficient in terms of the computational effort and has the essential quantum mechanical features still in the formalism. TB method can be made yet more efficient and fast by adopting the recursion technique [Zhon93] in diagonalizing the Hamiltonian matrix. With an exact numerical diagonalization of the Hamiltonian matrix, the CPU requirement scales as  $N^3$ , for  $N$  the number of particles. Using the recursive method makes the computational load scale as  $N$ . This factor makes a huge difference when we put more than a few hundred atoms in the system. Furthermore if you need to do a Molecular Dynamics (MD) study of these systems the benefit of a linearly scaling numerical method will let us afford to simulate large systems for a sufficiently long time span.

When the object of our study becomes bulk materials, such as a piece of superconductor connected to an external current source or a piece of metal bar clamped in a tensile-test machine, however, there are too many particles in the system to be analyzed or simulated by even the TB method. Moreover, when these bulk materials have random defects it would be hopeless to treat them as the collection of individual atoms or molecules. For systems like a dielectric medium or a superconductor, I use the continuous medium approximation and simply solve the relevant equations of state parameters such as Maxwell's equations and/or the London equation.

For mechanical stability calculations, many systems can be modeled by networks of nodes and bonds. A node denotes a point fixed in the bulk material and a bond represents the interaction between these nodes. By postulating the energy functional for these bonds and tuning the parameters therein this network model



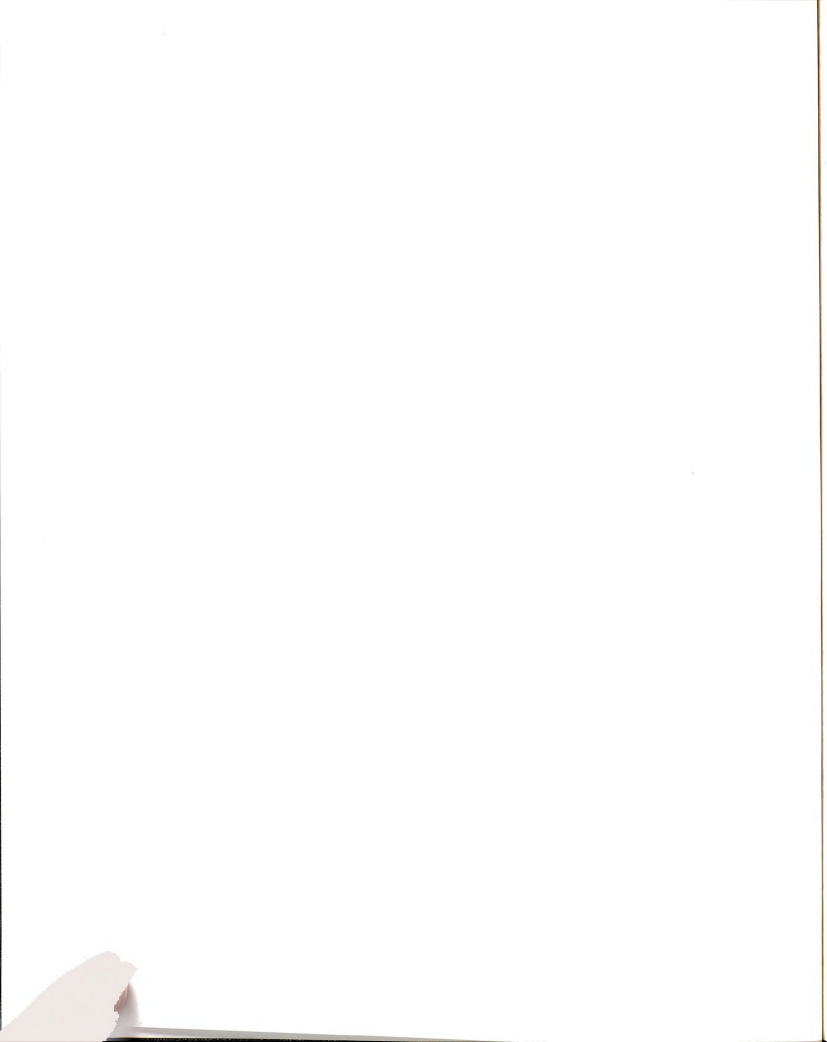
can reproduce the mechanical response of the bulk materials reasonably well. In the studies included in this thesis, I use one of the simplest energy functions, the “simple harmonic oscillator” model. The bond between nodes is represented by a linear Hooke’s spring. The strength of the material is represented by the strength of the springs and the defect can be introduced easily by modifying individual spring constants. The external stress or deformation is specified by setting the proper boundary conditions. The optimum configuration of the system is obtained by minimizing the total energy of the network using the Conjugate-Gradient (CG) method. For this method to be successful, the number of nodes should be sufficiently big and it is usually a couple of orders of magnitude bigger than the number of atoms we can deal with in tight-binding MD or similar methods.

During my years of training for completion of the Doctoral degree, I have worked on four major different subjects. Each subject is in a separate chapter and each chapter has its own introduction and conclusion. In the following, I introduce each chapter and its subject briefly.

## 1.1 Cracks and critical current

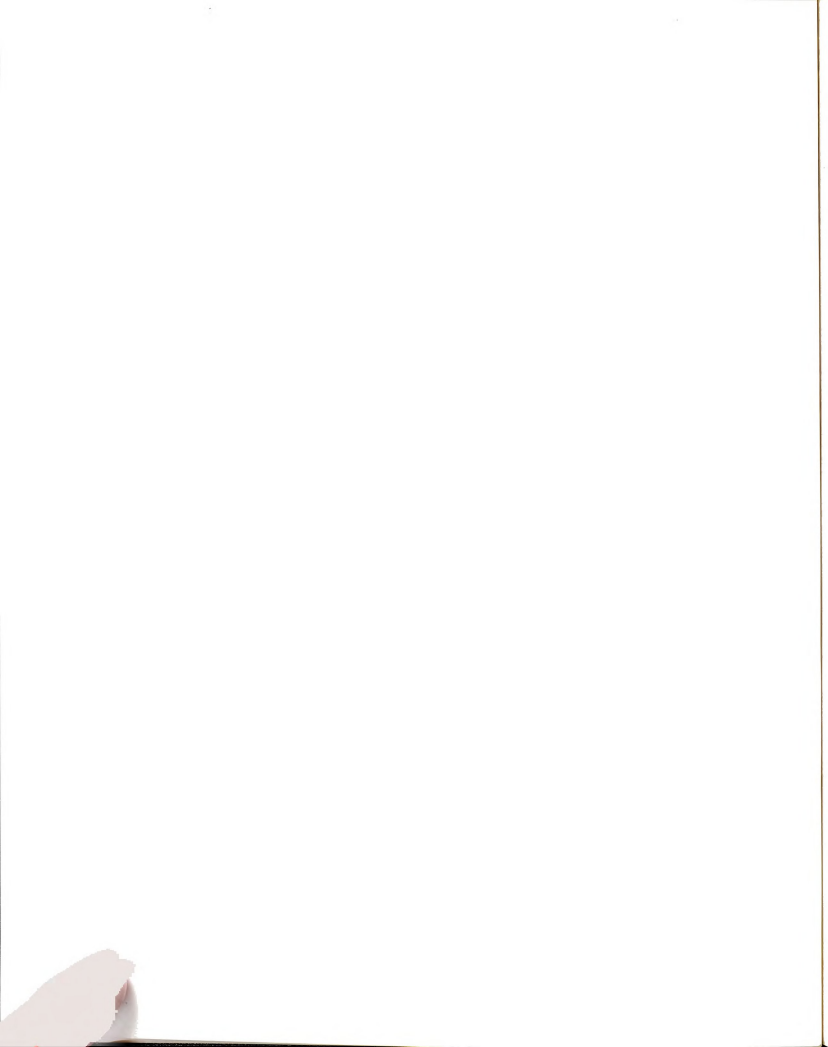
In Chapter 2, the effect of defects on the critical current density of superconductors is studied.

After Kamerlingh Onnes reported the first observation of superconductivity in April of 1911, superconductivity became one of the most researched subjects in the science community. There has been vast developments in terms of discovering more and more superconducting materials and enhancing the quality of the superconductors. It is a well known fact that superconducting materials are not



always superconducting. They need to have very special conditions to be superconducting. One of these conditions is the so-called “critical current density”,  $j_c$ , of a superconductor. There is a maximum current density a superconductor can support. Thus when you have an inhomogeneous current density distribution in the superconducting medium, the location where it has the maximum current density is the most vulnerable to this transition. It is well known that cracks (of width,  $w > \xi_s$ ) are effective in enhancing local current density.

In this chapter I calculate the size of these hotspot supercurrents as a function of the crack length,  $a$ , and the London penetration depth,  $\lambda$ , using 2D London theory. The current density enhancing factor for a given crack size is studied as a function of the penetration depth and the intensity of vortex pinning. We argue that large local supercurrents near a surface crack nucleate vortex creation. If flux pinning is weak enough these vortices flow under the influence of the large local Lorentz force. The dissipation so produced can lead to a reduction in observed critical current. If flux pinning is moderate, the first additional vortices nucleated near the crack tip are pinned, in a region we label  $\rho$ , the flux pinning zone. In the case of a through crack in a thin film, we then argue that  $j_c(a)$  reduces as  $j_c(a)/j_c(0) \sim (\rho/a)^x$  (for  $a/L \ll 1$ ), where  $L$  is the film width and  $x = 1/2$  for the simplest London theory. We compare this theory with the Bean (critical state) model which predicts that the critical current is (approximately) determined by the cross-section available for supercurrent, so that in a film containing a crack,  $j_c(a)/j_c(0) \sim 1 - a/L$  (ignoring self field effects). We argue that superconductors with sufficiently weak pinning should obey the hotspot theory, while sufficiently hard superconductors should obey the critical state model, and suggest experiments that should illustrate these two limiting cases.



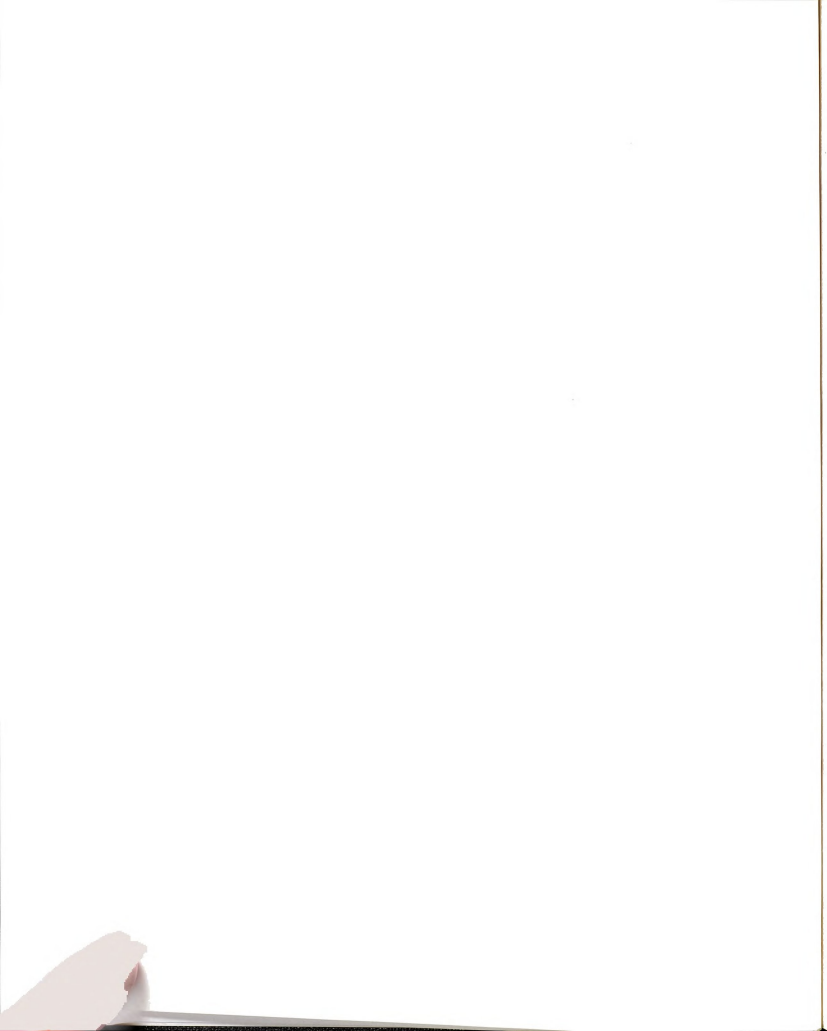


## 1.2 Elasticity and fracture of disordered networks

In Chapter 3 I discuss the elasticity and mechanical failure of random spring networks.

Many alloys and composites are disordered. In fact no material is perfect and the strength of a given material is very much dependent on these minor flaws or defects. Thus understanding the effects of random defects and their statistics is very crucial in analyzing material strength. The effective elastic properties of these materials can be calculated using effective medium theory and other "homogenization" methods. Due to the fact that fracture is initiated in regions of high stress, it is to be expected that homogenization methods, unless they focus in the crack growth region, should be poor predictors of the effect of disorder on failure strength.

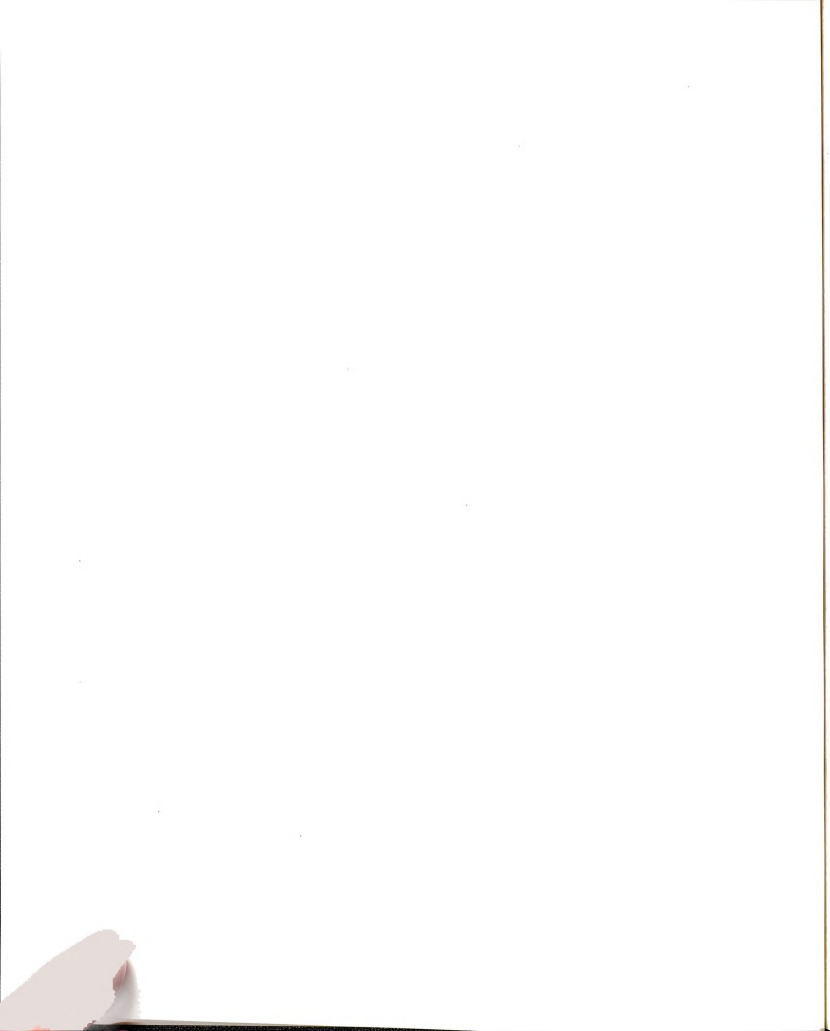
Random networks with "realistic" interatomic and many body potentials are now routinely simulated on a computer. Recently, detailed analytic and numerical analysis of idealised disordered microstructures have been performed [Herr90, Sahi91]. Along with new scaling theories specifically taking into account the extreme statistics of brittle fracture[Duxb87a, Duxb91, Beal88], these simulations have lead to new insights into the fracture of materials. In this chapter, we discuss the use of these methods to study fracture of brittle materials.



## 1.3 Melting of carbon fullerenes

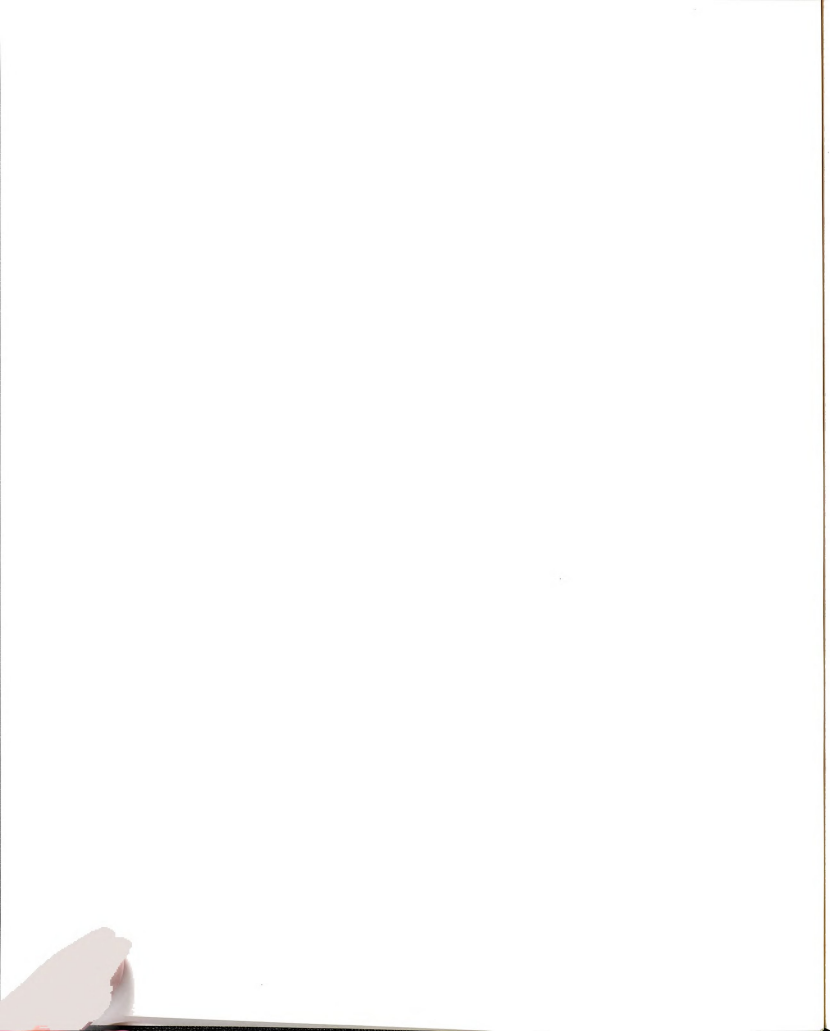
Chapter 4 contains the work I did for carbon fullerenes. Carbon fullerenes, such as  $C_{60}$  [Krot85], are intriguing molecules with a hollow soccer ball structure and a large range of interesting properties [Bill93]. Due to the high structural stability of these systems [Curl88], almost no information is available about their equilibrium phases at temperatures close to and exceeding the melting point of graphite. We expect the phase diagram of these strongly correlated structures to be very interesting and to consist of several well identifiable "molten" phases.

A second reason to study the high-temperature behavior of fullerenes is related to their formation. While bulk quantities of fullerenes can now be routinely synthesized in a carbon arc [Krat90], the microscopic mechanism of their aggregation from the gas phase is still the subject of a significant controversy [Waka92, Waka93, Ebbe92, Kern92, Held93, Hunt94]. During the formation process, fullerenes will be created from many different intermediate structures. They also will have many unsuccessful trials and to form such a high symmetry structure from the gas phase will require a tremendous amount of encounters between even correctly matching parts of the structures. Therefore to simulate the formation of fullerenes we will have to have many carbon atoms in a simulation box and wait for a long time to have some closed structures, without even counting the number of atoms in the cluster. As an alternative approach, we hope that a detailed study of the annealing process may shed new light on this controversy, since intermediate structures, which occur during thermal quenching in the rare gas atmosphere, may also be observed while heating up these structures to high temperatures.



A third motivating reason for this study are recent collision experiments which indicate that fullerene molecules are extremely resilient and only fragment at energies exceeding  $\approx 200$  eV [Camp93]. Since in the collision process the kinetic energy is transferred into internal degrees of freedom as "heat", additional information about the intermediate structures of colliding fullerenes could be obtained by investigating those of the superheated molecules.

In an attempt to elucidate the above three problem areas, we performed a detailed molecular dynamics (MD) study of the melting and evaporation process of three prototype fullerenes, namely  $C_{20}$ ,  $C_{60}$ , and  $C_{240}$ . In our simulation, we investigated the response of a canonical ensemble of fullerenes to gradually increasing heat bath temperatures using Nosé-Hoover molecular dynamics [Nose84, Hoov85, Alle90], complementing recent microcanonical ensemble simulations on  $C_{60}$  and  $C_{70}$  [KimE93]. Of course, the quality of simulation results depends primarily on the adequacy of the total energy formalism applied to the fullerenes. Since our simulation also addresses the fragmentation under extreme conditions, the formalism used must accurately describe the relative stability of fullerenes with a graphitic structure and their fragments, mostly short carbon chains. The corresponding transition from  $sp^2$  to  $sp$  bonding can only be reliably described by a Hamiltonian which explicitly addresses the hybridization between  $C2s$  and  $C2p$  orbitals. A precise evaluation of interatomic forces is required to obtain the correct long-time behavior of the system. On the other hand, the long simulation runs necessary to equilibrate the small systems during the annealing process, and the large ensemble averages needed for a good statistics, virtually exclude *ab initio* techniques as viable candidates for the calculation of atomic forces.

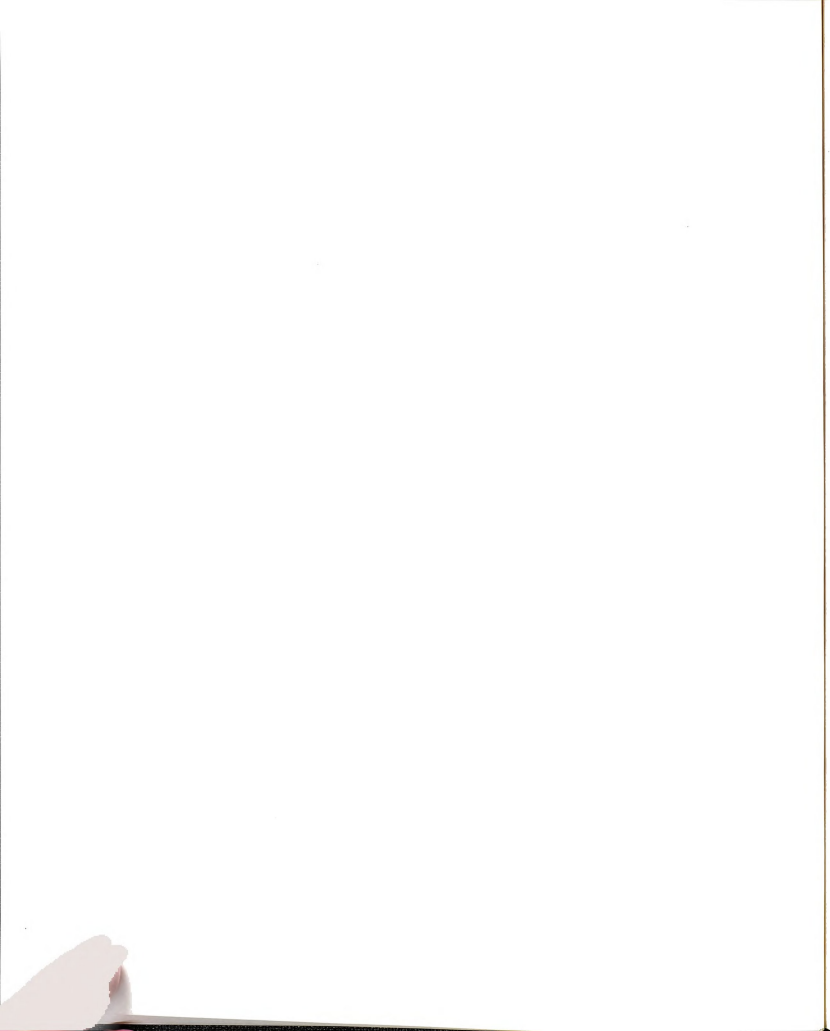


For this reason, we base our force calculation on a Linear Combination of Atomic Orbitals (LCAO) formalism which conveniently parametrizes *ab initio* Local Density Approximation (LDA) [Hohe64, Kohn65] results for structures as different as  $C_2$ , carbon chains, graphite, and diamond [Toma91]. We use an adaptation of this formalism to very large systems, which is based on the fact that forces depend most strongly on the local atomic environment and which has been implemented using the recursion technique [Zhon93]. The force calculation can be performed analytically to a large degree. This not only speeds up the computations significantly, but also provides an excellent energy conservation  $\Delta E/E \lesssim 10^{-10}$  between time steps in microcanonical ensembles, and a linear scaling of the computer time with the system size. Most importantly, forces on distant atoms can be efficiently calculated on separate processors of a massively parallel computer.

Using MD simulation, we heat up carbon fullerenes and monitor the changes in various structural and thermodynamic responses of the system. We identified many well defined intermediate structures of fullerenes. Among others, we found a most dramatic transition to a previously unknown “pretzel” phase to occur at a high temperature of  $T \gtrsim 4000$  K. The temperature where fullerenes disintegrate into carbon chains is explained using quantitative results for the entropy.

## 1.4 Stability of Magnetic Dipole Structures in Ferrofluids

Chapter 5 contains the work on ferrofluids. A ferrofluid is a magnetic colloid made of magnetite particles suspended in a liquid, usually a petroleum oil [Rose85, Wang94]. A typical electrorheological (ER) fluid consists of a suspension of fine

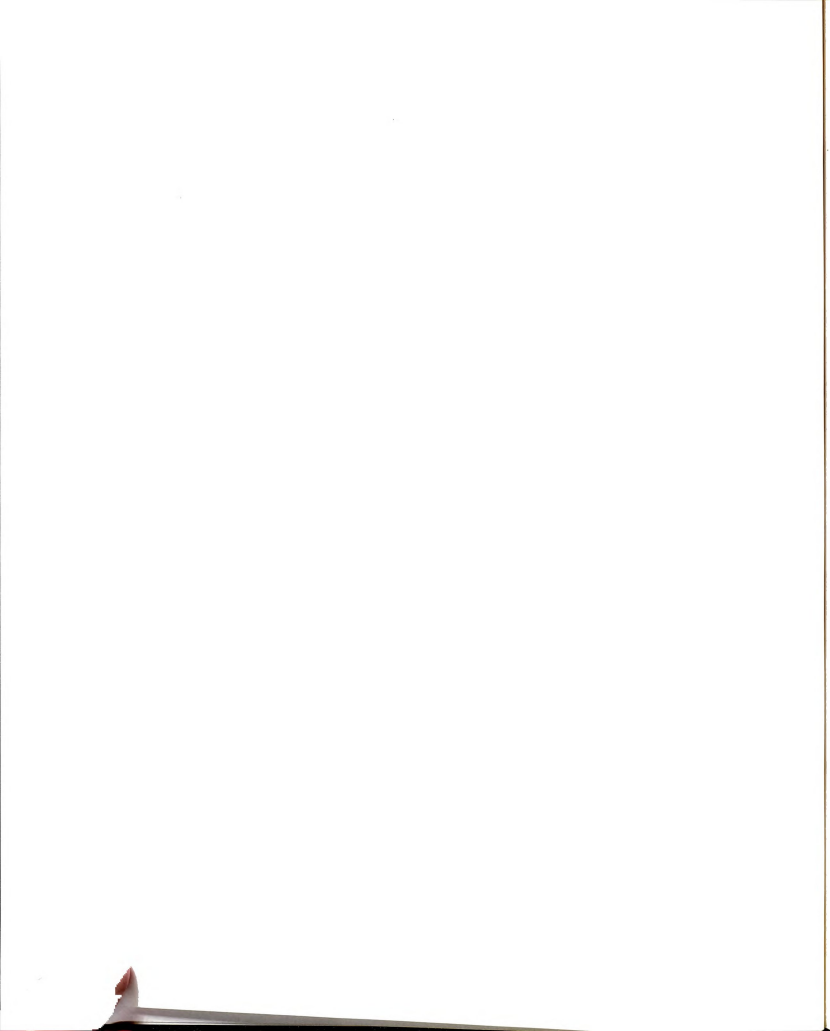




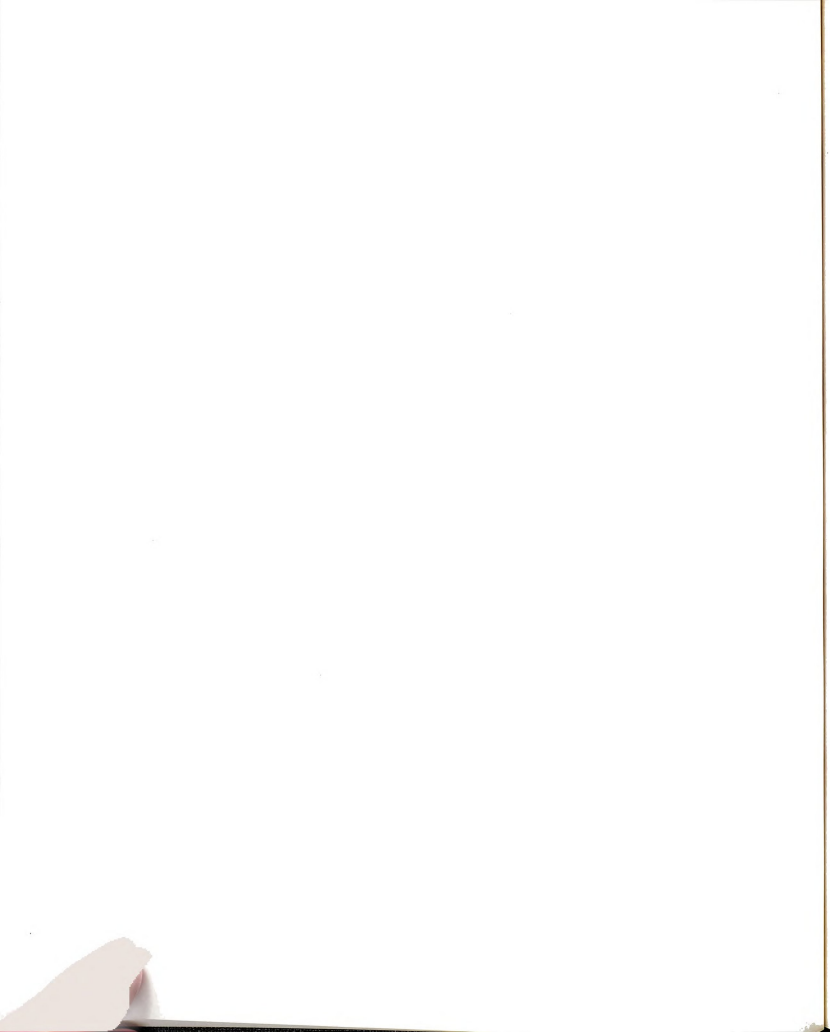
dielectric particles in a liquid of low dielectric constant [TaoR92, Bloc87, Fili88]. The aggregation of these particles has been the subjects of many experiments and numerical simulations. Experiments find that upon application of an electric field, dielectric particles in ER fluids rapidly form chains which then aggregate into thick columns [Hals90, Chen92, Mart92, Gind92]. Magnetic ferrofluids forms a similar structure of chains and thick columns. The dependence of the periodicity of columns on the sample thickness has been recently studied using the magnetite colloids [Wang94]. Also many numerical simulations using the molecular dynamics (MD) [Hass89, Klin89, Kusa90, Bonn92, TaoR94] has been carried out to find the orientational ordering in ER liquid crystals.

Even though a few MD simulation results have been published for ferroelectric dipole liquids [WeiD92a, WeiD92b], almost no MD simulation results are available for the magnetic ferrofluid systems except a few simulations using the Monte Carlo technique [Weis93, Stev94]. There is one fundamental difference between ER fluids and magnetic ferrofluids even though they have many common properties. In ER fluids, the dipoles are induced by an applied electric field and they are always along the field. The strength of their dipole moments depends on the local electric field and therefore they do not show any interesting properties in the absence of the external field. On the contrary, the magnetic particles in ferrofluids have their own pre-assigned magnetic moments. This means that in general they are not obliged to be aligned with the external field and we have to consider the rotations of these particles as well as their positions. Also we should expect that these fluids have some non-trivial structures even in the absence of the external field.

In this chapter I will discuss the early stages of colloidal aggregation in ferrofluids and the stability of the ring structure of these particles. We found that



the ring is more stable for ferrofluid particles in low field and low temperature as long as it has more than 4 particles per ring. An estimation of the energy barrier between the ring structure and chain structure is presented along with the melting temperature in an external magnetic field.



## Chapter 2

### Cracks and critical current

In superconductors, cracks (of width,  $w > \xi_s$ ) are effective in enhancing local supercurrent, and we calculate the size of these supercurrent hotspots as a function of the crack length,  $a$ , and the London penetration depth,  $\lambda$ , using 2D London theory. In the  $\lambda \rightarrow \infty$  limit and constant injected current density, we show that *this 2D solution is also exact for the current flow in a thin film containing a through crack*. We argue that large local supercurrents near a surface crack nucleate vortex creation. If flux pinning is weak enough these vortices flow under the influence of the large local Lorentz force. The dissipation so produced can lead to a reduction in observed critical current. If flux pinning is moderate, the first additional vortices nucleated near the crack tip are pinned, in a region we label  $\rho$ , the flux pinning zone. In the case of a through crack in a thin film, we then argue that  $j_c(a)$  reduces as  $j_c(a)/j_c(0) \sim (\rho/a)^x$  (for  $a/L \ll 1$ ), where  $L$  is the film width and  $x = 1/2$  for the simplest London theory. We compare this theory with the Bean (critical state) model which predicts that the critical current is (approximately) determined by the cross-section available for supercurrent, so that in a film containing a crack,  $j_c(a)/j_c(0) \sim 1 - a/L$  (ignoring self field effects). We argue that superconductors with *sufficiently weak pinning should obey the*

*hotspot theory*, while *sufficiently hard superconductors should obey the critical state model*, and suggest experiments that should illustrate these two limiting cases.

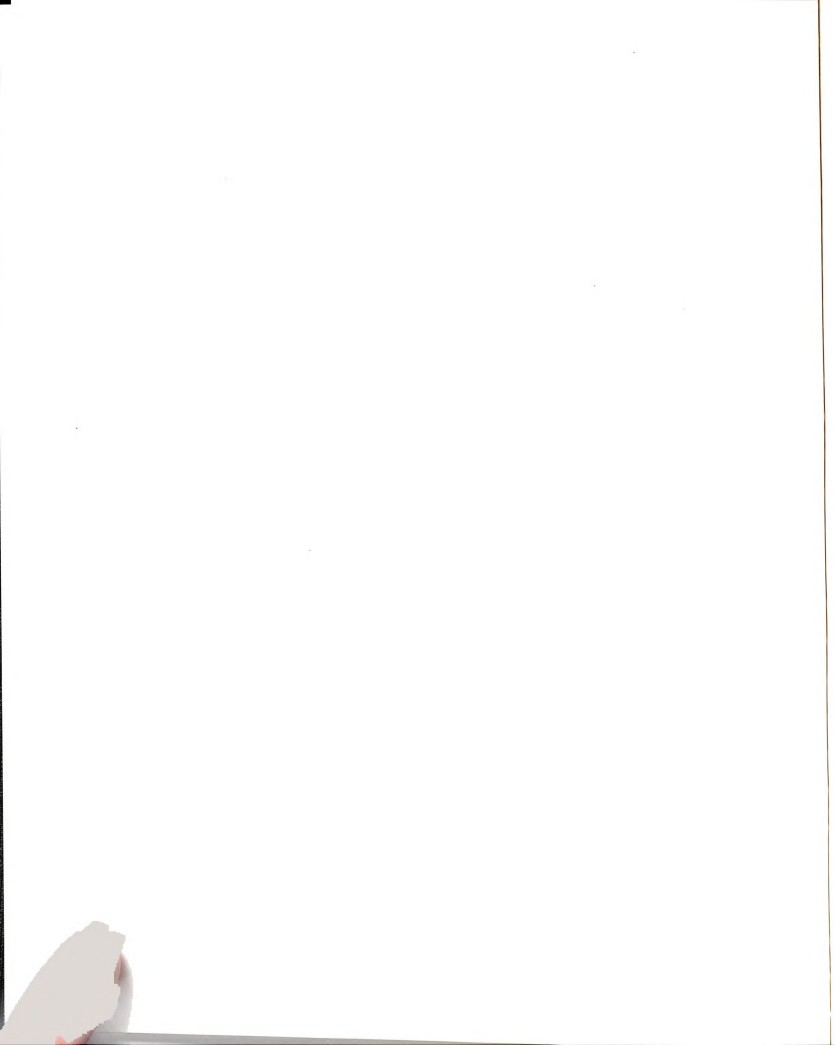
This chapter contains materials which have appeared in the following publication:

- [KimS91] S.G. Kim and P.M. Duxbury, *Cracks and critical current*, J. Appl. Phys. 70, 3164 (1991).

## 2.1 Introduction

In the Bean[Bean64] (critical state) model of hard type II superconductors, the supercurrent flows in shells in which the current is at its critical current level, and the remaining parts of the superconductor carry no current. The macroscopic critical current occurs when the “local” critical current flows throughout a cross-section of the sample. This model predicts that the observed critical current is relatively insensitive to extended defects such as cracks (critical current is reduced roughly according to the cross-section of the extended defect). In this paper we show that if pinning is sufficiently weak, a crack can cause a much more rapid reduction in observed critical current due to the nucleation and flow of vortices from the crack tip.

We initiate a study of the origins and consequences of large local supercurrents, by studying the effect of a crack on supercurrent flow in thin film superconductors. This is a natural starting point, as it is known from the study of electrical[Duxb87a, Duxb87b] and mechanical failure[Kell86] that cracks or crack shaped flaws are very efficient at enhancing current or stress. As the simplest non-trivial illustration of the effect, we use 2D London theory to show that a crack



can lead to large local supercurrents. This effect is demonstrated analytically in Sec. [2.2] and the analytic calculations are supported by numerical solutions to the London equation in Sec. [2.3]. In the limit  $\lambda \rightarrow \infty$ , we show that the 2D London theory is exact for a thin film containing a through crack.

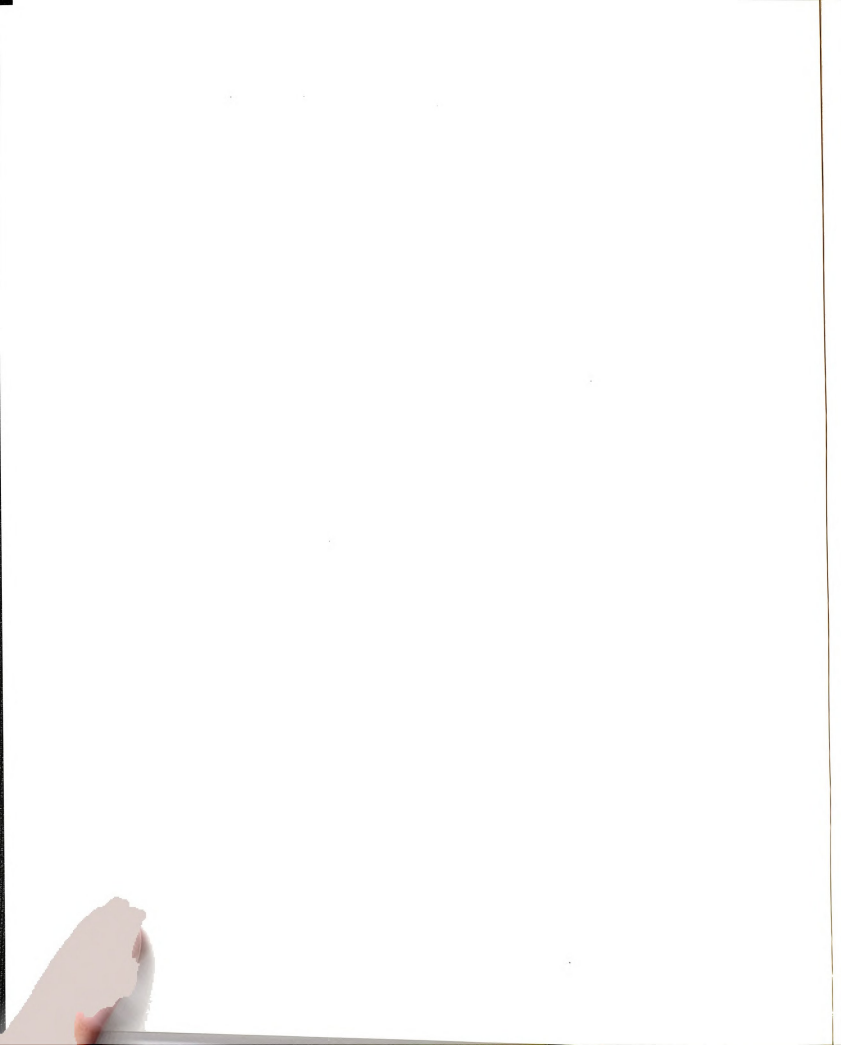
In Sec. [2.4] we consider the effect of large local supercurrents on critical current. We argue that large local supercurrents act as nucleation sites for vortex creation. Once created, the vortex lines will flow and cause dissipation, if the local flux pinning is insufficient to resist the Lorentz force on the vortex line. We thus argue that large local supercurrents degrade critical current most in weak pinning superconductors where flux lines can be depinned by the additional Lorentz force due to large local supercurrents. Using these ideas in combination with the London theory calculations of Sec. [2.2], we make some specific predictions for the dependence of the critical current of a superconducting film on the length of a (lithographically drawn) through crack in the film. These predictions are compared with the results one would expect using the simplest critical state model. Sec. [2.5] contains a summary of the main results of this study.

## **2.2 Supercurrent enhancement at a crack tip**

### **2.2.1 The Model**

To illustrate the effect of crack on supercurrent flow, we use 2D London theory. London theory is known to provide a good semi-quantitative description of strongly type II superconductors away from  $T_c$  [Tink65, Duze81, Till86, Orla91]. In particular the London model does a fairly good job of predicting the field profile and current flow near vortex lines. A crack can be modelled as a line of vortices,





so we expect that London theory will also provide a good first approximation in this problem. We must keep in mind though that the theory is incorrect on length scales shorter than  $\xi$ .

Although the 2D theory is only strictly valid for an infinitely thick film containing a through crack, we show later in this section, that in the  $\lambda \rightarrow \infty$  limit, it is also exact for the current flow pattern in a thin film containing a through crack. In the 2D geometry, current flow is in the  $x$ - $y$  plane, so that only the  $z$ -component of magnetic field is finite. This reduces the London theory to a scalar Helmholtz equation for the  $z$ -component of the magnetic field,  $B$ :

$$\nabla^2 B(x, y) = B(x, y)/\lambda^2. \quad (2.1)$$

Here  $B$  is a function of  $x$  and  $y$ , and the current is found from  $B$  via the Maxwell equation,

$$\mathbf{j} = \frac{c}{4\pi} \nabla \times [0, 0, B(x, y)]. \quad (2.2)$$

Using Eqs. (2.1) and (2.2), we will calculate the current flow in the geometry shown in Fig. 2.1.

We wish to calculate the current flow pattern using as a boundary condition

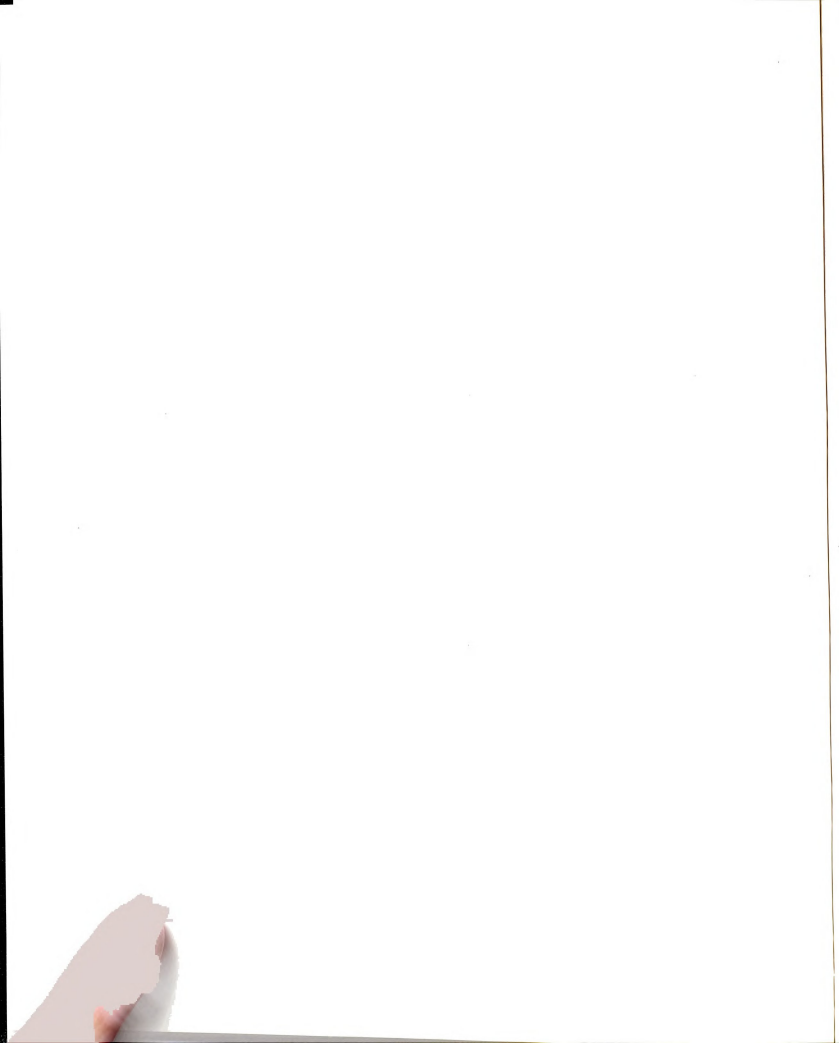
$$\mathbf{j}(x, y) = [0, j_0 \exp(-x/\lambda)] \quad \text{as } y \rightarrow \pm\infty. \quad (2.3)$$

This is achieved by imposing the field boundary condition,

$$B(x, y) = B_0(x) = A_0 \exp(-x/\lambda) \quad \text{as } y \rightarrow \pm\infty. \quad (2.4)$$

with

$$A_0 = \frac{4\pi\lambda j_0}{c}. \quad (2.5)$$



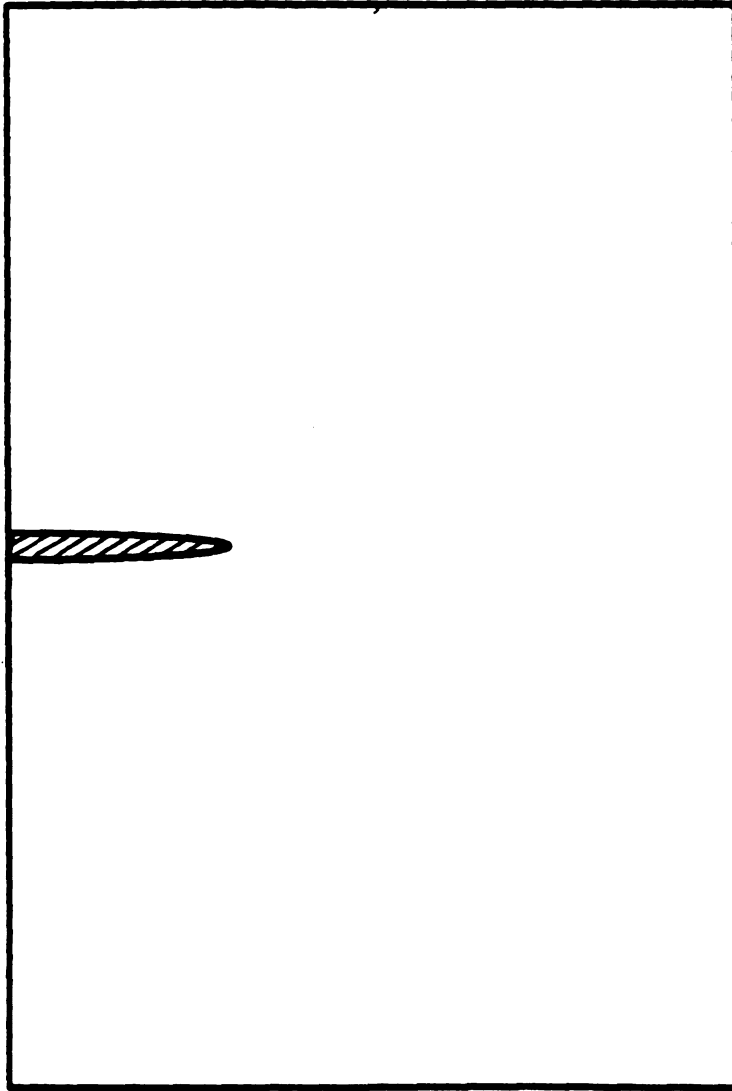
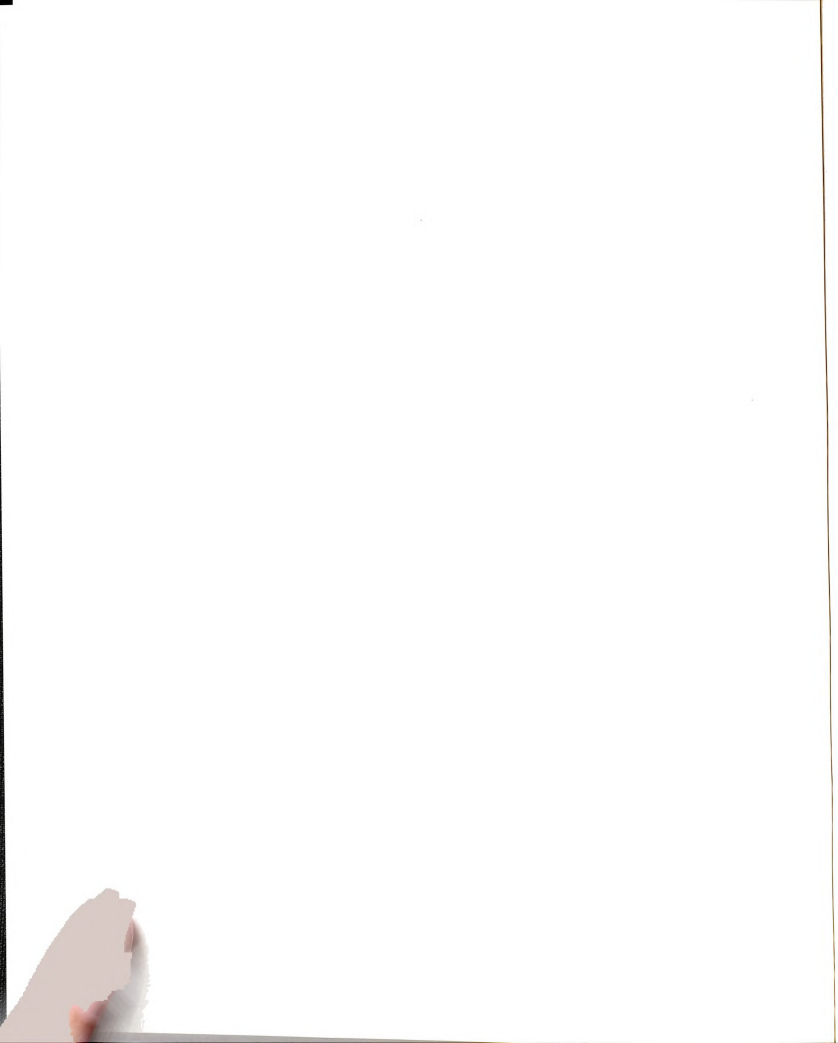


**Figure 2.1:** A superconductor with elliptic defect used in the analytic calculations.



Another boundary condition we impose is that there is no current normal to the surfaces of the superconductor (including the surfaces of the crack-like ellipse). Note that since we are solving for a problem with constant current boundary conditions inside the film and zero current outside the film, we in principal solve for the current pattern inside the film first and then generate the magnetic field patterns interior and exterior from it. It turns out that it is mathematically convenient to still work in terms of the magnetic field, but the physical geometry should be kept in mind when thinking about the solution. To satisfy the boundary conditions at the crack surface, it is convenient to use elliptic coordinates  $(\xi, \eta)$ [Mors53] as illustrated in Fig. 2.2. In this coordinates an ellipse defined by:

$$x^2/a^2 + y^2/b^2 = 1 \quad (2.6)$$

using the usual elliptic variables,

$$\begin{cases} x = C \cosh \xi \cos \eta \\ y = C \sinh \xi \sin \eta \end{cases} \quad (2.7)$$

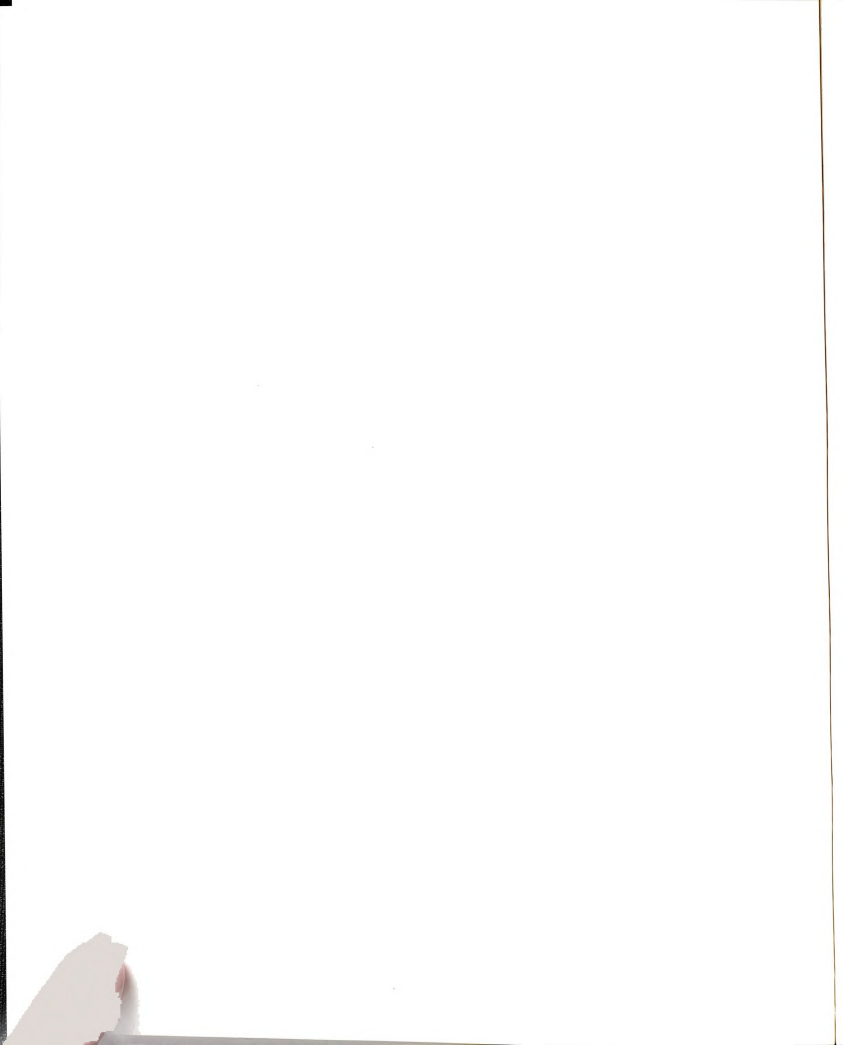
where

$$\begin{cases} a = C \cosh \xi_0 \\ b = C \sinh \xi_0 \\ C = \sqrt{a^2 - b^2} \end{cases} \quad (2.8)$$

Physically,  $\xi$  and  $\eta$  are the radial and angular coordinates respectively and the surface of an ellipse is generated by fixing  $\xi = \xi_0$  and allowing  $\eta$  to vary between  $-\pi/2$  and  $\pi/2$ .

Separation of variables:

$$B(\xi, \eta) = f(\xi)g(\eta) \quad (2.9)$$



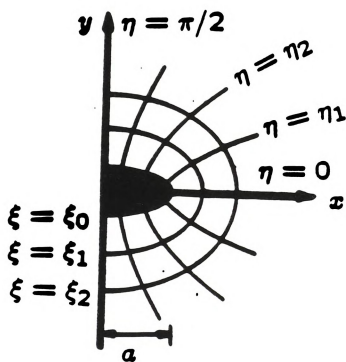
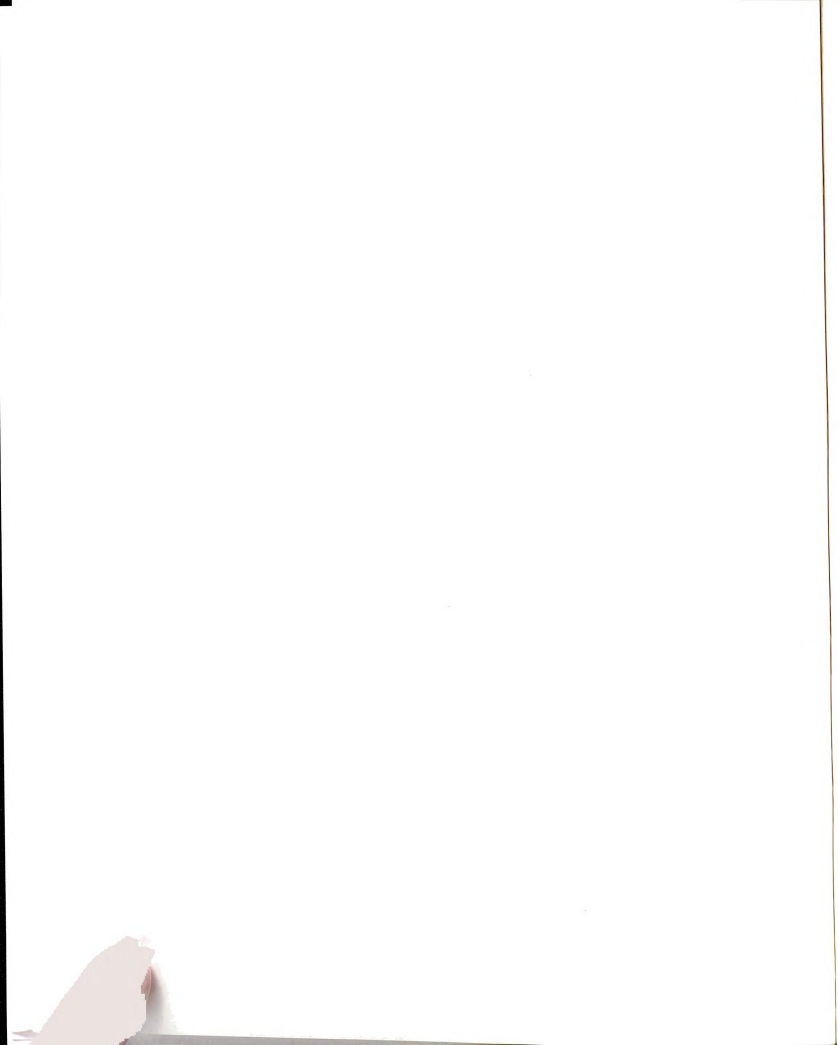


Figure 2.2: Elliptic coordinates.





leads to

$$\frac{d^2 g}{d\eta^2} + (s + 2q \cos 2\eta)g = 0 \quad (2.10)$$

and

$$\frac{d^2 f}{d\xi^2} - (s + 2q \cosh 2\xi)f = 0 \quad (2.11)$$

where  $q = (C/2\lambda)^2$  and  $s$  is a separation constant. Equations (2.10) and (2.11) are the original and modified Mathieu equations[McLa46, Abro72, Grad80] and arise in a variety of quantum and classical scattering problems[Bowm87, McLa47] (note though that the sign of  $q$  is opposite that occurring in such problems). To include the boundary condition of Eq. (2.4), we write

$$B(\xi, \eta) = B_0(x) + B_1(\xi, \eta) \quad (2.12)$$

and we choose radial solutions to Eq. (2.11) that ensure that  $B_1(\xi, \eta)$  goes to zero at large  $\xi$ .

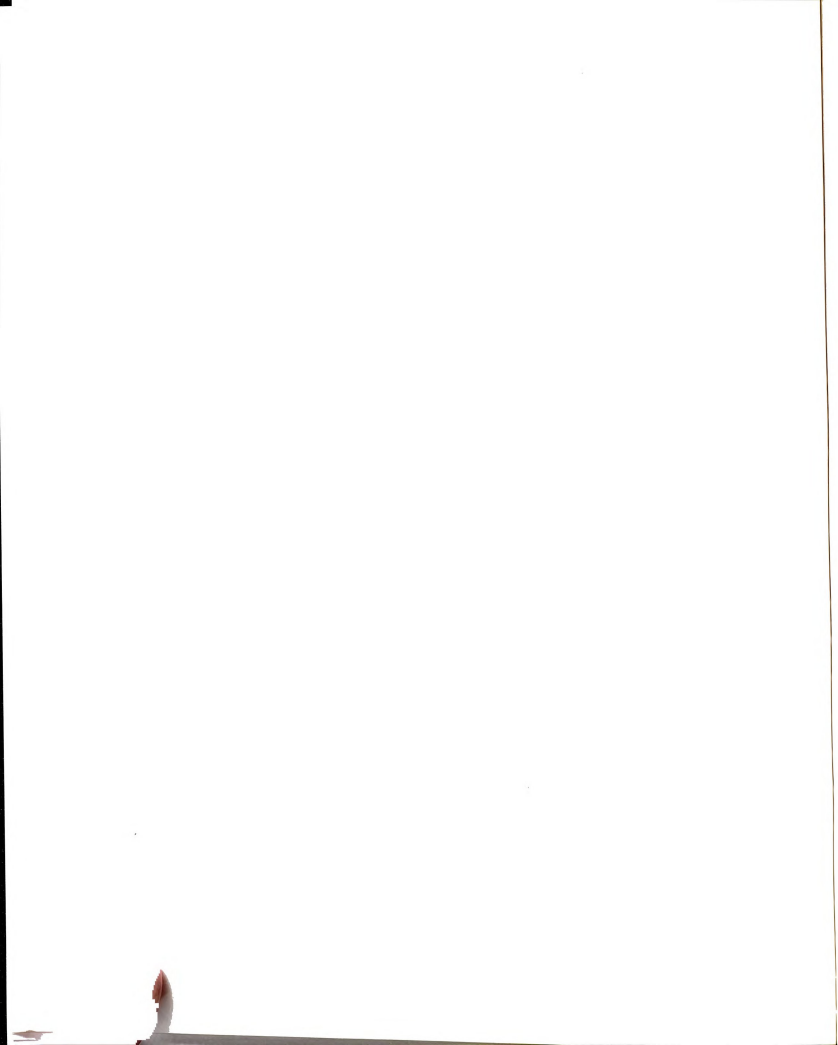
### 2.2.2 Exact solution as $a/\lambda \rightarrow 0$

Equations (2.10) and (2.11) do not yield to simple closed form solution, so it is instructive to consider the limit  $a/\lambda \rightarrow 0$  where a closed form solution is straightforward (this limit is also relevant to thin films where the effective penetration depth is large). In this limit, the boundary condition

$$B_0(x) = A_0(1 - x/\lambda) \quad \text{for } y \rightarrow \pm\infty \quad (2.13)$$

leads to

$$\begin{aligned} B(x, y) = & A_0(1 - x/\lambda) \\ & + A_0(a/\lambda) \exp(-[\xi - \xi_0]) \cos \eta \end{aligned} \quad (2.14)$$



for the magnetic field exterior to the ellipse. From this solution it is straightforward to calculate the supercurrent pattern in the film using Eq. (2.2). The results are

$$j_{\xi}(\xi, \eta) = (j_0/\tau)\{C \cosh \xi \sin \eta - a \exp[-(\xi - \xi_0)] \sin \eta\} \quad (2.15)$$

and

$$j_{\eta}(\xi, \eta) = (j_0/\tau)\{C \sinh \xi \cos \eta + a \exp[-(\xi - \xi_0)] \cos \eta\} \quad (2.16)$$

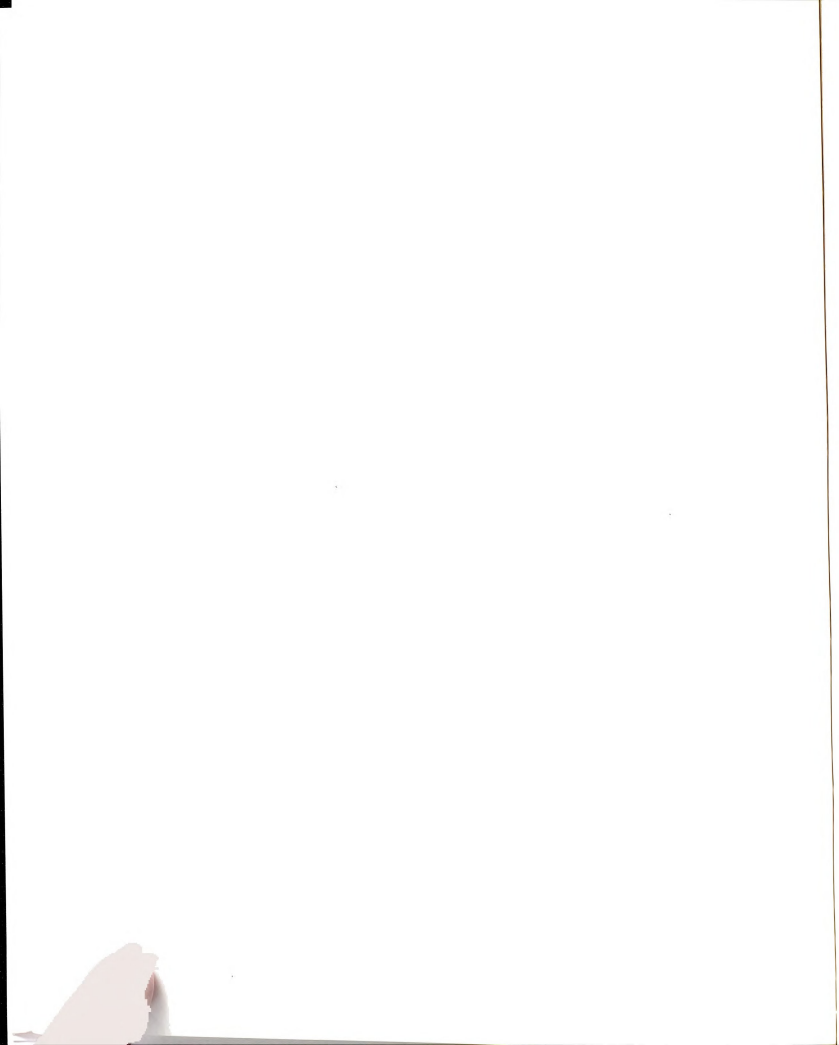
where

$$\tau^2 = C^2(\sinh^2 \xi + \sin^2 \eta). \quad (2.17)$$

A detailed study of these solutions near the crack tip shows that there is a large enhancement in the current density in the  $y$  direction at the crack tip. The current density may be calculated as a function of distance (in the  $x$ -direction - see Fig. 2.1) from the crack tip (on the central axis of the crack) by evaluating the current in the  $\eta$  direction as a function of  $\xi$ : Using  $\xi = \cosh^{-1}(x/C)$  at  $\eta = 0$  and taking  $x = a + r$ , we find the current behavior presented in Fig. 2.3 (the result is identical to that found in a classical conductor containing an insulating inclusion[LiYS89]).

The behavior of Fig. 2.3 can be asymptotically summarized as follows:

$$j_v(r)/j_0 \sim \begin{cases} 1 + (a/2\rho)^{1/2} & \text{if } r \ll \rho; \\ 1 + (a/2r)^{1/2} & \text{if } \rho \ll r \ll a; \\ 1 + a^2/(2r^2) & \text{if } r \gg a; \end{cases} \quad (2.18)$$



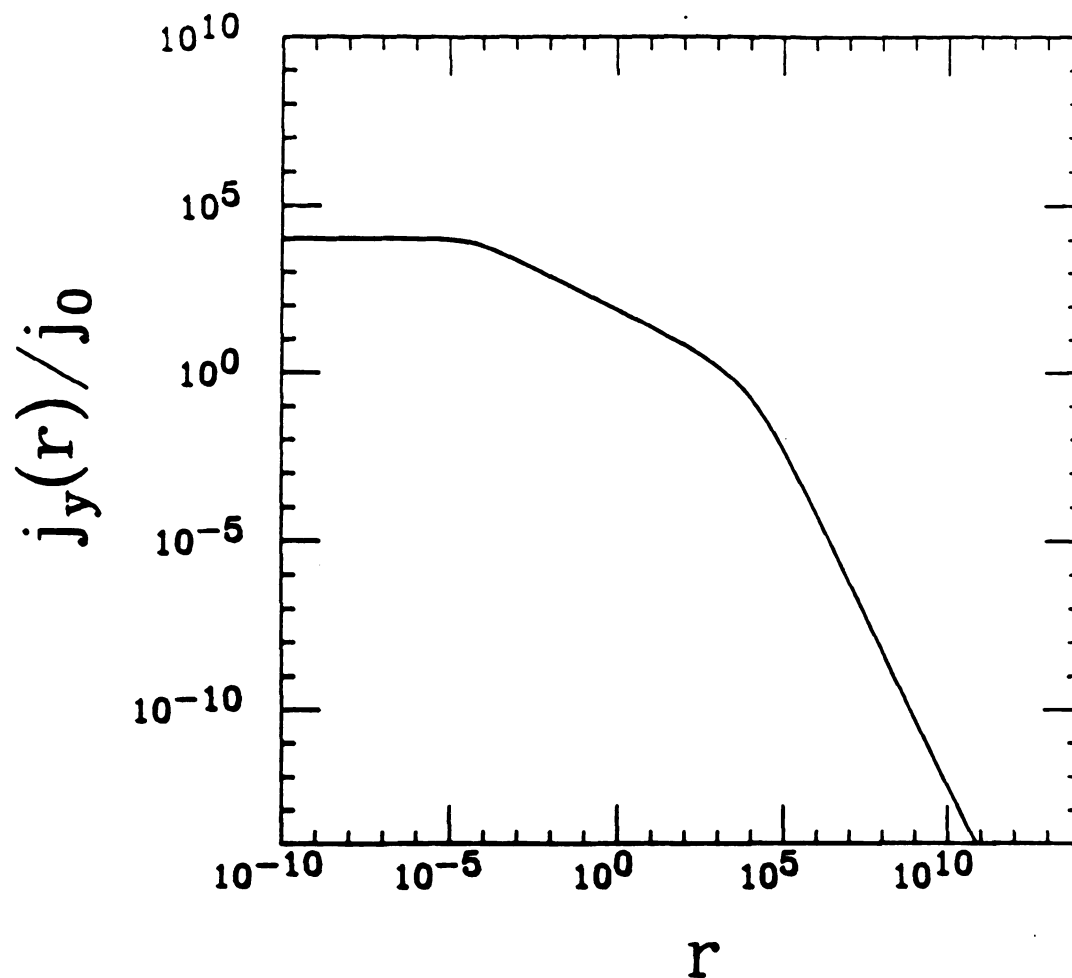
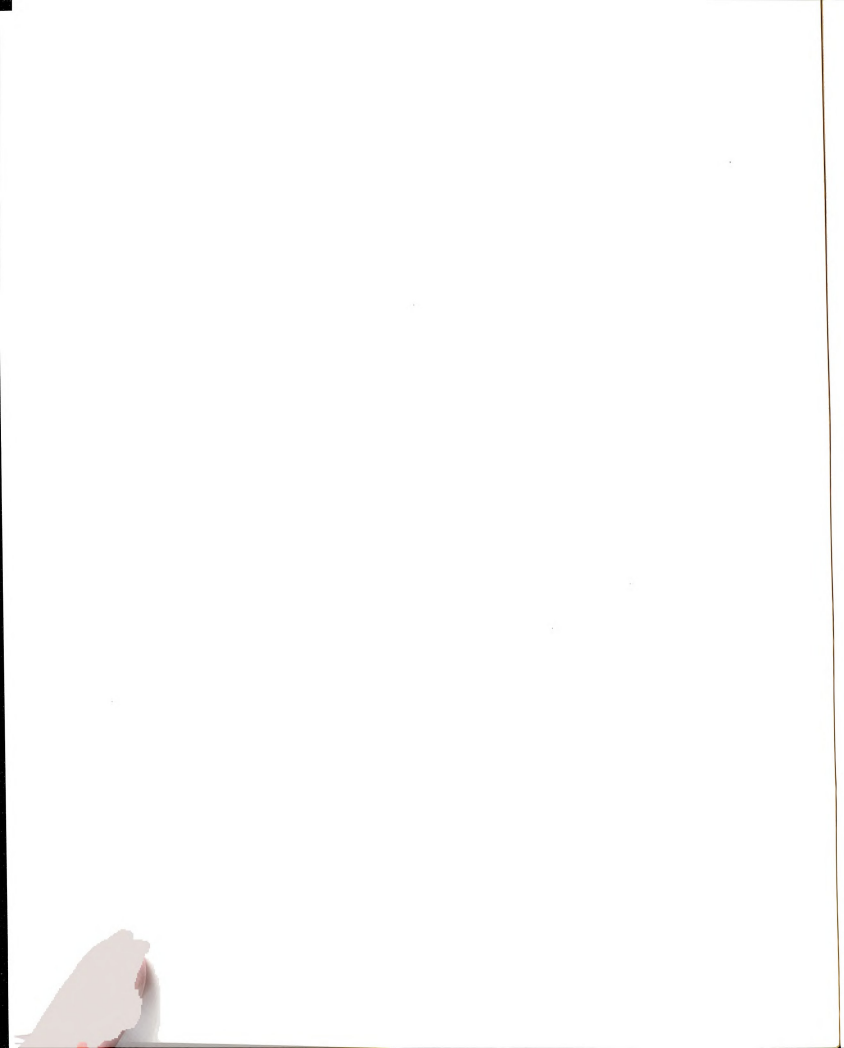


Figure 2.3: The magnitude of current density as a function of distance (in the  $x$ -direction) from the crack tip when  $\lambda \gg a$  and  $a/b = 1000$ . The asymptotic behaviours predicted by the analytic calculation of Eqs. (2.18) are clearly evident.



where  $\rho = b^2/2a$  is the crack tip curvature. One important feature of this result is that the magnitude of current in a region of size  $\rho$  near the crack tip is

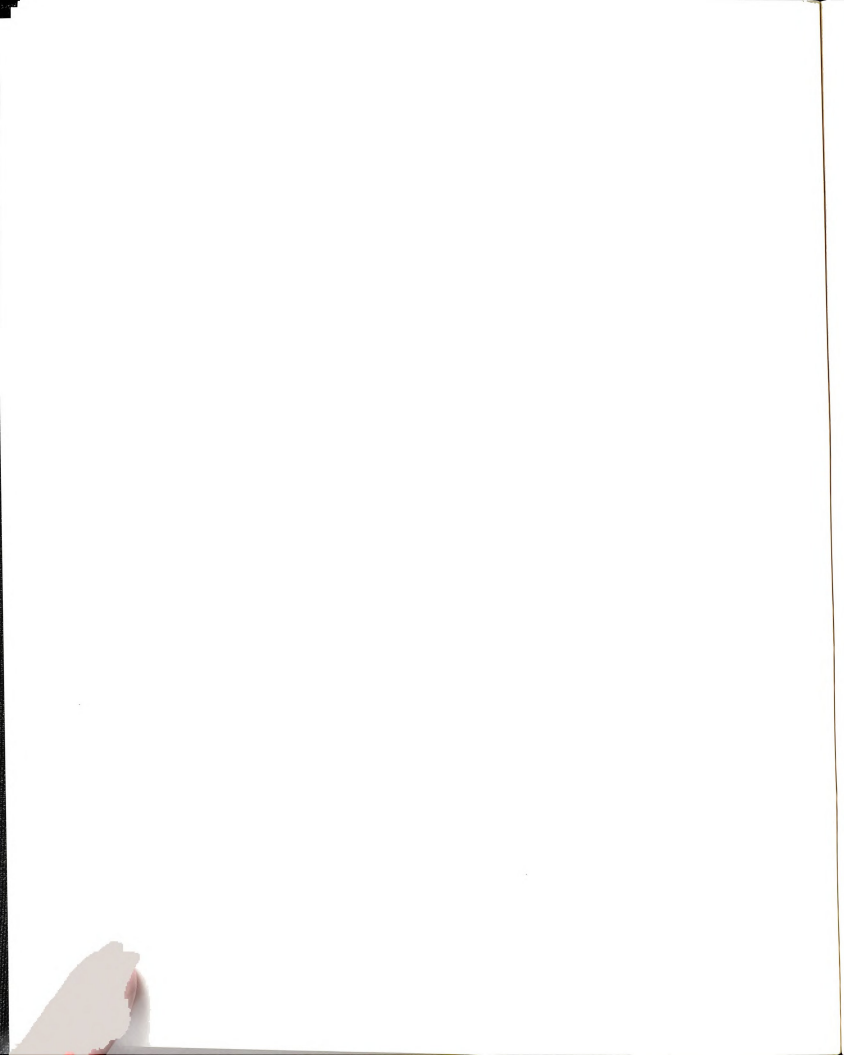
$$\begin{aligned} \frac{I_{\text{tip}}}{I_0} &= \frac{\int_0^\rho j_y(\tau) d\tau}{\int_0^\rho j_0 \exp(-x/\lambda) dx} \\ &\sim 1 + (a/2\rho)^{1/2}. \end{aligned} \quad (2.19)$$

The crack tip current increases as the square root of the crack length and becomes very large for large  $a$ .

Now consider a film of finite thickness in the  $z$ -direction, which has the same cross-section (that of Fig. 2.1) for every value of  $z$ . The current solution found above solves this problem also, as there is no  $z$ -direction current, and the boundary conditions in the  $x$ - $y$  plane are the same as for the 2D case. Every plane of the film thus has the same current pattern as the 2D problem, and there is no  $z$ -dependence to the magnetic field pattern *inside* the film. Of course outside the film there is a very strong  $z$ -dependence in the magnetic field generated by the current sources in the film. The magnetic field exterior to the film thus has  $x, y$ , and  $z$  components that depend on  $x, y$  and  $z$ . We are interested in the effect of the current pattern inside the film on critical current, and will concentrate on the interior solution for the remainder of this chapter.

For finite  $\lambda$ , the interior current pattern problem is truly three dimensional. We also expect the current enhancement effect [see Eqn. (2.19)] to be reduced, as current is already concentrated in a region of thickness  $\lambda$  near the surface of the superconductor. In fact, the reader may intuitively expect that for  $a \gg \lambda$ ,  $I_{\text{tip}}$  should saturate at large  $a$ . This intuition turns out to be correct, and we have quantified this "saturation effect" by developing asymptotic series for  $I_{\text{tip}}$  as  $a/\lambda \rightarrow \infty$ . We use 2D London theory, and so that the results we will derive are





only rigorously valid for infinitely thick films. We do however expect that they will also provide a good first approximation for thin films when  $\lambda$  is large, as we know from the above exact solution, that as  $\lambda \rightarrow \infty$  the 2D solution becomes exact.

### 2.2.3 Saturation Effect as $a/\lambda \rightarrow \infty$

In this limit, the angular function is rapidly decaying in  $\eta$ . In addition, we are interested in the limit  $b/a \rightarrow 0$  so that  $\xi_0 = \tanh^{-1}(b/a) \sim b/a$  is small. It thus makes sense to expand Eqs. (2.10) and (2.11) for small  $\eta$  and  $\xi$  and to use these expansions to develop approximate solutions for the magnetic field at the crack tip. A second order expansion in both  $\xi$  and  $\eta$  leads to

$$\frac{d^2 g}{d\eta^2} + (k - h^2 \eta^2)g = 0 \quad (2.20)$$

and

$$\frac{d^2 f}{d\xi^2} - (k + h^2 \xi^2)f = 0. \quad (2.21)$$

Choosing

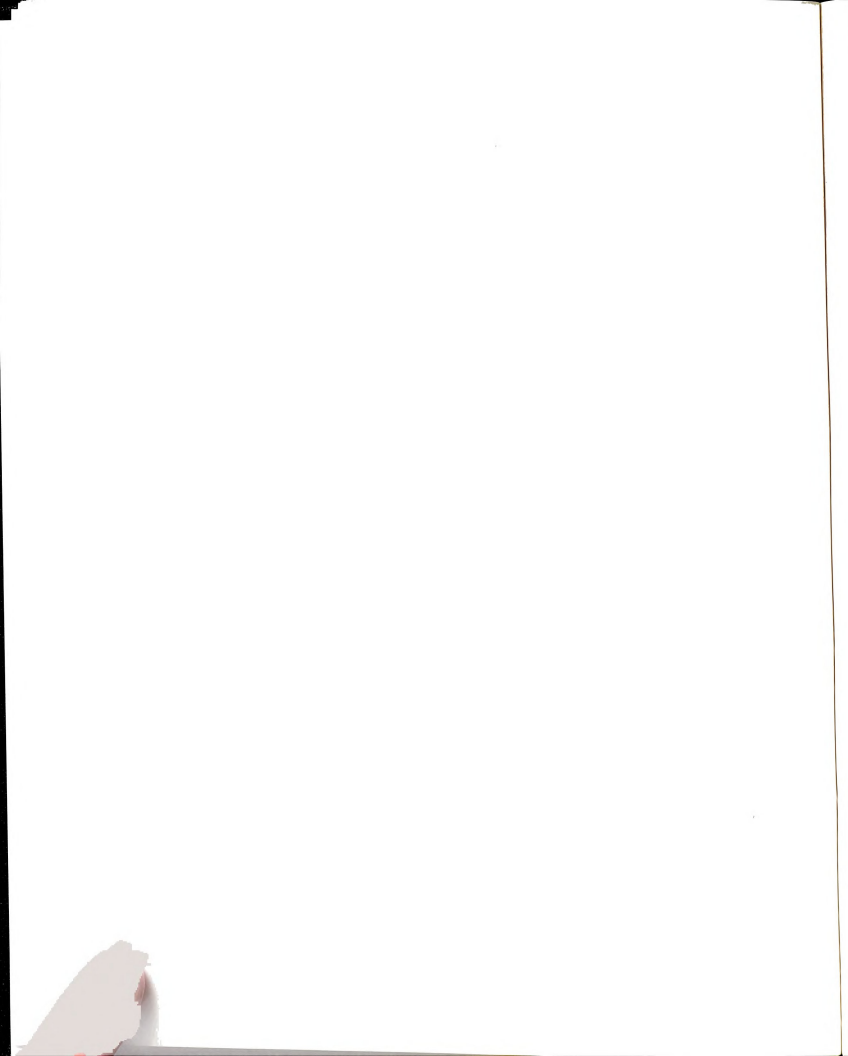
$$k = (2n + 1)h \quad \text{and} \quad h = C/\lambda \quad (2.22)$$

we find that  $g$  and  $f$  are given by

$$g(\eta) = \exp(-h\eta^2/2)H_{2n}(\sqrt{h}\eta) \quad (2.23)$$

$$f(\xi) = Y(2n + 1/2, \sqrt{2h}\xi) \quad (2.24)$$

where  $H_n(x)$  is a Hermite polynomial of order  $n$ , and  $Y(n, x)$  is a parabolic cylinder function [Abro72, Grad80] of order  $n$  [We have chosen the even Hermite polynomials to ensure the correct symmetry about  $\eta = 0$ ]. Both of these solutions can



be chosen to be rapidly decaying, which suggests that they will provide a useful representation of the true solutions near the crack tip. (Further mathematical justification for the truncation leading to Equations (2.20) and (2.21) may be obtained from a Sturm-Liouville analysis[Mors53].) Using these functions as our basis set and satisfying the boundary conditions, we find,

$$B(\xi, \eta) \sim B_0(x) + A_0 \sum_{n=0}^{\infty} S_n \exp(-h\eta^2/2) H_{2n}(\sqrt{h}\eta) Y\left(\frac{4n+1}{2}, \sqrt{2h}\xi\right) \quad (2.25)$$

with

$$\sqrt{\frac{\pi}{h}} 2^{2n} (2n)! Y\left(\frac{4n+1}{2}, \sqrt{2h}\xi_0\right) S_n = \int_{-\infty}^{\infty} \exp(-h\eta^2/2) H_{2n}(\sqrt{h}\eta) [1 - \exp(-\frac{a}{\lambda} \cos \eta)] d\eta. \quad (2.26)$$

Here we have extended the angular integration to infinity with negligible error, as  $H_n(\eta)$  is rapidly decaying in  $\eta$ . In the limit  $a/\lambda \rightarrow \infty$ , the integral on the right hand side of Eq. (2.26) reduces to

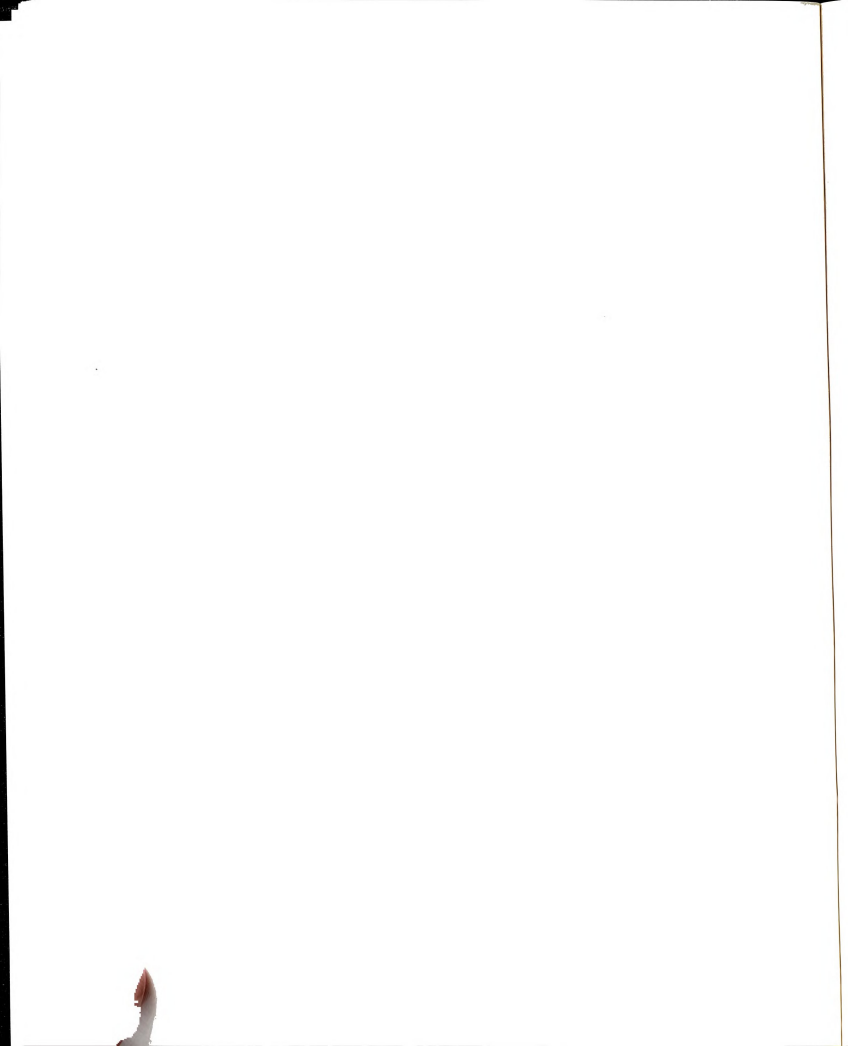
$$\int_{-\infty}^{\infty} \exp(-h\eta^2/2) H_{2n}(\sqrt{h}\eta) d\eta = \sqrt{\frac{2\pi}{h}} \frac{(2n)!}{n!}. \quad (2.27)$$

We then find that for  $a/\lambda \rightarrow \infty$ ,

$$B(\xi, \eta) \sim B_0(x) + A_0 \sum_{n=0}^{\infty} \frac{\sqrt{2} \exp(-h\eta^2/2) H_{2n}(\sqrt{h}\eta) Y[(4n+1)/2, \sqrt{2h}\xi]}{2^{2n} n! Y[(4n+1)/2, \sqrt{2h}\xi_0]} \quad (2.28)$$

and hence

$$j_n(\xi, \eta = 0) \sim j_0 e^{-a/\lambda} + j_0 \sum_{n=0}^{\infty} \epsilon_n \frac{Y'[(4n+1)/2, \sqrt{2h}\xi]}{Y[(4n+1)/2, \sqrt{2h}\xi_0]} \quad (2.29)$$



where

$$\epsilon_n = \frac{\sqrt{2}(-1)^n(2n)!}{(2^n n!)^2} \quad (2.30)$$

with

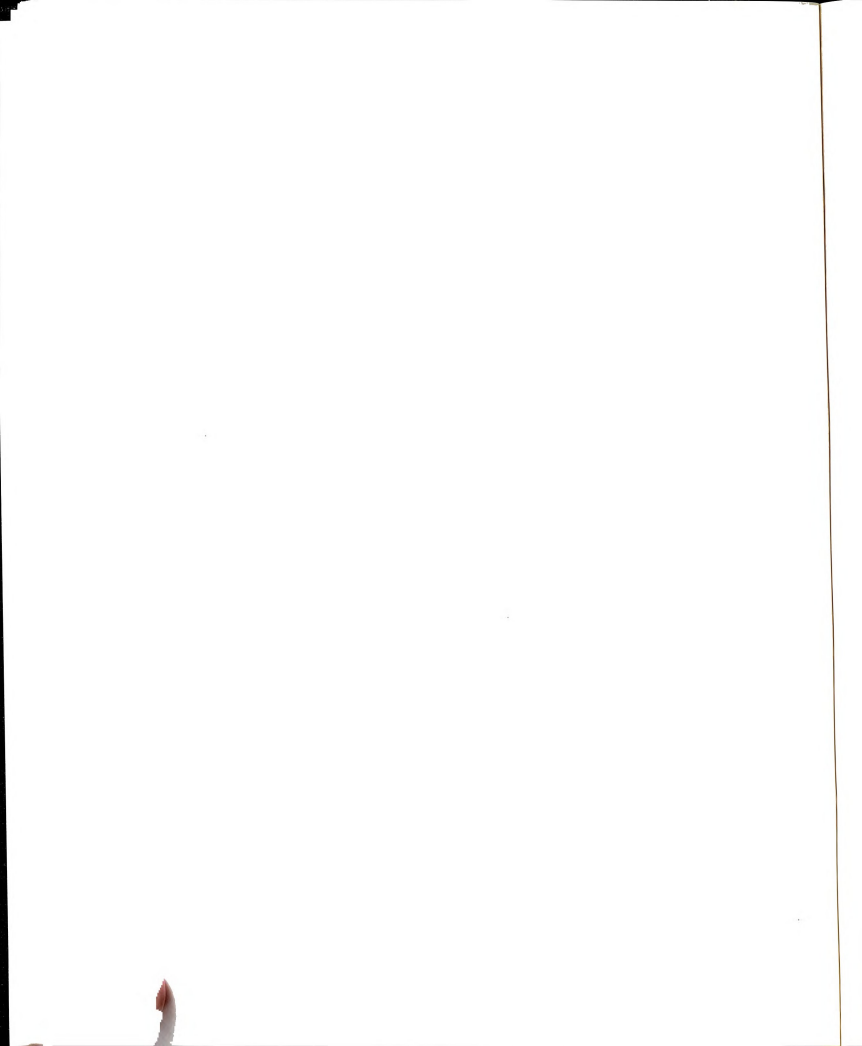
$$\sum_{n=0}^{\infty} \epsilon_n = 1. \quad (2.31)$$

Exactly at the crack tip, the series (2.30) is very slowly convergent ( $\sim n^{-3/2}$  at large  $n$ ) and 100,000 terms are required to achieve 3 figure accuracy for  $B$  right at the crack tip. For any finite distance,  $\rho$  from the crack tip, however, the series (2.28) is slowly convergent only up to terms  $N^* \sim \lambda/\rho$ , after it is exponentially convergent. In a similar way, the current density series (2.29) is poorly convergent (marginally convergent at best) right at the crack tip, but is exponentially convergent for large  $n$  provided  $\rho$  is finite. In applying our results to experiment, or in comparing with the numerical work described in Sec. [2.3], we must introduce a cut-off or coarse graining into the continuum theory. A study of the series (2.29) integrated up to a cut-off or lattice spacing  $\Delta$  yields

$$\frac{I_{\text{tip}}}{I_0} \sim \frac{B(\xi_0, \eta = 0) - B(\xi_c, \eta = 0)}{B_0(x = 0) - B_0(x = \Delta)} \quad (2.32)$$

where  $\xi_0 \sim b/a$  and  $\xi_c = \cosh^{-1}(a + \Delta)/C$ . Since  $\lambda \gg \Delta$ , the parabolic cylinder function may be approximated by its asymptotic behavior. We thus find,

$$\begin{aligned} \frac{I_{\text{tip}}}{I_0}(a/\lambda \rightarrow \infty) &\equiv \frac{I_{\text{sat}}}{I_0} \\ &\sim \frac{1 - \sum_{n=0}^{\infty} \epsilon_n \exp\{-\sqrt{(4n+1)\rho/\lambda}[(1+2\beta)^{1/2} - 1]\}}{1 - \exp(-\beta\rho/\lambda)}. \end{aligned} \quad (2.33)$$



Here we have written  $\Delta = \beta\rho$ , and  $\beta$  is the only free parameter in comparison with the numerical simulations of the next section. Finally, the scaling behavior of Eq. (2.33) for  $\rho \ll \lambda \ll a$  is found to be

$$\frac{I_{\text{sat}}}{I_0} \sim (\lambda/\rho)^{1/2} [1 + c_3 \log(\lambda/\rho)] \quad (2.34)$$

where  $c_3$  is a constant of order 1.

## 2.3 Numerical Simulation

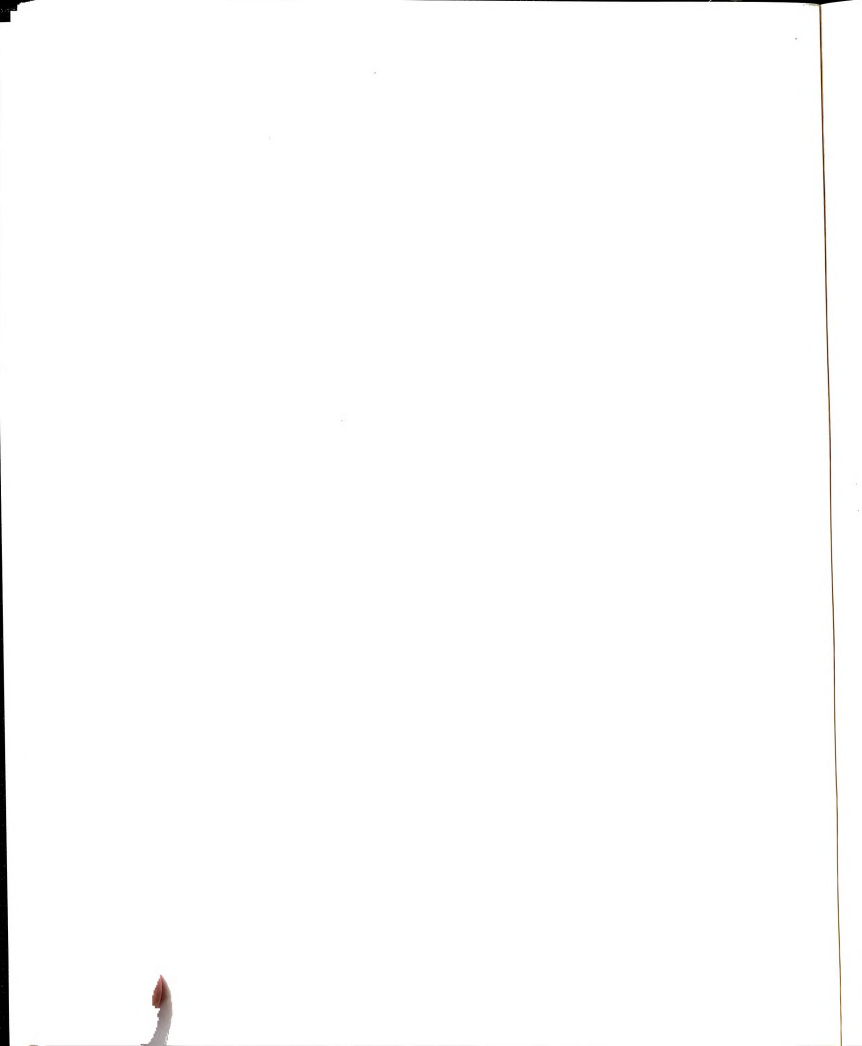
We have used numerical simulations to test the analytic theory of the previous section, and to calculate the current and field profiles around the crack tip. We use a  $L \times L$  square lattice, finite difference representation of the Laplacian operator, and put the two line defects of length  $a$  lattice spacings and width 1 lattice spacing, symmetrically at the both sides of the 2-dimensional array (see Fig. 2.4). The symmetry of the system allows us to work with a system 1/2 the size of the actual one. We inject current into the system from the bottom in the  $y$  direction. When there is no defect the field and current profiles can be solved analytically and the solutions are

$$B = A_0 \frac{\sinh[(L - x)/\lambda]}{\sinh(L/\lambda)}, \quad (2.35)$$

$$\mathbf{j} = j_0 \frac{\cosh[(L - x)/\lambda]}{\sinh(L/\lambda)} \hat{y}. \quad (2.36)$$

To simulate the effect of a crack, we ensure that the magnetic field a long way from the crack is that of Eqn. (2.35). We also fix the magnetic field at surface lattice sites and at the surfaces of the crack. This ensures that no current





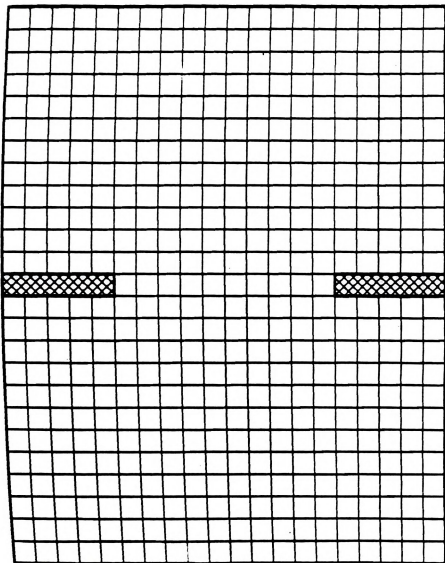
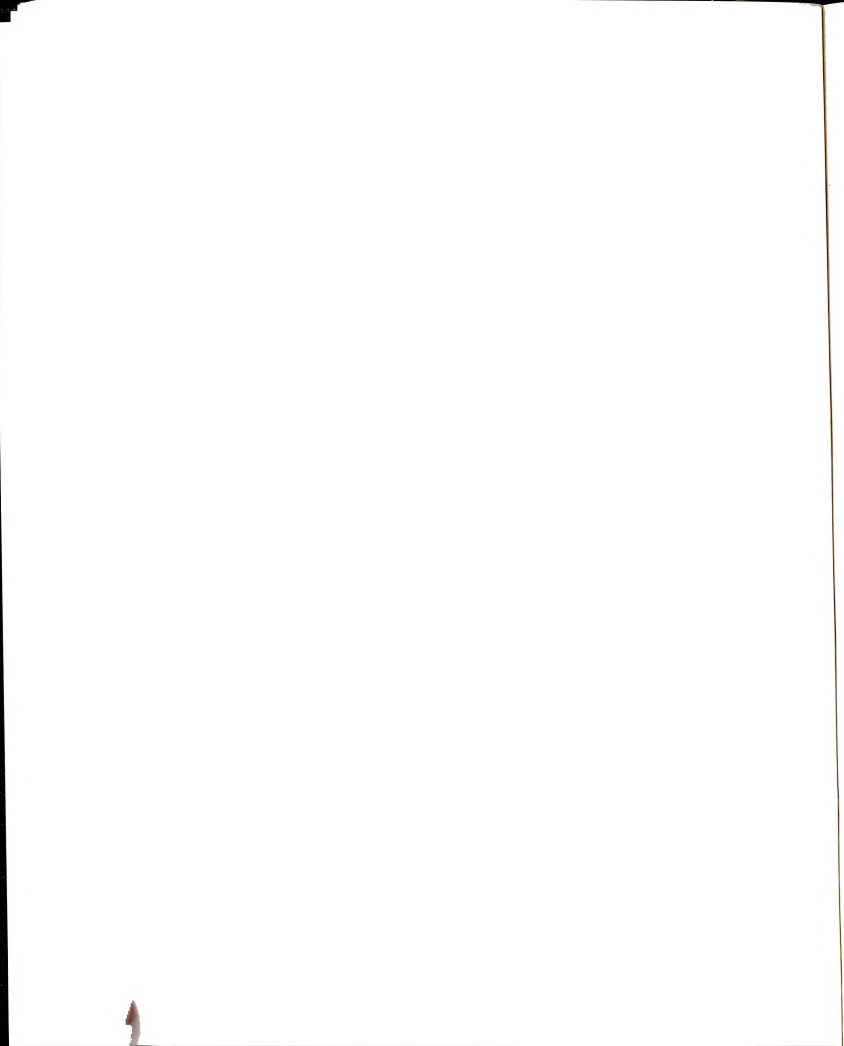


Figure 2.4: A superconducting square lattice with line defect used in the numerical calculations.

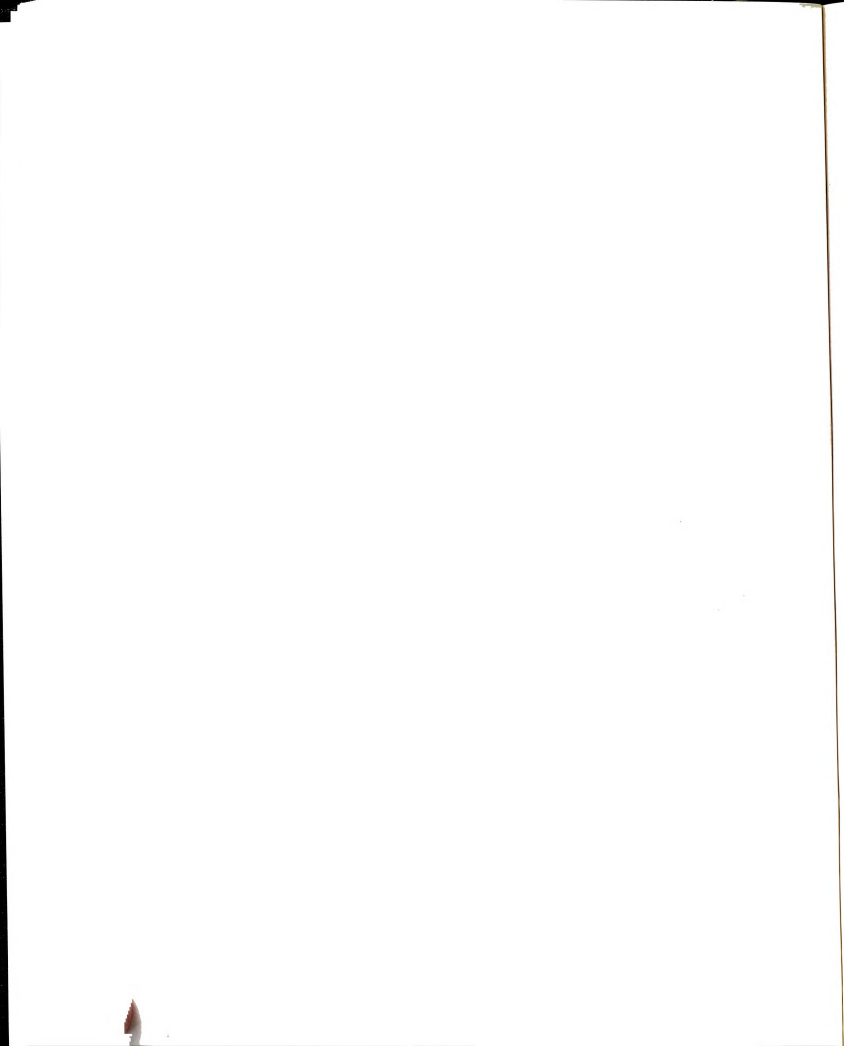


flows across these boundaries. With these boundary conditions, the magnetic field profile is calculated using the *conjugate gradient method* (For more details about the method, see Ref. [Pres86]).

The square lattice for our numerical simulation is depicted in Fig. 2.4 and the numerical result showing the magnetic field profile and magnitude of the current density are plotted in figures 2.5 and 2.6. The magnetic field profile has an exponential decay away from the crack tip (although it is faster than at a free surface). The current, however shows a marked peak near the crack tip. This current crowding near the crack tip is the effect of primary interest here, and was calculated analytically in the previous section, Eqs. (2.18), (2.19), (2.33) and (2.34) [Current is calculated from the difference of the magnetic field at adjacent sites - the lattice version of Eq. (2.2)]. We plot the current at the crack tip for various penetration depths and crack sizes in Fig. 2.7.

In this figure, the current is normalized to that occurring in a bond at the free surface a long way from the crack. For large  $\lambda$ , and  $a < L$ , the current enhancement obeys the square root increase of Eq. (2.19). When  $a$  gets close in size to  $L$ , finite lattice effects lead to a sharp rise in the current enhancement. For smaller  $\lambda$ , the current enhancement saturates for  $\lambda < a < L$ , and again shows a sharp increase as  $a$  approaches  $L$  due to finite size effects. The value at which the current enhancement saturates (for  $a \ll L$ ) is presented in Fig. 2.8.

In this figure, we also plot the predictions of Eq. (2.34) with  $\beta = 1$ . It is seen that the theory of the previous section provides an excellent fit to the numerical data, and this justifies the use of the equations (2.19) and (2.34) in the scaling analysis of critical current presented in the next section.



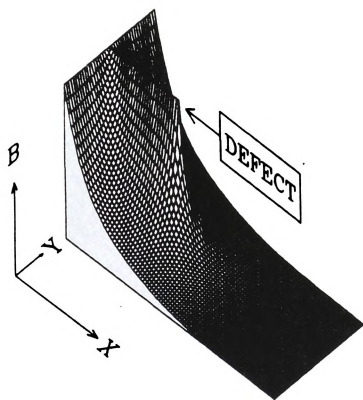
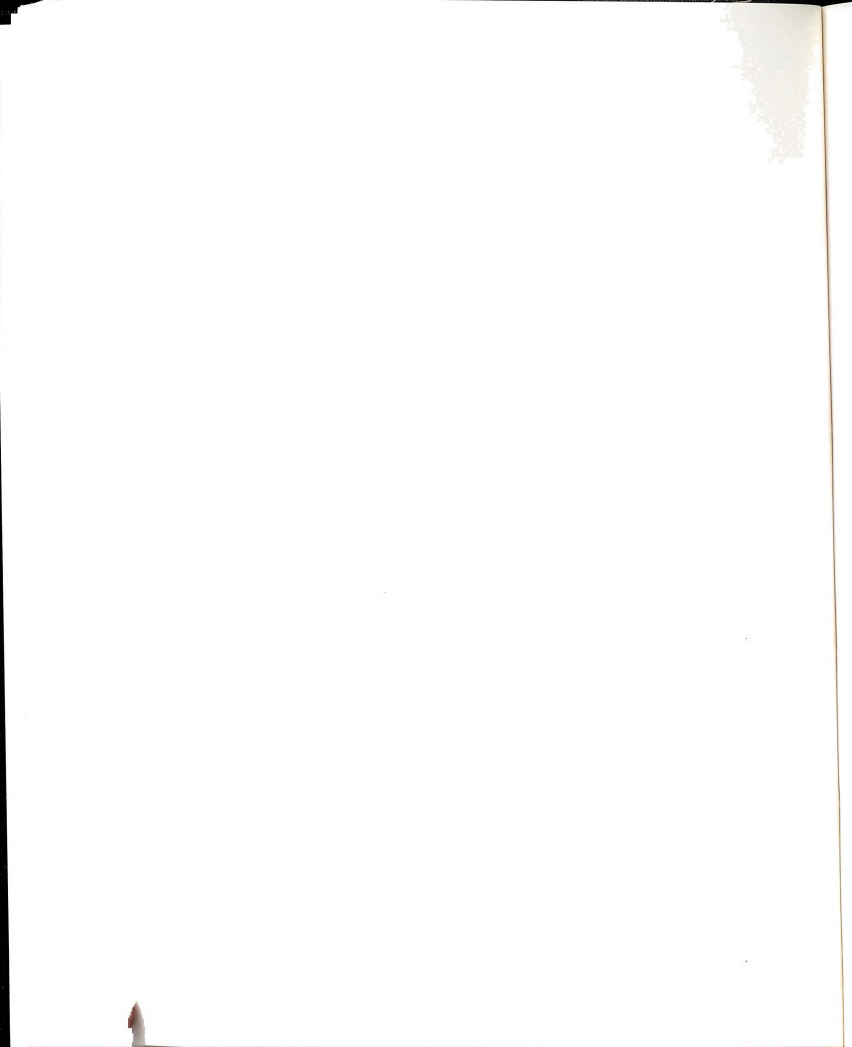


Figure 2.5: The profile of the magnetic field near a crack, found using numerical simulations on  $200 \times 120$  square lattice array for the case of  $\lambda/\Delta = 10$ ,  $a/\Delta = 30$  and  $b/\Delta = 1$ .



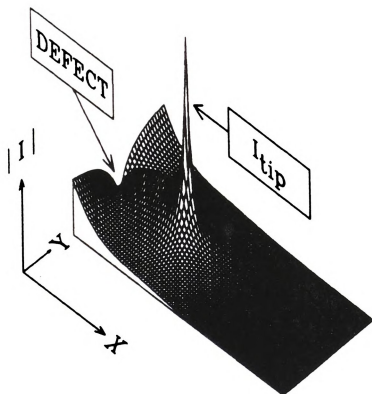
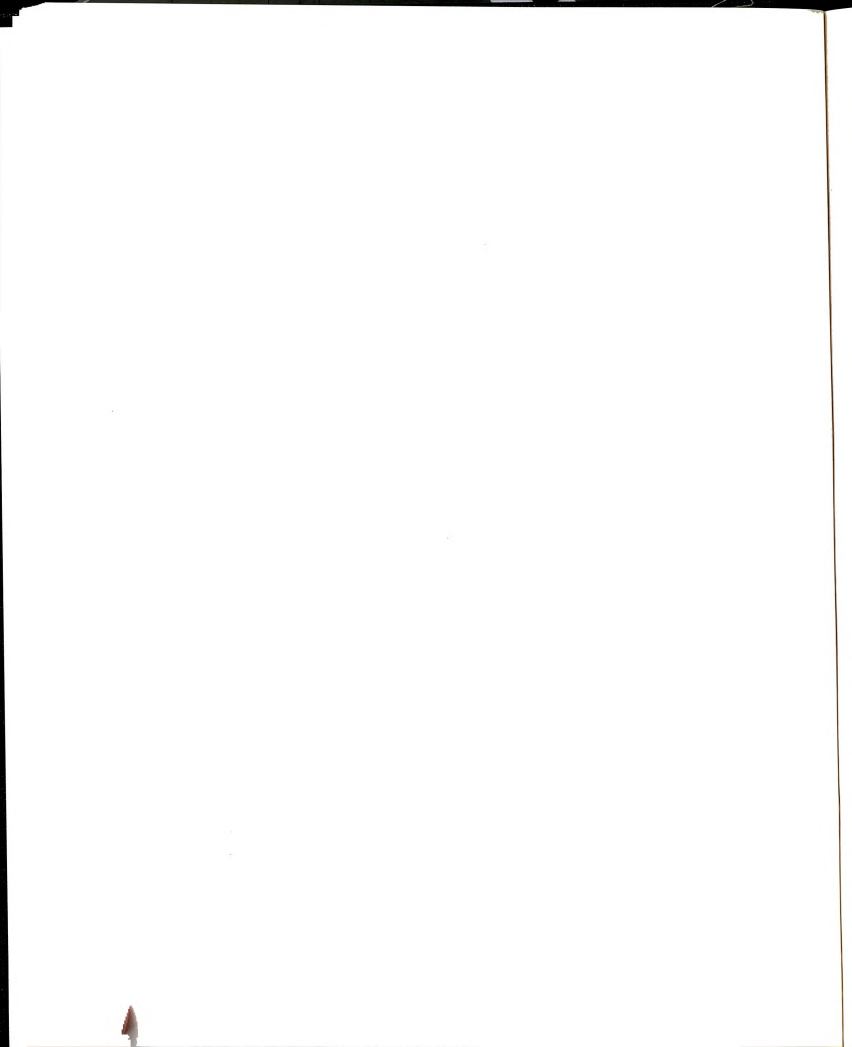


Figure 2.6: The profile of the magnitude of the current density near a crack, found in same numerical simulations for Fig. 2.5.





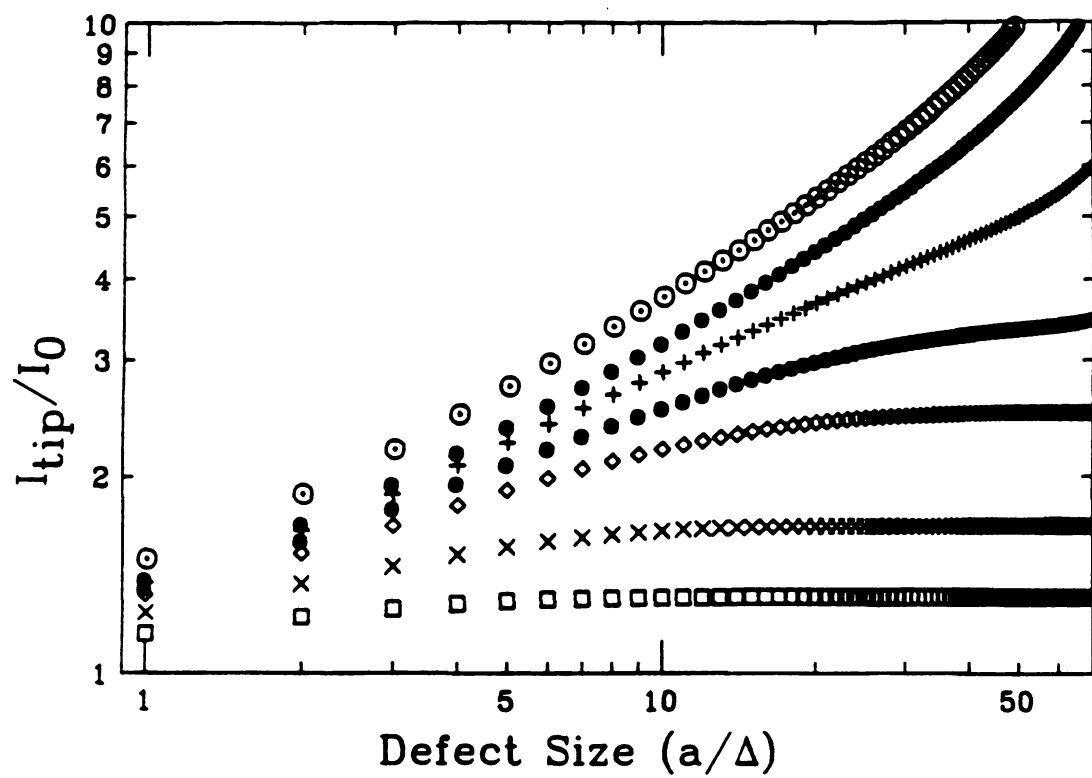


Figure 2.7: The current at the crack tip ( $I_{tip}/I_0$ ) as the function of the crack size ( $a/\Delta$ ) for :  $\lambda/\Delta = \infty(\odot)$ ,  $50(+)$ ,  $10(\diamond)$ ,  $4(\times)$ ,  $2(\square)$ .

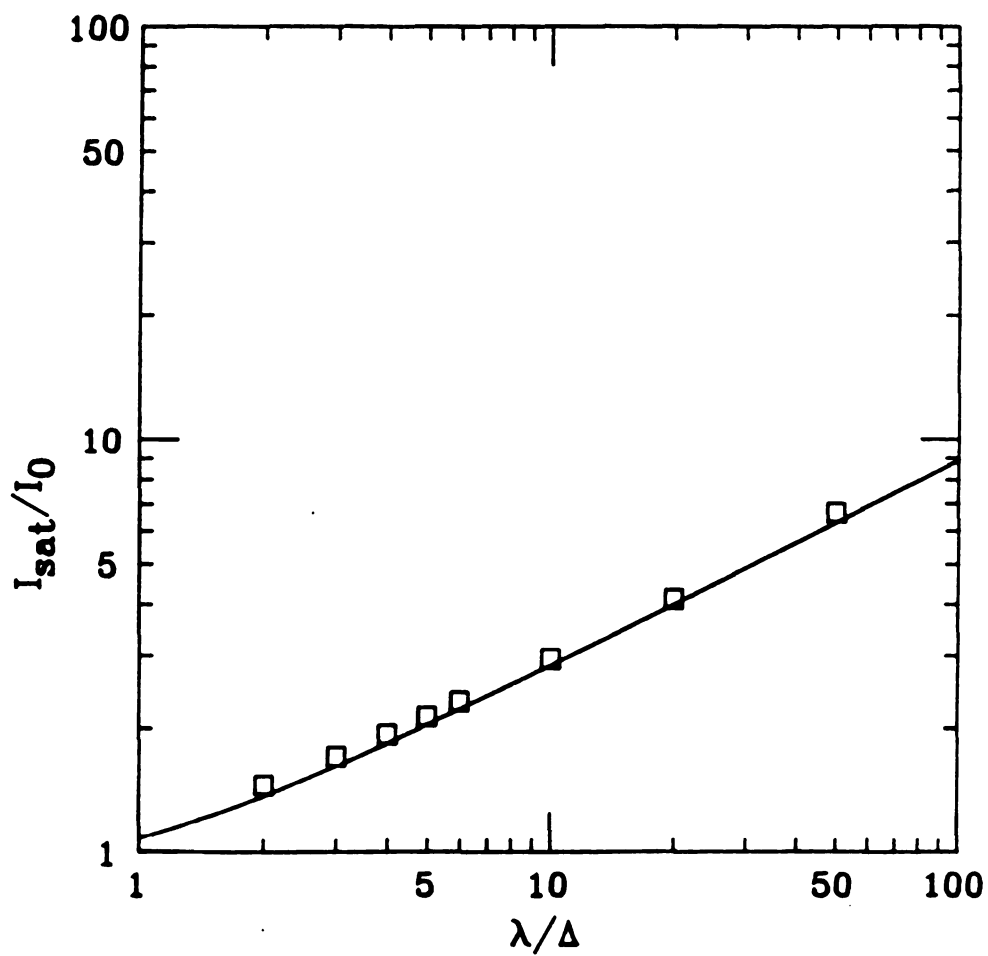
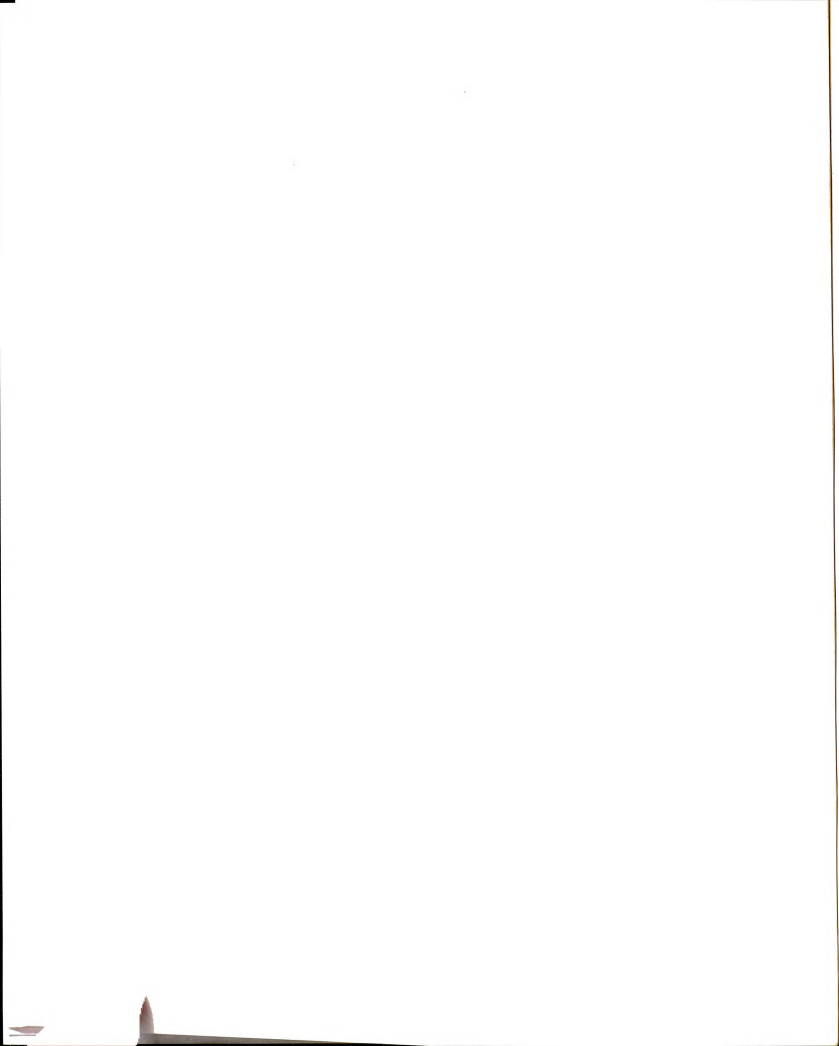


Figure 2.8: The saturation current ( $I_{\text{sat}}$ ) at the crack tip (see text) when  $\lambda \ll a \ll L$ . The solid line is obtained using Eq. (2.33).



## 2.4 The Effects of a Crack on Critical Current

In this section, we use the theory of Sections [2.2] and [2.3] to predict the effect of a crack on the observed critical current of a superconducting film. In all cases, we consider current injected into the film in a direction perpendicular to the long axis of a crack (see Fig. 2.9), that extends all the way through the film (a through crack). We first consider the prediction that the simplest critical state model makes for this geometry. We then go on to a discussion of the critical current reduction to be expected, if the large local supercurrent at the crack tip initiates the dominant dissipative mechanism.

### 2.4.1 The critical state model

In the critical state model[Bean62, Bean64] of hard superconductors, the critical current occurs when the current density is at its critical value all the way across the sample. At lower values of external field or current, the critical current density only flows in a shell near the surfaces of the film as depicted for a 2D geometry in Fig. 2.9.

As the external current is increased, the current shells increase in size until they fill the smaller cross-section extending outwards from the crack tip. Still ignoring self-field corrections, the film case is also straightforward. Current shells now occur on all edges of the film, and there is a  $z$ -dependence to the magnetic field and current flow, but the total current carrying capacity of the film is still proportional to the smallest cross-section available for superflow. The critical current reduction

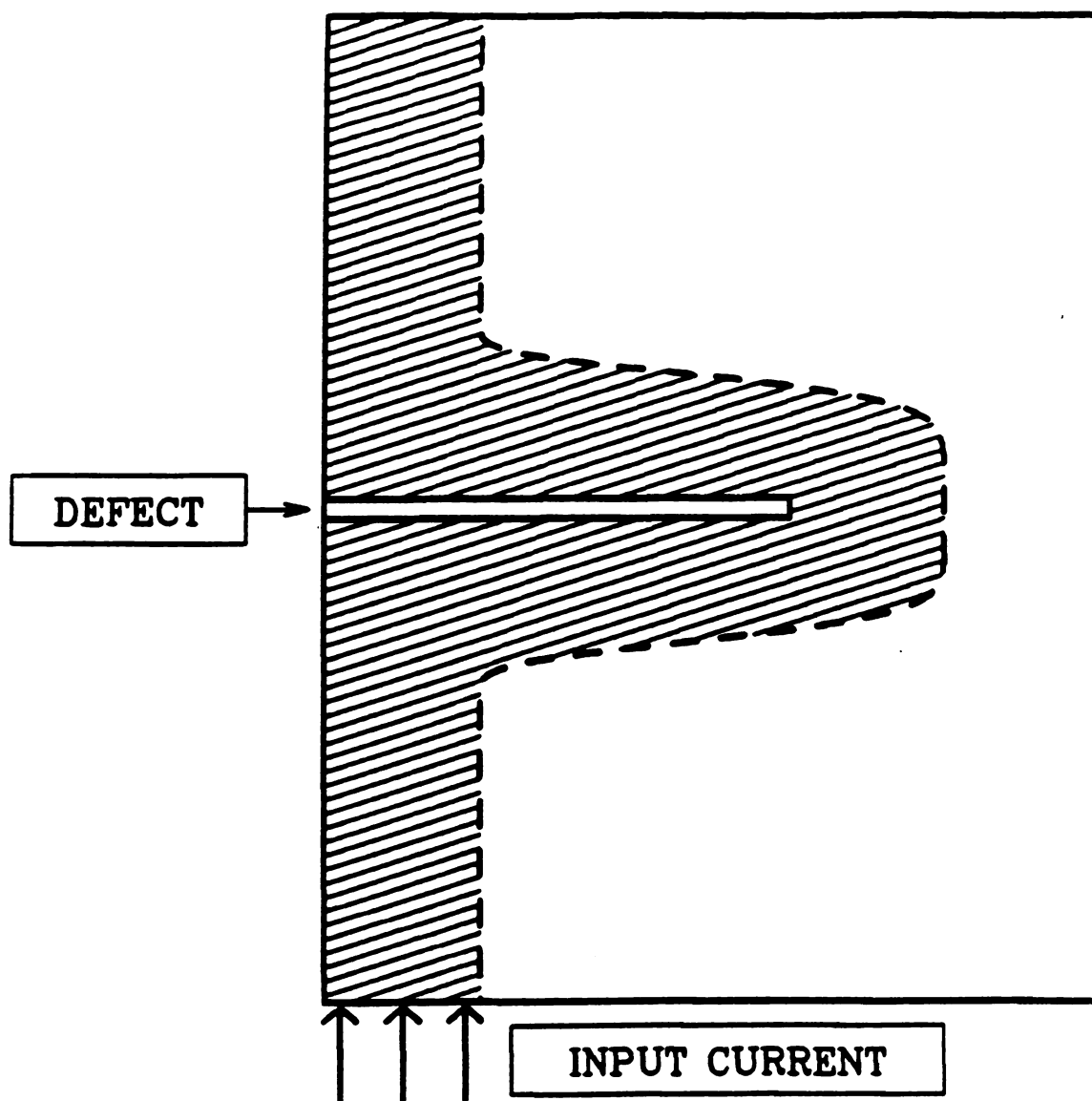


Figure 2.9: The Bean model (schematic). Current flows in the shaded region. Here we have rounded the sharp edges inherent in the model on a length scale of  $\lambda$ , as is expected on physical grounds.

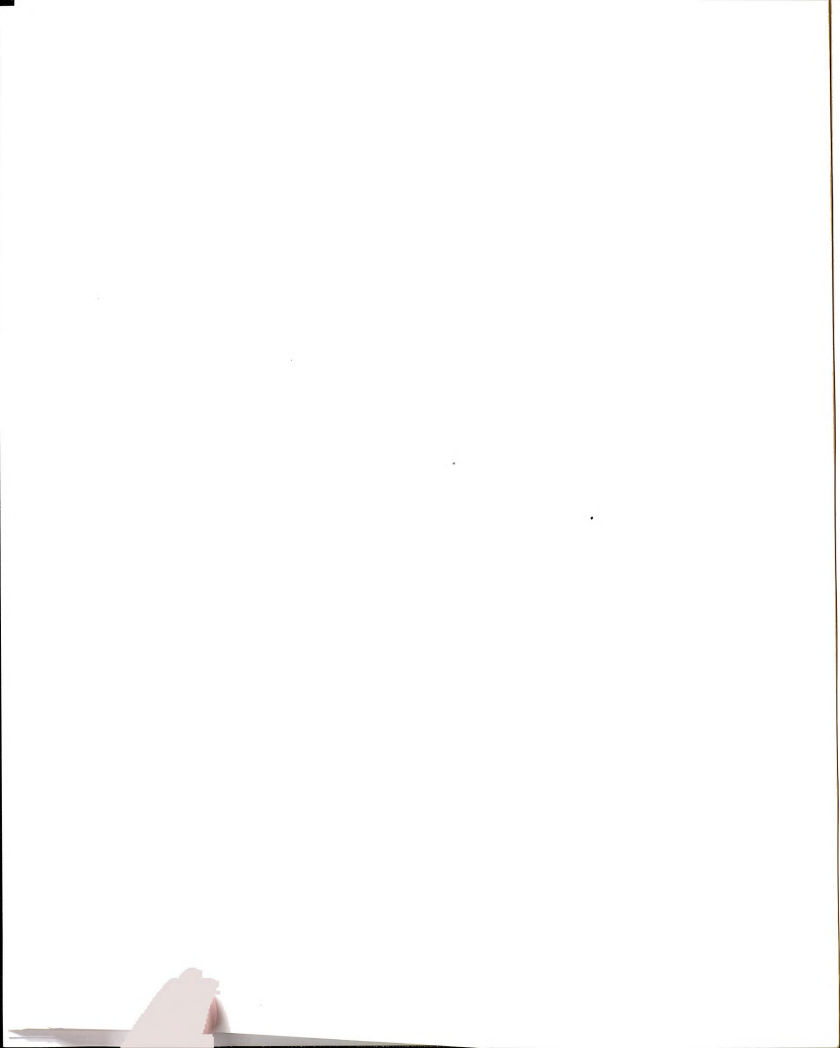
due to a through crack in the geometry of Fig. 2.9 is then given by

$$\frac{j_c(a)}{j_c(0)} \sim \frac{(L-a)}{L} \quad (2.37)$$

ignoring self-field effects. This result shows a very weak dependence on crack length compared to that of the hotspot theory discussed below. Including self-field corrections (for example within the Kim model[KimY62, Ande62]) does modify the result (2.37) and makes the supercurrent patterns more complex [Bean64] but the crack sensitivity of the model is still weak.

### 2.4.2 Hotspot theory

We wish to put forward an alternative perspective on the effect of a crack on critical current. Consider the limit of weak pinning, and slowly increase the current injected into the film containing the crack (again the direction of current flow is perpendicular to the long axis of the crack). Due to the current enhancement effect at the crack tip [see Eqns. (2.18) and (2.34)] vortex nucleation will first occur at the crack tip. If flux pinning is weak, the vortices so nucleated will flow causing dissipation. (This has been explicitly seen in simulations of current flow in the closely related problem of a crack in a 2D Josephson junction containing a crack [XiaW89]). As pinning increases, the first vortices nucleated at the crack tip will be pinned, and the film will support a higher external current before dissipation sets in. As pinning increases further, a larger number of the newly nucleated vortices remain pinned in the nucleation zone near the crack tip. We label the zone in which these vortices reside the pinning zone, and ascribe to it a radius  $\rho$  (note that we assume that there is no difference between the pinning strength of the superconductor at the crack tip compared to elsewhere in the



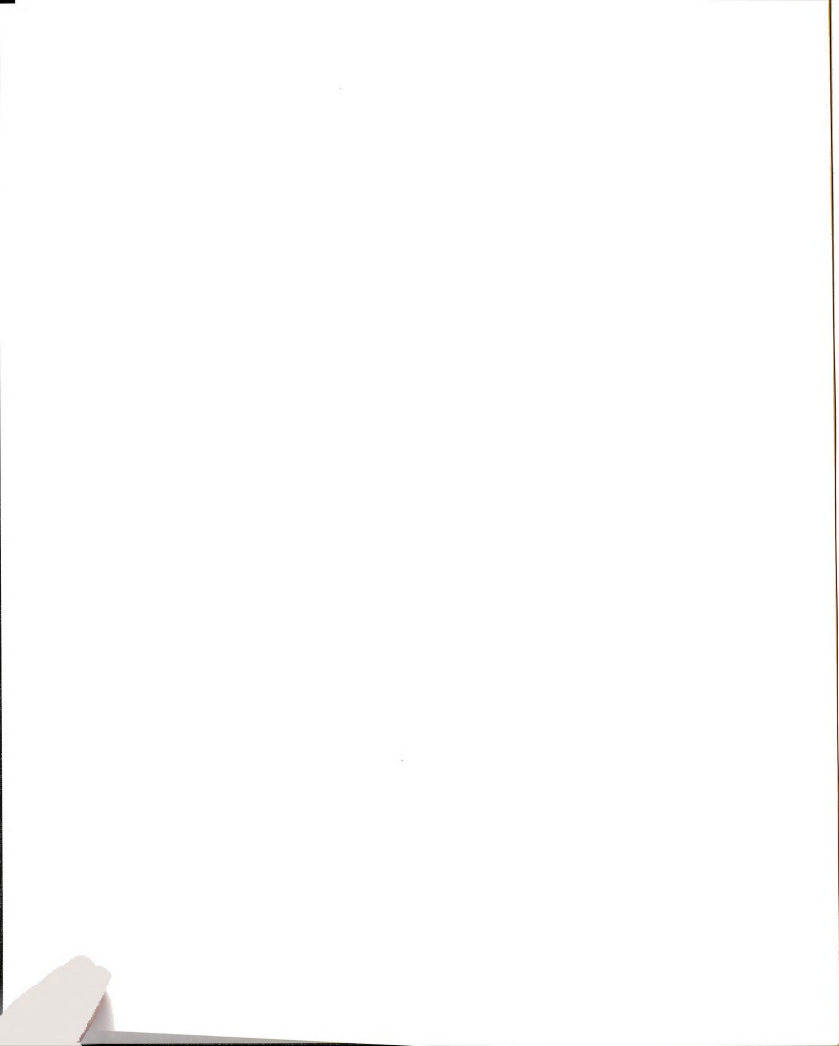


material). In the pinning zone, the system is in a critical state, with supercurrent density at the critical value. The pinning zone mitigates the current enhancing effect of a crack by producing an effective crack tip radius of curvature of size  $\rho$ . Provided  $\rho \ll a$ , we can combine the concept of a pinning zone with the explicit calculations of Secs. [2.2] and [2.3] to predict the effect of a crack on critical current. Using Eqs. (2.19) and (2.34) of Sec. [2.2] we thus find (for  $\rho \ll a \ll L$  and ignoring logarithmic corrections)

$$\frac{j_c(a)}{j_c(0)} \sim \begin{cases} c_1(\rho/a)^{1/2}, & \text{if } \rho \ll a \ll \lambda \\ c_2(\rho/\lambda)^{1/2}, & \text{if } a \gg \lambda \gg \rho. \end{cases} \quad (2.38)$$

where  $c_1$  and  $c_2$  are undetermined constants that are independent of  $a$ . As is seen from Eqn. (2.38), the main trend for  $j_c(a)/j_c(0)$  is that it reduces as the inverse of the square root of crack size or penetration depth, whichever is smaller. This prediction breaks down when pinning becomes sufficiently strong that the flux pinning zone  $\rho$  becomes of order  $a$ , or  $L - a$ , whichever is smaller. When  $\rho$  is of order  $L$  the critical state region extends across the sample, and we return to the critical state model prediction of Eqn. (2.37).

The above predictions may be tested experimentally using superconducting films. We suggest an experiment where a controlled crack of length  $a$  is introduced into a high quality thin film (one in which we can control the pinning strength relatively well, and which contains no extended defects which might compete with the controlled crack). The crack can be drawn lithographically and the transport critical current should be measured as a function of the crack length. We predict that Eqn. (2.37) should apply if the film has sufficiently strong pinning (e.g. highly polycrystalline Nb), while equation (2.38) should apply if the pinning is weak (e.g. amorphous Nb<sub>3</sub>Ge).



Before closing this section, we make some comments concerning the effect of finite film thickness and the attendant  $z$ -dependent current intensity on the prediction (2.38). It is known that in films of finite thickness, there is both a  $z$ -dependence and an  $x$ -dependence in the current density [Tink65, Duze81, Till86, Orla91]. We are interested in the ratio  $j_c(a)/j_c(0)$ , and we thus ask whether these effects make a significant modification to the simplest estimates of this ratio. Firstly the  $z$ -dependence. This is due to the complex form of the magnetic field lines around the thin film, and may be calculated either within the Bean model or within London theory. This effect will only modify (2.38) if the field profile around the film is significantly different for a film containing a crack than it is for a film without a crack. If the crack is much smaller than the film width (this is the limit that we are primarily interested in), then this external field correction is negligible, as can be qualitatively seen by considering the dependence of the demagnetisation factor on crack length. This implies that the form of the  $z$ -dependence of the current density is, at most, weakly dependent on the addition of the crack. Assuming that the dominant part of the supercurrent is in the  $x$ - $y$  plane (as is expected for a thin film with current injected in the  $y$  direction and the thin axis in the  $z$ -direction), we can use the theory of Secs. [2.2] and [2.3] to estimate the current enhancement due to the crack, albeit with a  $z$  dependent boundary field. Now, note that since the  $z$ -dependence is, to first order, only in  $j_0$ , the  $z$ -dependence drops out in ratio (2.18), and hence in (2.38).

A second possible complication for thin films is that there is an  $x$ -dependence in the current density which is not given by the simple London form, but rather is well approximated by  $j(x) \sim j(0)[1 - (x/L)^2]^{1/2}$ , for  $x \gg \lambda$  and by an exponential form for  $x \ll \lambda$ . Since  $L$  is large compared to the  $x$  range (of order  $a$ ) that we

are considering, we can consider the current flow to be essentially uniform for the purposes of our calculations. This implies again, that the result (2.38) should provide a useful first estimate for a thin film, but now with a large effective  $\lambda$ .

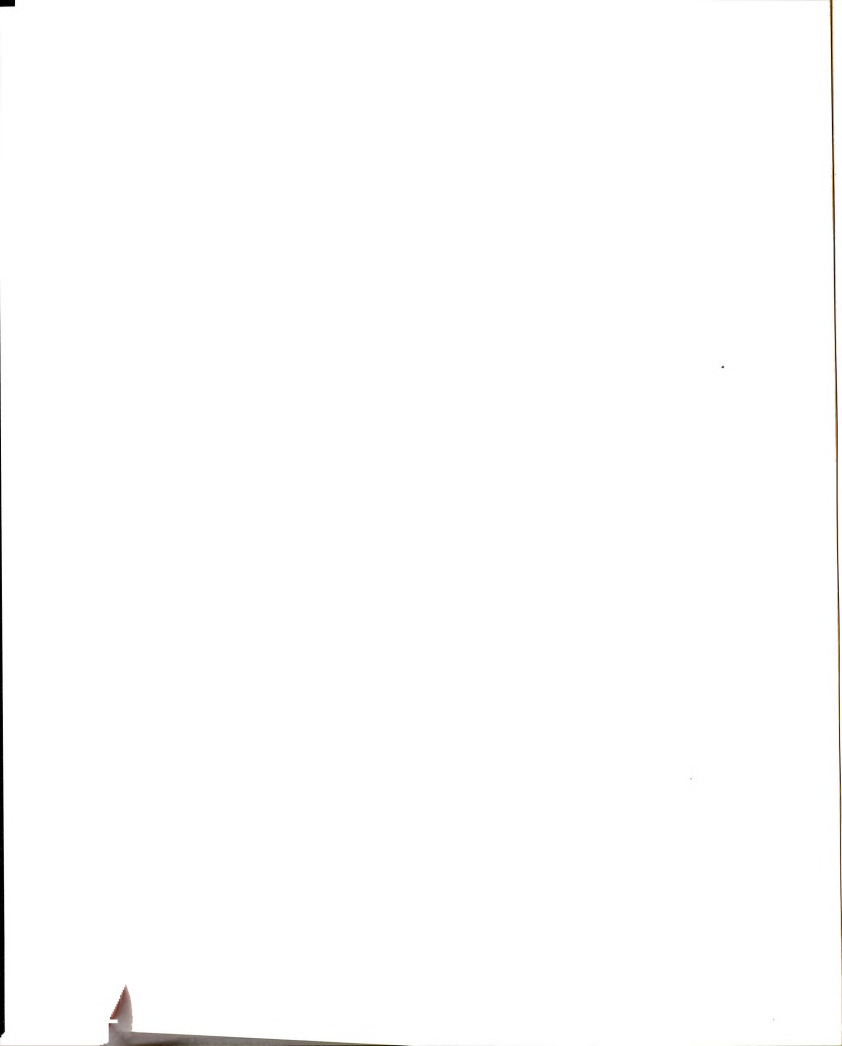
## 2.5 Conclusions

We have argued that there is a strong enhancement of supercurrent near cracks which have a width greater than  $\xi$ , and length  $a \gg$  width. We have illustrated the effect using 2D London theory where a crack of length,  $a$ , leads to a strong current enhancement as given in Eqs. (2.18), (2.19), (2.33) and (2.34). The main scaling behavior contained in these equations is that the supercurrent increases as the square root of the crack length,  $a$ , or the penetration depth,  $\lambda$ , whichever is smaller. Cracks can thus lead to large local current enhancements, especially in geometries where the effective  $\lambda$  is large.

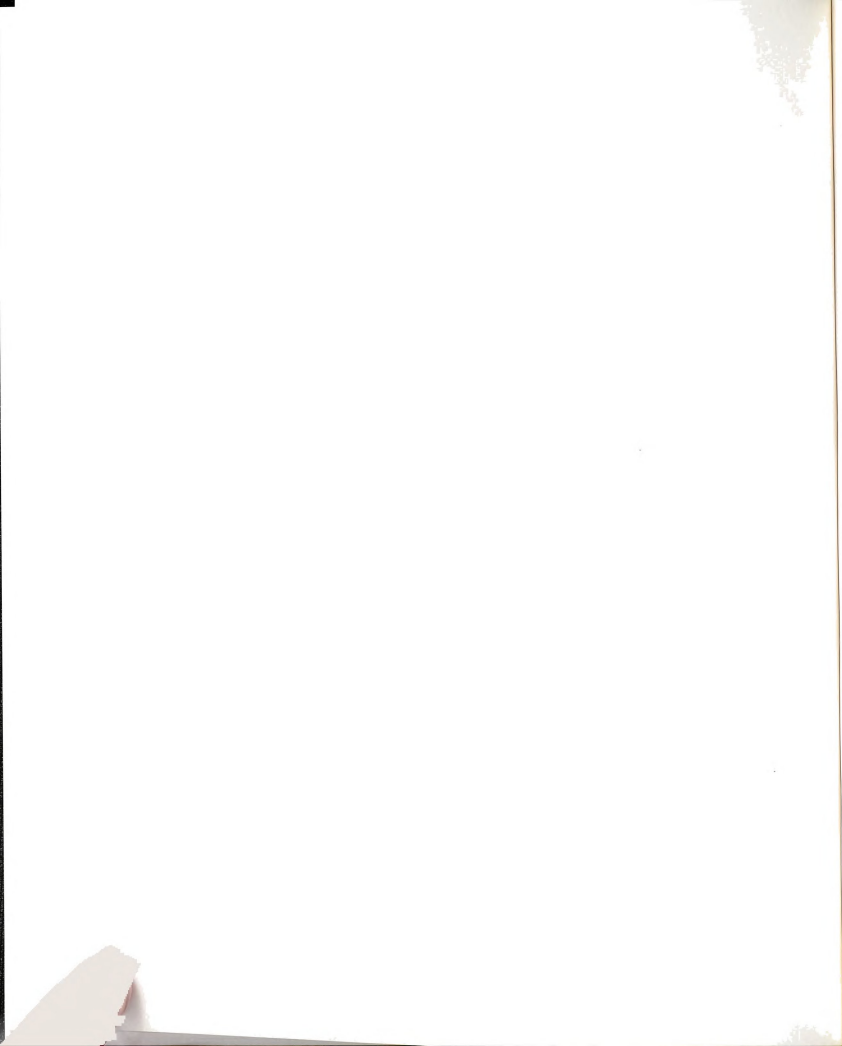
We have also discussed the effect of large local supercurrents on critical current measurements. We argued that large local supercurrents act as nucleation sites for vortex penetration, and that these vortices feel a Lorentz force that tends to make them move and hence cause dissipation. Balancing this, is the pinning strength of the material. If the pinning is sufficiently weak, dissipation (vortex nucleation and flow) is initiated by the large supercurrent at the crack tip. In this case equation (2.38) should apply, and the superconducting material, is very crack sensitive. If pinning is sufficiently strong, the vortices nucleated by the large supercurrent at the crack tip are pinned and resist the strong local Lorentz force at the crack tip. In this case the critical state model applies [see e.g. equation (2.37)], and the superconductor is relatively crack insensitive.

To test these predictions, we propose that experiments which measure the critical current as a function of the size of a controlled crack of length,  $a$ , and width,  $w > \xi_s$ , should provide a new and useful measure of the current carrying capacity and reliability of superconductors. The thin film geometry (thickness  $\leq \lambda$ ) may be most useful, as there, current flows almost uniformly throughout the cross-section of the film. A crack perpendicular to the direction of current flow will cause a large amount of supercurrent to be channeled around the crack tip, leading to strong enhancement effects as predicted by equations (2.18) and (2.34). In addition, in thin films, the crack may be drawn in a controlled manner using lithographic techniques. For weak pinning films, the simplest London theory [see Eqn. (2.38)] predicts that the critical current reduces as the square root of the crack length or penetration depth, whichever is smaller, provided  $a \ll L$ . For experiments over a broader range of crack lengths, the square root law of Eqn. (2.38) may need to be replaced by a more general exponent (i.e.  $x$  as defined in the abstract not equal to  $1/2$ ). Experiments comparing crack effects in weak pinning films (e.g.  $\text{Nb}_3\text{Ge}$ ), where the hotspot theory [e.g. Eqn. (2.38)] should apply; with strong pinning films (e.g. highly polycrystalline Nb) where the critical state model [e.g. Eqn. (2.37)] should apply, would be especially useful.

Finally, we note that the ideas of this study have many analogies in mechanical fracture. Vortices are analogous to dislocations, and the pinning zone near the crack tip is analogous to the process zone near the tip of a mechanical crack. Controlled notch testing is standard in fracture and is analogous to the controlled crack test proposed above. The analogy between mechanical fracture and critical current in superconductors becomes closer as supercurrents become more inhomogeneous, and the pinning becomes weaker. In this limit, the current flow patterns



and critical current develop an extreme defect sensitivity that is characteristic of fracture and other breakdown problems.



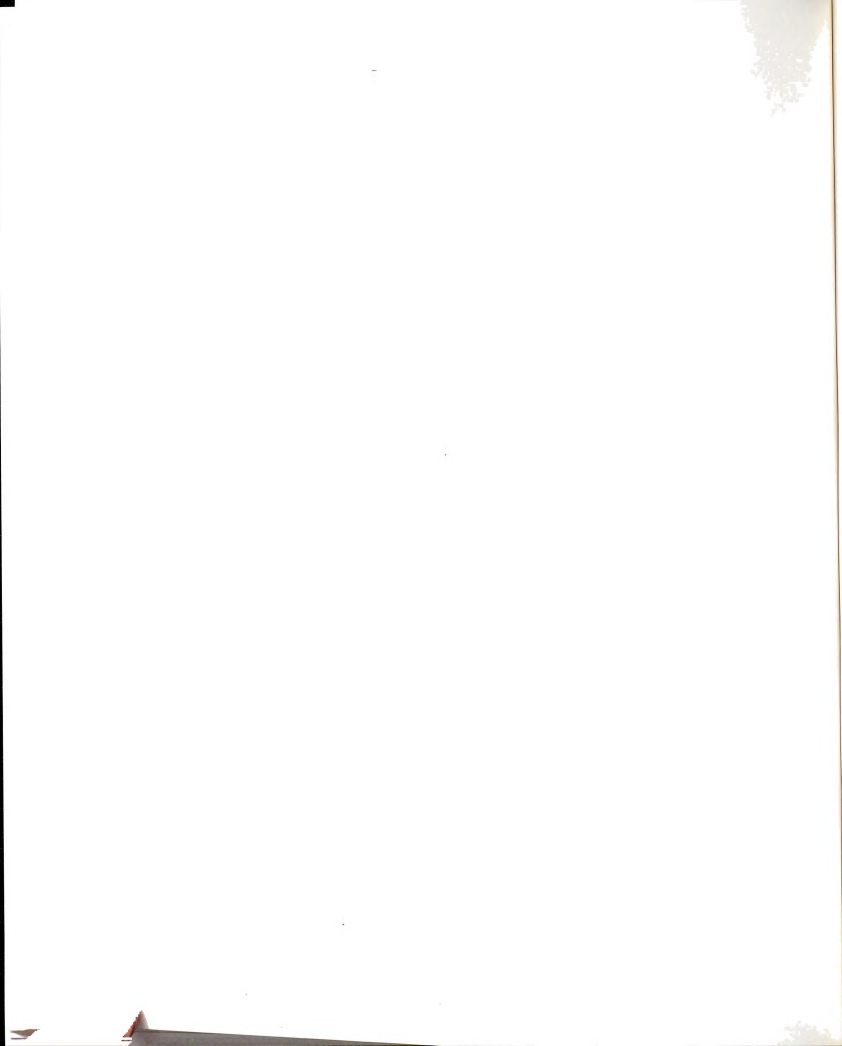


## Chapter 3

# Elasticity and fracture of disordered networks

### 3.1 Introduction

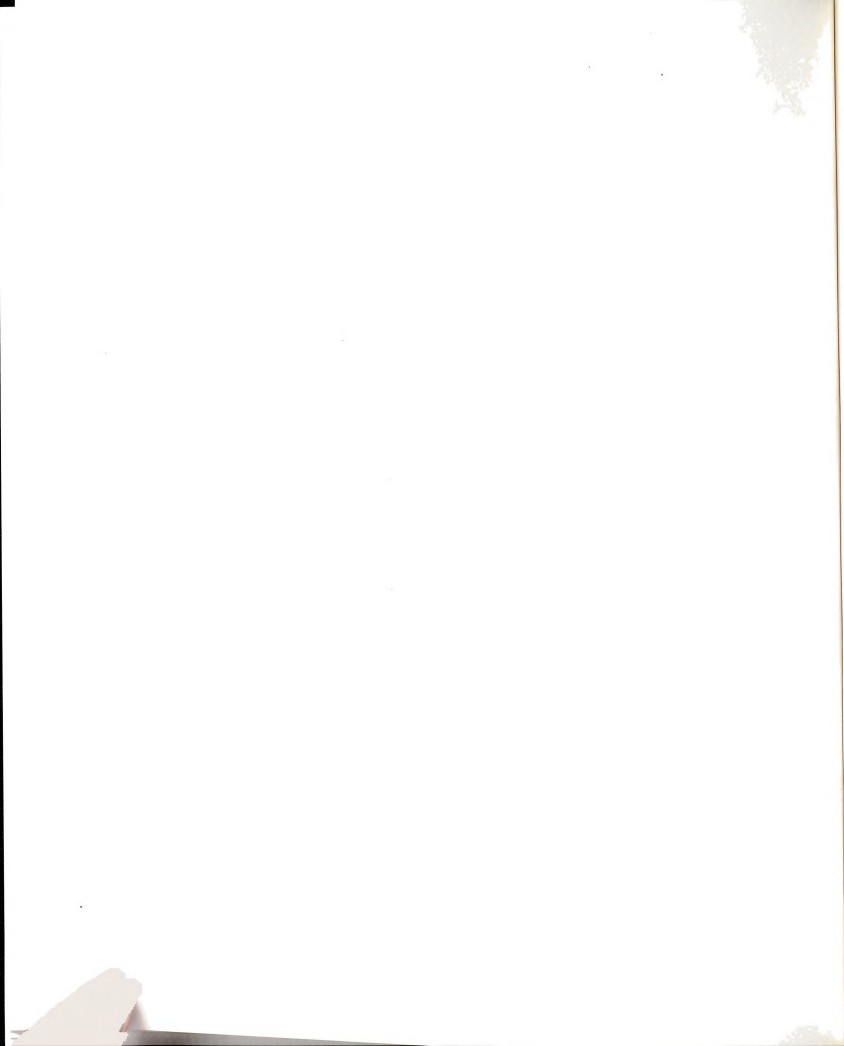
Many alloys and composites are disordered. In fact no material is perfect and the strength of a given material is very much dependent on these minor flaws or defects. Thus understanding the effects of random defects and their statistics is very crucial in analyzing the material strength. The effective elastic properties of these materials can be calculated using effective medium theory and other "homogenization" methods. Random networks with "realistic" interatomic and many body potentials are now routinely simulated on a computer. In combination with perturbation theory near the pure limit, rigorous bounds, and scaling analysis in the case of fractal geometries, there is now a well defined set of tools to accurately predict the elastic properties of many random materials. With this success there has been a growing desire to extend our understanding to the effect of random microgeometries on the non-linear elastic response and especially the failure strength of alloys and composites. It is known from the classic work of Griffith, that penny shaped voids can act as nucleation sites for fracture. However, the way



in which crack nucleation and growth is affected by a disordered microstructure is still poorly understood.

During the last few years, researchers, predominantly from the statistical mechanics and solid state physics communities, have introduced several new ideas into the study of fracture. Firstly, the idea of a fractal geometry was applied to fracture surfaces[Mand84, Unde86, Mech89]; secondly fracture patterns were studied using the ideas of non-equilibrium growth [Taka86, Term86, Loui87, Meak88, Hinr89]; and thirdly the methods of disordered systems were used to calculate the average strength and statistics of random materials.

Due to the fact that fracture is initiated in regions of high stress, it is to be expected that homogenization methods, unless they focus in the crack growth region, should be poor predictors of the effect of disorder on failure strength. Recently it has been shown that in random networks, failure strength is singular in the pure limit[Duxb87a, Duxb91, Beal88], so perturbation theory, in the conventional sense, is unable to probe strength behavior. Useful bounds on tensile strength have not been developed, probably because standard bounds lead to strength limits that are so far apart that they offer no useful information. Understanding of failure is then based on Griffith's "single crack" ideas, extended in myriad ways, attempts to homogenize the microstructure (probably incorrect in most systems) and more recently, detailed analytic and numerical analysis of idealised disordered microstructures[Herr90, Sahi91]. Along with new scaling theories specifically taking into account the extreme statistics of brittle fracture[Duxb87a, Duxb91, Beal88], these simulations have lead to new insights into the fracture of materials.



In Sec. [3.2] the central force networks are discussed. The networks consist of nodes and bonds. The nodes are connected by the simple harmonic springs (or Hooke's springs). The theory of elasticity based on the effective medium theory is reviewed in Sec. [3.2.1] and the numerical simulation results using the conjugate-gradient method is presented in Sec. [3.2.2]. In Sec. [3.3] the scaling behaviour of the tensile fracture stress is developed based upon these results.

For some materials, such as graphene layers, the central force network can not model the mechanical behaviour of the materials properly. In Sec. [3.4] I consider the bond bending networks and their mechanical response by the numerical simulation on honeycomb networks.

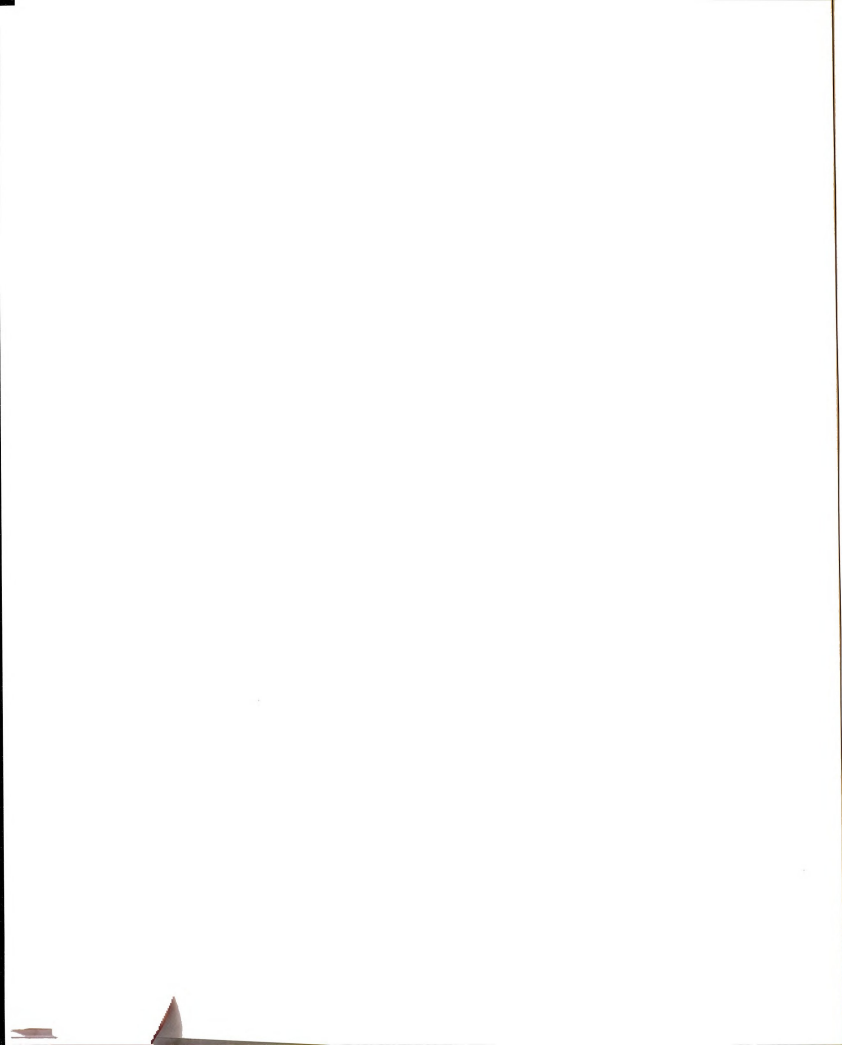
In Sec. [3.5] I summarize this chapter and draw conclusions.

This chapter contains materials which have appeared in the following three publications:

- [Duxb90a] P.M. Duxbury and S.G. Kim, *Scaling theory and simulations of fracture in disordered media*, Proc. ASME (1990).
- [Duxb91] P.M. Duxbury and S.G. Kim, *Scaling theory of elasticity and fracture in disordered networks*, Mat. Res. Symp. Proc. 207, 179 (1991).
- [Duxb94b] P.M. Duxbury, S.G. Kim and P.L. Leath, *Size effect and statistics of fracture in random materials*, Mat. Sci. and Eng. A176, 25 (1994).

## 3.2 Central force networks

Consider a regular lattice containing  $N$  central force springs which connect the nearest neighbor sites of the lattice. Randomly remove volume fraction,  $f$ , of the



springs. As  $f$  increases, the elastic moduli decrease, upto the rigidity percolation point[Thor87],  $f_*$  ( $\approx 0.33$  for the triangular lattice), at which the elastic moduli vanish. If the springs are allowed to break when strained beyond a threshold value,  $\epsilon_c$ , the network maybe used to study damage evolution. In this case we slowly increase the strain, allowing local spring rupture until the damage spreads across the network and catastrophic failure occurs. The total energy,  $E$ , of a spring configuration is given by

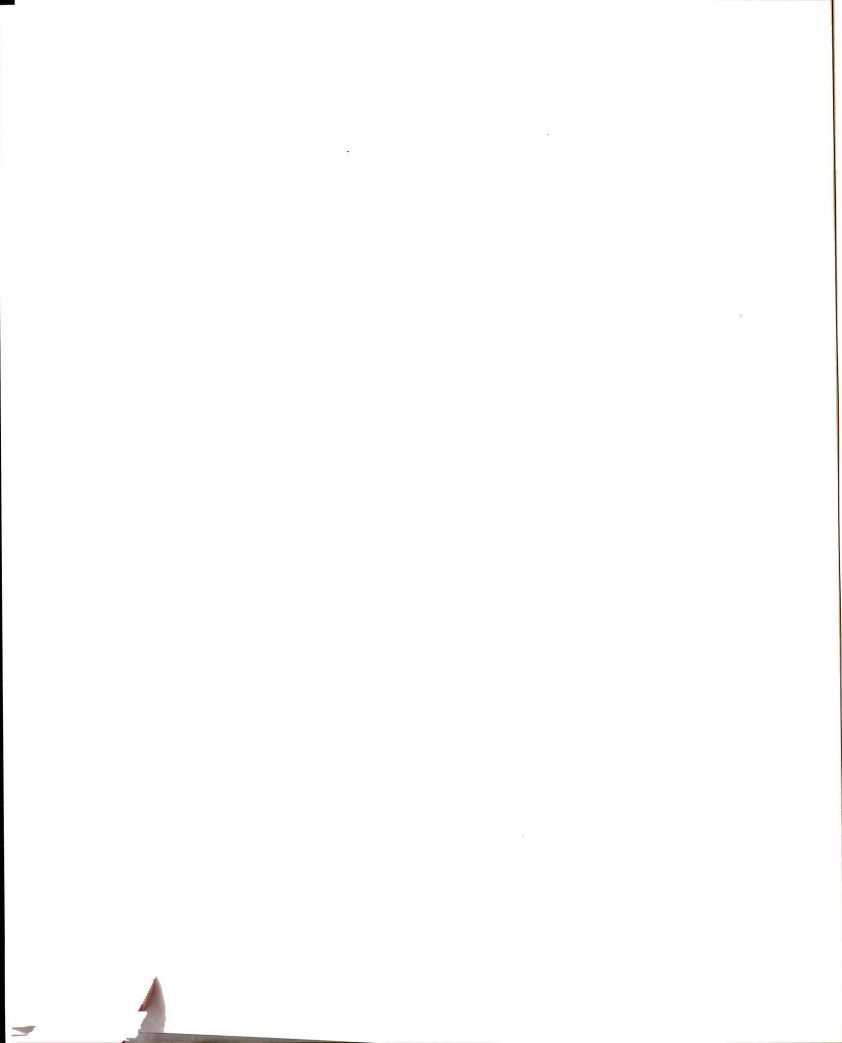
$$E = \sum_{ij} \frac{1}{2} k_{ij} (l_{ij} - l_0)^2 \quad (3.1)$$

where  $k_{ij}$  is the normalized Young's modulus (spring constant) between adjacent sites of the lattice,  $l_{ij}$  is the length of the spring connecting the sites  $i$  and  $j$ , and  $l_0$  is the natural length of the springs (assumed constant). Disorder is introduced through  $k_{ij}$ , which in the case of dilution are either 0 or  $k_0$ .

### 3.2.1 Effective medium theory for elasticity

The simplest estimate of  $p_* = 1 - f_*$  is found using a constraint counting argument[Feng87, Thor83]. When the bond occupation probability,  $p$ , is small the system consists of disconnected pieces and hence has many zero frequency modes. The number of such modes being approximated by the number of degrees of freedom ( $Nd$ ) minus the number of constrains ( $zNp/2$ ). Here,  $d$  is the spatial dimension and  $z$  is the nearest neighbor co-ordination number of the lattice. Thus the effective medium theory estimate of the fraction of zero frequency mode is

$$x = \frac{Nd - zNp/2}{Nd} = 1 - \frac{zp}{2d}. \quad (3.2)$$





When  $z \rightarrow 0$ , the network is no longer "floppy", and this defines the rigidity threshold to be,

$$p_* = 1 - f_* \approx 2d/z \quad (3.3)$$

Effective medium theory has been used to find effective elastic properties on approach to  $f_*$ . The spirit of the theory is to replace the random network with a regular lattice having an effective spring constant  $k_m$  on each bond. This assumes that the macroscopic symmetry is unaltered by disorder. Several different methods have been used to estimate  $k_m$  and they all lead to the result

$$\frac{k_m}{k_0} = \frac{C_{ij}^m}{C_{ij}} = \frac{p - p_*}{1 - p_*} \quad (3.4)$$

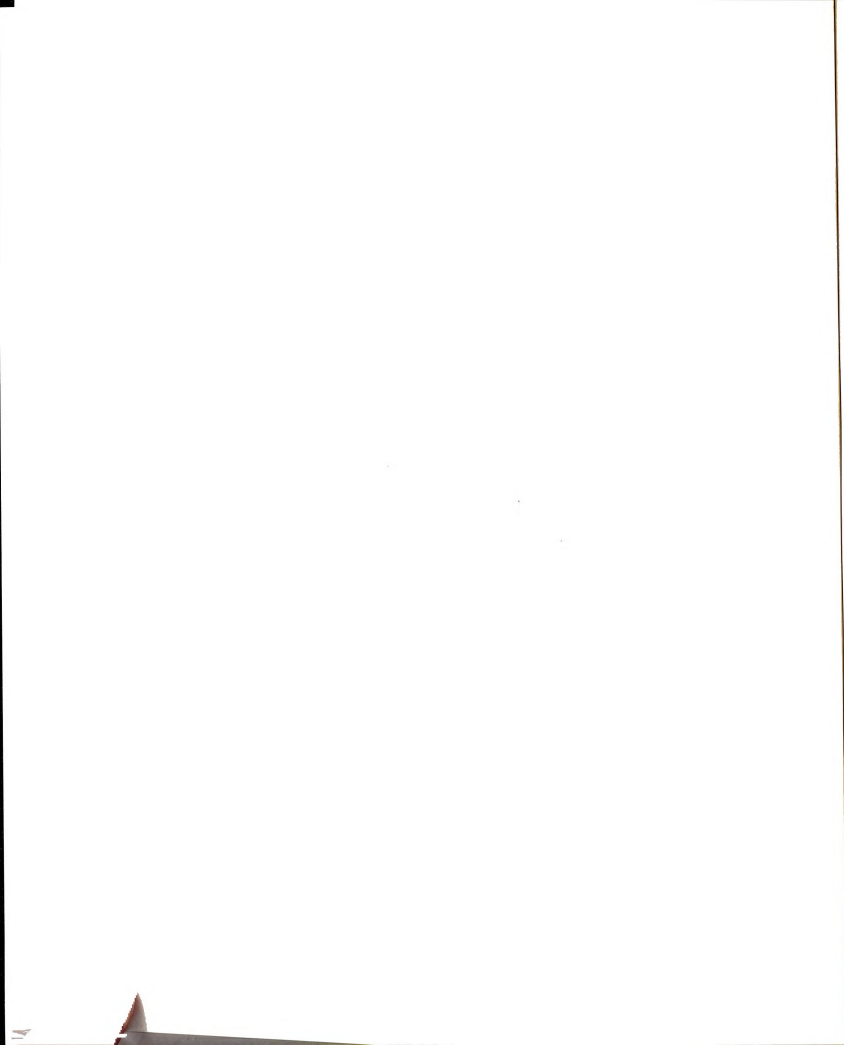
where  $C_{ij}$  are the elastic constants of the network, and the subscript or superscript,  $m$ , denotes the effective medium value. Numerical simulations on triangular and fcc lattice show that Eq. (3.4) provides an excellent approximation for the elastic properties of random but rigid networks, for all but a very small region near the rigidity percolation point (see also Fig. 3.6 for a comparison with the triangular lattice result).

The tensile fracture stress of spring networks has also been recently studied, and it is useful to first review the algorithm used in these calculations. It turns out that there are many possible algorithms, and the choice of algorithm strongly affects the final pattern of fractures springs. In contrast, the fracture strength appears to be robust, and this is due to the fact that these networks are *brittle*.



### 3.2.2 Numerical simulation of damage and fracture

We apply an external strain to the networks and relax them using a conjugate gradient method, with a convergence criterion of  $10^{-8}$  in the energy. When one of the springs is strained beyond a critical strain,  $\epsilon_c = (l_{ij} - l_0)/l_0 = 10^{-4}$ , the spring breaks (we set its  $k_{ij}$  to zero). In the results to be described below, we take a diluted triangular spring network, and slowly increase the external tensile strain. At each external tensile strain we relax the network to minimize the total energy of the system, Eq. (3.1) and check the strain in each bond against the spring rupture criterion. If at a given external strain, a spring breaks, we fix the external strain at that level, and continue relaxing the network and breaking the spring carrying the largest strain (provided it is greater than  $\epsilon_c$ ) until either catastrophic failure occurs, or until no more springs break. We call this the hottest bond algorithm. We then slowly increase the external strain until it is just large enough to break another spring in the network and again iterate the hottest bond procedure described above. The stress-strain relationship of a single spring, along with the stress-strain behavior found from these simulations on a  $50 \times 50$  triangular network are shown in Fig. 3.1 and 3.2. It is seen from Fig. 3.2 that a catastrophic event usually occurs very soon after the first spring in the network breaks. We call the stress at which this event occurs  $\sigma_1(f)$ . A second important stress is the stress required to rupture the entire network. This is the maximum stress in the stress strain curve, and we label this  $\sigma_b(f)$ . In networks with small dilution ( $f$  small),  $\sigma_1(f) \simeq \sigma_b(f)$  while at larger dilution this is not always the case. Here, as in previous works[Beal88, Hass89], we concentrate on  $\sigma_1(f)$ , as this models the brittle fracture of the networks. The large strain behavior



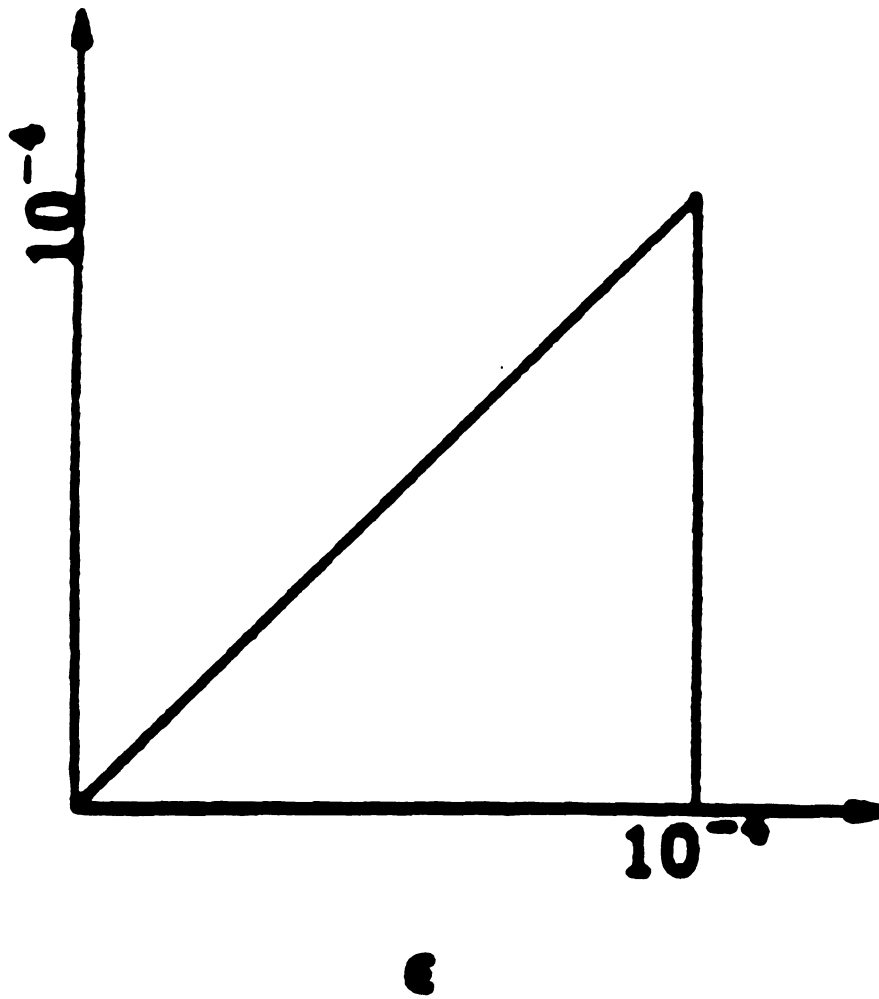


Figure 3.1: The stress strain behavior of a single spring.



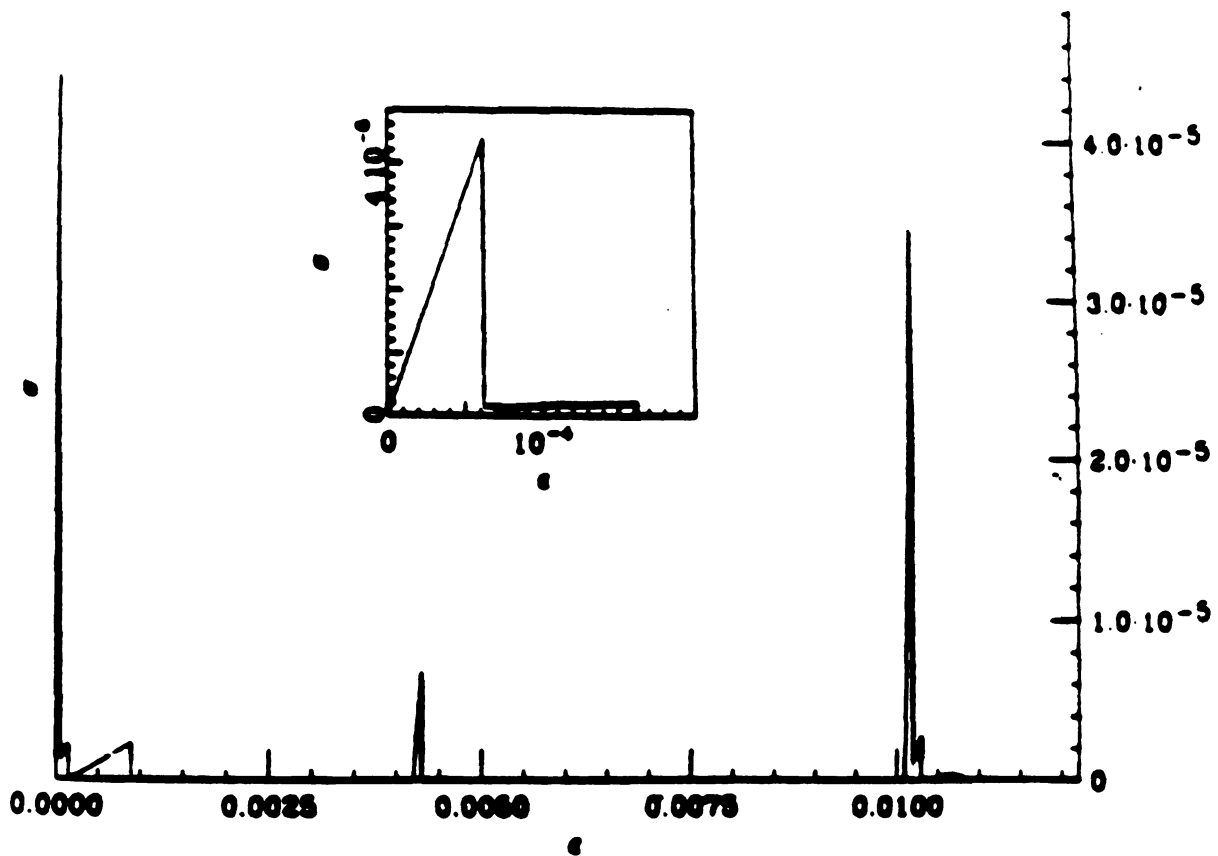
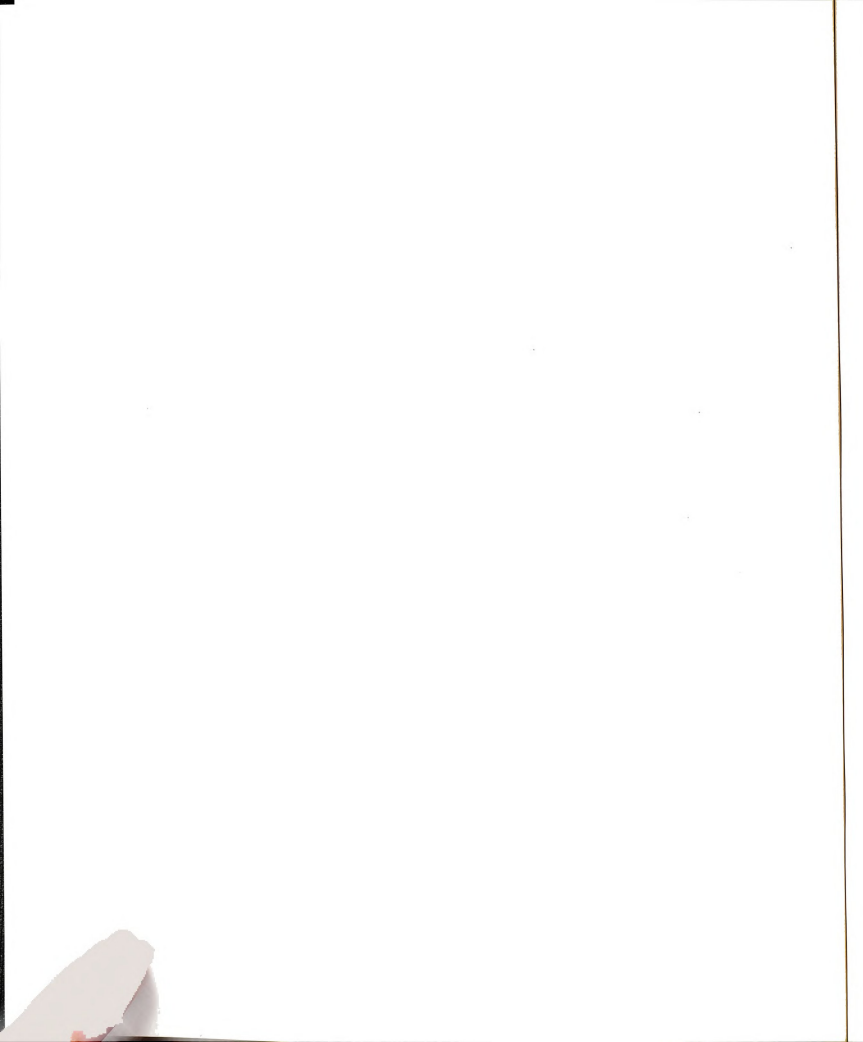


Figure 3.2: The stress strain behavior of 50x50 triangular network with  $f=0.1$





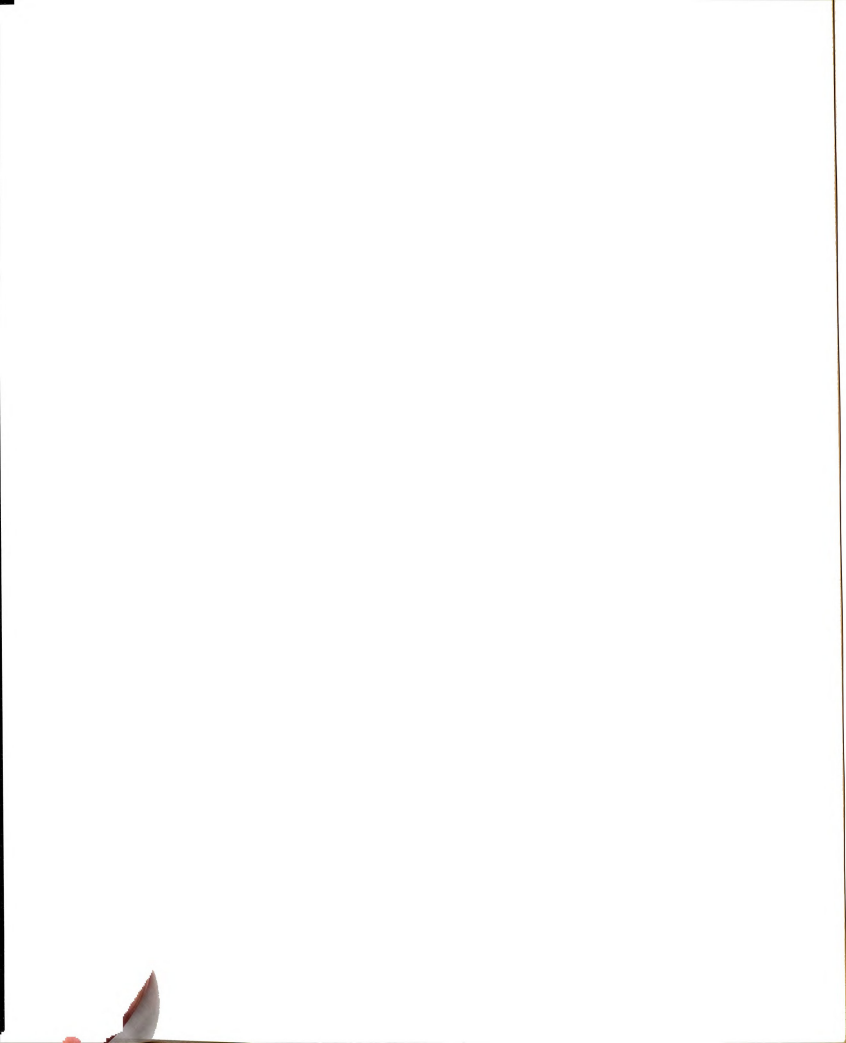
involves a great deal of bond rotation, and is probably not relevant to either brittle or ductile fracture. To illustrate the model network response, we show in Fig. 3.3 to 3.5 three snapshots of the microstructural evolution of damage and fracture in a 50x50 lattice. The initial catastrophic event (usually at  $\sigma_1(f)$ ), leads to a path of broken bonds across the network, but not total fracture. Final fracture occurs at much larger strain, though the final fracture path is often close to the path of catastrophic event, and is usually preceded by bond rotation along the fracture path. There are exceptions to this rule however, and crack branching events do sometimes occur. As the initial  $f$  increase, the crack path becomes more tortuous, though the structure of crack path is dependent on the model and damage evolution algorithm used. The fracture strength however is more robust and its scaling behavior appears to be fairly model independent [Beal88, Hass89]. This makes the use of simple models most valid for the calculation of strength and strength statistics, while the crack topologies found using these models are only valid for the specific loading condition and microstructure that applies to the model.

### 3.3 Scaling theory of tensile fracture stress

Since for small  $f$ ,  $\sigma_1(f) \simeq \sigma_b(f)$  we can approximately calculate the fracture stress from the relationship

$$\frac{\sigma_b(f)}{\sigma_b(0)} \simeq \frac{\sigma_0}{\sigma_{\max}(f)} \quad (3.5)$$

where  $\sigma_0$  is the applied stress.  $\sigma_{\max}(f)$  is the stress in the spring with the largest strain, prior to any bond fracture. Eq. (3.5) uses the (small strain) linearity of the system to extrapolate from a linear elasticity calculation of  $\sigma_{\max}(f)$  to deduce



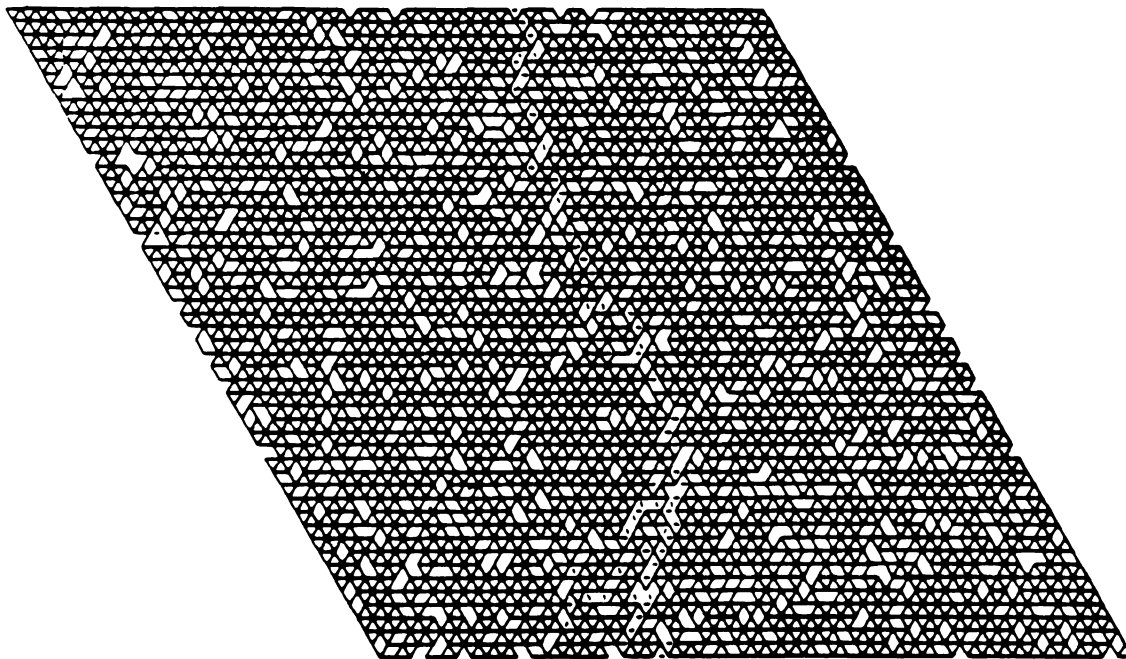
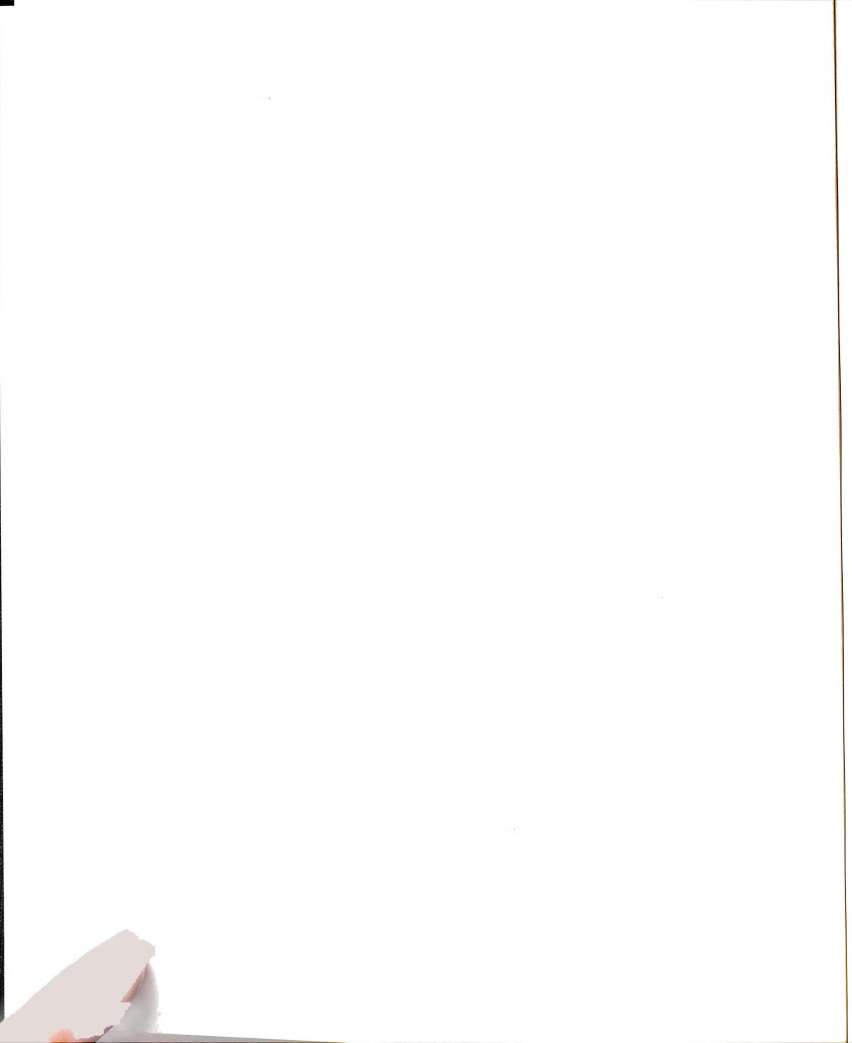
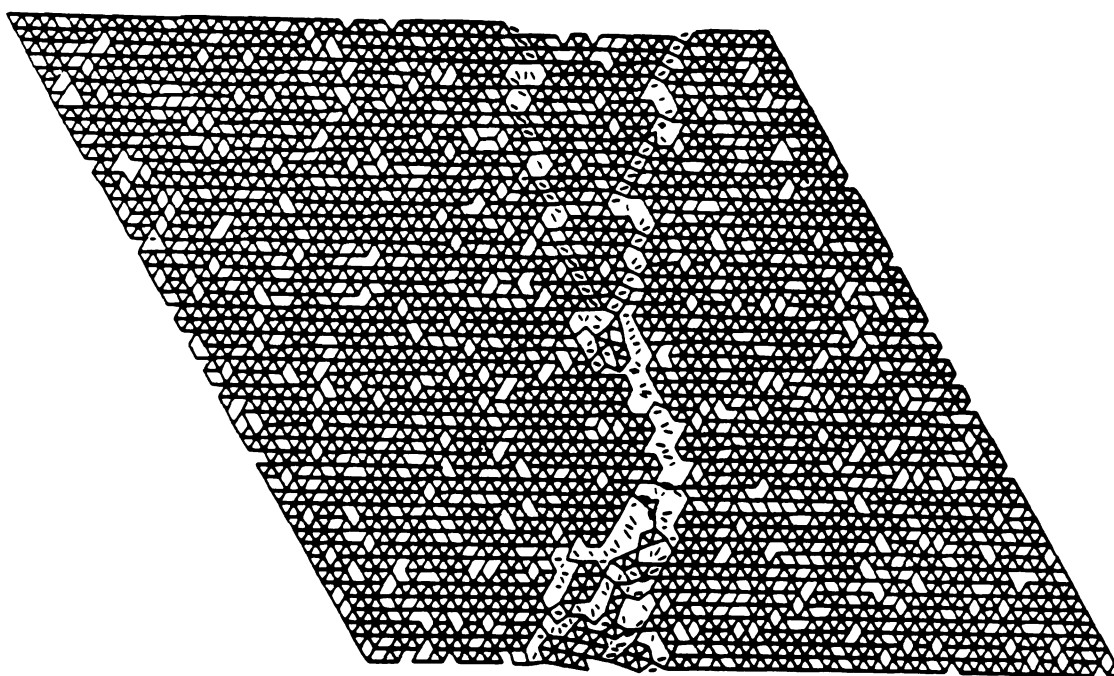
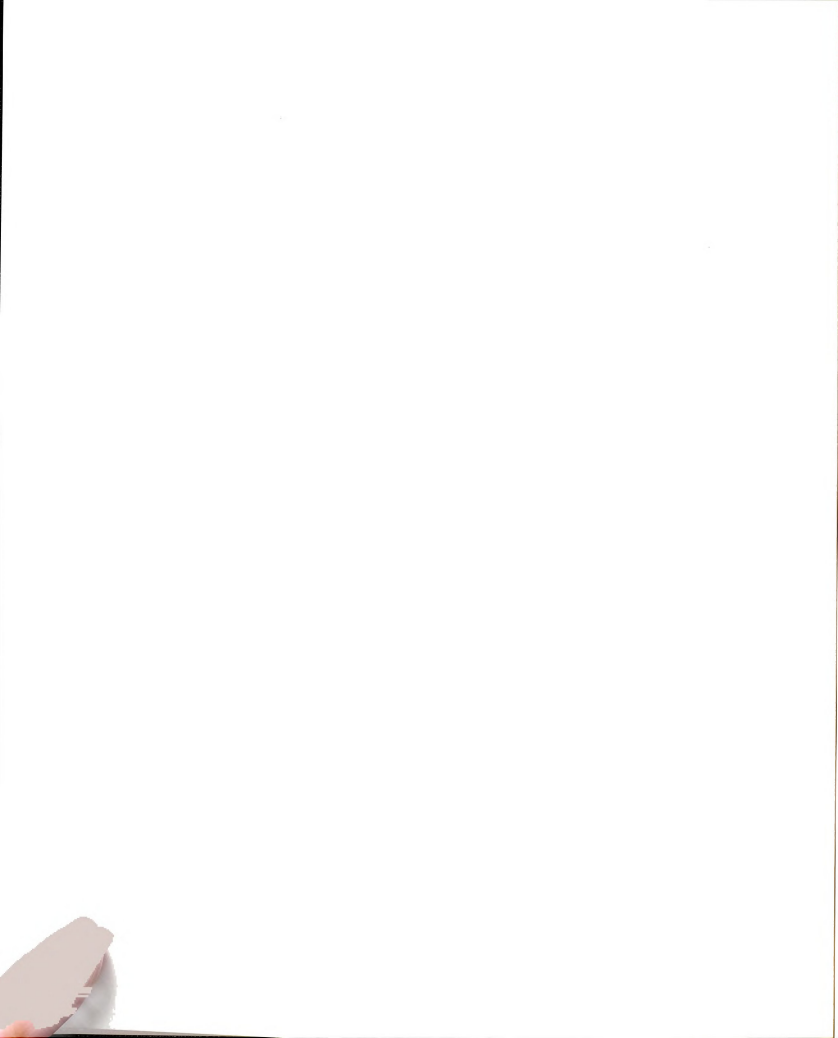


Figure 3.3: The the network configuration after the first catastrophic event at  $\sigma_1(f)$ . The simulation were on 50x50 lattices with  $f$  (initially) = 0.10





**Figure 3.4:** An intermediate configuration just before the second major peak in Fig. 3.2.



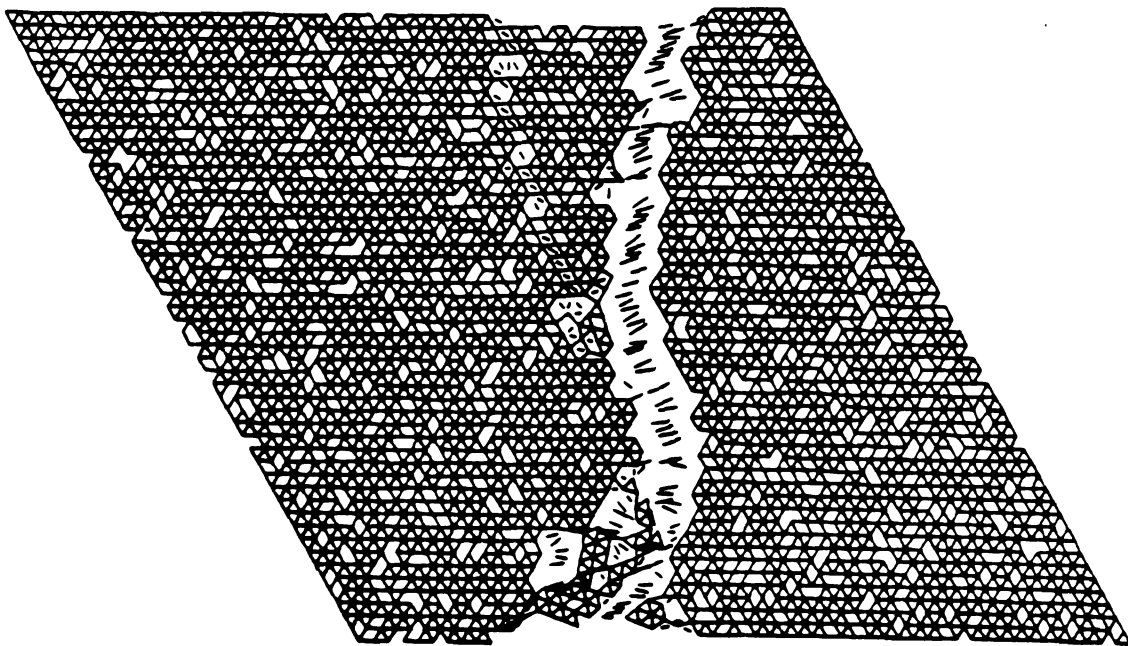
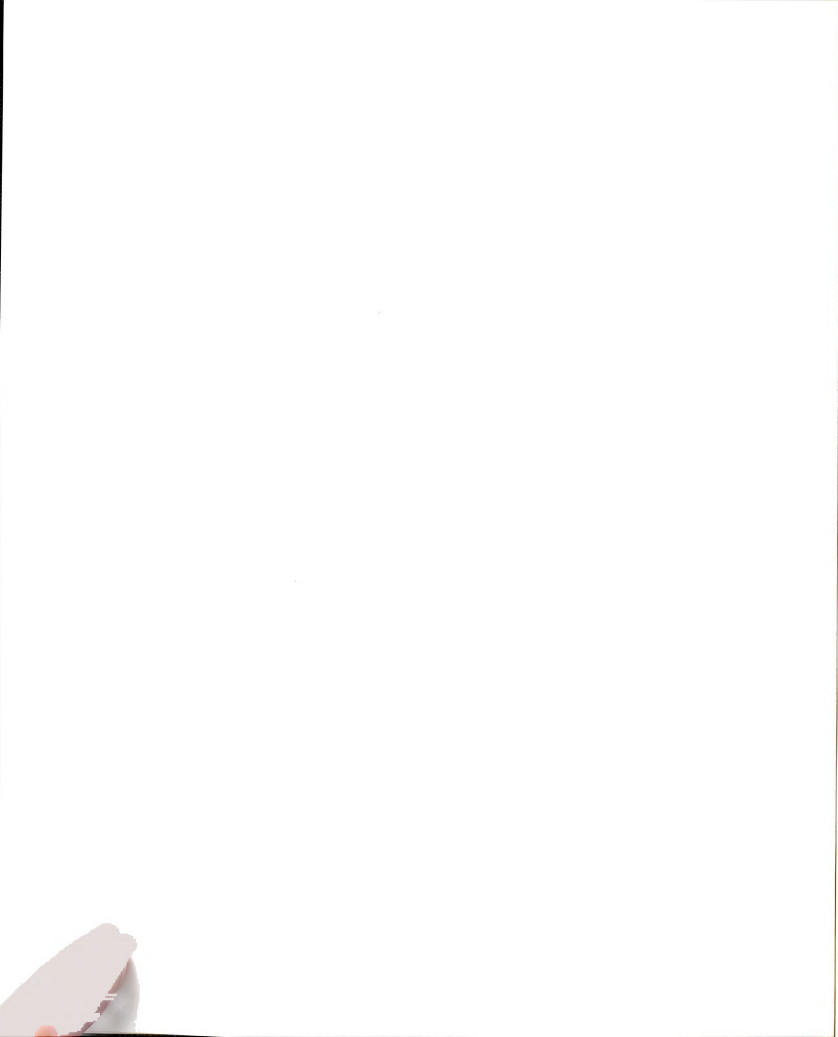


Figure 3.5: The final fracture configuration. Full line from one node to its neighbors represent the connected bonds while the truncated lines represent the bonds which were initially present but which broke in the damage evolution process.





$\sigma_b(f)$ . The problem now reduces to estimating  $\sigma_{\max}(f)$  for the initial disorder in the network.

It is well known that cracks lead to large local stress enhancements. In dilute networks, crack-like flaws are unlikely, but do occur with finite probability somewhere in the networks. It is these unlikely flaws that dominate the strength of the networks. The simplest crack-like flaw contains  $n$  adjacent removed bonds. The probability of occurrence of such a configuration is approximately

$$P(n) \simeq L^d f^n \quad \text{as } n, L \rightarrow \infty \quad \text{and} \quad f \rightarrow 0 \quad (3.6)$$

where  $L$  is the linear dimension of the networks in lattice units. The largest such configuration that occurs with finite probability is estimated from

$$L^d f^{n_{\max}} \simeq 1 \quad (3.7)$$

which implies

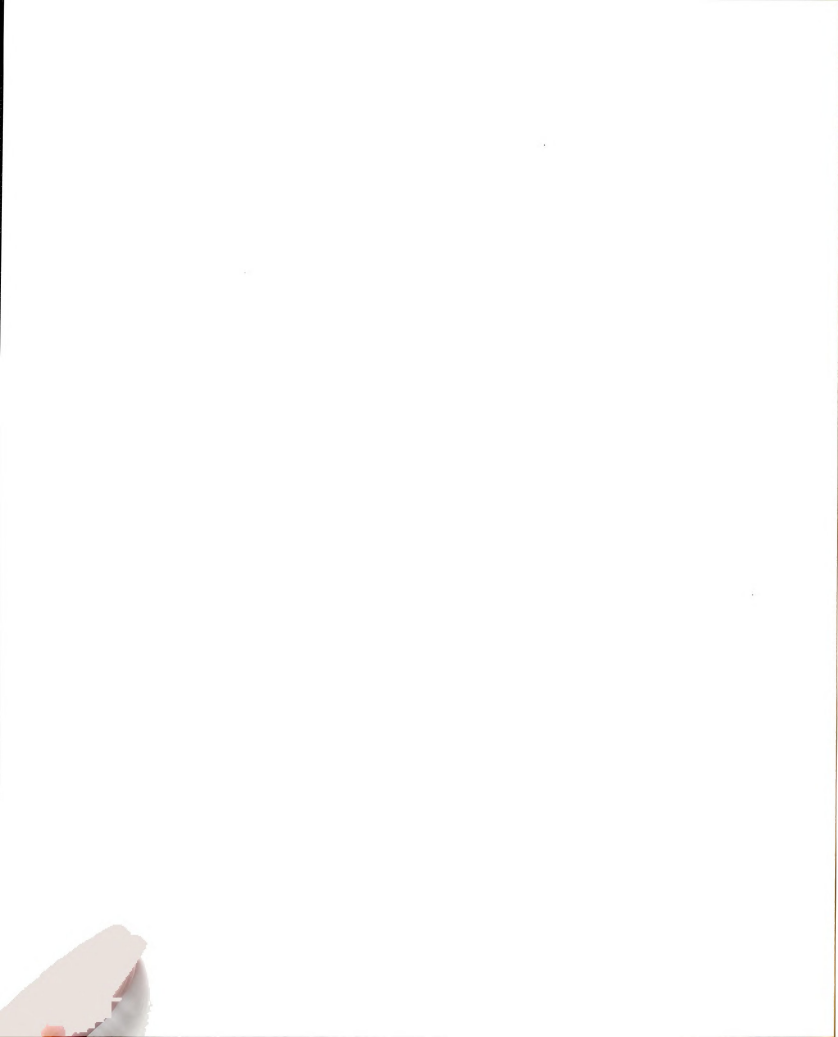
$$n_{\max} \simeq -d \ln L / \ln f. \quad (3.8)$$

Such a crack-like defect configuration has a stress intensity at its tips that scales as (for  $-\ln L / \ln f$  large);

$$\frac{\sigma_{\max}(f)}{\sigma_0} \simeq 1 + K_m (-d \ln L / \ln f)^{1/2} \quad (3.9)$$

where  $K_m$  is an unknown constant that depends on the curvature of the crack tip and the size of a plastic zone (this is the continuum elasticity result for tensile loading of a through crack).

In two dimensions (and for cracks for fixed finite separation), it is known that two adjacent cracks enhance the stress between them by a factor approximately



proportional to crack length[LiYS87]. In this case the exponent in (3.9) is changed to 1 [Beal88, Hass89]. From these arguments and (3.5) we then find;

$$\frac{\sigma_b(f)}{\sigma_0} \simeq \frac{1}{1 + K_m(-d \ln L / \ln f)^\beta},$$

for  $-d \ln L / \ln f \rightarrow \infty$  and  $f \rightarrow 0$  (3.10)

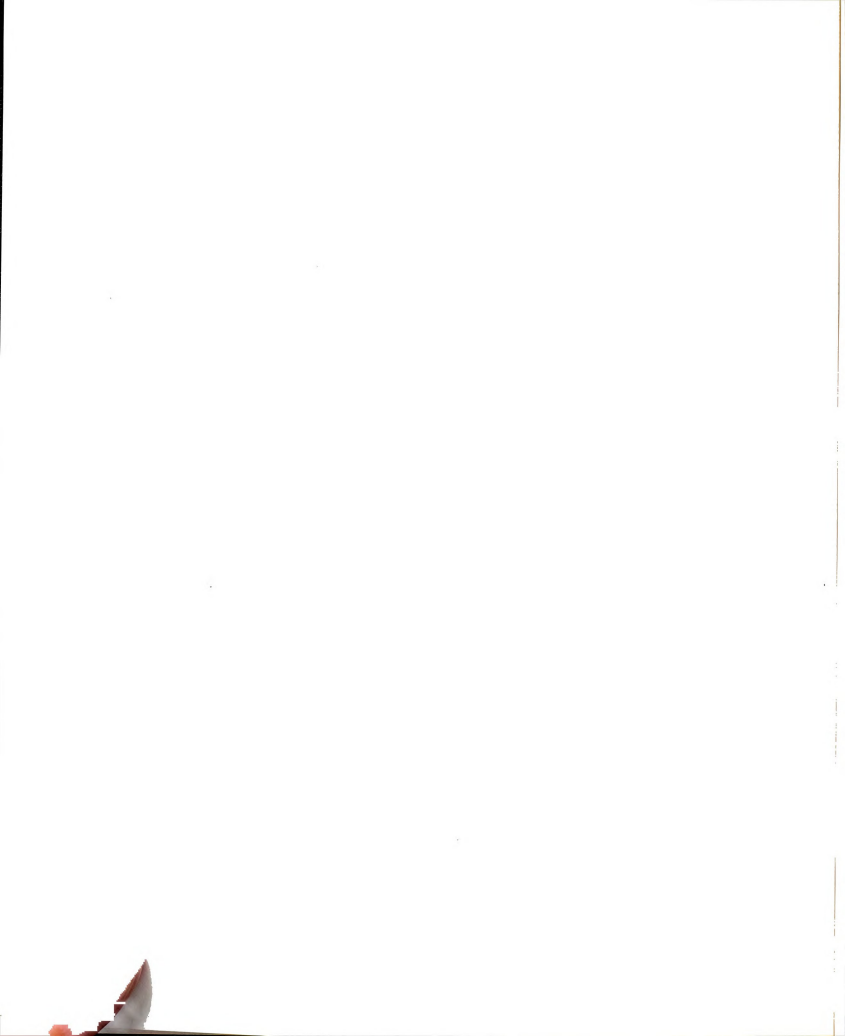
where  $1/2(d-1) \leq \beta \leq 1$ . Eq. (3.10) also applies to the tensile fracture stress of three dimensional system, with only minor modifications of  $K_m$  and  $\beta$ . Eq. (3.10) contains two interesting affects:

1. At fixed  $f$ , a logarithmic size effect in fracture stress occurs.
2. the fracture stress is rapidly decreasing for small  $f$ , and in fact is singular as  $f \rightarrow 0$ .

Eq. (3.10) is only strictly valid for  $-d \ln L / \ln f \rightarrow \infty$ , which does not apply to the lattice sizes available for simulations. Despite this, the general trends outlined in points 1. and 2. above are present in the numerical data presented in Fig. 3.6 and 3.7. For comparison the Young's modulus which in this limit is linear in dilution and clearly non-singular. The difference in dilute limit scaling behavior of the Young's modulus and the tensile fracture stress is clearly evident in Fig. 3.6 with the theoretical prediction (3.10) suggests that the scaling behavior of small systems may be well represented by the form;

$$\frac{\sigma_b(f)}{\sigma_0} \simeq \frac{1}{1 + B|\ln f|^{-\beta}} \quad (3.11)$$

where  $\beta$  and  $B$  are system size dependent parameters. A test of this form using the tensile fracture data of Fig. 3.6 is presented in Fig. 3.7. It is seen from Fig. 3.7 that  $\beta = 1.7 \pm 0.1$  gives an excellent fit to the data in the singular region



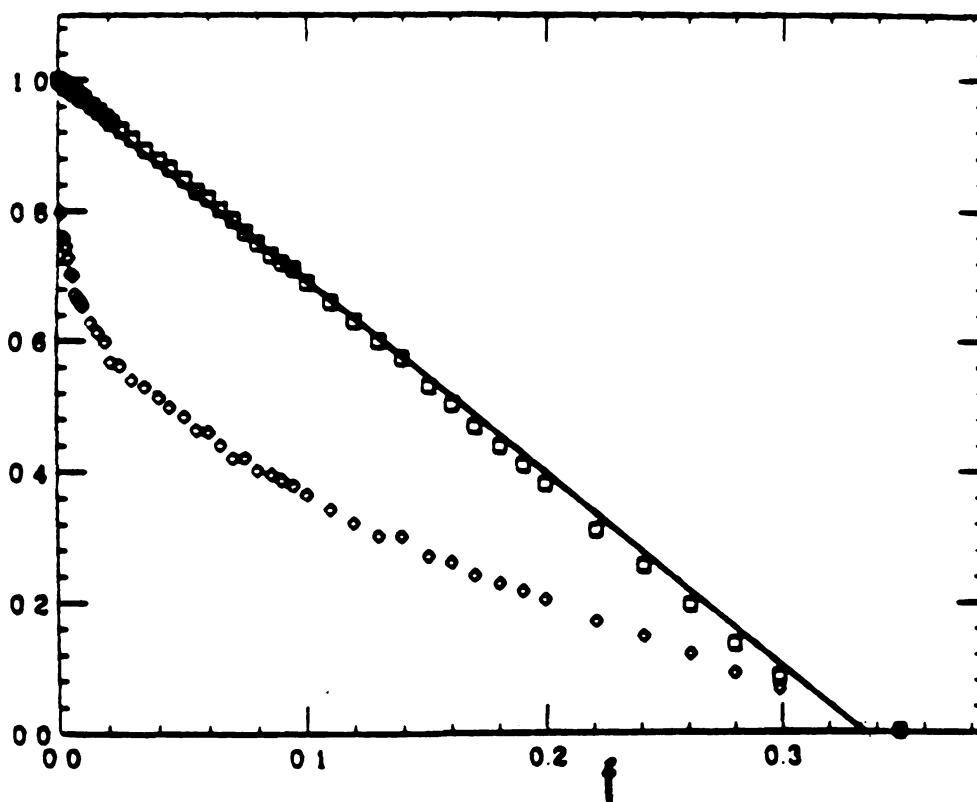
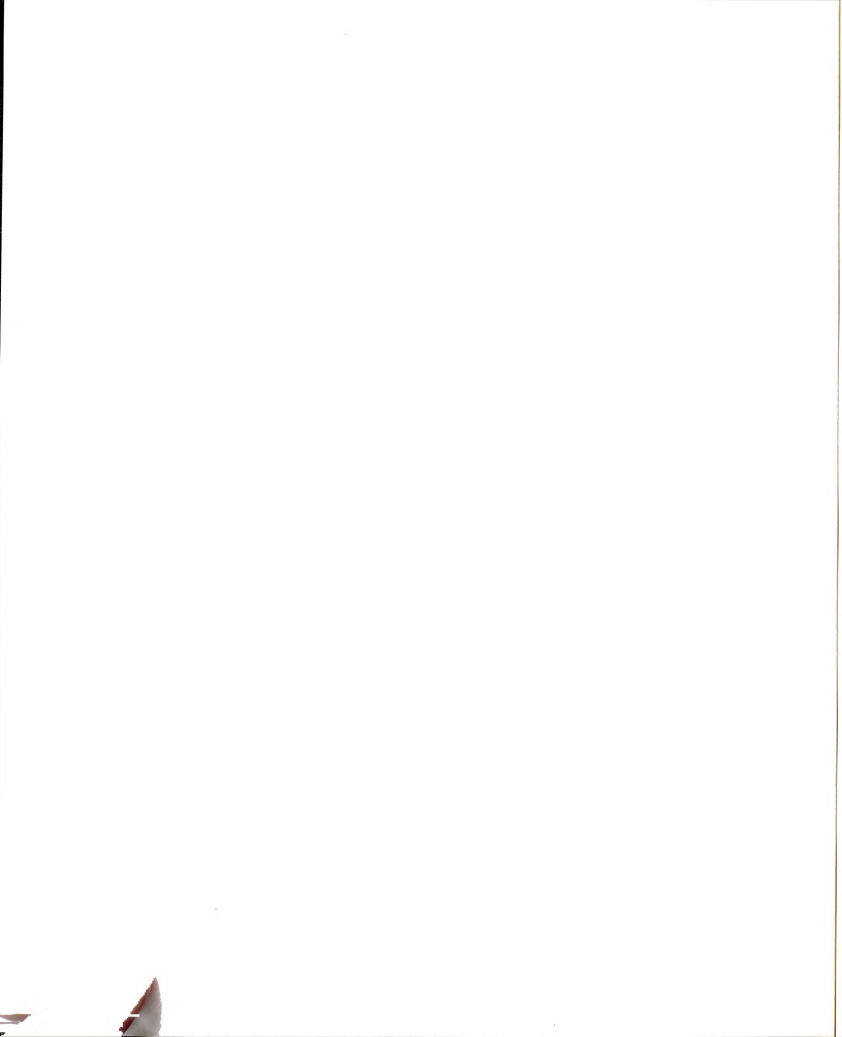


Figure 3.6: The Young's modulus,  $Y(\square)$ , and tensile fracture stress,  $\sigma_1(f)(\diamond)$  of  $L = 60$  central force networks. Each point is an average over 40 configurations. The solid line is from Eq. (3.4) applied to the triangular lattice.



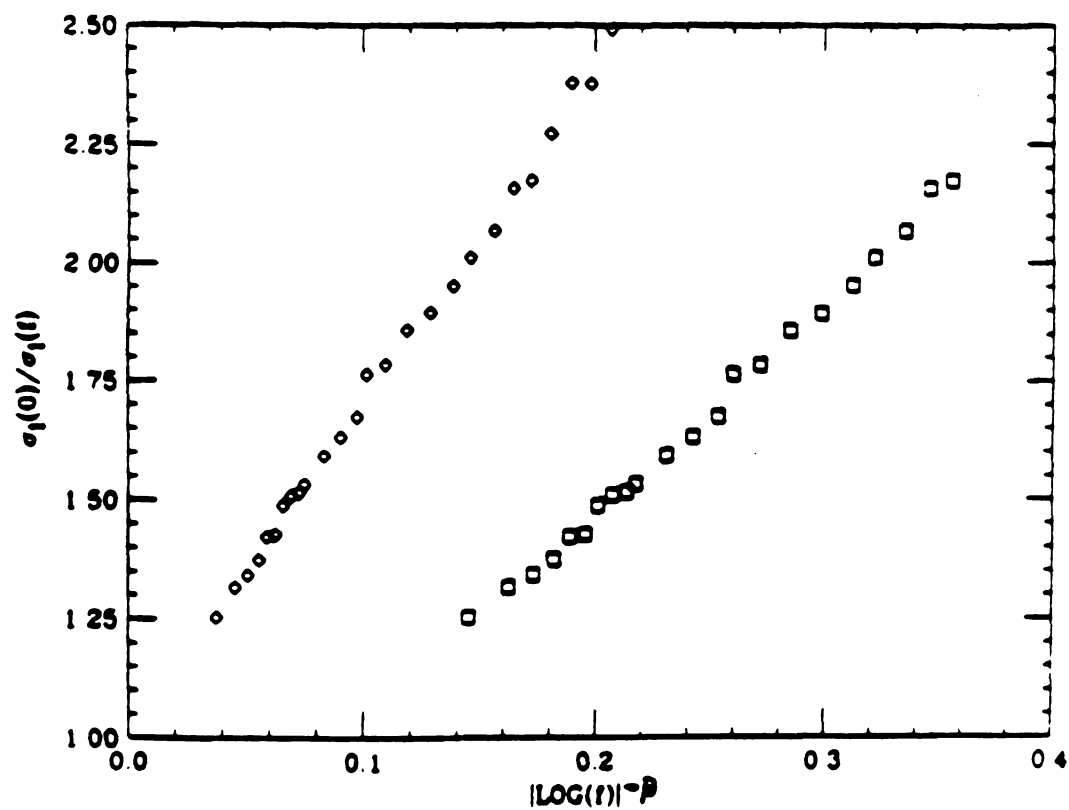


Figure 3.7: A test of the scaling of  $\sigma_b(f)$  of the form (3.11) for  $\sigma_1(f)$  for  $\beta = 1.0$  ( $\diamond$ ) and  $\beta = 1.7$  ( $\square$ ).





$f < 0.10$ . We thus suggest that Eq. (3.11) provides a useful representation of the strength of the dilute random networks for a wide range of system sizes and that  $\beta$  only lies in the range  $1/2(d-1) \leq \beta \leq 1$  in the infinite lattice limit. We expect that in the dilute limit, models with bond bending forces should show a behavior similar to the central force networks. This may be understood if we consider a lattice constructed of blobs of central force elements. Since the lattice is rigid on most length scales near pure limit, most of these central force blobs are rigid. We can thus renormalize the problem on to an effective model with bond bending forces. In contrast, the behavior of the bond bending and central force problems are very different at higher  $f$ . The bond bending problems lose rigidity at  $f_c$ , the connectivity percolation point, while the central force networks lose rigidity at  $f_*$  ( $f_* < f_c$ ) [Thor87].

In bond bending problems,  $\sigma_b(f)$  exhibits the critical scaling;

$$\frac{\sigma_b(f \rightarrow f_c)}{\sigma_0} \simeq (f_c - f)^x. \quad (3.12)$$

Several workers have placed bounds on  $x$ , though its precise value is as yet unknown. A node links and blobs picture[Guyo87] which states that the problem may be replaced by a network with effective lattice constant  $\xi$  (the percolation correlation length) implies the upper bound,

$$\sigma_b(f) < \sigma_0(f_c - f)^{(d-1)\nu} \quad (3.13)$$

where  $\nu$  is the critical exponent for  $\xi$ . If the effective lattice constant,  $\xi$ , acts as a rigid moment arm on a given bond, the fracture stress will be greatly reduced. This leads to the lower bound;

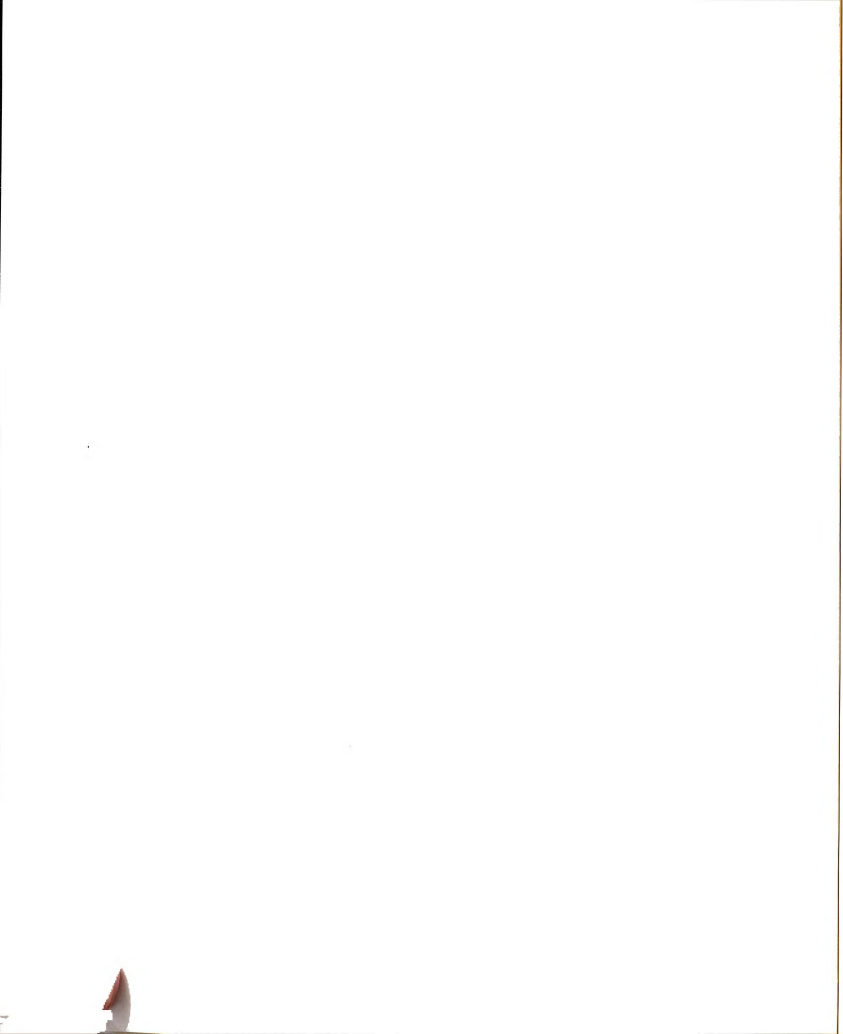
$$\sigma_b(f) > \sigma_0(f_c - f)^{d\nu}. \quad (3.14)$$

We thus deduce that  $\alpha$  in Eq. (3.12) lies in the range  $(d - 1)\nu < \alpha < d\nu$ . We do not at present have any bounds on  $\alpha$  for the central force problem, but it is evident from Fig. 3.6, that  $\alpha$  is nearly 1 for  $f$  quite close to  $f_*$ . Some experiments have been attempted to find  $\alpha$ . Using a 2mm thick aluminum sheet with holes drilled to form a triangular lattice, Sieradzki and Li [Sier86] found  $\alpha = 1.7 \pm 0.1$ . This value lies within the bounds given above (with  $\nu = 4/3$  in 2-D). It must be remembered though that the experiment is not truly in 2-D, the aluminum is ductile and the lattice size is small (20x20) so this agreement may be fortuitous. A second interesting feature of the Sieradzki and Li paper (see Fig. 2 of [Sier86]) is that it shows some experimental evidence of the qualitative difference between dilute limit scaling of the elastic modulus and that of the fracture stress, despite the small system size. A second experiment to find  $\alpha$  was published by Benguigui *et al* [Beng87] who randomly punched holes in a copper sheet. They used a square lattice and found  $\alpha \simeq 2.5 \pm 0.4$ . This also lies within the bounds given above but is also subject to the caveats stated above.

## 3.4 Bond Bending Networks

### 3.4.1 Background

In carbon fibers, the basic building blocks of the fibers are planar networks made up of connected benzene rings. These graphene layers are imperfect [Kell81, Dres88, Donn90], and contain many vacancy and vacancy cluster defects. In this and following chapter we attempt to assess the effect of atomic scale defects on the in plane strength of graphite sheets and tubes. The recent reports of “buckytubes”, which appear to be composed of nanoscale graphite tubes, lends



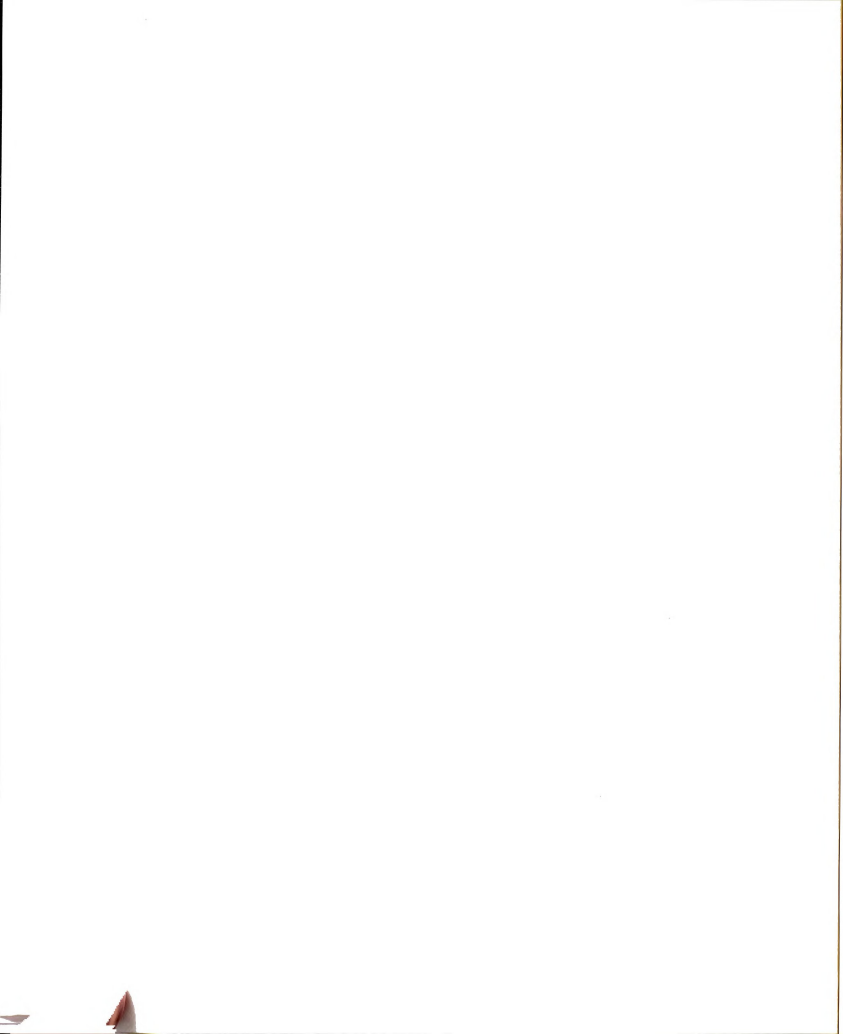
further impetus to this effort [Iji91]. The model we use only considers the elastic energy of the graphite sheets, and ignores the re-hybridization and charge transfer that occurs near defects. The purely elastic model provides a reference against which later calculations, which include these effects, will be compared.

The model and algorithm we use is as follows. The lattice is assigned an elastic energy given by the Kirkwood energy;

$$E = \frac{1}{2} \sum_{ij} \alpha_{ij} (l_{ij} - l_{ij}^0)^2 + \frac{1}{2} \sum_{ijk} \beta_{ijk} (\cos \theta_{ijk} - \cos \theta_{ijk}^0)^2 \quad (3.15)$$

$i, j$  label nodes of a honeycomb lattice, while  $l_{ij}$  ( $l_{ij}^0$ ) is the length (equilibrium length) of the bond between  $i$  and  $j$  and  $\alpha_{ij}$  is the central force spring constant between nodes  $i$  and  $j$ .  $\theta_{ijk}$  is the angle subtended by nodes  $ijk$ , and  $\beta_{ijk}$  is the angular spring constant associated with deviations in this angle from its equilibrium value  $\theta_{ijk}^0$ . This potential is similar to the Keating potential, which has been successfully applied to covalently bonded materials and illustrates the points we make in this work [Keat66, Kirk39]. We choose the Kirkwood potential for our initial study, as previous studies of the effect of bond defects on the elasticity of honeycomb structures have used this potential, and provide a check on our analysis [Zabo86]. The change to a Keating potential will only make small changes to the numbers calculated here.

For pure graphite, the ratio  $\beta/\alpha \sim 1/4$ , and this is the value that we use in our simulations. We assume that bond rupture only occurs in tension, and that the strain at which this bond rupture occurs is 20%, as found from calculation of the strain at the peak of the force-displacement curve of the carbon-carbon

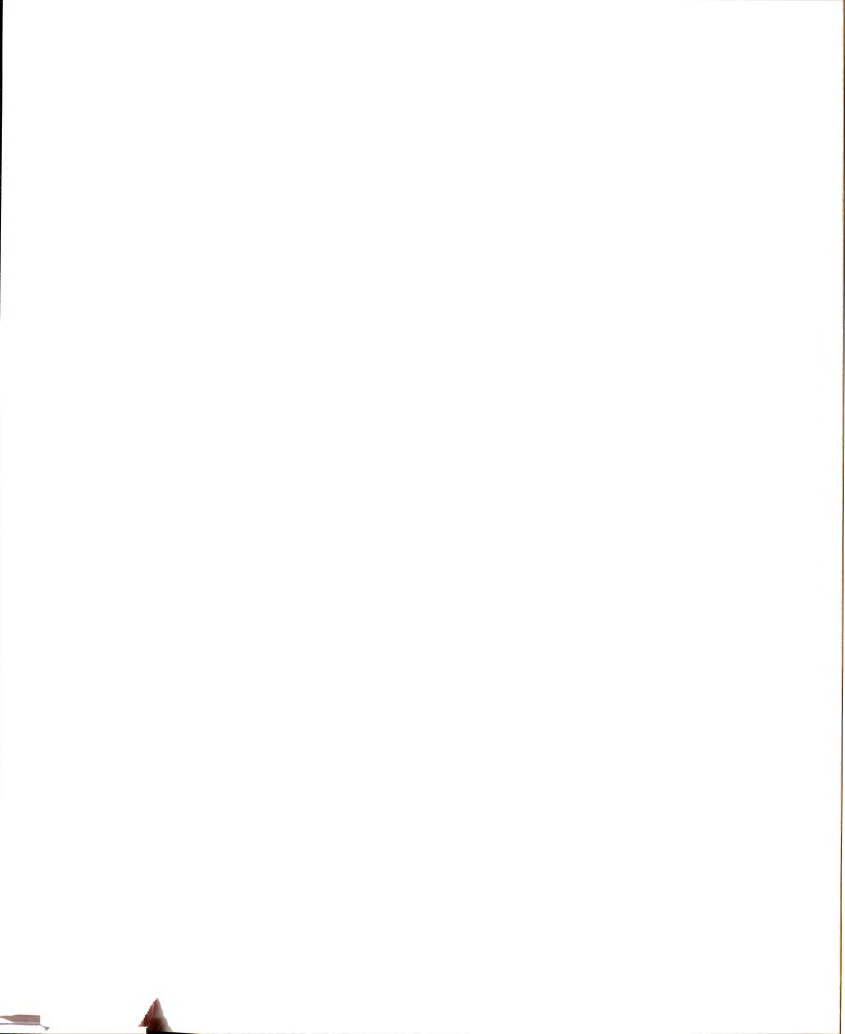


bond (other strong atomic bonds have a similar value for the strain at the peak force). When a bond exceeds this tensile strain, it is removed from the network. No deformation is allowed out of the plane of the graphite sheet (no buckling), and in the fracture simulations, the tube maintains the same average diameter (Poisson ratio = 0).

To simulate tensile fracture, we carry out the following algorithm [Arca85, Sahi86, Duxb87a, Duxb91, Beal88]:

1. Increment the applied tensile strain by a small amount.
2. Search through the bonds in the network to see if any bond carries a tensile strain which is larger than the critical value of 20%. If any bonds exceed this value, remove the one carrying the largest strain. Then return to the start of 2. and iterate until no further bond failure occurs.
3. If no bond carries a strain larger than the threshold value, return to 1.

Practically, we find that it is possible to predict the applied strain at which the next bond will fail from the previous relaxation, so the applied strain increments are variable. This leads to a large increase in the efficiency of the algorithm. The fracture algorithm is based on our ability to find the equilibrium strain configuration for a honeycomb lattice described by the strain energy (3.15), with arbitrary defect configurations. To find this lowest energy state, we use a non-linear conjugate gradient technique. This is composed of successive linear conjugate gradient steps, with non-linear interpolation after each linear conjugate gradient step. The relaxation is stopped when the largest residual force in the lattice is  $10^{-4}$ , which corresponds to a residual energy which is always less than  $10^{-8}$ . Relaxation of



a 400 node lattice typically takes 1 minute of CPU time on a Convex CX240 processor.

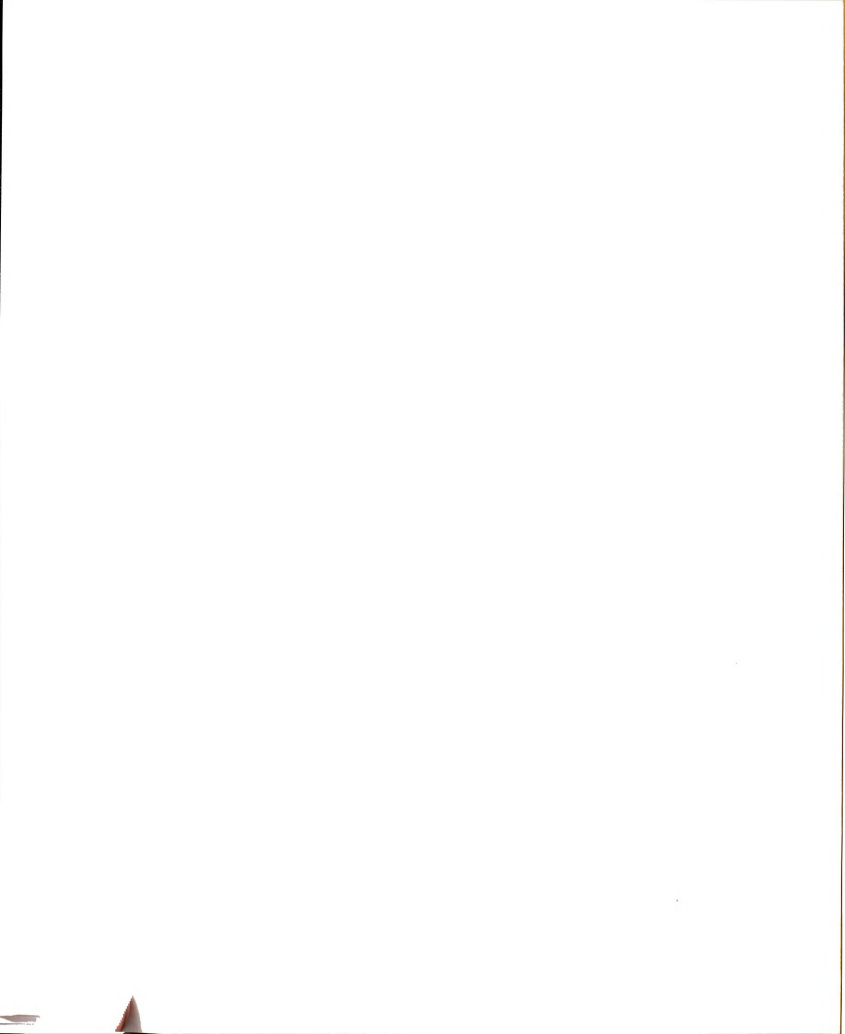
The fracture algorithm described above is “quasi-static” because after each bond failure, the network elastic energy is relaxed completely. The corresponding experiment would have a very low applied strain rate. Use of a network and the lattice energy (3.15) restricts the calculation to brittle materials, as no atomic sliding is allowed in the model (no plasticity or dislocation creation). This is complimentary to the molecular dynamics (MD) technique which corresponds to very high strain rates (a typical MD simulation runs for less than a nanosecond), but which does allow bond sliding and the plasticity associated with it.

### 3.4.2 Simulations of honeycomb networks

The elastic properties of the model represented by Eq. (3.15) on honeycomb lattices, have been previously studied in some detail [Zabo86], and it is known that the behavior near the percolation point is given by  $C_{11} \sim \mu \sim (f_c - f)^T$ , where  $\mu$  is the shear modulus and  $T = 3.96 \pm 0.04$ . For the bond diluted honeycomb lattice  $p_c = 1 - 2 \sin(\pi/18) \sim 0.6527$  ( $f_c = 1 - p_c$ ). Most simulations have been performed for small ratios of  $\beta/\alpha$  which are convenient to emphasize the difference between the behavior of rigid lattices (e.g. triangular) and non-rigid lattices (e.g. square and honeycomb). For  $\beta/\alpha = 1/4$  as is typical for graphite and related materials, the dependence of the elastic moduli on random bond vacancies is presented in Fig. 3.8

Using the failure algorithm, we find the stress-strain curve for a sheet with 5% random bond defects to be as shown in Fig. 3.9.  $\sigma_c$  is the tensile fracture stress of this random honeycomb. The stress-strain curve of this disordered tube is close





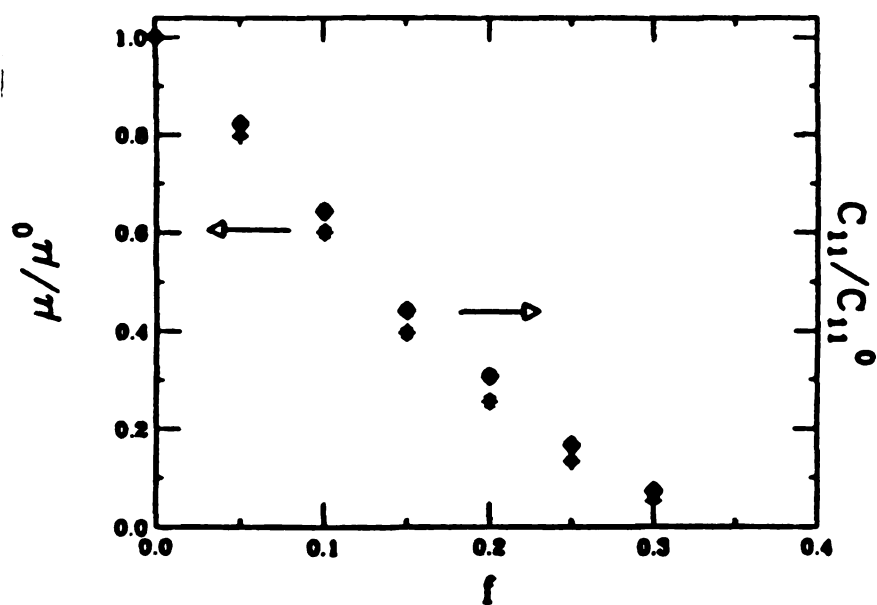
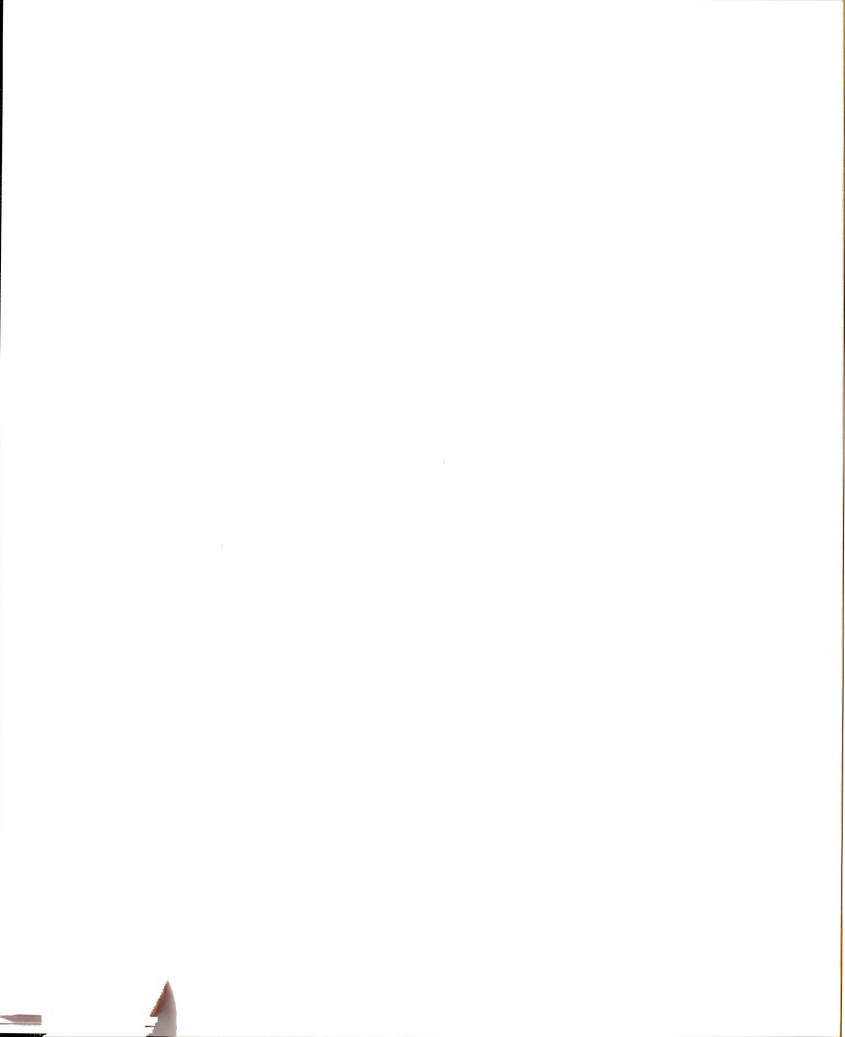


Figure 3.8:  $C_{11}$  and  $\mu$  for a 400 node tube as a function of the volume fraction of removed bonds.  $C_{11}^0$  and  $\mu^0$  are the values in the pure limit.



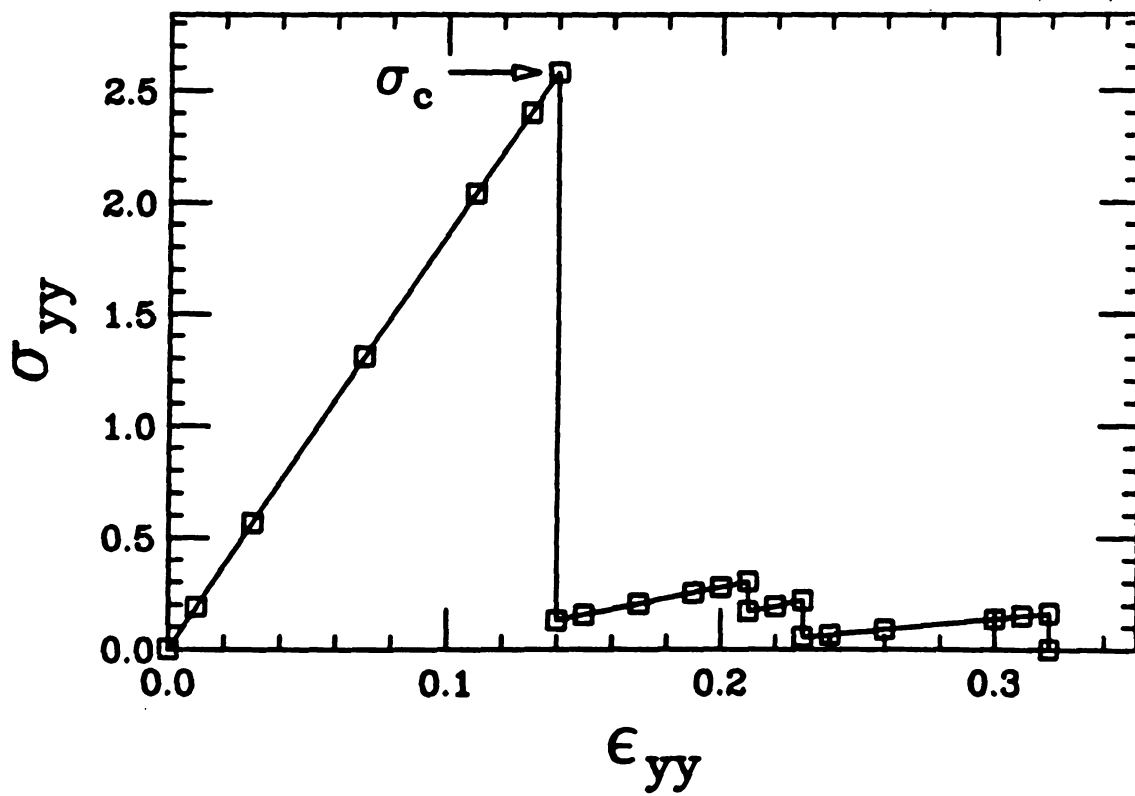
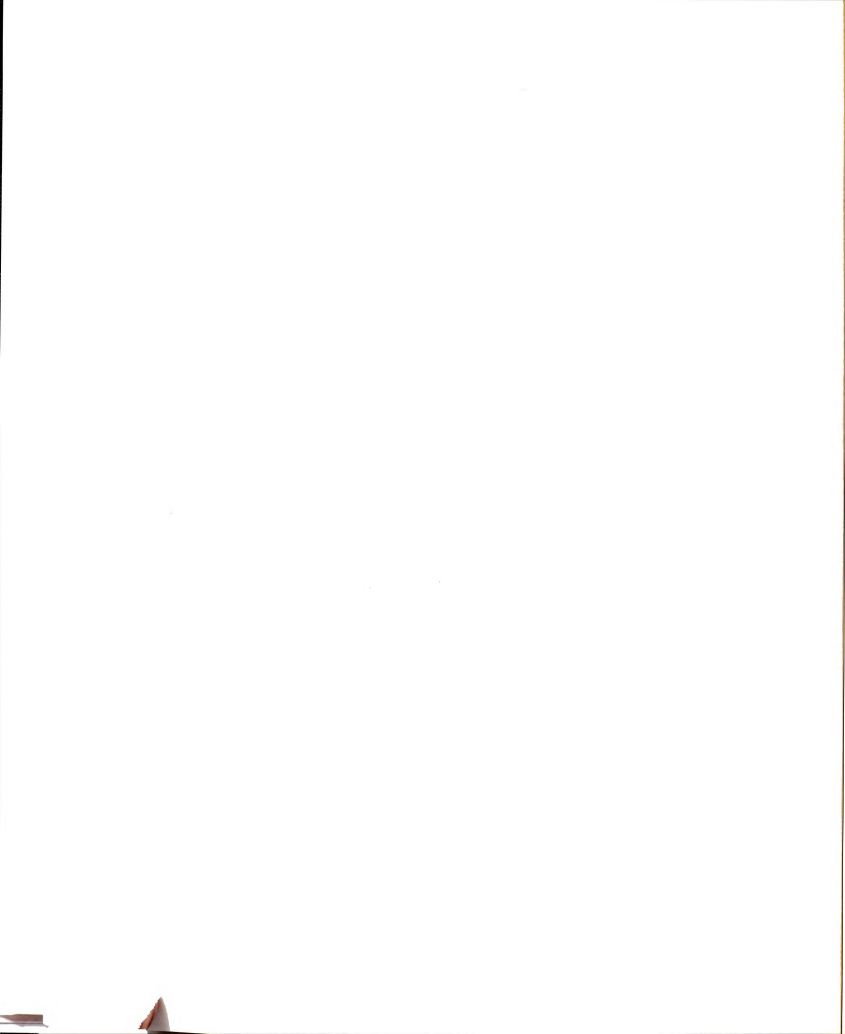


Figure 3.9: The stress-strain curve for a 900 node tube with 5% random voids.

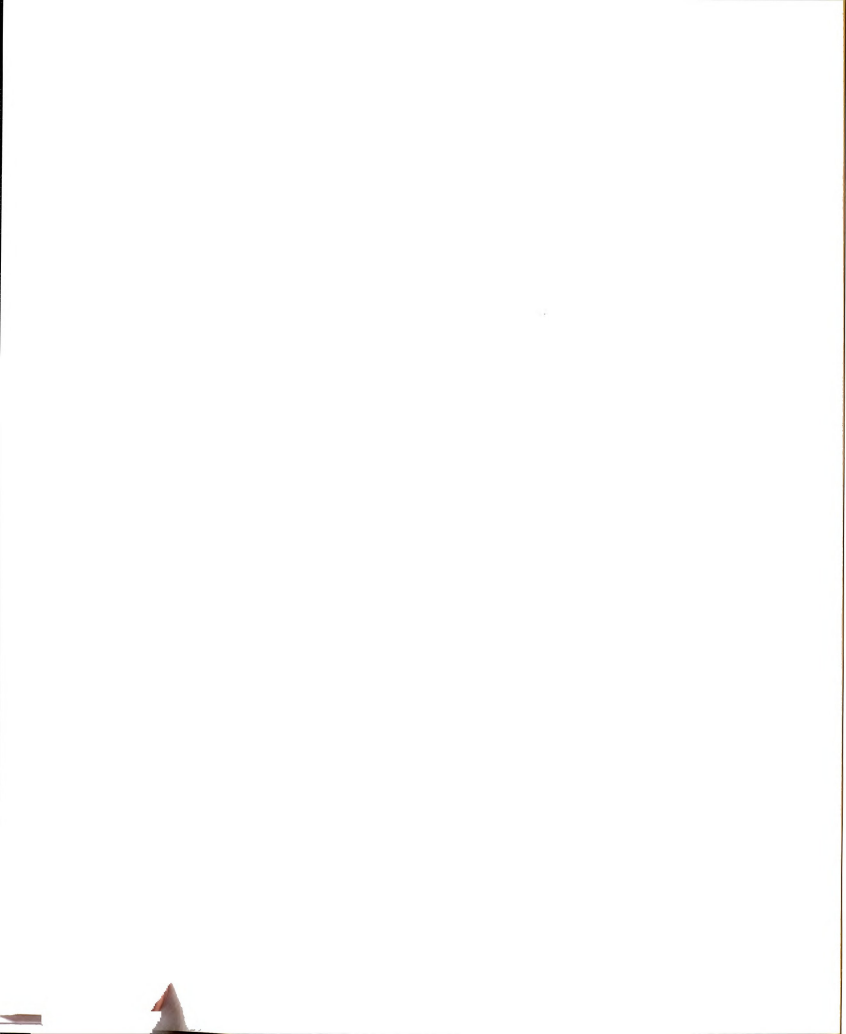


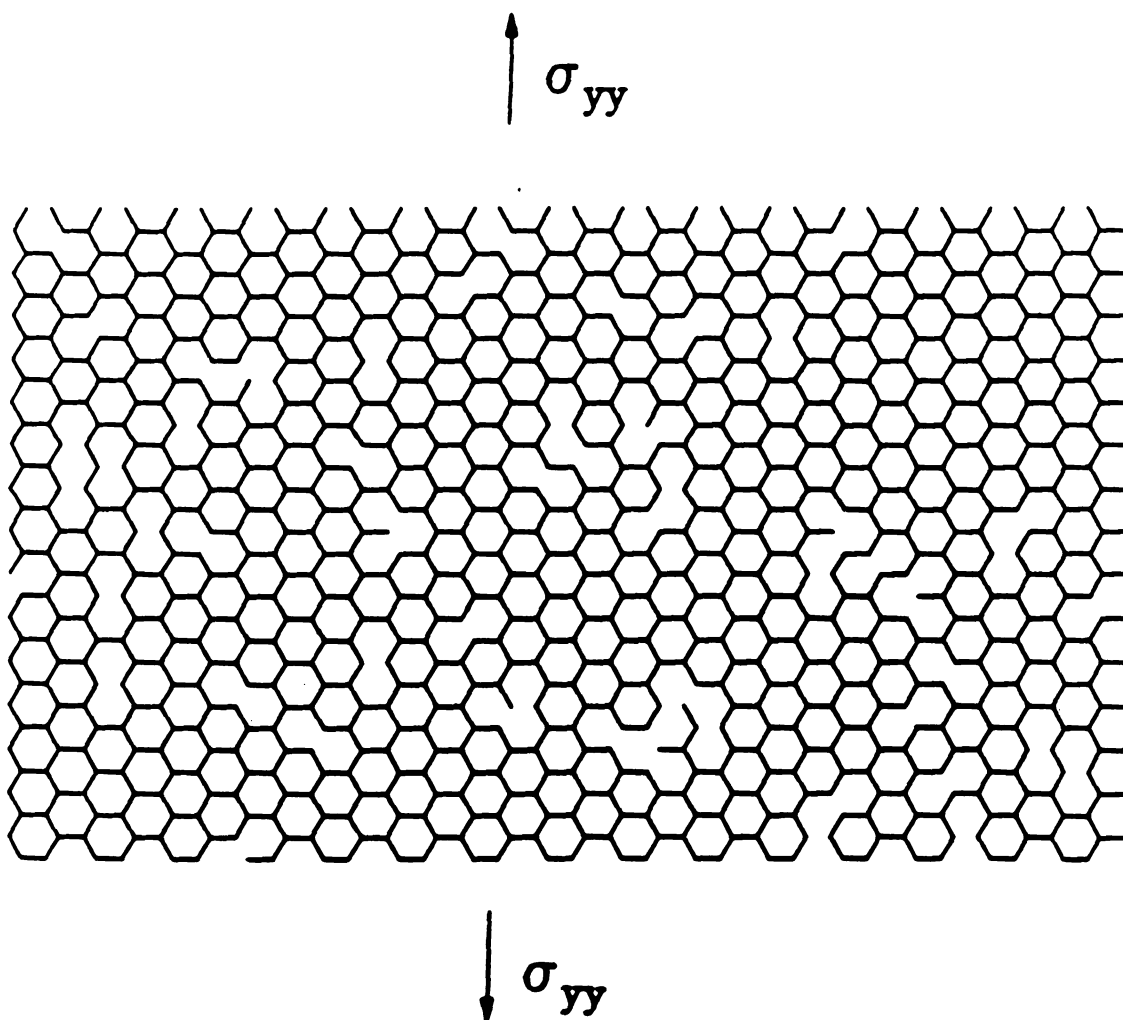
to linear elastic up to  $\sigma_c$ . In Fig. 3.10 and 3.11 the initial defect configuration used to produce Fig. 3.9, and the final fracture configuration produced by the simulation are presented.

The simulations are carried out with periodic boundary conditions, so the simulations are for tubes. Since  $f$  is small, the fracture path is almost linear, as there is little crack deflection to take advantage of pre-existing flaws. Despite this fact, the fracture stress is reduced appreciably from its pure lattice value. From Fig. 3.9, it is seen, for example, that the fracture stress,  $\sigma_c$  is 2.52, as compared to the pure lattice value of about 5.924. It is known that bulk graphite fails at a strain  $\epsilon_c \sim 0.1 - 0.3\%$ , while carbon fibers have failure strains that vary from 1% (high modulus graphite fibers) to 5% (low modulus carbon fibers that are composed predominantly of graphene sheets)[Kell81, Dres88, Donn90]. As we shall discuss below, random defects cause  $\epsilon_c$  and  $\sigma_c$  to decrease as the lattice size (sample size) becomes larger.

To illustrate the effect of atomic defect clusters on fracture, we show in Fig. 3.12, the response of a graphite sheet at 20% external strain, to a crack like defect cluster containing 10 missing bonds. The stress enhancement in the bonds at the ends of the defect cluster is 2.56. The applied strain required to break this flawed tube is then reduced from its pure lattice value by this factor.

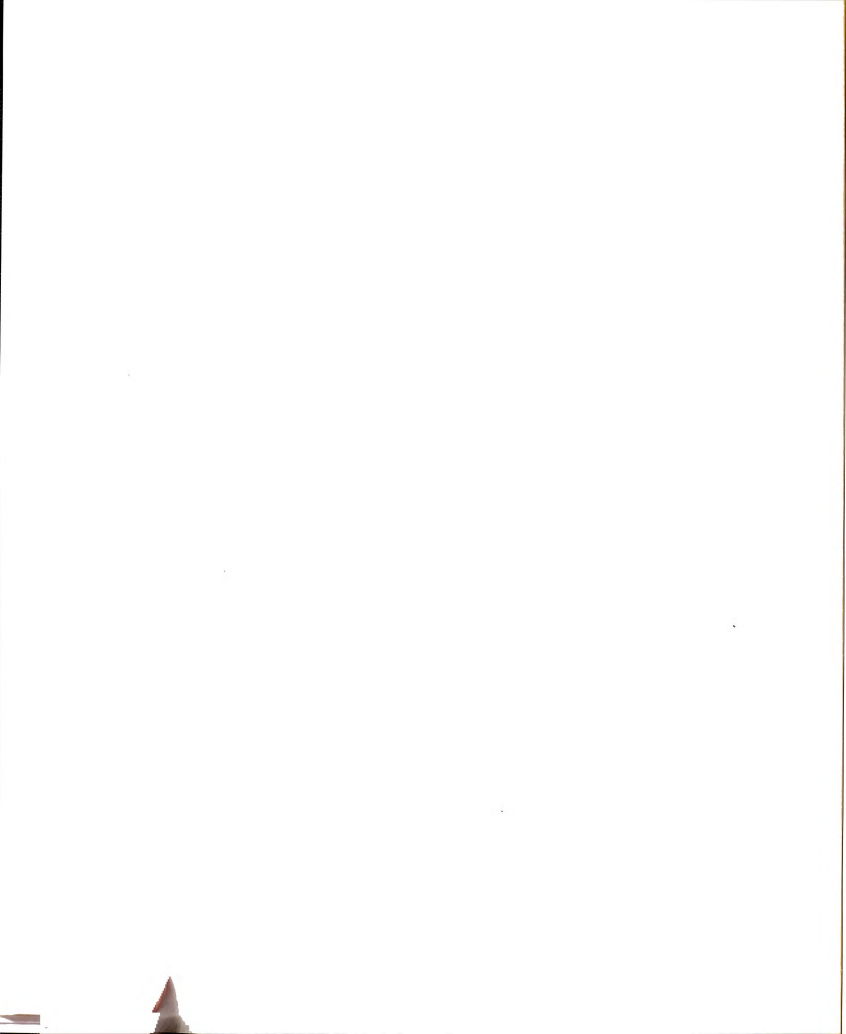
When bond defects randomly occur in a graphite sheet, the strength is reduced by infrequently occurring large defect clusters. To calculate the average value of this reduction for our honeycomb lattices, we average the value of  $\sigma_c$  found from curves such as Fig. 3.9 over many configurations. Results for  $\sigma_c$  for various values of  $N$  and  $f$  are presented in Fig. 3.13.

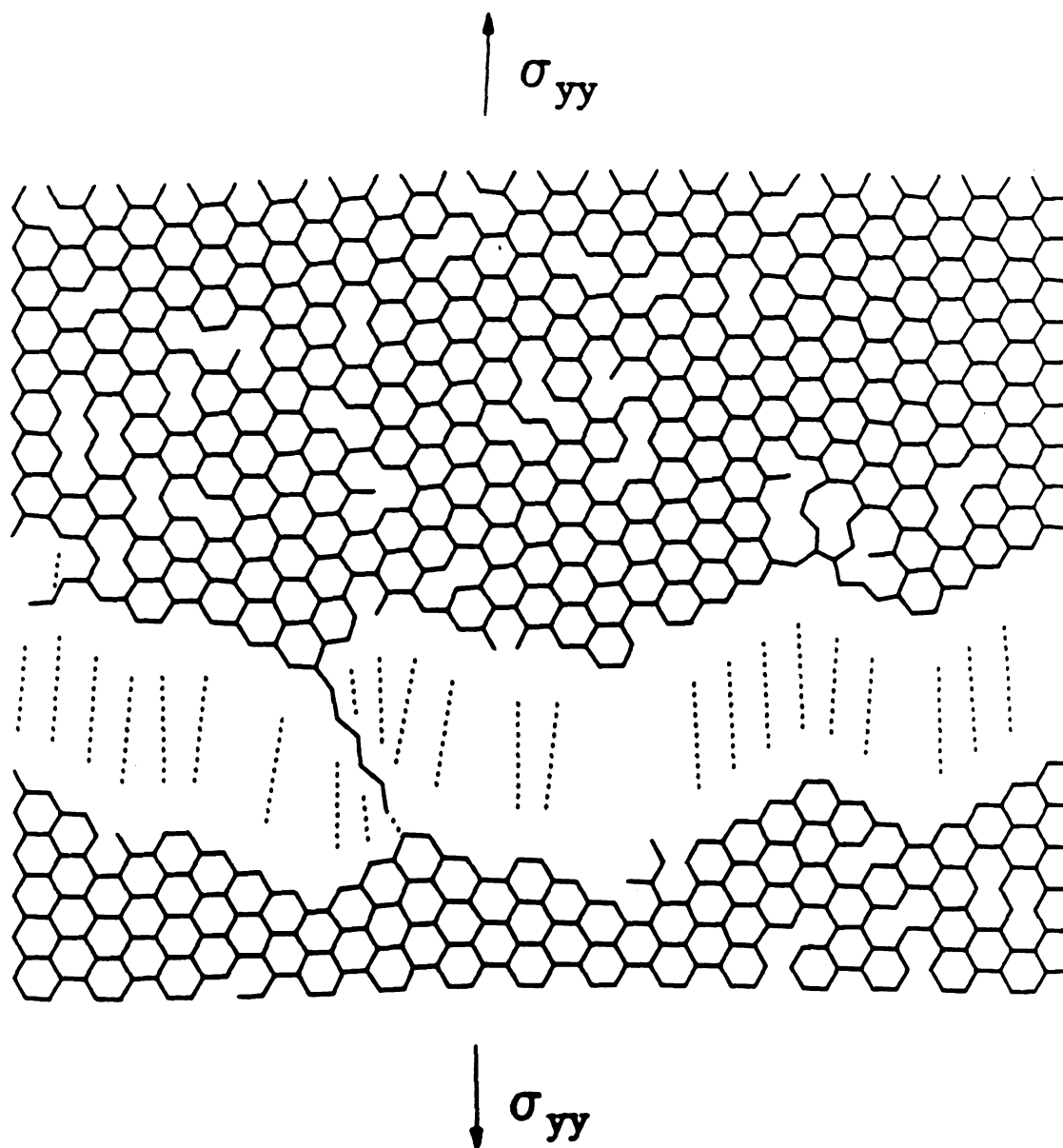




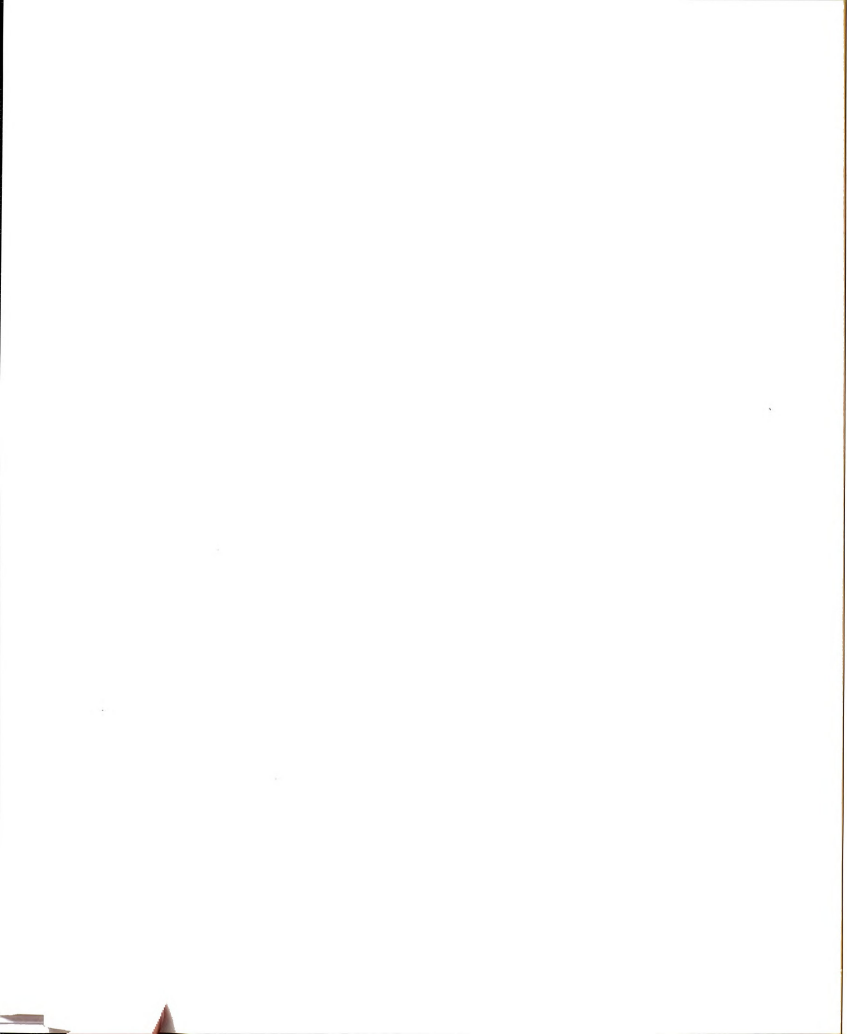
**Figure 3.10:** The initial configuration of tensile fracture of a hexagonal lattice containing 5% void volume fraction.

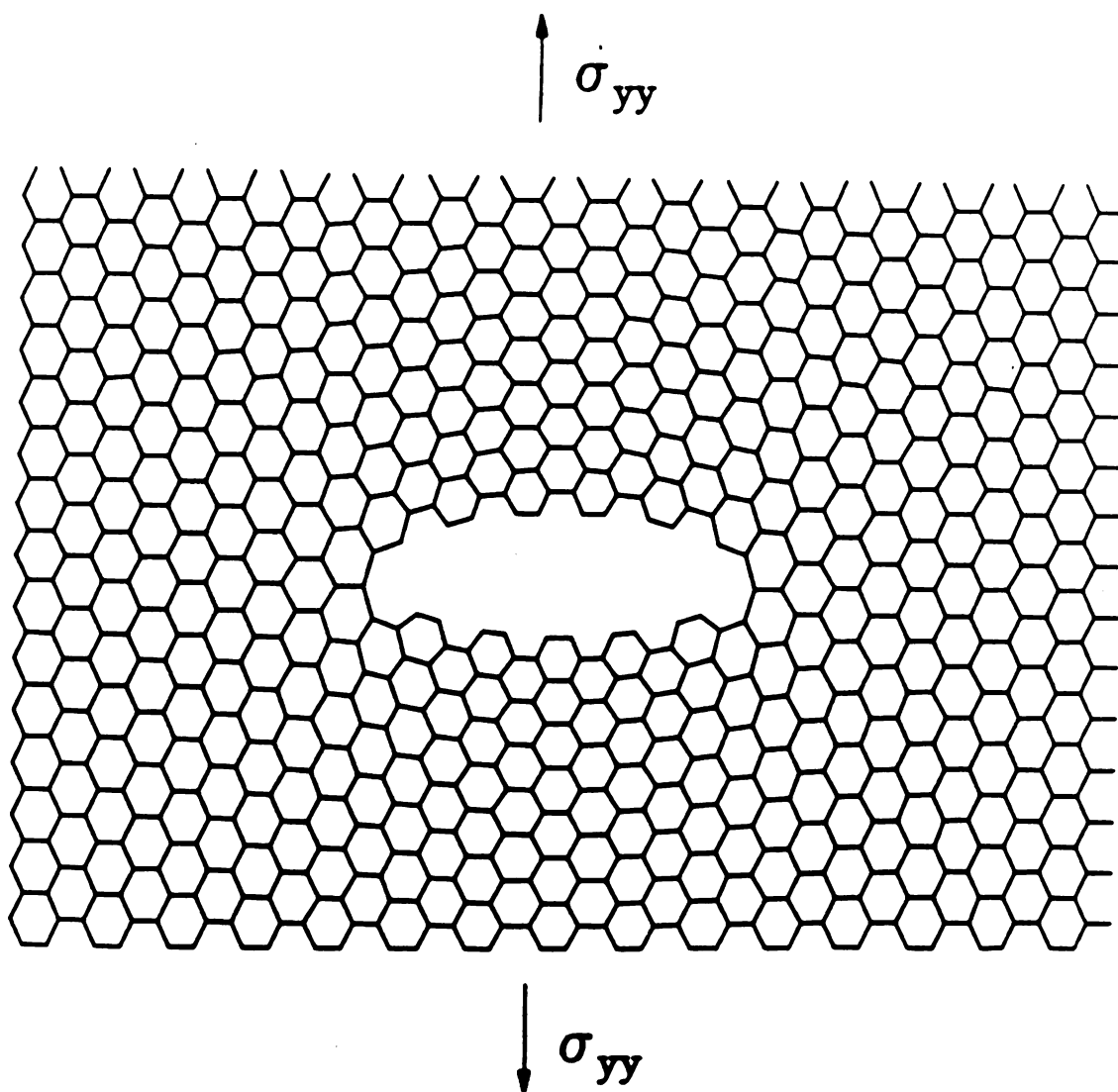




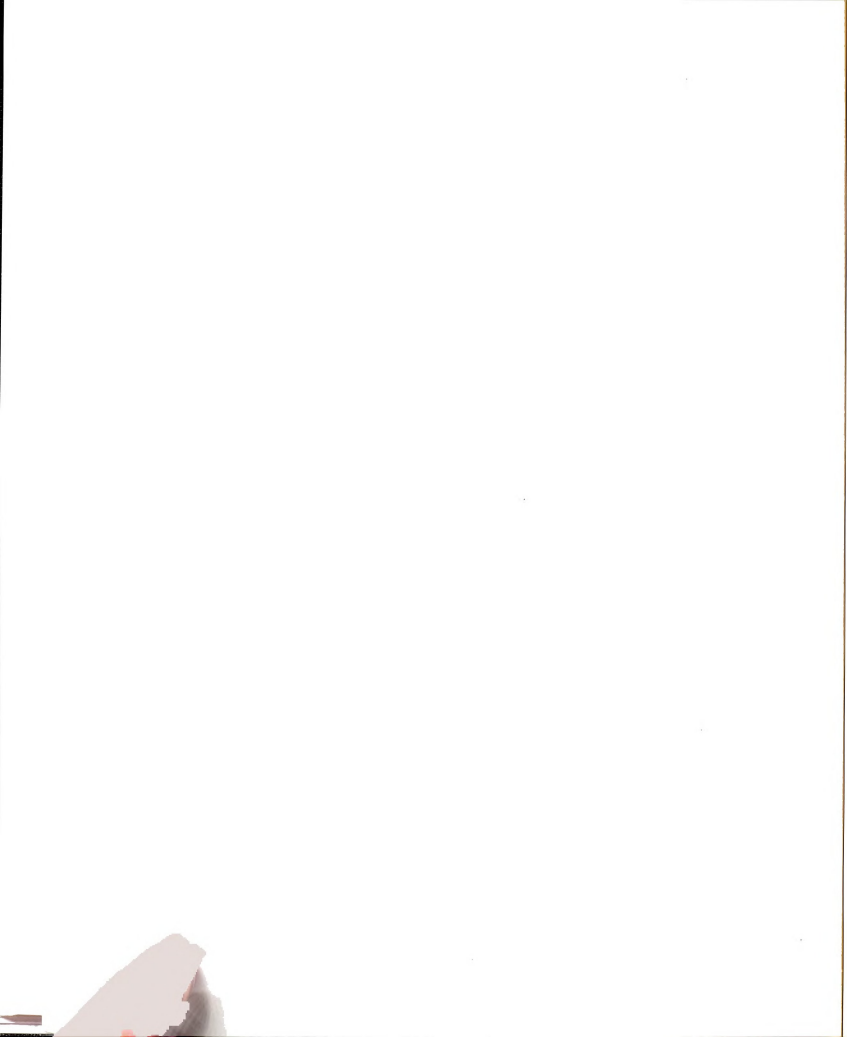


**Figure 3.11: The final path of tensile fracture of a hexagonal lattice. The dotted lines indicate the broken bonds.**





**Figure 3.12: The response of a graphite sheet containing a crack-like defect cluster, at applied strain of 20%**



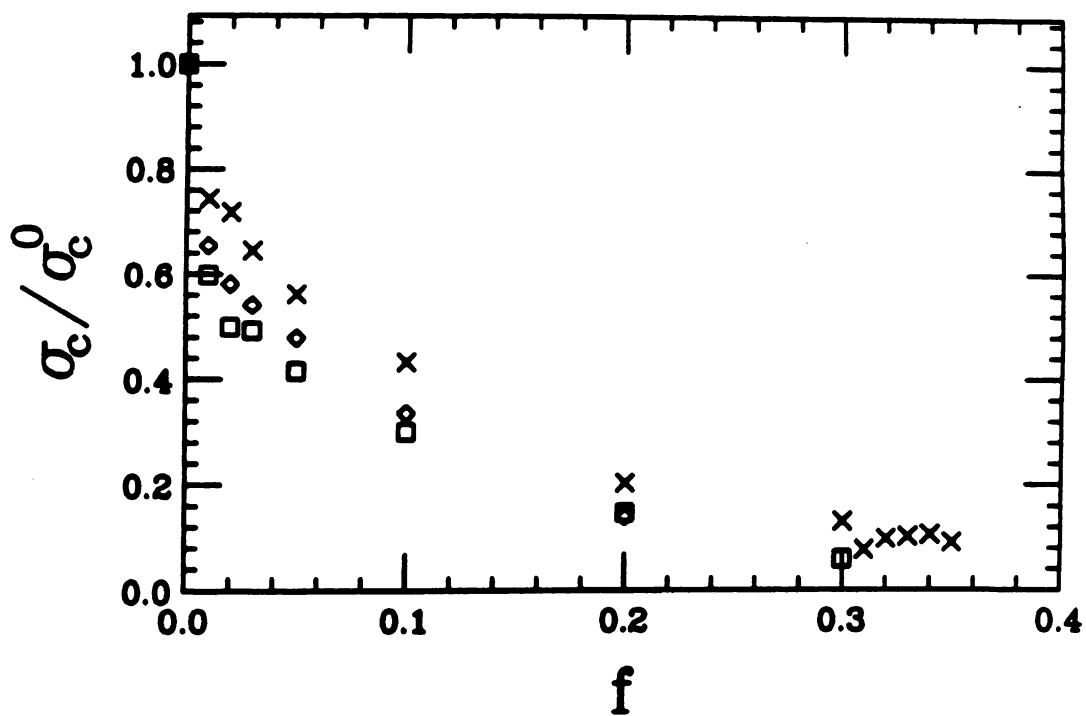


Figure 3.13: The average fracture stress as a function of void volume fraction,  $f$ , for networks containing 100( $\times$ ), 400( $\diamond$ ) and 900( $\square$ ) nodes. Each point is an average over 20 configurations at fixed  $f$ .

It is seen from Fig. 3.13, that there is a rapid drop in tensile strength at small  $f$  for all values of  $N$ . A scaling analysis that we have previously applied to other failure problems in both electrical and mechanical systems may be used for this problem [Duxb87a, Duxb91, Beal88]. We find that as  $N \rightarrow \infty$ , with  $f$  finite but small,

$$\frac{\sigma_c(f, N)}{\sigma_c^0} \sim \frac{1}{1 + k(-\ln N / \ln f)^\alpha} \quad (3.16)$$

where  $k$  is a constant, typically in the range 0.1 – 0.6, while  $\alpha$  is an exponent that lies in the range  $1/2(d - 1) < \alpha < 1$ . The analytic analysis [Duxb87a, Duxb91, Beal88] shows that  $\sigma_c$  is logarithmically singular as  $f \rightarrow 0$ , although the system size must be large for the analysis to apply. Another very important feature of both the numerical and analytic analysis is that  $\sigma_c$  decreases logarithmically with  $N$ . In fact as  $N \rightarrow \infty$ ,  $\sigma_c = 0$ . However, because the decrease is only logarithmic, even with  $N = \text{Avogadro's number}$ , the reduction in  $\sigma_c$  from its pure lattice value, is only about a factor of 100. Nevertheless this factor of about 100 is vitally important in the consideration of materials for structural applications. It is also important to note that from a theoretical viewpoint, the thermodynamic limit ( $N = \infty$ ) is meaningless in brittle failure problems as there  $\sigma_c = 0$ . In the theoretical analysis  $N$  must always be finite, and often the interesting analysis is the behavior at large  $N$ . Note that in the limit  $f \rightarrow 0$ , (and large  $N$ ),  $C_{11}$  is linear in  $f$  (and obviously non-singular).

Fracture behavior as a function of flaw volume fraction is thus markedly different than that of elastic moduli, and this difference has been related to the different scaling behavior of the moments of the bond stress distribution[LiYS89].

It is difficult to test the theoretically predicted logarithmic size dependence

in these graphite sheets as we are only able to simulate samples over two orders of magnitude in  $N$ . Work on simpler models however allows a more detailed theoretical and numerical analysis [Duxb87a, Duxb91, Beal88, Phoe92], which confirms the logarithmic size effect, and suggests that it should be present in models like that treated in our study. The analytic analysis also shows that the variability in the mean of  $\sigma_c$  should be anomalous. In contrast, the elastic moduli, for example the Young's modulus, for two configurations at the same  $f$  of a sheet with  $N$  nodes have values which are nearly the same:  $E^1(N) \sim E^2(N) + O(1/\sqrt{N})$ . However the same two configurations can have  $\sigma_c$  values which show much more scatter, and typically,  $\sigma_c^1(N) \sim \sigma_c^2(N) + O(1/\ln N)$ . Thus although  $\sigma_c$  self-averages to a unique value as  $N \rightarrow \infty$  it does so only logarithmically. In contrast, the elastic modulus (away from  $p_c$ ) self-averages like a Gaussian random variable.

### 3.5 Conclusions

A comparison of the elasticity and fracture of random networks illustrates the different scaling behavior of these properties in the presence of disorder. Eqs. (3.3) and (3.10) along with Fig. 3.6, show that the elastic constants are non-singular except near special points such as the rigidity or connectivity percolation points. In contrast, the brittle fracture stress exhibits the following features.

1. There is a dilute limit singularity in tensile strength (see Fig. 3.6, which is well represented by Eq. (3.11)). A dilute limit singularity is present in some published experimental works (see e.g. Fig. 2 of [Sier86]), though the specific form (3.11) has not been tested experimentally. It should be



emphasized that experiments on fracture strength trends must be performed on several samples, as sample to sample variations can mask the predicted trends in average strength. This is illustrated for example in the analogous problem of dielectric breakdown in metal loaded dielectrics where the trend analogous to Eq. (3.11) was observed, but about 10 samples at each value of  $f$  were required to reliably see the trend[Copp89, Duxb90b]. A logarithmic size effect also occurs in the dilute limit [see Eq. (3.10)].

2. The statistics of fracture in the dilute limit obey a modified Gumbel form rather than the usual Weibull distribution. Although many hundreds of samples are required to differentiate between Weibull and modified Gumbel statistics [Duxb87a, Beal88, Hass89], extrapolations to a reliabilities of order  $10^{-6}$  leads to design predictions that can differ by order of 30%.

## Chapter 4

# Melting of carbon fullerenes

### 4.1 Introduction

Recent success in synthesizing  $C_{60}$  “buckyball” clusters in macroscopic quantities by Krätschmer *et al.* [Krat90] triggered enormous interest of physicists, chemists and materials scientists alike in search of new man-made materials with unusual properties. The uncommon “hollow soccer ball” (or “fullerene”) structure was originally postulated for carbon cluster by Kroto *et al.* [Krot85]. For carbon alone, a whole spectrum of structures has been proposed (An extensive survey of carbon cluster literature up to 1989 has been given by Welter and Van[Welt89]), ranging from giant hollow fullerenes (A good review of fullerenes has been presented in Ref. [Curl91]) to elongated “bucky tube” or “nanotube” [Iiji91] and three-dimensional graphitic membranes with “plumber’s nightmare” structures [Leno92, Vand92]. Some of these structures are illustrated in Fig. 4.1. The icosahedral  $C_{60}$ , called “buckminsterfullerenes” or “buckyball”, is the most spherical molecule in nature. Each of the 60 carbon atoms that are located at the vertices of the truncated icosahedron are equidistant from the center-of-mass of the “buckyball”. The  $C_{120}$  isomer in Fig. 4.1 can also be considered to be a short carbon nanotube: extension



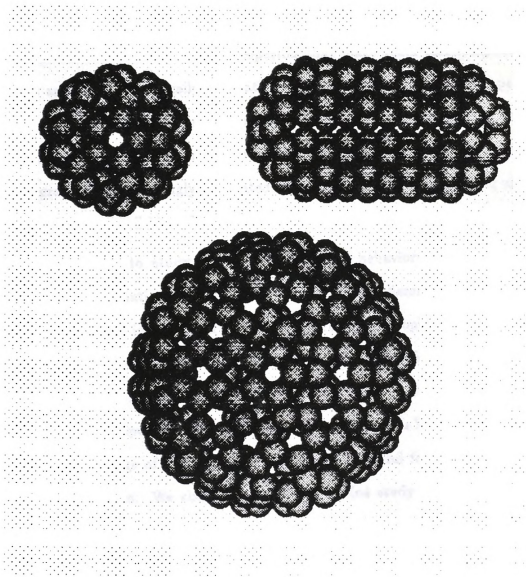
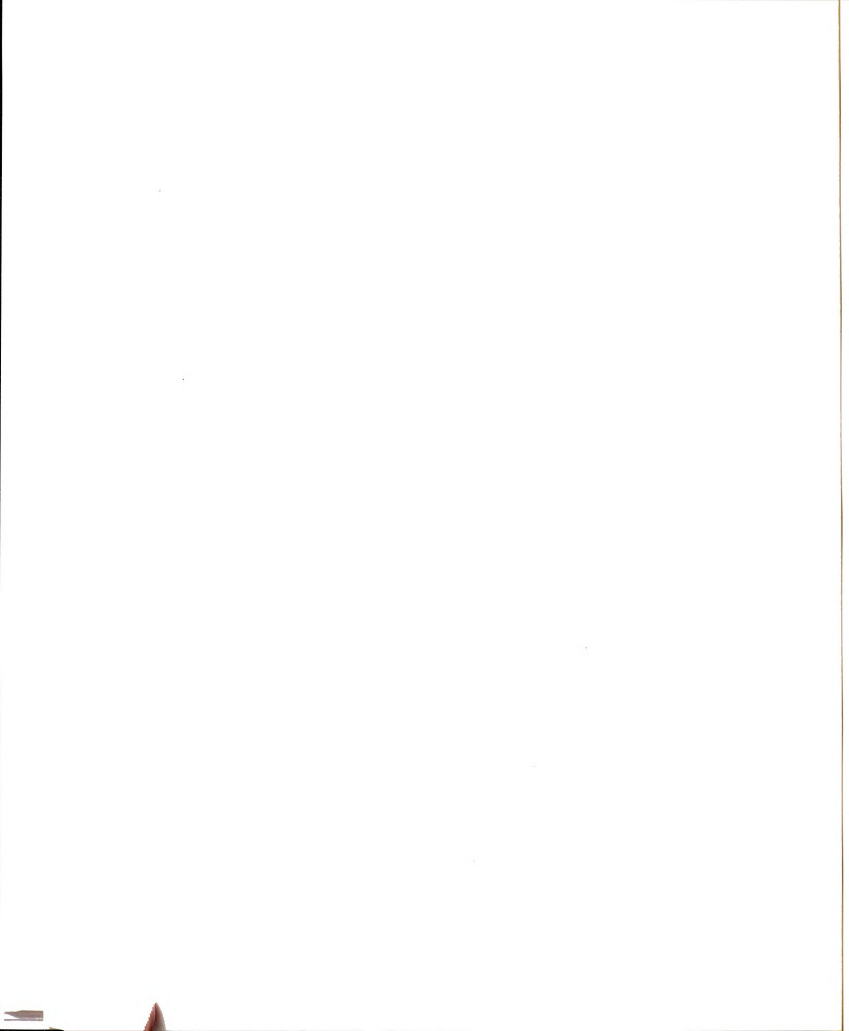


Figure 4.1: Carbon fullerenes. C<sub>60</sub> "buckyball", C<sub>120</sub> and C<sub>240</sub> isomers.

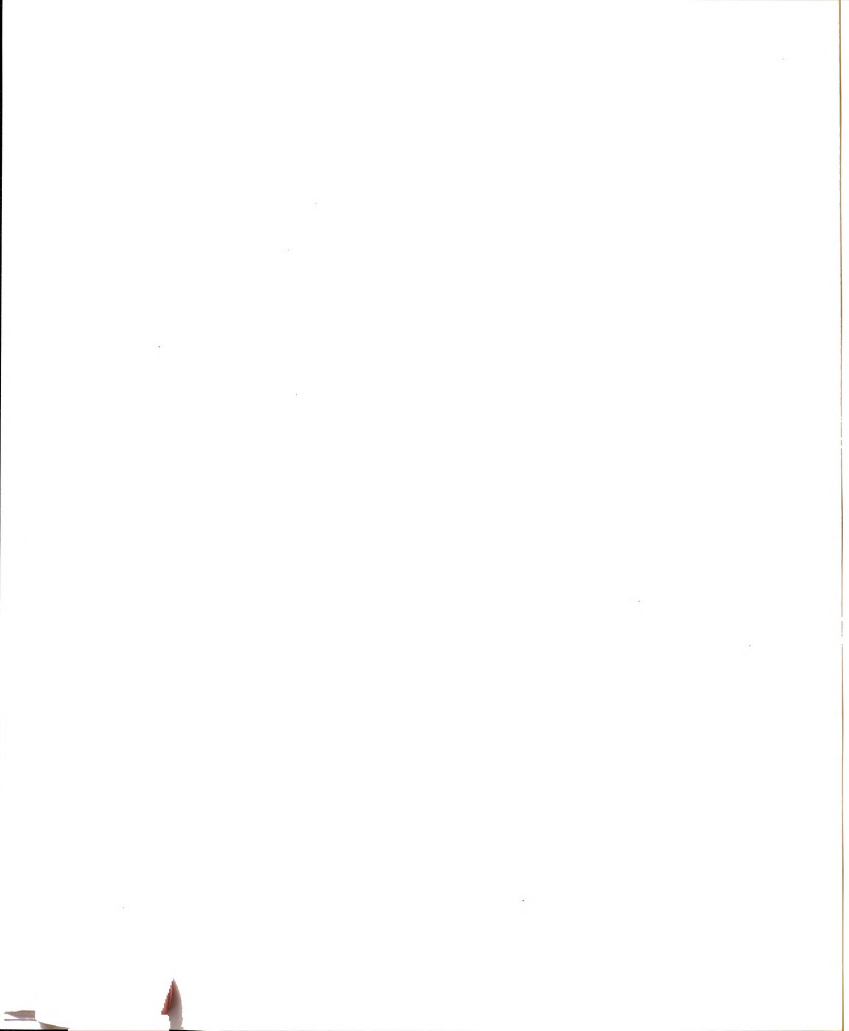


along the long axis of symmetry would yield a carbon nanotube similar to those actually produced and studied by transmission electron microscopy (TEM) [Iiji91].

Due to the high structural stability[Curl88] and strong bonds with light mass, carbon fullerenes have many unique properties that make them technologically important as well as scientifically fascinating. Despite extensive studies over past few years, almost no information is available about their equilibrium phases at temperatures close to and exceeding the melting point of graphite. We expect the phase diagram of these strongly correlated structures to be very interesting and to consist of several well identifiable "molten" phases.

A second reason to study the high-temperature behavior of fullerenes is related to their formation. While bulk quantities of fullerenes can now be routinely synthesized in a carbon arc [Krat90], the microscopic mechanism of their aggregation from gas phase is still the subject of a significant controversy [Waka92, Waka93, Ebbe92, Kern92, Held93, Hunt94]. Since the fullerenes are produced in the high temperature processes, such as arc burning or laser vaporization of graphite, knowledge of the thermal stability will be useful for controlling the synthesis of fullerenes. We also believe that a detailed study of the annealing process may shed new light on this subject, since intermediate structures, which occur during thermal quenching in the rare gas atmosphere, may also be observed while heating up these structures to high temperatures.

A third motivating reason for this study are recent collision experiments which indicate that fullerene molecules are extremely resilient and only fragment at energies exceeding  $\approx 200$  eV [Camp93]. Since in the collision process the kinetic energy is transferred into internal degrees of freedom as "heat", additional infor-

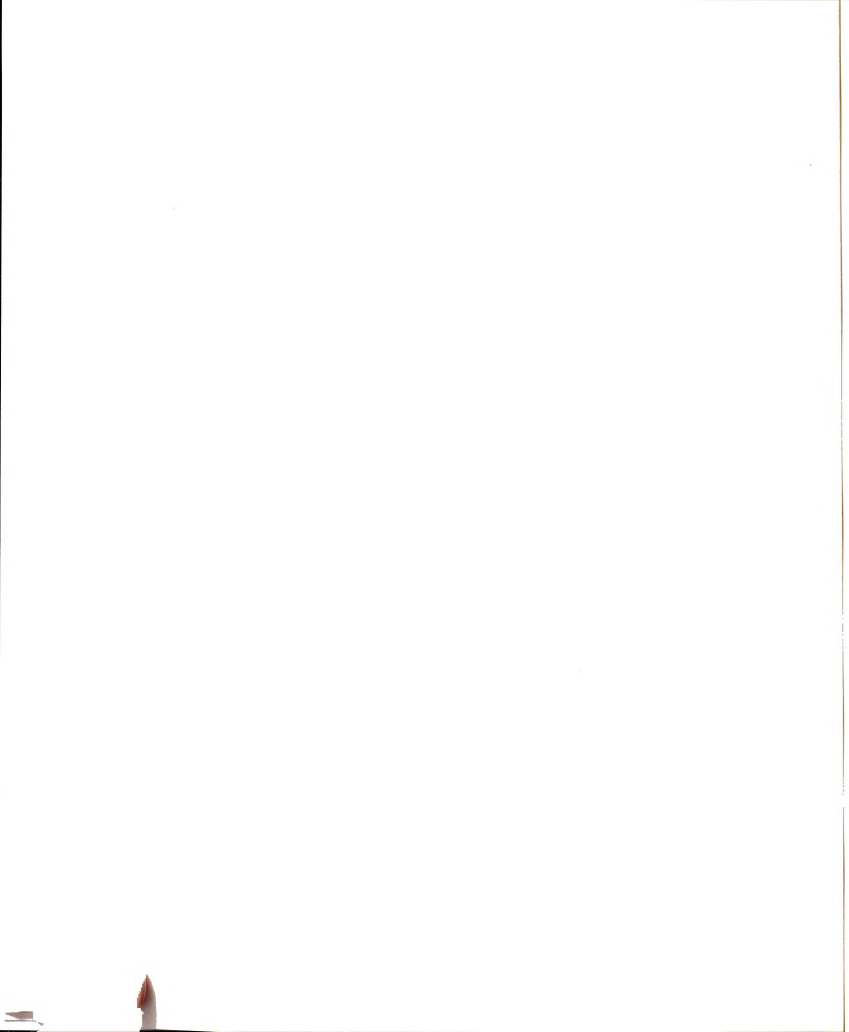


mation about the intermediate structures of colliding fullerenes could be obtained by investigating those of the superheated molecules.

In an attempt to elucidate the above three problem areas, we performed a detailed molecular dynamics (MD) study of the melting and evaporation process of three prototype fullerenes, namely  $C_{20}$ ,  $C_{60}$ , and  $C_{240}$ . In our simulation, we investigated the response of a canonical ensemble of fullerenes to gradually increasing heat bath temperatures using Nosé-Hoover molecular dynamics [Nose84, Hoov85, Alle90], complementing recent microcanonical ensemble simulations on  $C_{60}$  and  $C_{70}$  [KimE93]. Of course, the quality of simulation results depends primarily on the adequacy of the total energy formalism applied to the fullerenes. Since our simulation also addresses the fragmentation under extreme conditions, the formalism used must accurately describe the relative stability of fullerenes with a graphitic structure and their fragments, mostly short carbon chains. The corresponding transition from  $sp^2$  to  $sp$  bonding can only be reliably described by a Hamiltonian which explicitly addresses the hybridization between  $C2s$  and  $C2p$  orbitals. A precise evaluation of interatomic forces is required to obtain the correct long-time behavior of the system. On the other hand, the long simulation runs necessary to equilibrate the small systems during the annealing process, and the large ensemble averages needed for a good statistics, virtually exclude *ab initio* techniques as viable candidates for the calculation of atomic forces.

For this reason, we base our force calculation on a Linear Combination of Atomic Orbitals (LCAO) formalism which conveniently parametrizes *ab initio* Local Density Approximation (LDA) [Hohe64, Kohn65] results for structures as different as  $C_2$ , carbon chains, graphite, and diamond [Toma91]. We use an adap-





tation of this formalism to very large systems, which is based on the fact that forces depend most strongly on the local atomic environment and which has been implemented using the recursion technique [Zhon93]. The force calculation can be performed analytically to a large degree. This not only speeds up the computations significantly, but also provides an excellent energy conservation  $\Delta E/E \lesssim 10^{-10}$  between time steps in microcanonical ensembles, and a linear scaling of the computer time with the system size. Most importantly, forces on distant atoms can be efficiently calculated on separate processors of a massively parallel computer.

In Sec. [4.2] I will introduce the tight-binding method as the simplified LCAO method. I will summarize the LCAO formalism as well as the parameters used for carbon.

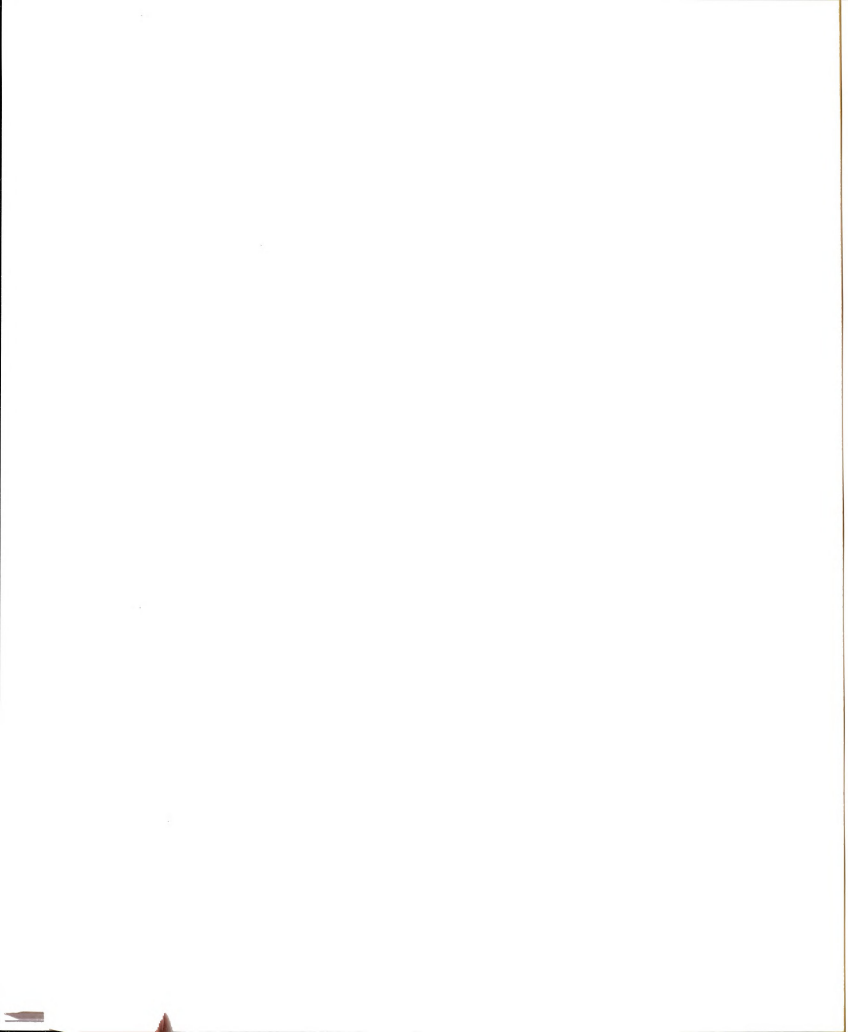
In Sec. [4.3] I will review the recursion method as used for carbon clusters and present the implementation to carbon tight-binding formalism. I will also demonstrate the accuracy of this technique.

Sec. [4.4] is devoted to the molecular dynamics formalism. Nosé-Hoover canonical dynamics method will be briefly summarized.

Sec. [4.5] contains my main simulation results. Using the tight-binding molecular dynamics with the recursion method, I simulate the melting of carbon fullerenes. I present snapshots of the intermediate phases and investigate the fundamental driving force for the “melting” by analyzing the entropy. I will identify a previously unknown “pretzel” phase of  $C_{60}$ .

In Sec. [4.6] I draw conclusions of the simulations and summarize.

This chapter contains material of the following two separately published manuscripts:

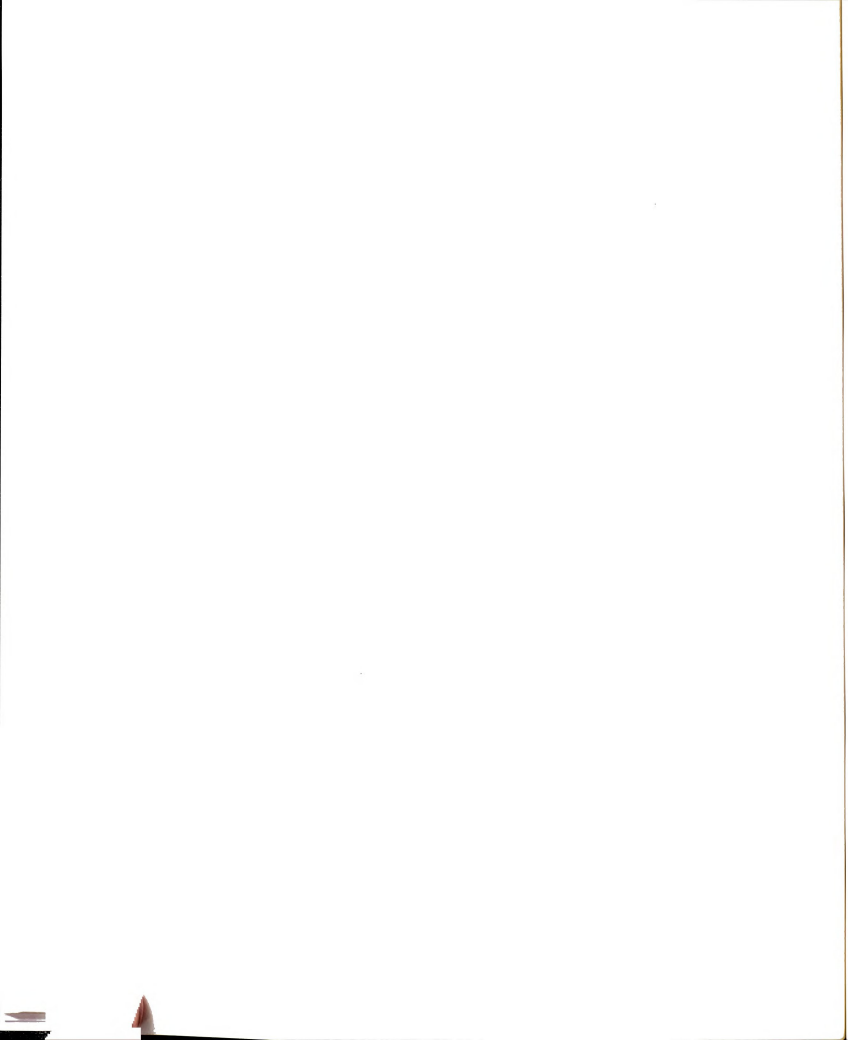


- [KimS94a] Seong Gon Kim and David Tománek, *Melting the fullerenes: A molecular dynamics study*, Phys. Rev. Lett. **72**, 2418 (1994).
- [KimS94b] S.G. Kim, W. Zhong and D. Tománek, *Synthesizing Carbon Fullerenes*, preprint (1994).

## 4.2 The tight-binding potential for carbon

The total energy functional for carbon which we used for the fullerene melting process was proposed by Tománek and Schluter [Toma91] and its implementation using the recursion approach was fully discussed in Refs. [Zhon93] and [KimS94b]. It is briefly summarized in this and the following sections.

Recently, *ab initio* molecular dynamics simulations of liquid and amorphous carbon with 54 atoms have been carried out using the Car-Parrinello method [Gall89a, Gall89b]. Nevertheless, first-principles studies are at present still limited by their heavy demand on computational effort, especially to do the detailed molecular dynamics simulation in the thermal disintegration process of fullerenes. The strong covalent nature and environment dependence of interactions between carbon atoms make the classical potential approach very difficult. With two-body and three-body interactions included, the Tersoff potential or similar approximate schemes [Ters88, Ball90, Chel91] have been tuned to reproduce graphite and diamond structures and dynamical properties very accurately. But such potentials will have difficulties dealing with fullerene melting or collision process which involves both high coordination number environments (graphite or diamond like) as well as less coordinated structures like linear chains and the C<sub>2</sub> molecule. The tight-binding approach, which includes electronic structure explicitly in the Hamil-



tonian, has proven to be more successful in this respect[Toma91, XuCH92].

In LCAO methods[Root51, Root60, Mull49a, Mull49b], introduced to crystal calculations by Bloch[Bloc29], the one-electron wave functions are expanded in a basis of atomic orbitals  $\{|\phi_\alpha\rangle\}$

$$|\psi_i\rangle = \sum_{\alpha} c_{i\alpha} |\phi_\alpha\rangle \quad (4.1)$$

with

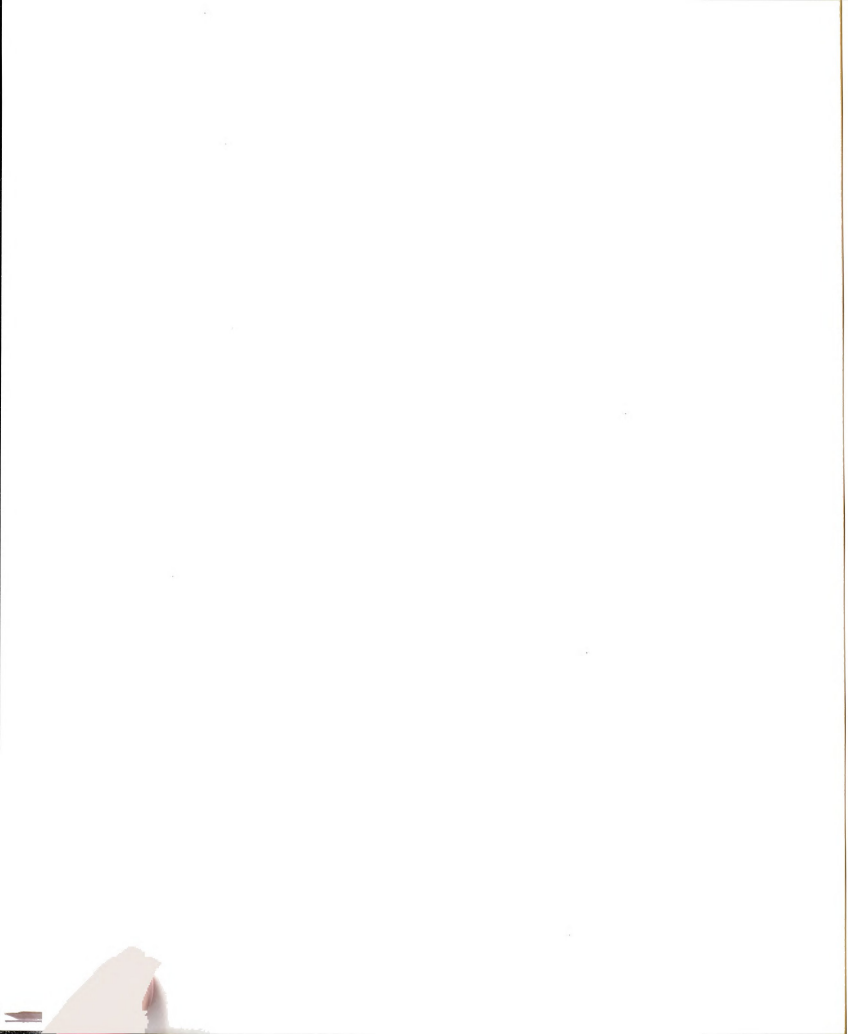
$$H |\phi_\alpha\rangle = \epsilon_\alpha |\phi_\alpha\rangle. \quad (4.2)$$

The one-electron Hamiltonian for the electron systems can then be written as

$$H = \sum_{i\alpha} \epsilon_\alpha c_{i\alpha}^\dagger c_{i\alpha} + \sum_{i\alpha j\beta} t_{i\alpha j\beta} c_{i\alpha}^\dagger c_{j\beta}. \quad (4.3)$$

Here  $c_{i\alpha}^\dagger$  is the operator to create an electron orbital  $|\phi_\alpha\rangle$  at site  $i$  and  $t_{i\alpha j\beta}$  is the hopping integral describing the hopping of an electron from orbital  $|\phi_\alpha\rangle$  at site  $i$  to orbital  $|\phi_\beta\rangle$  at site  $j$ .

Slater and Koster have shown that the hopping integrals between two given orbitals can be simply represented as a combination of hopping integrals with  $\sigma$ ,  $\pi$ , and  $\delta$  symmetry, hence reducing the number of independent quantities [Slat54]. Moreover, it has proven useful to restrict intersite hopping to the nearest neighbors only, in the tight-binding approximation. The tight-binding method is much simpler than *ab initio* calculations, yet preserves the basic physics by allowing mixing and intersite hopping of  $s$  and  $p$  electrons. Instead of computing the various hopping integrals by first determining the true crystal potential using an *ab initio* technique, we treat them as disposable constants chosen to fit accurate *ab initio*



calculations for selected structures at restricted symmetry points of the Brillouin zone. In the following, we will use the tight-binding technique with Slater-Koster parameters as an “intelligent interpolation” technique between results obtained using *ab initio* techniques such as LDA. We adopt the hopping integrals from Ref. [Toma91].

We have found it useful to separate the cohesive energy of the system (with respect to isolated atoms) into two parts [Foul89], as

$$-E_{\text{coh}} = E_{\text{bs}} + E_{\text{rep}}. \quad (4.4)$$

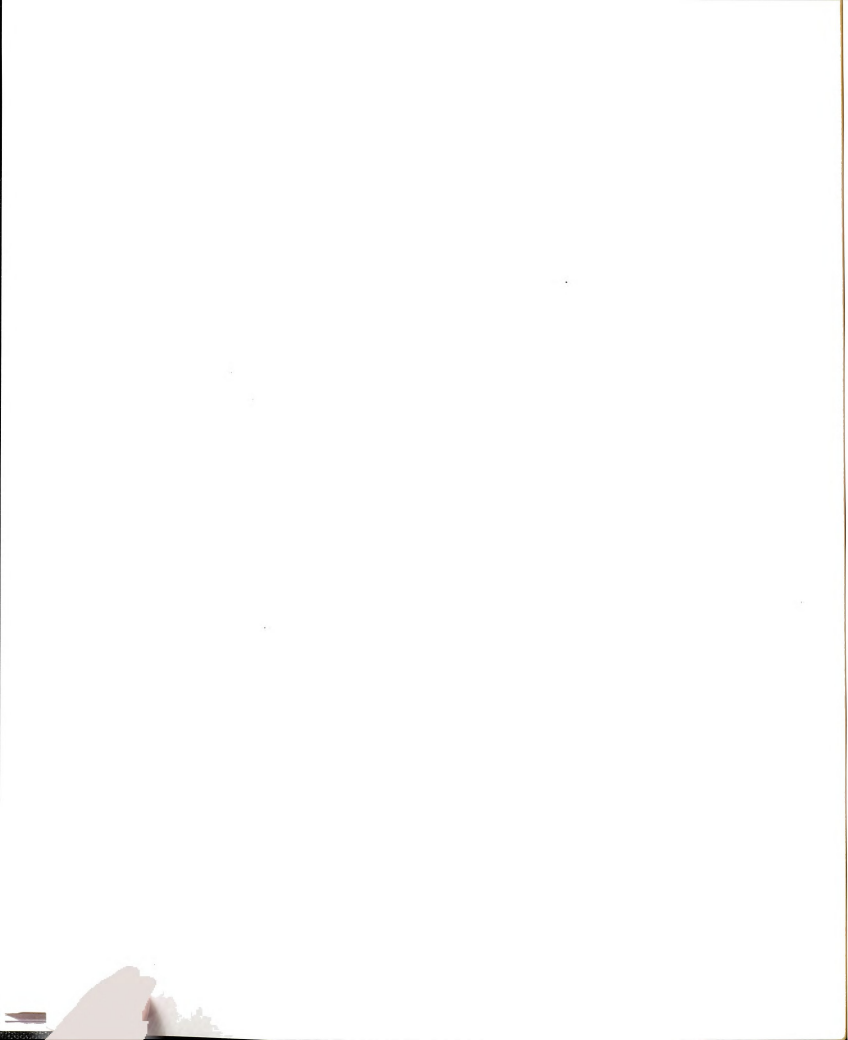
The first energy contribution,  $E_{\text{bs}}$ , is the electronic band-structure energy, which is nonlocal by nature and reflects the hybridization in the system. The second term,  $E_{\text{rep}}$ , contains the internuclear repulsion and all other corrections to  $E_{\text{bs}}$  such as the closed-shell repulsion, exchange-correlation and energy double-counting corrections. As shown previously [Toma91], the one-electron spectra of different carbon structures can be obtained to a sufficient accuracy by mapping *ab initio* LDA band structures for the corresponding systems onto a tight-binding Hamiltonian. In this procedure, the essential information about the electronic structure and many-body effects in the system is kept intact.

The one-electron band-structure energy is given by

$$E_{\text{bs}} = \sum_i \left[ \int_{-\infty}^{E_F} E N_i(E) dE - \sum_{\alpha} n_{i,\alpha} \epsilon_{\alpha} \right]. \quad (4.5)$$

Here, the summation extends over all atomic sites  $i$ ,  $N_i(E)$  is the local electronic density of states, and  $E_F$  is the Fermi energy which is a global quantity. The reference energy of an isolated atom is expressed in terms of the energy levels  $\epsilon_{\alpha}$





and the corresponding occupation numbers  $n_{i,\alpha}$  which satisfy the condition

$$\sum_{\alpha} n_{i,\alpha} = \int_{-\infty}^{E_F} N_i(E) dE . \quad (4.6)$$

With this definition,  $E_{bs}$  is zero for both empty and full bands.

For carbon systems, we base our electronic structure calculation on a Slater-Koster parametrized [Slat54] four-state ( $s$ ,  $p_x$ ,  $p_y$ ,  $p_z$ ) tight-binding Hamiltonian [Toma91]. The diagonal elements of the Hamiltonian are  $s$ - and  $p$ -level energies  $E_s$  and  $E_p$ . The off-diagonal matrix elements are the hopping integrals with an exponential distance dependence

$$V_{\beta}(r_{ij}) = V_{\beta}^0 S_{\beta}(r_{ij}) \quad (4.7)$$

where  $\beta$  labels the hopping parameter.  $S(r)$  is a scaling function of interatomic distance  $r$

$$S_{\beta}(r) = \exp \left\{ n_{\beta} \left[ 1 - \left( \frac{r}{r_0} \right) \right] \right\} \exp \left\{ n_{\beta} \left[ \left( \frac{r_0}{r_c} \right)^{n_c} - \left( \frac{r}{r_c} \right)^{n_c} \right] \right\} \quad (4.8)$$

where  $r_0$  is the equilibrium nearest-neighbor distance in bulk diamond [Kitt86]. Unlike the previous scaling functions [Good89, XuCH92],  $n_{\beta}$  is not necessarily same for different hopping parameters and we replaced the power-law dependence of leading factor by the exponential to remove the divergence at small distances. In our Hamiltonian, we consider those atoms as first nearest neighbors which are closer than the cutoff distance  $d_c$  and we include interactions up to second nearest neighbors. The parameters involved in the band structure energy are listed in Table 4.1.

The second term in Eq. (4.4),  $E_{rep}$ , contains the internuclear repulsion and all other corrections to  $E_{bs}$  such as the closed-shell repulsion, exchange-correlation

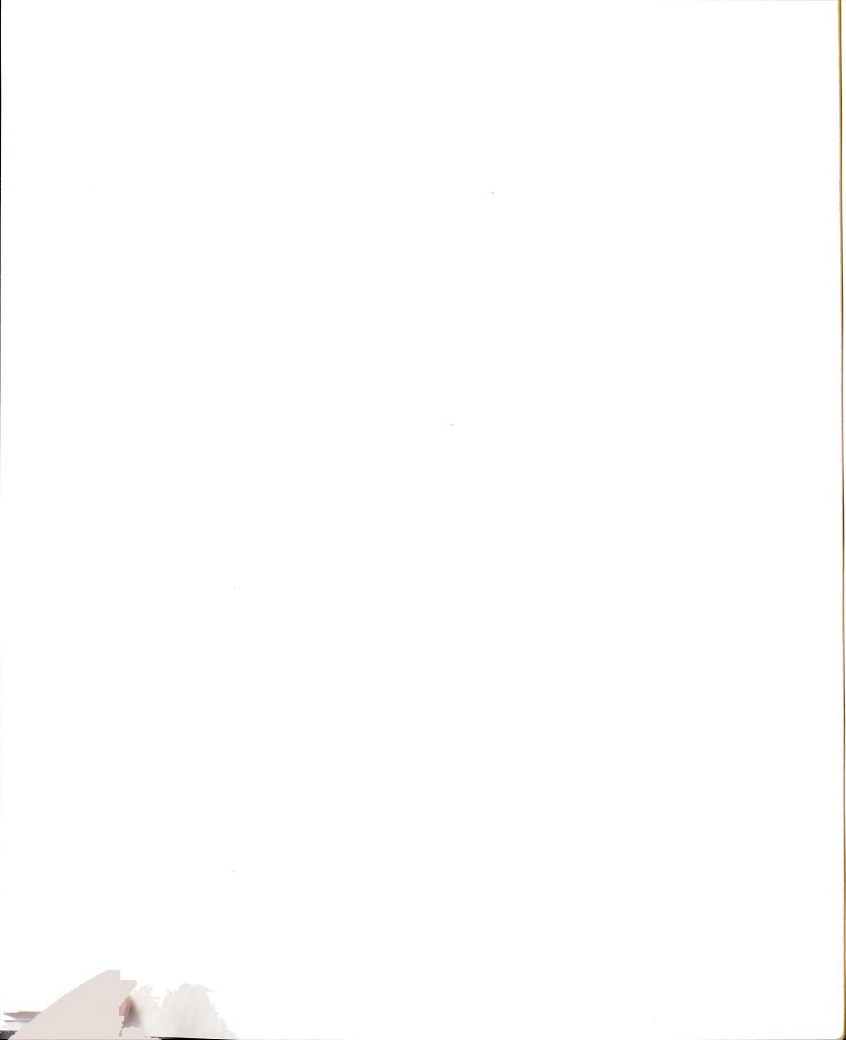
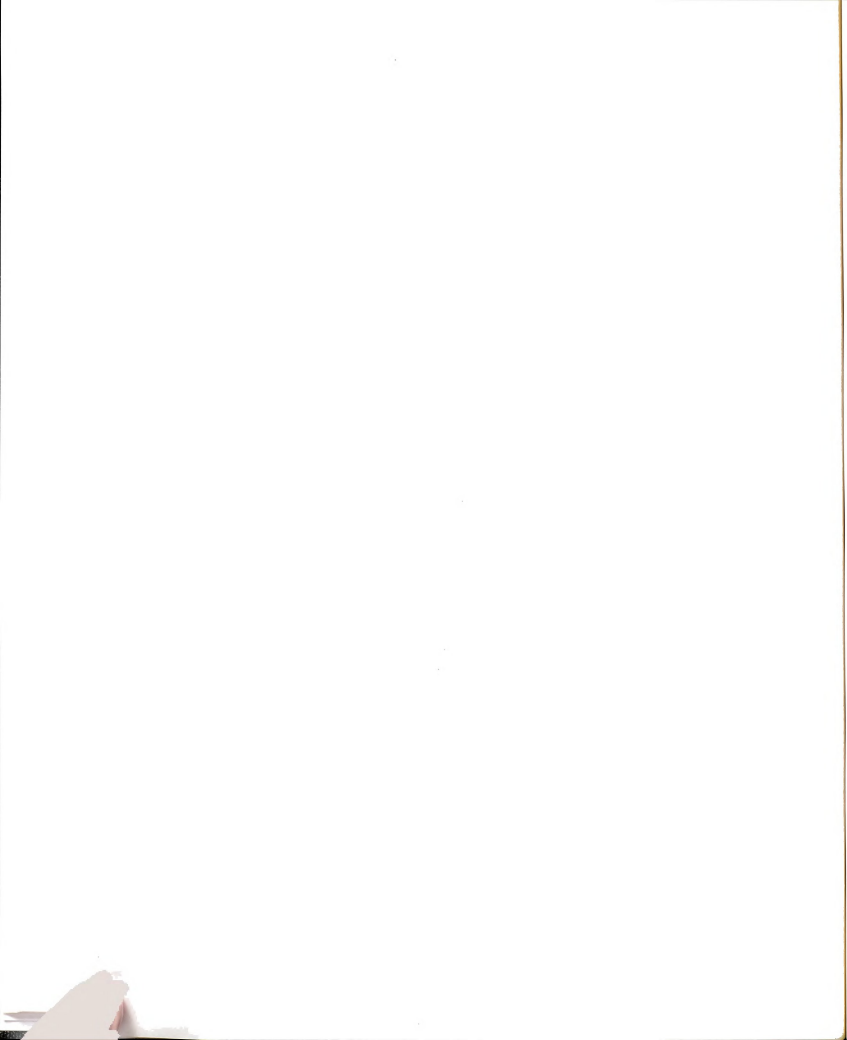


Table 4.1: Parameters for the band structure energy

$E_s$	$E_p$		
-3.65 eV	3.65 eV		
$V_{ss\sigma}^0$	$V_{sp\sigma}^0$	$V_{pp\sigma}^0$	$V_{pp\pi}^0$
-3.63 eV	4.20 eV	5.38 eV	-2.24 eV
$n_{ss\sigma}$	$n_{sp\sigma}$	$n_{pp\sigma}$	$n_{pp\pi}$
2	2	2	3
$r_0$	$r_c$	$n_c$	
1.546 Å	2.16 Å	10	



and energy double-counting corrections. We approximate  $E_{\text{rep}}$  by a sum of "quasi-pairwise" functions  $E_r$ ,

$$E_{\text{rep}} = \sum'_{i,j} E_r(r_{ij}, z_i). \quad (4.9)$$

I used the word "quasi" because it is not really pairwise. There is a small contribution from coordination number [see Eq. (4.10)] which introduces a deviation from a pairwise form. But in most cases, this deviation is negligible. In the summation, each pair of nearest neighbor sites  $i$  and  $j$  is counted twice. The function  $E_r$  can be written as the sum of major contributions from the interatomic separation and a small coordination number dependent contribution

$$E_r(r_{ij}, z_i) = [E_1(r_{ij}) + E_2(z_i)]\phi(r_{ij}). \quad (4.10)$$

Here  $\phi(r)$  is another distance scaling function with the form:

$$\phi(r) = \exp \left[ -m \left( \frac{r}{r_c} \right)^{m_c} - \left( \frac{r_0}{r_c} \right)^{m_c} \right] \quad (4.11)$$

and  $z_i$  in Eq. (4.10) is the effective coordination number of atom  $i$  defined by

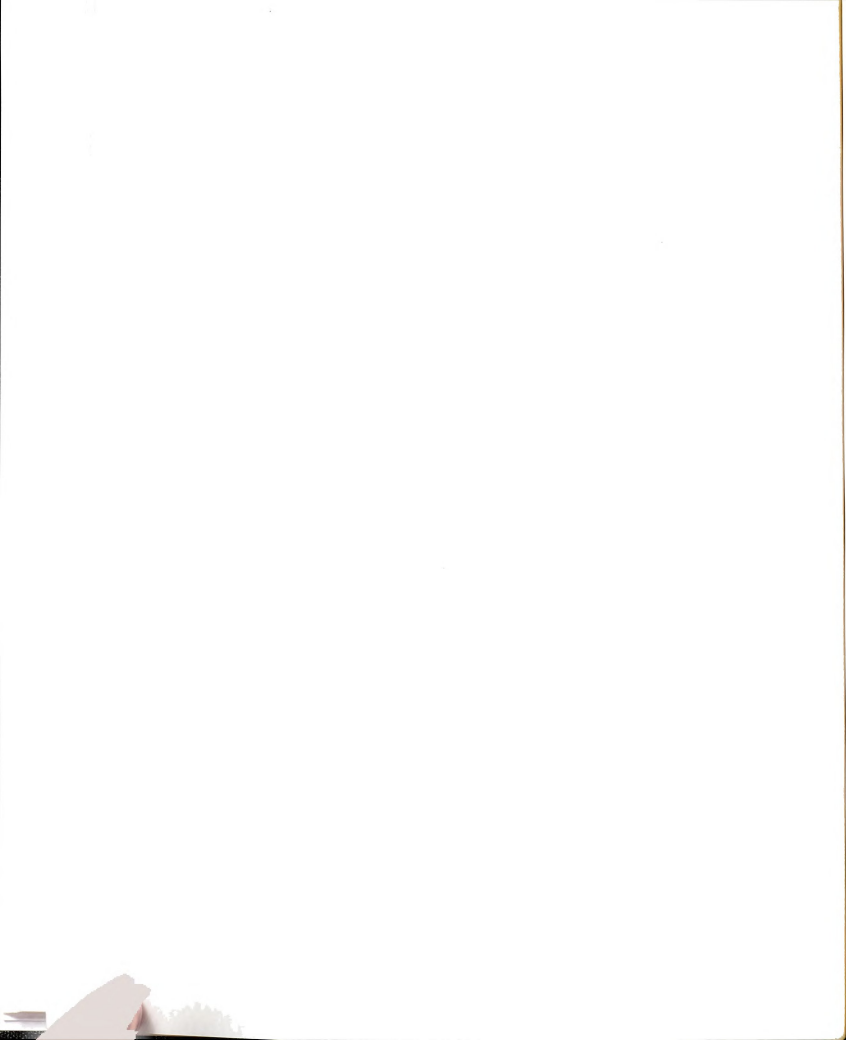
$$z_i = \sum_j \frac{1}{1 + \exp[\tau(r_{ij}/r_r - 1)]}. \quad (4.12)$$

$E_1$  is given by an exponential function of  $r$  and  $E_2$  is a function of  $z$ ,

$$E_1(r) = V_1 \exp(-r/r_1) + V_2 \exp(-r/r_2) + V_3 \exp(-r/r_3) \quad (4.13)$$

$$E_2(z) = E_2^0(1 - \gamma z^{-3}). \quad (4.14)$$

The parameters involved in the repulsive energy are listed in Table 4.2. This repulsive energy will ensure correct total energies for  $\text{C}_2$ , carbon chain, graphite,



and diamond structures with a large range of bond lengths, if the band structure energies are calculated exactly. It guarantees a smooth transition between different structures and thus is suitable for molecular dynamics simulations.



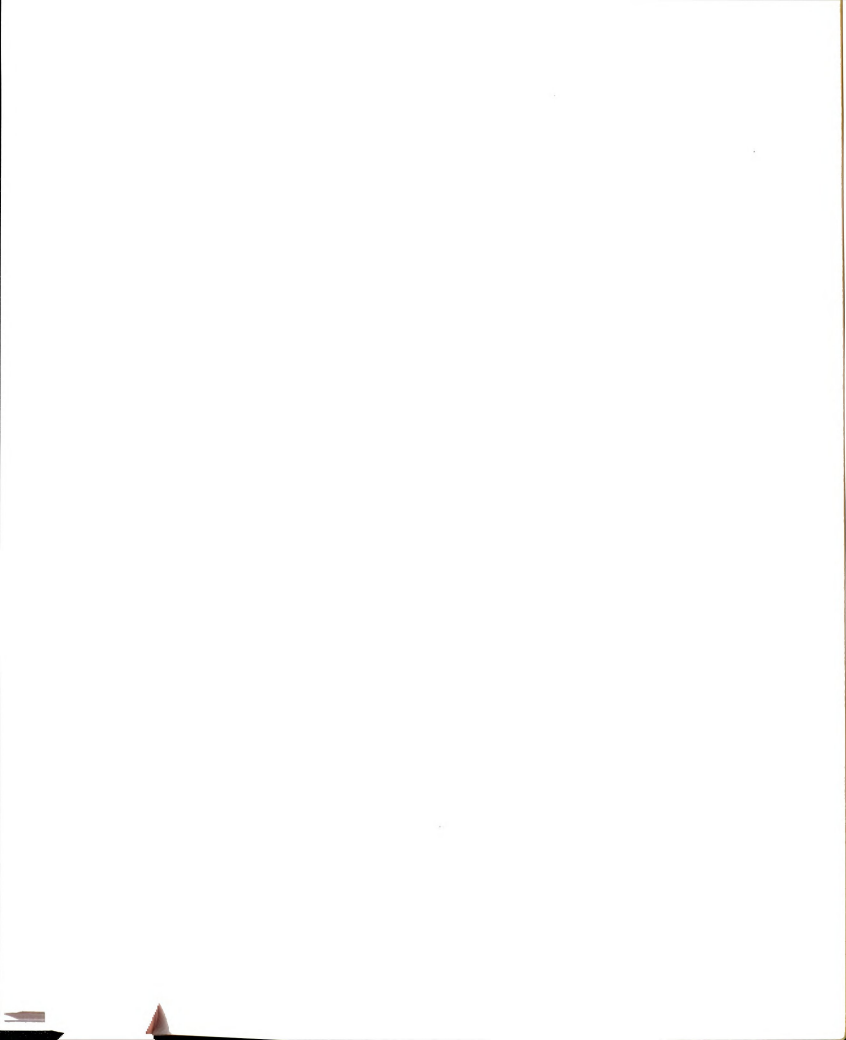


Table 4.2: Parameters for the repulsive energy

$m$	$m_c$	$\tau$	$\gamma$
2	11	50	0.474
$V_1$	$V_2$	$V_3$	$E_2^0$
10.34 eV	317.41 eV	$5.0 \times 10^9$ eV	-0.42 eV
$r_1$	$r_2$	$r_3$	$r_r$
0.9 Å	0.35 Å	0.05 Å	1.95 Å



### 4.3 The recursion method

The inclusion of electronic degrees of freedom allows for accurate and physically more insightful calculations at the expense of a heavier computational load. Typically the most expensive part of the calculation is the diagonalization of the total Hamiltonian matrix, which increases rapidly with increasing system size  $N$ . The typical scaling is  $N^3$  or  $N^2 \log N$ , which makes calculation of a large system very expensive. This computational requirement is not acceptable when studying the dynamics of very large structures or performing molecular dynamics simulations of the aggregation process. However, in a covalent system, a local disturbance will only affect neighboring atoms, and its effect will decrease exponentially with increasing distance. On the other hand, local properties are affected mainly by the neighboring atoms. Most linearly scaling methods to compute the electronic structure such as the recursion techniques[Hayd80] and the density matrix approach[LiXP93], are based on this fact. In this Section we present a new approach to calculating the electronic structure, which scales as  $N$  rather than as  $N^3$ .

The most difficult part of the total energy evaluation is an efficient scheme to determine the local density of states. While  $N_i(E)$  in Eq. (4.5) should contain the essential physics associated with the nonlocality of bonding, the exact function is not very important since the band structure energy, given by Eq. (4.5), is an integral quantity of  $N_i(E)$ .

As mentioned above, the idea underlying this approach is that the interactions between two sites do not depend significantly on the bonding topology far away. This approach has been used successfully in the calculation of the electronic struc-



ture of amorphous semiconductors [Joan74]. It has been proven [see, for example, Eqs. (1.11) to (1.17) of Ref. [Hein80]] that the local density of states at the site  $i = 0$  can be given by

$$N_0(E) = \lim_{\epsilon \rightarrow 0} \left( -\frac{1}{\pi} \right) \text{Im} G_{00}(E + i\epsilon). \quad (4.15)$$

The  $G_{00}$  element of the Green function matrix is given by the Dyson equation as

$$\begin{aligned} G_{00}(E) &= \left( \frac{1}{E - H} \right)_{00} \\ &= \left( \begin{array}{cccc} E - a_0 & -b_1 & 0 & \dots \\ -b_1 & E - a_1 & -b_2 & \dots \\ 0 & -b_2 & E - a_2 & \dots \\ \dots & \dots & \dots & \ddots \end{array} \right)^{-1}_{00} \\ &= \frac{1}{E - a_0 - \frac{b_1^2}{E - a_1 - \frac{b_2^2}{E - a_2 - \dots}}}. \end{aligned} \quad (4.16)$$

The continued fraction coefficients  $a_n$  and  $b_n^2$  are related to energy moments  $\mu_\alpha = \int_{-\infty}^{+\infty} dE E^\alpha N_0(E)$  of the local density of states at the site  $i = 0$ . These coefficients are obtained by tridiagonalizing the Hamilton matrix of the system,

$$H_{\text{TB}} = \left( \begin{array}{cccc} a_0 & b_1 & 0 & \dots \\ b_1 & a_1 & b_2 & \dots \\ 0 & b_2 & a_2 & \dots \\ \dots & \dots & \dots & \ddots \end{array} \right). \quad (4.17)$$

But if only the first few recursion coefficients are needed, it is more convenient to use their recursion relations[Hein80, Kell80, Luch87]. The method involves setting up a new orthonormal basis set  $|u_n\rangle$ ,  $n = 0, 1, 2, \dots$ , the first of which  $|u_0\rangle$ , we choose as the particular atomic orbital  $|\phi_\alpha\rangle$  or linear combination of orbitals

for which we want the local density of states or the atomic orbital of the atom being considered. With given  $|u_0\rangle$  and

$$\begin{aligned} |u_{-1}\rangle &= 0 \\ b_0^2 = \langle u_0 | u_0 \rangle &= 1 \end{aligned} \quad (4.18)$$

we generate for  $i = 0, 1, 2, \dots$ ;

$$\begin{aligned} a_i &= \langle u_i | H_{TB} | u_i \rangle, \\ |u_{i+1}\rangle &= (H_{TB} - a_i) |u_i\rangle - b_i^2 |u_{i-1}\rangle, \\ b_{i+1}^2 &= \langle u_{i+1} | u_{i+1} \rangle / \langle u_i | u_i \rangle. \end{aligned} \quad (4.19)$$

Charge transfer between inequivalent sites in the structure is reduced by an on-site Coulomb interaction which, in the mean-field approximation, can be mapped onto a crystal potential. Variations of the crystal potential impose, to a leading order, a rigid shift on the local densities of states. This shift of the core and valence levels does not affect the crystal cohesion, yet is reflected in different core level binding energies. In our calculation, we determine this shift by imposing a local charge neutrality condition Eq. (4.6).

The main advantage of using the recursion method is that in most cases, we only need the first few recursion coefficients to have a reasonable local density of states from Eqs. (4.15) and (4.16). Furthermore we can increase our accuracy by simply including more levels in the continued fraction.

Carbon is the one of the most computationally demanding elements in terms of the number of recursion coefficients needed, due to the complexity of its bonding. Directional bonding, i.e. the preference for definite bond angles for  $sp$ ,  $sp^2$  or  $sp^3$  type bonding, requires that at least the four lowest moments  $\mu_\alpha$  be included in

the continued fraction. Furthermore, it is essential to treat the  $s$ ,  $p_x$ ,  $p_y$  and  $p_z$  subbands in the density of states separately in order to represent correctly the bond stretching and bond bending forces.

The fifth moment of the density of states depends only on the first and second neighbors of any given site. The corresponding information, contained in the recursion coefficients  $a_n$ , and  $b_n^2$ ,  $n = 0, 1, 2$ , is determined by tridiagonalizing the corresponding small submatrix of the Hamilton matrix. Truncation of the continued fraction after  $b_2^2$  would lead to a set of  $\delta$ -functions for the density of states, corresponding to a small isolated cluster with many dangling bonds[Luch87]. A physically more reasonable approach to describe very large structures is to embed the small cluster in an averaged environment with similar bonding. This can be achieved by attaching a Bethe lattice to the cluster [Joan74] which, to a large degree, is equivalent to using

$$t(E) = \frac{b_\nu^2}{E - a_\nu - t(E)}, \quad (4.20)$$

giving the square root terminator  $t(E)$  [Beer82] in the continued fraction in Eq. (4.16). The terminating coefficients  $a_\nu$  and  $b_\nu^2$  are easily determined in the bulk limit from the lower and upper band edges. In our calculation, these values are taken from the linear chain, the graphite monolayer or bulk diamond, depending on the local coordination of the site  $i = 0$ .

The essential information for the calculation of deformation energies is contained in the recursion coefficients  $a_n$ ,  $b_n^2$  with  $n \leq \eta$ ,  $\eta \approx 2$ . Attaching a square root terminator to the continued fraction of Eq. (4.16) at this point would mean to ignore the specific bonding topology and the corresponding connected loops which modify the *higher* moments and continued fraction coefficients beyond  $\eta$ .





We have found it useful to consider continued fraction coefficients beyond  $\eta = 2$  in the expression for the density of states. Rather than calculating these coefficients explicitly by tridiagonalizing an accordingly much larger Hamilton submatrix, we use pre-tabulated coefficients  $a_n, b_n^2$  ( $3 \lesssim n \lesssim 8$ ) for the bulk structures as a “patch” which we splice onto the continued fraction. The set of coefficients is taken from the graphite structure. In order to avoid strong oscillations in the density of states due to this “patch” and the square root terminator, we mix in the “patch” coefficients with  $a_\eta, b_\eta^2$  and the terminating coefficients  $a_\nu, b_\nu^2$  so that no strong discontinuities occur in  $a_n$  and  $b_n^2$  at  $n = \eta$  and  $n = \nu$  [Luch87]. The continued fraction coefficients in the “patch”  $\eta < n < \nu$  are given by

$$\begin{aligned}\bar{a}_n &= \frac{1}{2} \left[ \left(1 - \sin \frac{\pi\alpha}{2}\right) a_\eta + \left(1 + \sin \frac{\pi\alpha}{2}\right) a_\nu \right] \\ \bar{b}_n^2 &= \frac{1}{2} \left[ \left(1 - \sin \frac{\pi\alpha}{2}\right) b_\eta^2 + \left(1 + \sin \frac{\pi\alpha}{2}\right) b_\nu^2 \right]\end{aligned}\quad (4.21)$$

with  $\alpha = (2n - \eta - \nu)/(\nu - \eta)$ . While the above procedure gives an improved description of the density of states, the higher “patched” coefficients do not affect the lower moments of the density of states and hence have a small effect on the band structure energy. It should be pointed out that our method of termination is tolerant of a possible inaccuracy in the terminating coefficients and does not induce unphysical oscillations in the local density of states. With this terminator, the local density of states can be written

$$N_0(E) = -\frac{1}{\pi} \text{Im} \frac{1}{E - a_0 - \frac{b_1^2}{E - a_1 - \frac{b_2^2}{E - a_2 - t(E)}}}. \quad (4.22)$$

The validity of our formalism has been demonstrated by W. Zhong and *et al.* [Zhon93], as shown in Fig. 4.2. The densities of states for three most common

carbon structures, obtained using the recursion method, are compared with the results of conventional tight-binding band-structure calculations which diagonalize the Hamiltonian matrix directly. Electronic local density of states  $N(E)$  (solid lines), integrated density of states  $\int_{-\infty}^{E_F} dE N(E)$  (dashed lines), and the band structure energy  $-E_{bs}(E_F)$  as a function of band filling (dotted lines) is plotted for different carbon structures. Results of a tight-binding band-structure calculation for an infinite carbon chain (bondlength  $d_{CC} = 1.286 \text{ \AA}$ ) (a), a graphite monolayer ( $d_{CC} = 1.418 \text{ \AA}$ ) (b) and bulk diamond ( $d_{CC} = 1.546 \text{ \AA}$ ) (c) are compared with the results obtained with our simplified recursion method in (d), (e) and (f), respectively. Even though the recursion method misses some of the details in the local density of states, it is very evident that the integrated quantities, such as the band structure energies, are reproduced within excellent agreement. The interested reader should be referred to Ref. [Zhon93] for a more complete list of examples which demonstrate the sound basis for using the recursion method for carbon clusters.

## 4.4 Molecular dynamics

Once the total potential energy calculation scheme is constructed using the recursion method, the next step is to find the equations of motion according to which the system evolves.

The dynamics of an isolated (microcanonical)  $N$ -particle system in three-dimensional space is governed by the Lagrangian

$$L = \sum_{i=1}^N \frac{1}{2} m_i \dot{\mathbf{q}}_i^2 - V(\{\mathbf{q}_i\}). \quad (4.23)$$

Here,  $\mathbf{q}_i$  is the position vector of atom  $i$  in the system and  $V(\{\mathbf{q}_i\})$  is the total po-

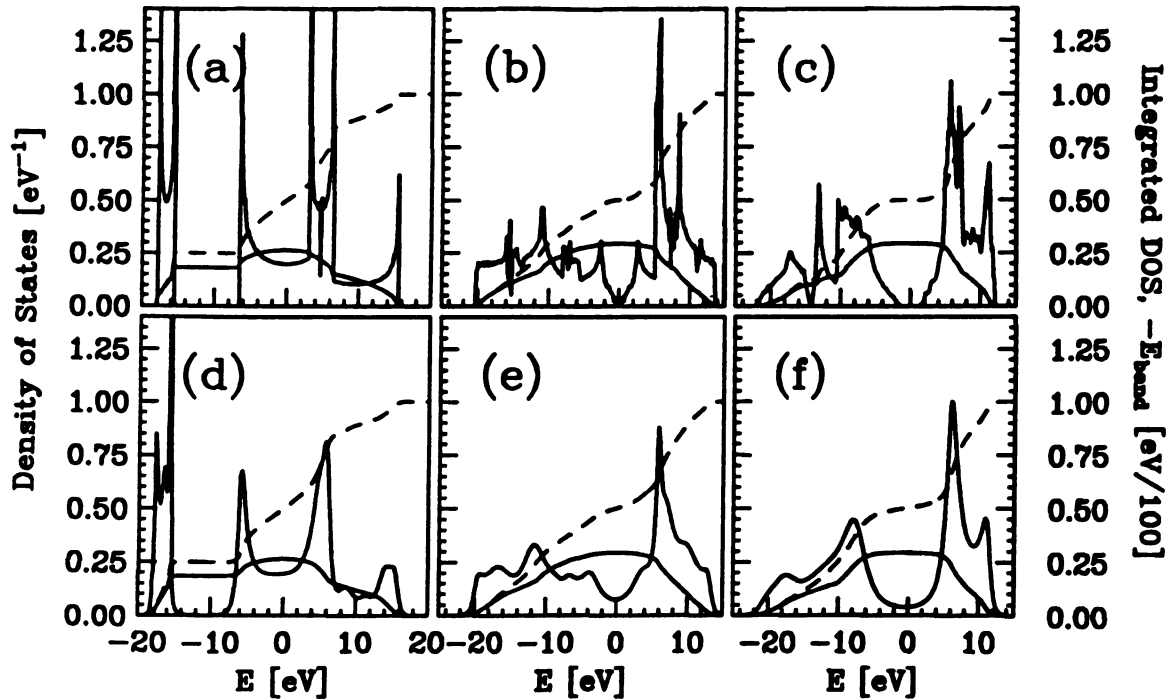


Figure 4.2: Comparison of recursion method vs. conventional tight-binding method. Electronic local density of states  $N(E)$  (solid lines), integrated density of states  $\int_{-\infty}^{E_F} dE N(E)$  (dashed lines), and the band structure energy  $-E_{bs}(E_F)$  as a function of band filling (dotted lines) for different carbon structures. Results of a tight-binding band-structure calculation for an infinite carbon chain (bondlength  $d_{CC} = 1.286 \text{ \AA}$ ) (a), a graphite monolayer ( $d_{CC} = 1.418 \text{ \AA}$ ) (b) and bulk diamond ( $d_{CC} = 1.546 \text{ \AA}$ ) (c) are compared with the simplified recursive results in (d), (e) and (f). The energy zero coincides with the Fermi level for a half-filled band, corresponding to neutral carbon. (Fig. 1 from Ref. [Zhon93] used with the permission from the authors.)



tential energy of the system. In present case it is given by the tight-binding Hamiltonian. The dynamical evolution of the system is described by Euler-Lagrange equations derived from the above Lagrangian. This procedure yields statistics for a microcanonical ensemble. Since we are studying the melting process of carbon fullerenes, we want to fix the "temperature" of the system to a given heat bath temperature. We define the temperature in such a small system by its instantaneous kinetic energy. We need to adapt molecular dynamics algorithm so as to sample a constant-temperature ensemble. Several different methods of prescribing the temperature in a molecular dynamics simulation exist. A recent review [Ande84] has attempted to summarize these methods and highlight their advantages and disadvantages. Here I will discuss only one of these which I used for melting the fullerenes.

We used the *extended system method*, or so-called Nosé-Hoover method. This method treats the dynamics of a system in contact with a thermal reservoir by including an extra degree of freedom which represents that reservoir. I carried out a simulation of this 'extended system'. Energy is allowed to flow dynamically from the reservoir to the system and back; the reservoir has a certain 'thermal inertia' associated with it, and the whole technique is rather like controlling the volume of a sample by using a piston which has certain mass.

Nosé achieved a major advance in this method by showing that the canonical distribution can be generated with smooth, deterministic, and time-reversible trajectories[Nose84]. To do this he introduced a time-scaling variable  $s$ , its conjugate momentum  $p_s$ , and a parameter (Nosé-Hoover parameter)  $Q$ . Nosé wrote

an augmented Hamiltonian

$$H_{\text{Nosé}} = \sum p^2/2ms^2 + V(\{q_i\}) + p_s^2/2Q + (X+1)kT \ln s, \quad (4.24)$$

where  $X$  is the total number of degrees of freedom of the system. This Hamiltonian contains a nonlinear collective potential in which the time-scale variable  $s$  oscillates. Thus the system is coupled to a heat bath (described by the variables  $s$  and  $p_s$ ). Nosé proved that the microcanonical distribution in the augmented set of variables is equivalent to a canonical distribution of the variables  $q, p'$ , where the  $p'$  are the scaled momenta  $p/s$ . Thus the Hamiltonian (4.24) generates the canonical probability distribution *independent of the values chosen for  $H_{\text{Nosé}}$  and  $Q$ .*

The equations of motion from Nosé Hamiltonian (4.24) are

$$\begin{aligned} \dot{q} &= p/ms^2 \\ \dot{p} &= F(q) \\ \dot{s} &= p_s/Q \\ \dot{p}_s &= \sum p^2/ms^3 - (X+1)kT/s. \end{aligned} \quad (4.25)$$

Hoover made a great improvement in implementing Nosé's method computationally, by deriving a simpler form of the above coupled first-order differential equations[Hoov85]. He noted that if the time scale is reduced by  $s$ , then  $dt_{\text{old}} = s dt_{\text{new}}$ . All of the rates given in Eq. (4.25) can then be expressed as derivatives with respect to  $t_{\text{new}}$  (for which we will still use the superior dot notation)

$$\dot{q} = p/ms$$





$$\begin{aligned}
\dot{p} &= sF(q) \\
\dot{s} &= sp_s/Q \\
\dot{p}_s &= \sum p^2/ms^2 - (X+1)kT.
\end{aligned} \tag{4.26}$$

The somewhat inconvenient variable  $s$  can then be eliminated from Eq. (4.26) by rewriting the coordinate time evolution equations in terms of  $q, \dot{q}$ , and  $\ddot{q}$ :

$$\begin{aligned}
\ddot{q} &= \dot{p}/ms - (p/ms)\dot{s}/s \\
&= F/m - \dot{q}p_s/Q \\
&\equiv F(q)/m - \zeta\dot{q}.
\end{aligned} \tag{4.27}$$

The thermodynamic friction coefficient  $\zeta \equiv p_s/Q$ , which appears in the second-order Eqs. (4.27), evolves in time according to a first-order equation

$$\dot{\zeta} = [\sum m\dot{q}^2 - (X+1)kT]/Q. \tag{4.28}$$

To have set of first-order equations, we redefine  $p \equiv m\dot{q}$  and replace Nosé's  $X+1$  by  $X$  obtaining

$$\begin{aligned}
\dot{q} &= p/m \\
\dot{p} &= F(q) - \zeta p \\
\dot{\zeta} &= [\sum p^2/m - XkT]/Q.
\end{aligned} \tag{4.29}$$

This is the so-called Nosé-Hoover equations of motion. Hoover proved that the distribution resulting from Eqs. (4.29) is canonical in the variables  $q$  and  $p$  [Hoov85]. It can be shown easily that we can arrive at the above equations by generalizing the microcanonical Lagrangian (4.23) to the augmented Lagrangian

$$L = \sum_{i=1}^N \frac{1}{2} m_i \dot{\mathbf{q}}_i^2 - V(\{\mathbf{q}_i\}) + \frac{1}{2} Q \dot{s}^2 - (X+1)T \ln s \tag{4.30}$$

and applying Euler-Lagrange equations:

$$\begin{aligned}\frac{d}{dt} \left( \frac{\partial L}{\partial \dot{q}_{i\alpha}} \right) - \left( \frac{\partial L}{\partial q_{i\alpha}} \right) &= 0, \\ \frac{d}{dt} \left( \frac{\partial L}{\partial \dot{s}} \right) - \left( \frac{\partial L}{\partial s} \right) &= 0.\end{aligned}\tag{4.31}$$

The parameter  $Q$  controls how fast the system explores the available phase space. For a large  $Q$  the trajectories gradually fill the phase space as expected for an ergodic system, and for a small  $Q$  the trajectories develop more singular turning points in phase space. For very large  $Q$  these equations simply reproduce the microcanonical behavior. The proper range of  $Q$  values should be determined by actual simulations for the given system at hand.

## 4.5 Simulation and Results

In our molecular dynamics simulations, we use the leapfrog technique to integrate the equations of motion over time steps  $\Delta t = 5 \times 10^{-16}$  s. We found that the temperature of the system is controlled reasonably well when we use the value for the Nosé-Hoover parameter  $Q = 1/250$  (amu·Å). This value corresponds, in crude sense, to using imaginary thermal particles which are almost 3,000 times lighter than carbon atoms as the mediator or carrier of the heat between the system and the heat reservoir.

We begin each MD run by equilibrating the particular fullerene for over several thousand time steps at a temperature  $T_i = 200$  K, after the directions of the initial atomic velocities have been randomized according to the Maxwell-Boltzmann velocity distribution at that temperature. We increase the temperature of the heat bath in steps of  $\Delta T = 400$  K from  $T_i$  to the final temperature

$T_f = 10,000$  K, and let the fullerenes equilibrate for 800 time steps at each new temperature. Each simulation run consists of more than 20,000 time steps and takes several hours of CPU time on a high-speed single-processor workstation. Statistical (time-averaged) data for the structure and energetics are collected after the system has adjusted to the new temperature, which occurs typically after 400 time steps following a temperature increase. This procedure is necessary to remove any undesired oscillation in the data due to the sudden increase of the heat bath temperature. A separate ensemble averaging at each temperature is necessary since ergodicity is not guaranteed especially in very small systems. We perform ensemble averaging over 50 complete runs with different initial states of  $C_{20}$ , 50 runs for  $C_{60}$ , and 15 runs for  $C_{240}$ . This reflects the decreasing fluctuations of thermodynamic quantities with increasing system size.

In Fig. 4.3, we present results for the temperature dependence of the total energy  $E$  *per atom* for the  $C_{60}$  molecule. We observe a steady increase of the total energy  $E$  with increasing temperature, with a well-formed step at  $T \approx 4,000$  K indicative of a "phase transition". To get a better understanding of the structural transformations in this and other fullerenes, we investigated the specific heat not only of the  $C_{60}$ , but also the  $C_{20}$  and the  $C_{240}$  molecules. The calculated temperature dependence of the specific heat *per atom* of these systems, obtained from  $c_V = dE/dT$ , is shown in Fig. 4.4.

In the temperature range addressed in this study, we found significant deviations from the classical value  $c_V = 3k_B$  to occur only for  $T \gtrsim 2,000$  K. We found all features in the rich structured  $c_V(T)$  to be reproducible from run to run up to a temperature of  $T \approx 6,000$  K. Individual peaks in  $c_V$  reflect the latent heat of transition between different "phases". As we discuss in the following, these

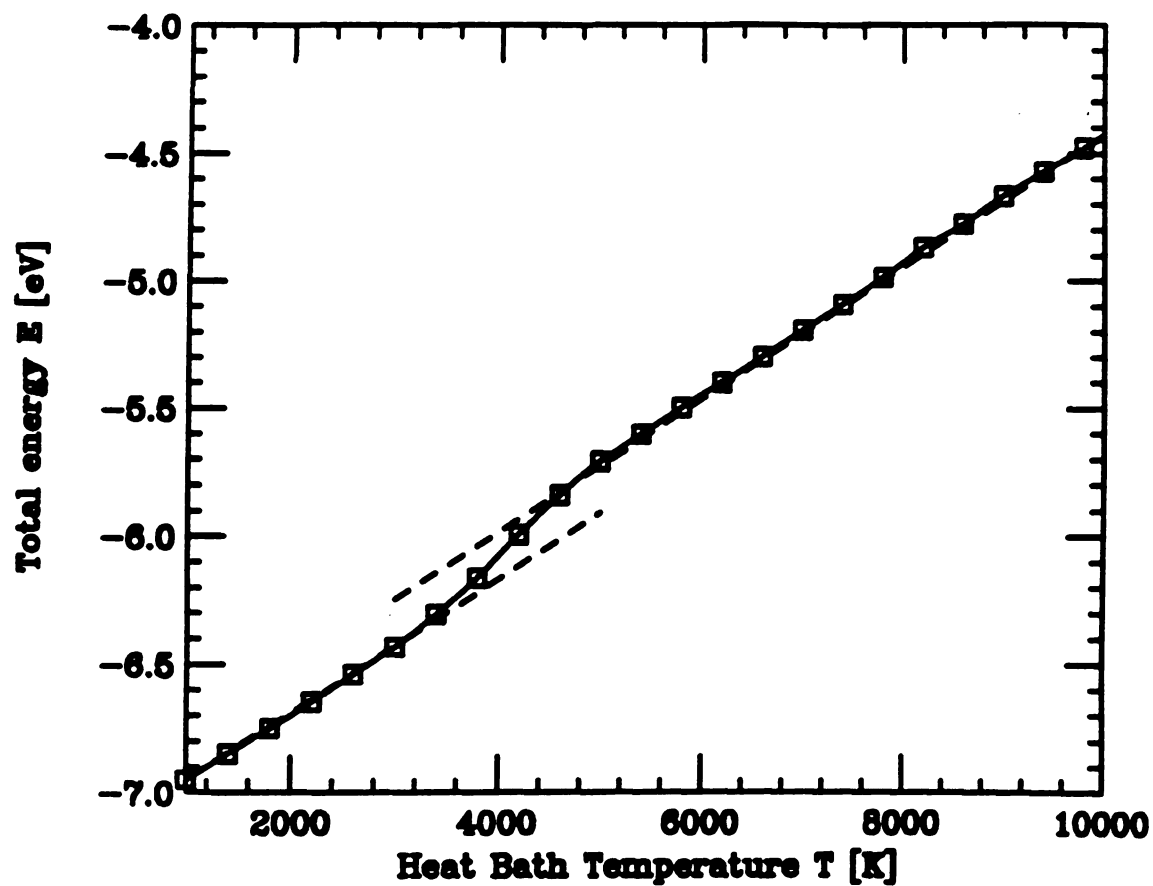


Figure 4.3: Temperature dependence of the total energy  $E$  per atom for the  $C_{60}$  fullerene (solid line). The data points in the  $E(T)$  curve for the fullerene mark the discrete steps of the heat bath temperature used, and the dashed lines with a slope of  $3k_B$  are guides to the eye.

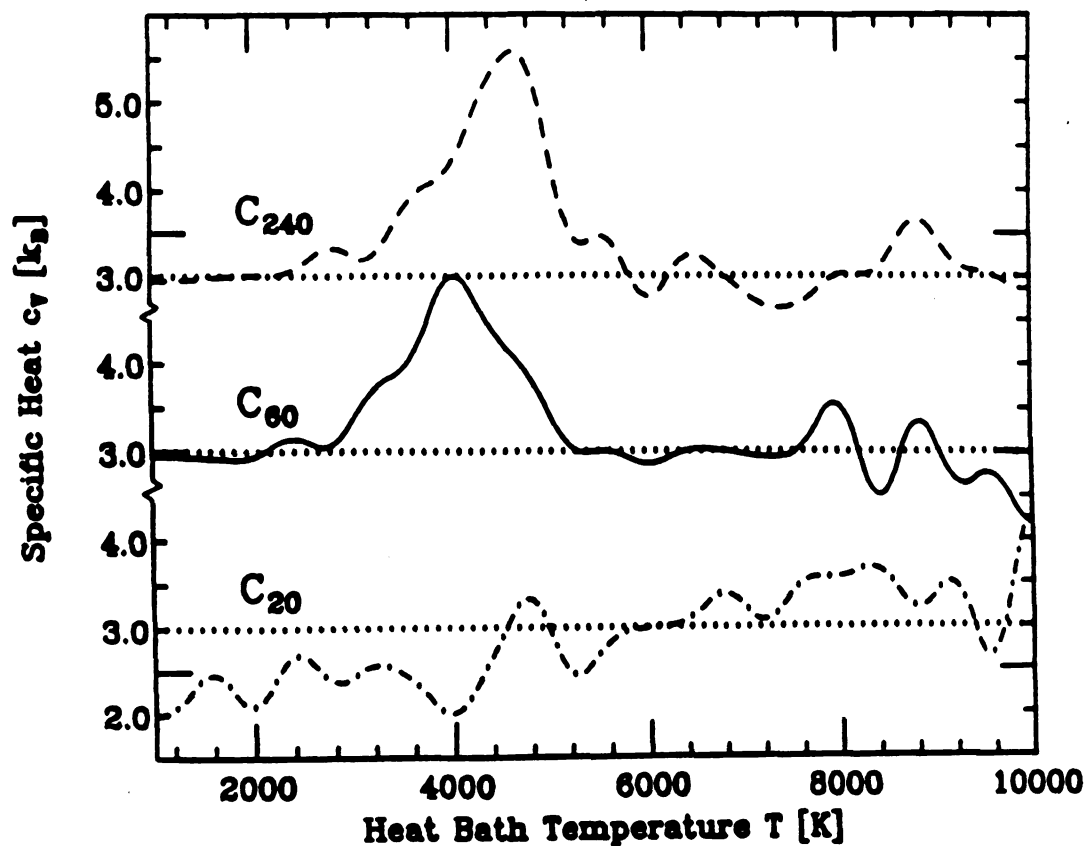


Figure 4.4: Specific heat  $c_v(T)$  per atom of icosahedral fullerenes  $C_{240}$  (dashed line),  $C_{60}$  (solid line), and  $C_{20}$  (dash-dotted line), in the temperature range  $T < 10,000$  K, in units of  $k_B$ . The ordinate is displaced vertically between successive plots for clarity; the classical value  $c_v = 3k_B$  is indicated by the dotted lines.

“phases” can be characterized by their topology and atomic binding energy distributions. In contrast to phase transitions in solids, the analogous transitions in fullerenes are not sharp owing to the finite size of these systems.

Due to the similarity of the  $c_V(T)$  results for the different fullerenes, we concentrate in the following on the  $C_{60}$  molecule. Each peak in the  $c_V(T)$  curve corresponds to the transition from one intermediate “phase” to next one. In order to identify the characteristics of its individual “phases”, we first take the “snap shots” of the  $C_{60}$  molecule at selected heat bath temperatures as shown in Fig. 4.5.

To have some quantitative criterion to characterize the “phase” we also plot the atomic binding energy distribution in Fig. 4.6 at the temperatures chosen for Fig. 4.5. The atomic binding energy for a given atom is defined as *the contribution of the given atom to the total cohesive energy of the whole system*. Thus the cohesive energy in Eq. (4.4) can be written as

$$E_{\text{coh}} = \sum_{i=1}^N E_b(i) \quad (4.32)$$

where the binding energy of atom  $i$  is given by

$$E_b(i) = \left[ \int_{-\infty}^{E_F} E N_i(E) dE - \sum_{\alpha} n_{i,\alpha} \epsilon_{\alpha} \right] + \sum_j' E_r(r_{ij}, z_i), \quad (4.33)$$

with  $E_r(r_{ij}, z_i)$  defined in Eq. (4.9). We find the binding energy distribution to provide a better signature of the different “phases” than topological quantities (such as coordination numbers) which depend on the definition of cutoff distances. We also monitored the change in the distribution of bond lengths for each atom and plotted them in Fig. 4.7 at the same temperatures as in the previous two figures. Only the atom pairs within the cutoff distance (2.0 Å in this case) were

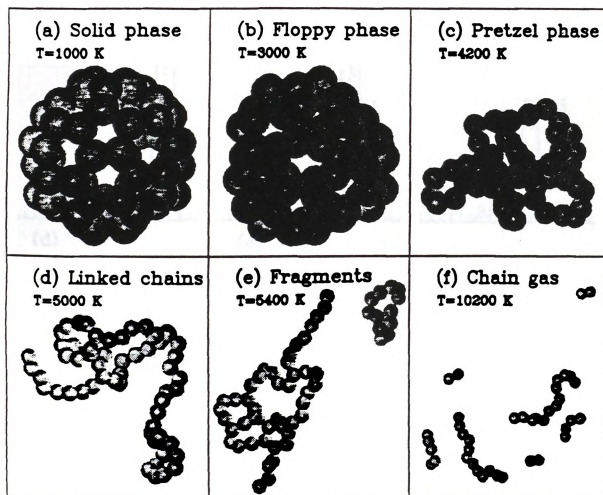
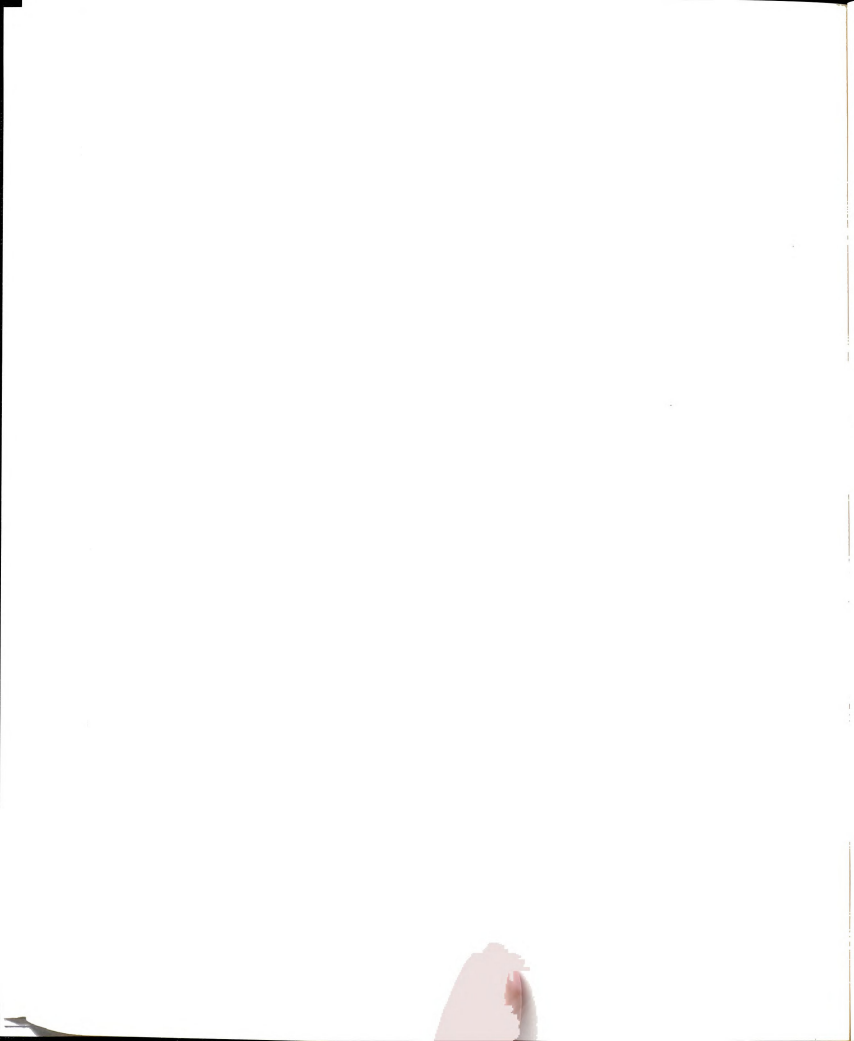


Figure 4.5: "Snap shots" illustrating the geometry of a  $C_{60}$  cluster at temperatures corresponding to the different "phases" discussed in the text.





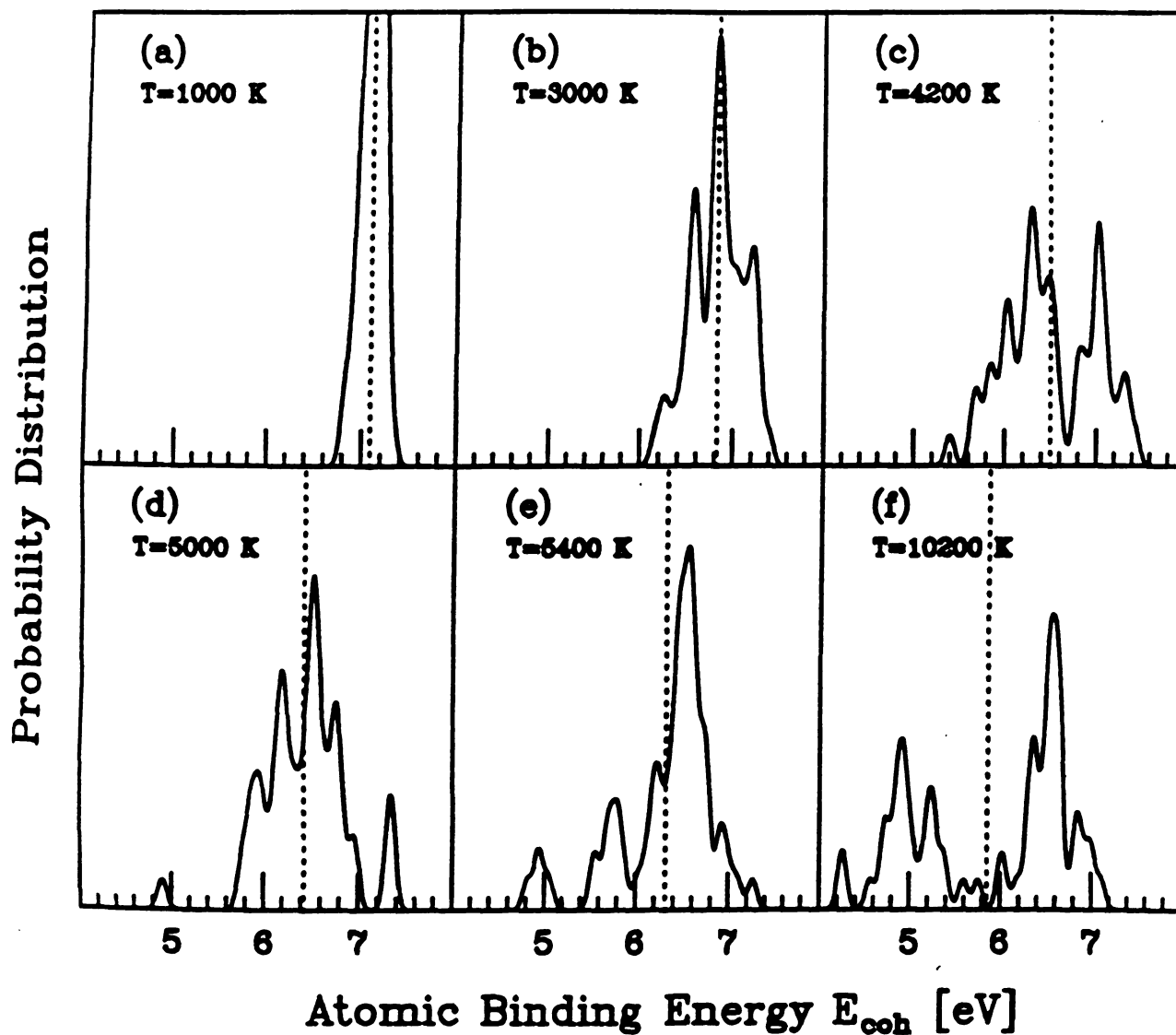


Figure 4.6: Atomic binding energy distribution in a  $C_{60}$  cluster at temperatures characteristic of the different "phases" discussed in the text and in Fig. 4.5. For each structure, the average binding energy is given by the dotted line.

considered in Fig. 4.7. In Fig. 4.8, we plot the distribution of bond angles at the selected temperatures. If an atom is connected to more than one neighbor within the cutoff distance, the angles between these bonds were calculated and their distribution is collected. As the final monitoring quantity, we calculated the mass spectrum of the fragments of the  $C_{60}$  molecule at selected time steps. The atoms are considered to be part of the same cluster when they are connected by bonds within the cutoff distance (2 Å). The changes of the mass spectrum as a function of the heat bath temperature are depicted in Fig. 4.9. When the system consist of one (connected) cluster, this spectrum will show only one peak at the value of the total mass. When the structure is fragmented into smaller pieces, several peaks will occur at lower mass values.

In the *solid phase*, occurring at  $T \lesssim 2,400$  K and depicted in Fig. 4.5(a), the  $C_{60}$  is intact. As shown in Fig. 4.6(a), the binding energy of all atoms is approximately the same, but decreases gradually with increasing temperature due to thermal expansion. The bond length distribution shows a very prominent single peak around 1.46 Å [Fig. 4.7(a)]. The experimental values of two bond lengths for  $C_{60}$  at ground state are 1.40 Å (double bonds) and 1.45 Å (single bonds) [Yann91].

A peak in the  $c_V(T)$  curve at  $T \approx 2,400$  K indicates the gradual onset of the *floppy phase*, depicted in Fig. 4.5(b). While the system is topologically intact in this phase, as documented by a relatively narrow bond length distribution [Fig. 4.7(b)], we observe the bond angle distribution to spread out [Fig. 4.8(b)], resulting in a significantly broadened binding energy distribution [Fig. 4.6(b)]. Assisted by local shear motion, carbon pentagons and hexagons tilt easily with respect to the surface normal especially in large fullerenes with flat faces. In  $C_{60}$ , this floppy motion creates a distribution of carbon sites which are either closer to

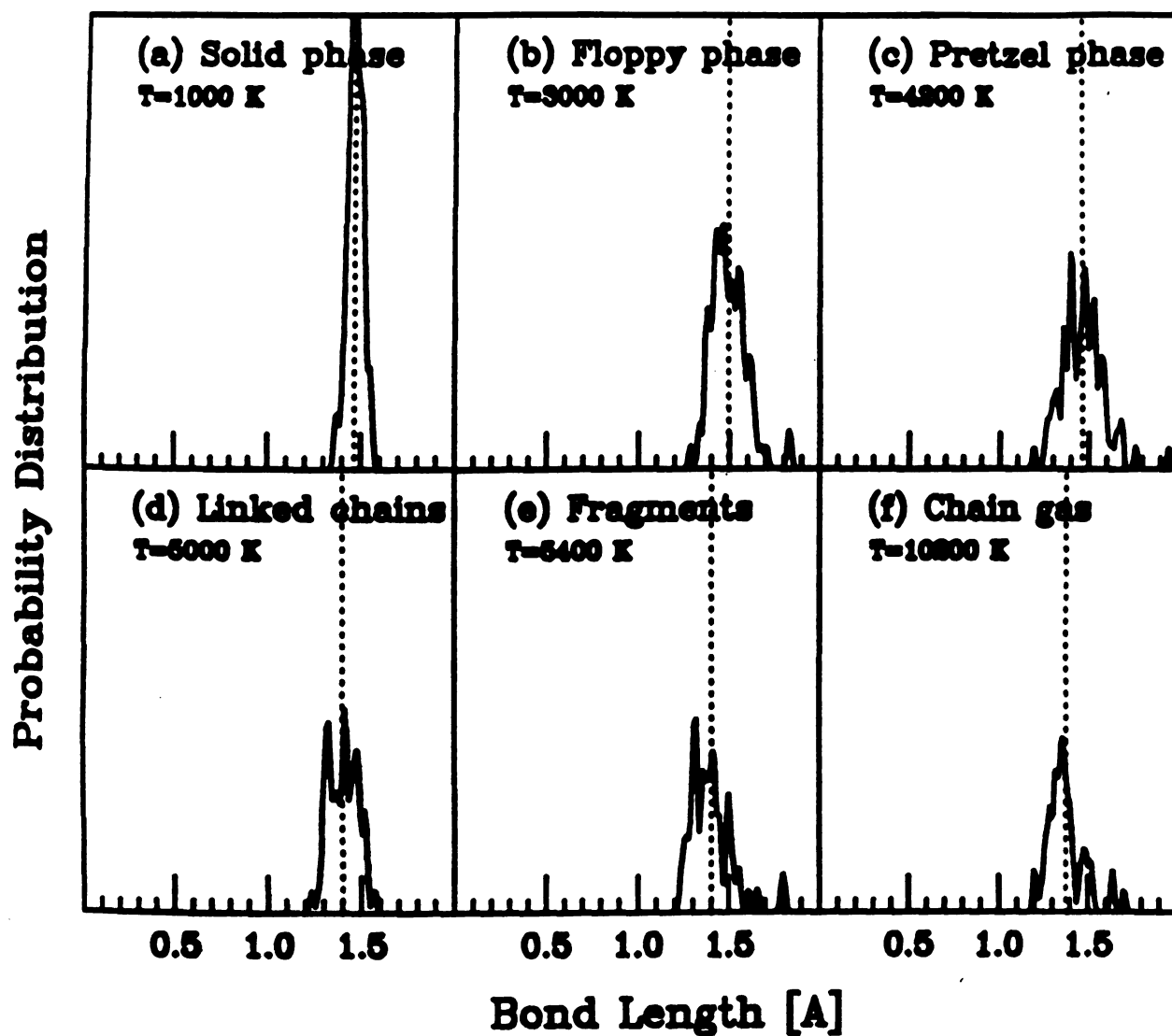


Figure 4.7: Bond length distribution in a  $C_{60}$  cluster at temperatures characteristic of the different "phases" discussed in the text and in Fig. 4.5. For each structure, the average bond length is given by the dotted line.



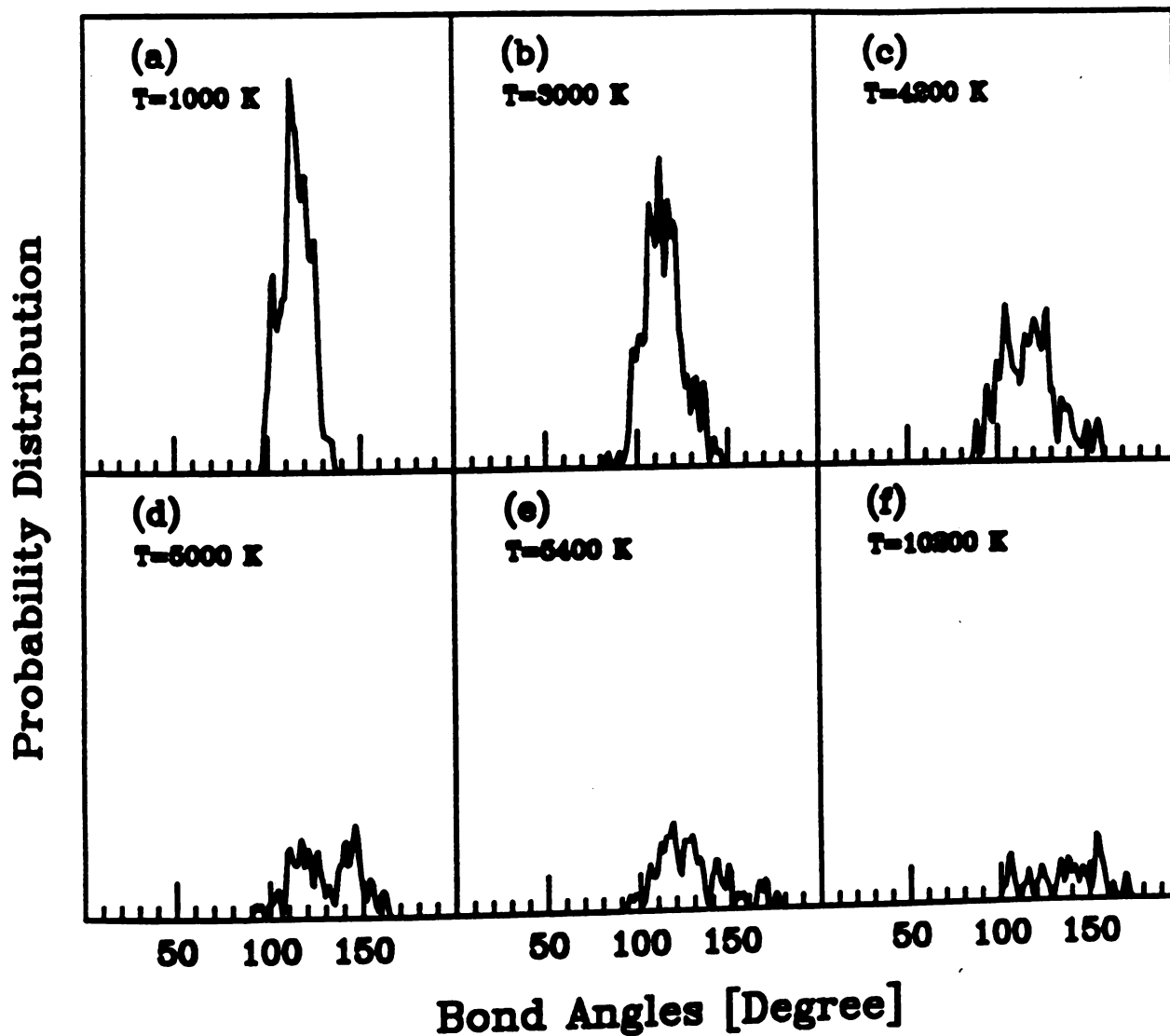


Figure 4.8: Bond angle distribution in a  $C_{60}$  cluster at temperatures characteristic of the different "phases" discussed in the text and in Fig. 4.5.



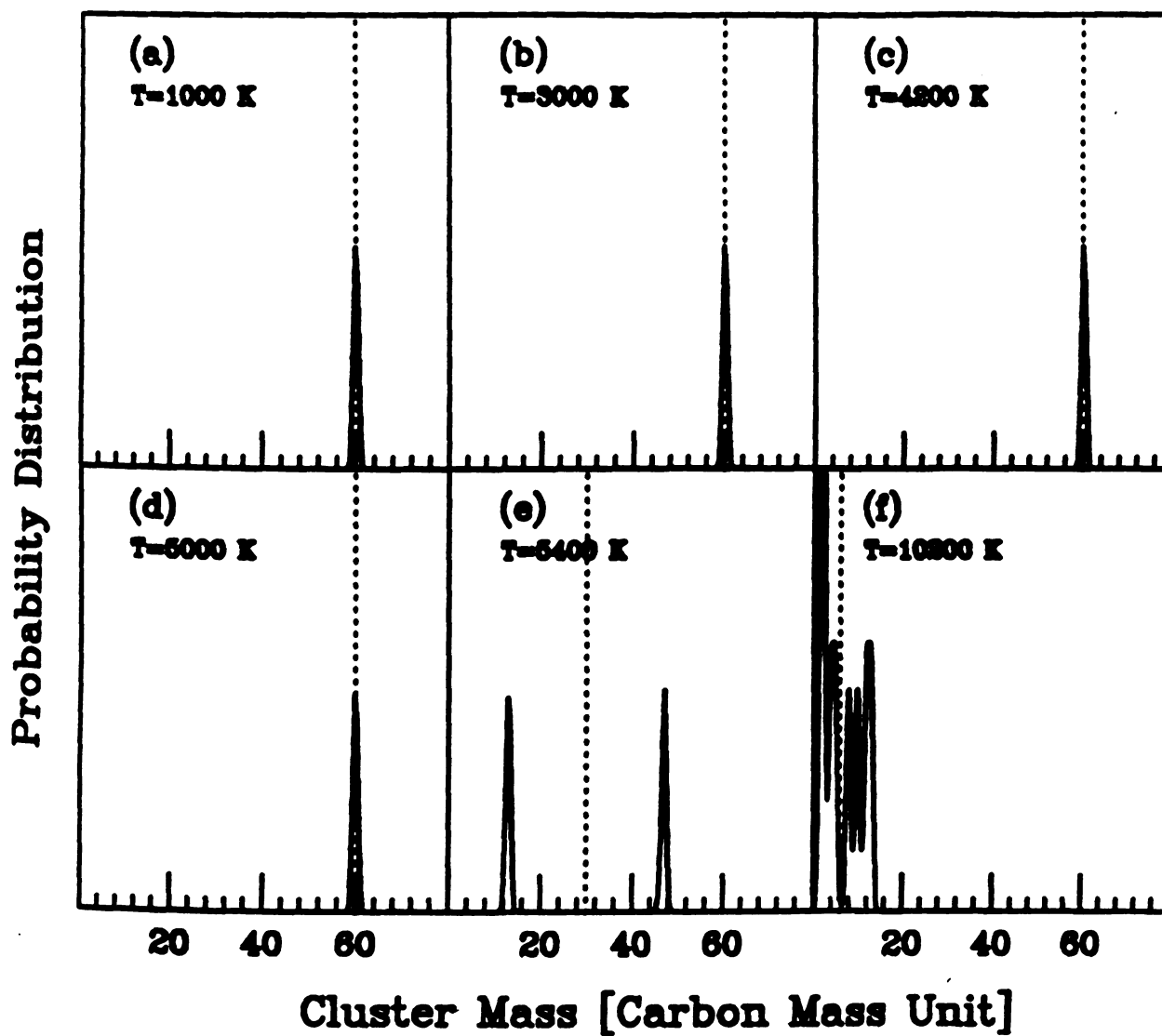


Figure 4.9: Mass spectrum in a  $C_{60}$  molecule at temperatures characteristic of the different "phases" discussed in the text and in Fig. 4.5. The cutoff length 2.0 Å is used to determine the cluster boundary.

or further away from the optimum graphitic bonding geometry than the average structure. We found that the local shear motion leads to substantial cluster shape deformations.

Above  $T \approx 4,000$  K, we observe a dramatic transition to the *pretzel* phase, consisting of interconnected carbon rings and depicted in Fig. 4.5(c). They are still all one single connected body as depicted by a single peak in mass spectrum [Fig. 4.9(c)]. A similar, yet not as complex structure has recently been proposed as a high temperature phase of  $C_n$  clusters based on diffusion data [Held93, Hunt94]. In our calculation, we find this structure to be initiated by the rupture of a single bond connecting a pentagon to a hexagon, which creates a large opening at the surface. As temperature approaches to this transition temperature, this bond opening is amplified and propagates in a "zipper" motion through the molecule. Suddenly the closed structure "unwraps" to become a "pretzel" structure. As shown in Fig. 4.3, the transition from a (two-dimensional) fullerene to a (one-dimensional) linked chain structure is clearly reflected in a sharp increase of the entropy towards a value characteristic of a (metastable)  $C_{60}$  chain. The energetically less favorable *sp* bonding of a growing number of two-fold coordinated atoms in the "pretzel" phase is reflected in the broadening of the binding energy distribution especially towards lower values. This is shown in Fig. 4.6(c) for a fully developed "pretzel" at  $T = 4,200$  K. One thing to note about this distribution is that it has two major peaks. The atoms which are part of the chain is mainly two-fold coordinated and has smaller binding energies and responsible for the peak at lower value. On the other hand, the atoms which are part of the connecting joints of the rings have three or even higher coordination numbers and contribute to the peak at the higher binding energy value. The specific heat data



of Fig. 4.3 suggest that the critical temperature shifts upward with increasing fullerene size. The bond angle distribution shows a lot of new peaks over 150 degrees representing the chain structure [Fig. 4.8(c)].

Closed carbon chains of the  $C_{60}$  "pretzel" open up at  $T \gtrsim 5,000$  K, as shown in Fig. 4.5(d). The number of structural constraints in this *linked chain* phase decreases, allowing individual atoms to relax. This leads to a smaller number of inequivalent sites and more pronounced peaks in the binding energy distribution, depicted in Fig. 4.6(d).

Starting at  $T \approx 6,000$  K, we observe fragmentation of all fullerenes which we studied. The mass spectrum finally shows split peaks at the values other than 60 [Fig. 4.9(e)]. Typical fragments, such as those shown in Fig. 4.5(e) for  $T = 5,400$  K, have "pretzel" and "linked chain" structures discussed above. Above this temperature, the thermodynamics of the system is that of fullerene fragments; strong run-to-run fluctuations are caused by the differences in the specific heat of the individual fragments. While the binding energy range is similar to that in the "linked chain" phase, the distribution is smoother at this higher temperature, as shown in Fig. 4.6(e). Finally, at temperatures close to  $T \approx 10,000$  K, a conversion to a chain gas is completed, as illustrated in Fig. 4.5(f). The mass spectrum shows many peaks at the small mass numbers [Fig. 4.9(f)].

The temperature scale relevant to structural transitions in fullerenes can be linked to well established thermodynamic data for graphite [Weas90]. We find the "floppy phase" of fullerenes to occur at temperatures close to the melting point of graphite,  $T_{m.p.} = 3,823$  K [Weas90]. On the other hand, the calculated fragmentation temperature  $T \approx 5,400$  K lies close to the observed boiling point

of graphite,  $T_{b.p.} = 5,100$  K [Weas90].

In order to understand the rich “phase diagram” of fullerenes, we have to investigate the free energy  $F$  as a function of temperature. It is intuitively clear that the more “floppy” chain structures have a larger entropy and hence should be preferred over the more compact fullerene structures at sufficiently high temperatures. As mentioned above, we have determined the entropy *per atom*  $S(T)$  from MD simulation runs of  $C_{60}$  fullerenes and metastable  $C_{60}$  chains. Our results, shown in Fig. 4.10, indicate that the entropy values are equal at very high temperatures where also the fullerenes have converted to linear structures. *Prior to the conversion*, we find for the entropy difference

$$S(C_{60} \text{ chain}) - S(C_{60} \text{ fullerene}) \approx 2k_B. \quad (4.34)$$

This allows us immediately to estimate the conversion temperature from fullerenes to chains from low temperature data. Noting at the moment of conversion

$$\begin{aligned} F(\text{chain}) - F(\text{fullerene}) &= [E(\text{chain}) - E(\text{fullerene})] \\ &\quad - T_c[S(\text{chain}) - S(\text{fullerene})] \\ &= 0, \end{aligned} \quad (4.35)$$

we have

$$T_c = \Delta E / \Delta S. \quad (4.36)$$

Using the result obtained previously[Toma91]

$$\begin{aligned} \Delta E &= E(\text{chain}) - E(\text{fullerene}) \\ &\approx 1 \text{ eV} \end{aligned} \quad (4.37)$$

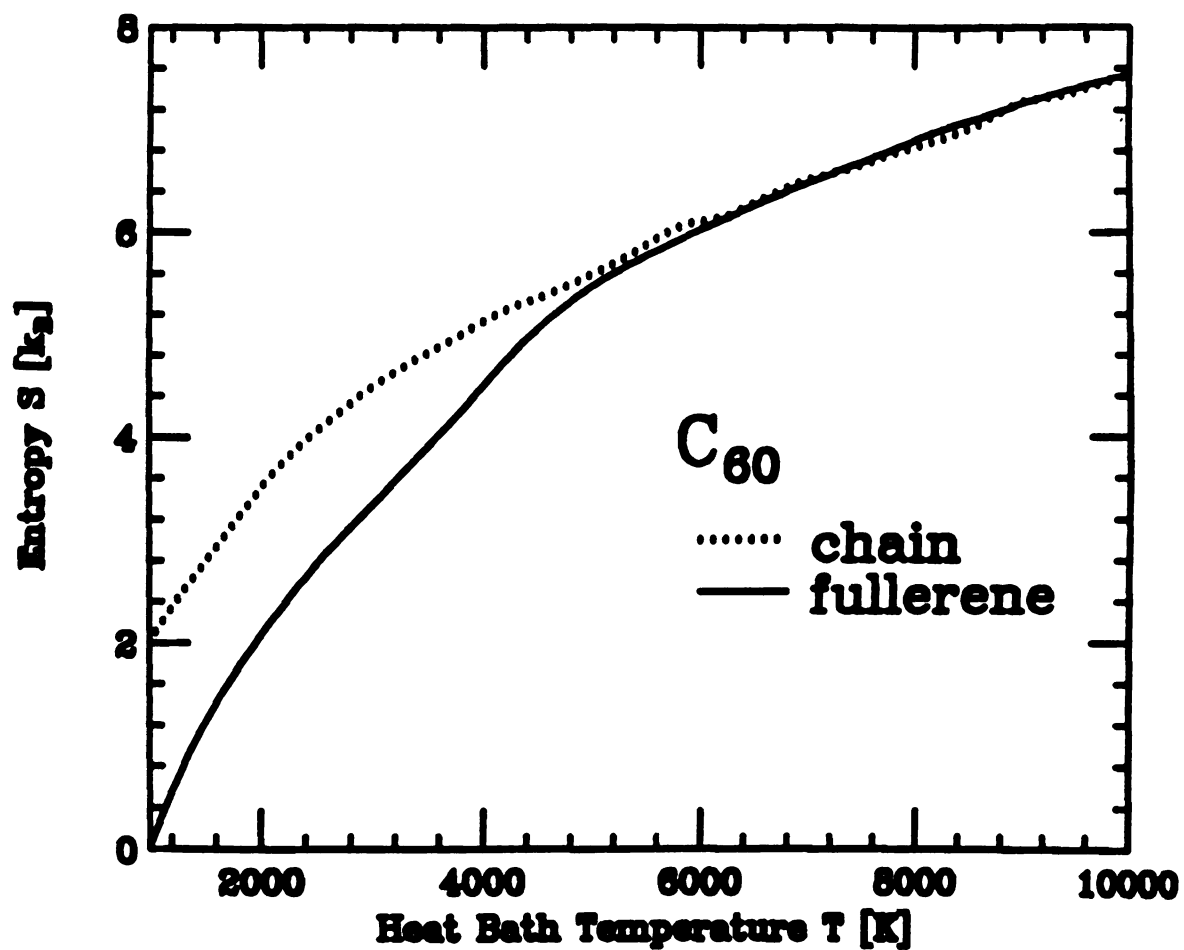


Figure 4.10: The entropy  $S$  per atom for the  $C_{60}$  fullerene (solid line) and the metastable  $C_{60}$  chain (dotted line).



and assuming that the values for  $\Delta E$  and  $\Delta S = S(\text{chain}) - S(\text{fullerene})$  are nearly temperature independent, we obtain  $T_c \approx 5,800$  K for the fullerene-to-chain conversion. This is in remarkable agreement with our simulation results considering the crude arguments we have used in this estimate.

It is interesting to note that the open fullerene phases, which were identified in our simulation, also occur during energetic collisions between fullerenes. In particular, the final state of a  $C_{60}$  cluster undergoing an inelastic collision with a  $C_{240}$  cluster at 300 eV center-of-mass kinetic energy heats up during the collision process to temperatures close to 5,000 K and shows a final structure similar to that presented in Fig. 4.5(d) [KimS94b].

Our results shed new light also on the formation process of fullerenes from the gas phase. While time reversal of the evaporation process studied here would provide *one possible* aggregation path, the general formation mechanism is clearly more complex. We expect that many structures which occur during the fragmentation also reoccur during the aggregation. Of course, most of the “random” aggregation paths will not lead immediately to a closed fullerene, yet are likely to contain stable structural elements such as chains and rings. Once such a “linked chain” or “fragmented pretzel” structure is formed, the aggregation dynamics will be governed by many unsuccessful attempts to reversibly “roll up” the chains to a fullerene, followed by one successful attempt to create an inert structure. This picture agrees with the fullerene formation mechanism suggested in Ref. [Hunt94] and the isotope scrambling results of Ref. [Ebbe92] suggesting that gas phase assembly of fullerenes starts from atoms and very small carbon clusters.

## 4.6 Conclusions

We presented the new and efficient recursion method applied to the tight-binding molecular dynamics for carbon atoms. The carbon potential parameters fitted to LDA calculations have been presented and the reliability of the recursion technique treatment has been demonstrated. Finally, we presented molecular dynamics simulation results of the melting and evaporation of the carbon fullerenes  $C_{20}$ ,  $C_{60}$ , and  $C_{240}$ . Among others, we found a most dramatic transition to a "pretzel" phase to occur at a high temperature of  $T \gtrsim 4000$  K. The temperature where fullerenes disintegrate into carbon chains was explained using quantitative results for the entropy.

## Chapter 5

# Stability of Magnetic Dipole Structures in Ferrofluids

### 5.1 Introduction

A ferrofluid is a magnetic colloid composed of magnetite particles suspended in a liquid, usually a petroleum oil [Rose85, Wang94]. In many ways, ferrofluids behave similar to electrorheological (ER) fluids which consist of a suspension of fine dielectric particles in a liquid of low dielectric constant [TaoR92, Bloc87, Fili88]. The aggregation of particles in ferrofluids and ER fluids has been the subjects of many experiments and numerical simulations. It has been observed that the aggregated Co particles, produced by inert-gas evaporation in Ar, show very different fractal dimensions depending on the strength of the magnetic interactions between the particles[Nick88]. Remarkable labyrinthine patterns are formed when a droplet of ferrofluid is trapped between two horizontal glass plates in a vertical magnetic field [Lang92, Dick93]. The effective viscosity of an ER fluid increases dramatically if an electric field is applied, and when the field exceeds a critical value, the ER fluid turns into a solid. Experiments also find that upon application of electric fields, dielectric particles in ER fluids rapidly form chains which

then aggregate into thick columns [Hals90, Chen92, Mart92, Gind92]. Magnetic ferrofluids form similar structures of chains and thick columns [Wang94]. The dependence of the periodicity of columns on the sample thickness has been recently studied using magnetite colloids [Wang94]. Also many numerical simulations using molecular dynamics (MD) [Hass89, Klin89, Kusa90, Bonn92, TaoR94] have been carried out to find the orientational ordering in ER liquid crystals.

Even though a few MD simulation results have been published for ferroelectric dipole liquids [WeiD92a, WeiD92b], almost no MD simulation results are available for the magnetic ferrofluid systems except a few simulations using the Monte Carlo technique [Weis93, Stev94]. Although ER fluids and magnetic ferrofluids have many common properties there is one fundamental difference. In ER fluids, the dipoles are induced by applied electric field and they are always aligned with the field. Consequently, the dipole moments vanish in the absence of a local electric field and therefore do not show any interesting behaviour in that situation. In contrast to this, the magnetic particles in ferrofluids have their own pre-assigned magnetic moments. This means that in general case they are not necessarily aligned with the external field, and we have to consider the rotations of these particles as well as their positions. Also, we should expect that these fluids have some non-trivial structures even in the absence of the external field.

In this Chapter, I will discuss the early stages of colloidal aggregation in a ferrofluid and the stability of the ring structure of these particles. In an ER fluid it is very unlikely to observe such a ring structure for the reasons I give in the previous paragraph. As I will show in later sections, a ring is the most stable configuration in zero-field, where it is established by the dipole-dipole interactions. In an ER system such interactions only occur upon applying an external field.



In Sec. [5.2] I will describe the theoretical model used to simulate the magnetic ferrofluid. The interaction potentials for these colloidal particles will be introduced. Since the magnetic colloidal particles have permanent magnetic moments pointing in a particular direction, we need to treat their rotational degrees of freedom properly, as well as translational. Sec. [5.3] will be devoted to the techniques involved in doing MD simulations for rigid bodies, especially spherical tops. Since the standard equations of motions for the Euler angles which are used to represent the rotation of rigid bodies, have a well-known singularity, the quaternion formalism is introduced in Sec. [5.4] as a better alternative. Before we use all these techniques and start the MD simulations, in Sec. [5.5] the stability of the chains and rings made of magnetic dipoles is discussed under various physical conditions with static or energy minimization method. The dynamical response of the magnetic dipole structures is the subject of Sec. [5.6]. The phase diagram of the ring configuration will also be presented. The ongoing projects in ferrofluid will be briefly described in Sec. [5.7] and in Sec. [5.8] I summarize this chapter and draw conclusions.

This chapter contains material of the following two separately published manuscripts:

- [Jund94] P. Jund, S.G. Kim, D. Tománek and J. Hetherington, *Stability of Magnetic Dipole Structures in Ferrofluids*, preprint (1994).
- [KimS94c] S.G. Kim, P. Jund, D. Tománek and J. Hetherington, *Structure Formation in Ferrofluids*, in preparation (1994).

## 5.2 Modeling of the ferrofluid

The physical system we attempt to simulate in this study is very much related to the ferrofluid system used in Ref. [Wang94]. The sample used by Wang *et al* is a magnetic colloid made of magnetite particles coated with oleic acid and suspended in *n*-eicosane. The volume fraction of magnetic particles is 12% with mean diameter of particles 89 Å. The thickness of the coated surfactant layer is about 20 Å.

Based on these experimental data, we choose 100 Å for the diameter of particles. From the density of the magnetite, 5.2 g/cc, and their size we also set the mass of our magnetic dipoles to be  $1.64 \times 10^6$  amu. Using the magnetization of magnetite and the volume of the particles, we can estimate the magnetic moment of these particles by assuming that they have a single magnetic domain. We take  $2.1 \times 10^4 \mu_B$ , with  $\mu_B$  being Bohr magneton, to be the amplitude of the magnetic moments of all particles.

In this calculation, the ferrofluid particles are modeled by soft spheres of diameter  $\sigma$  and carrying a magnetic dipole moment  $\vec{\mu} = \mu_0 \hat{\mu}$ . We take  $\mu_0$  to be constant for all dipoles and  $\hat{\mu}$  is the unit vector along the magnetic dipole moment. The potential energy of the system of these dipoles can be written as

$$U = \sum_i \left[ u_B(i) + \sum_{j>i} u(ij) \right] \quad (5.1)$$

where the pair potential between particles  $i$  and  $j$  is

$$u(ij) = u_{DD}(ij) + u_{SC}(ij). \quad (5.2)$$

The first term in Eq. (5.1) is the field energy

$$u_B(i) = -\vec{\mu}_i \cdot \vec{B} \quad (5.3)$$

gained by each particle when an external magnetic field,  $\vec{B}$  is applied.

The magnetic interaction between the particles is

$$\begin{aligned} u_{DD}(ij) &= \vec{\mu}_i \cdot \vec{\mu}_j / r_{ij}^3 - 3(\vec{\mu}_i \cdot \vec{r}_{ij})(\vec{\mu}_j \cdot \vec{r}_{ij}) / r_{ij}^5 \\ &= \frac{\mu_0^2}{r_{ij}^3} [\hat{\mu}_i \cdot \hat{\mu}_j - 3(\hat{\mu}_i \cdot \hat{r}_{ij})(\hat{\mu}_j \cdot \hat{r}_{ij})] \end{aligned} \quad (5.4)$$

which is the usual dipole-dipole interaction[Jack75]. Here  $\vec{\mu}_i$  and  $\vec{r}_i$  are the dipole moment and position vector of particle  $i$ , respectively. Obviously,  $\vec{r}_{ij} = \vec{r}_j - \vec{r}_i$ , and  $r_{ij}$  is the magnitude of  $\vec{r}_{ij}$  and  $\hat{r}_{ij}$  is the unit vector along  $\vec{r}_{ij}$ . Using the magnetic moments and diameter of the particles the energy scale of the dipole-dipole interaction is

$$\frac{\mu_0^2}{\sigma^3} \simeq 2.368 \times 10^{-2} \text{eV}. \quad (5.5)$$

There has been a significant amount of efforts to measure the pair interaction potential between the colloidal particles [Cald94, Croc94]. In this study we use following general form for soft-core potential

$$u_{SC}(ij) = \epsilon \Phi(r_{ij}/\sigma) \quad (5.6)$$

with

$$\Phi(r) = \alpha \left[ \exp\left(-\frac{r-\sigma}{\rho_1}\right) - \exp\left(-\frac{r-\sigma}{\rho_2}\right) \right], \quad \rho_1 < \rho_2. \quad (5.7)$$

This functional form is similar to the one suggested by Tejero *et al.* [Teje94] except the  $1/r$  factor which is in their potential. Here  $\epsilon$  fixes the energy scale of this potential and  $\sigma$  is the distance where

$$u_{SC}(\sigma) = 0 \quad (5.8)$$

and defines the length scale of the soft-core. The three parameters  $(\alpha, \rho_1, \rho_2)$  of Eq. (5.7) are seen to determine the steepness of the repulsion ( $\rho_1$ ), the range of the attraction ( $\rho_2$ ), and the well depth ( $\alpha$ ). If we fix the well depth to be  $\epsilon$ ,

$$\Phi(r_0) = -1 \quad (5.9)$$

with  $r_0$  denoting the position of the minimum of  $\Phi(r)$ , viz.

$$\Phi'(r_0) = 0. \quad (5.10)$$

This condition will fix  $\alpha = \alpha(\rho_1, \rho_2)$  for given  $\rho_1$  and  $\rho_2$

$$\alpha = \frac{1}{\left(\frac{\rho_1}{\rho_2}\right)^{\rho_1/(\rho_2-\rho_1)} - \left(\frac{\rho_1}{\rho_2}\right)^{\rho_2/(\rho_2-\rho_1)}}. \quad (5.11)$$

To simulate the effect of surfactant layer in ferrofluid, we choose the depth of the potential well to be about 10% of the dipole-dipole interaction, or  $2.0 \times 10^{-3}$  eV and the range of two exponential terms to be  $\rho_1 = 2.5$  Å,  $\rho_2 = 5.0$  Å. These parameters gives  $\alpha = 4$  and generates the potential which decays to 10% of its depth at the distance of surfactant layer thickness, 20 Å, away from the particle diameter  $\sigma$ , 100 Å. Fig. 5.1 is a plot of  $u_{SC}(r)$  with this set of parameters. The maximum of the plot is  $2.0 \times 10^{-2}$  eV which is the typical value for the dipole-dipole interaction.

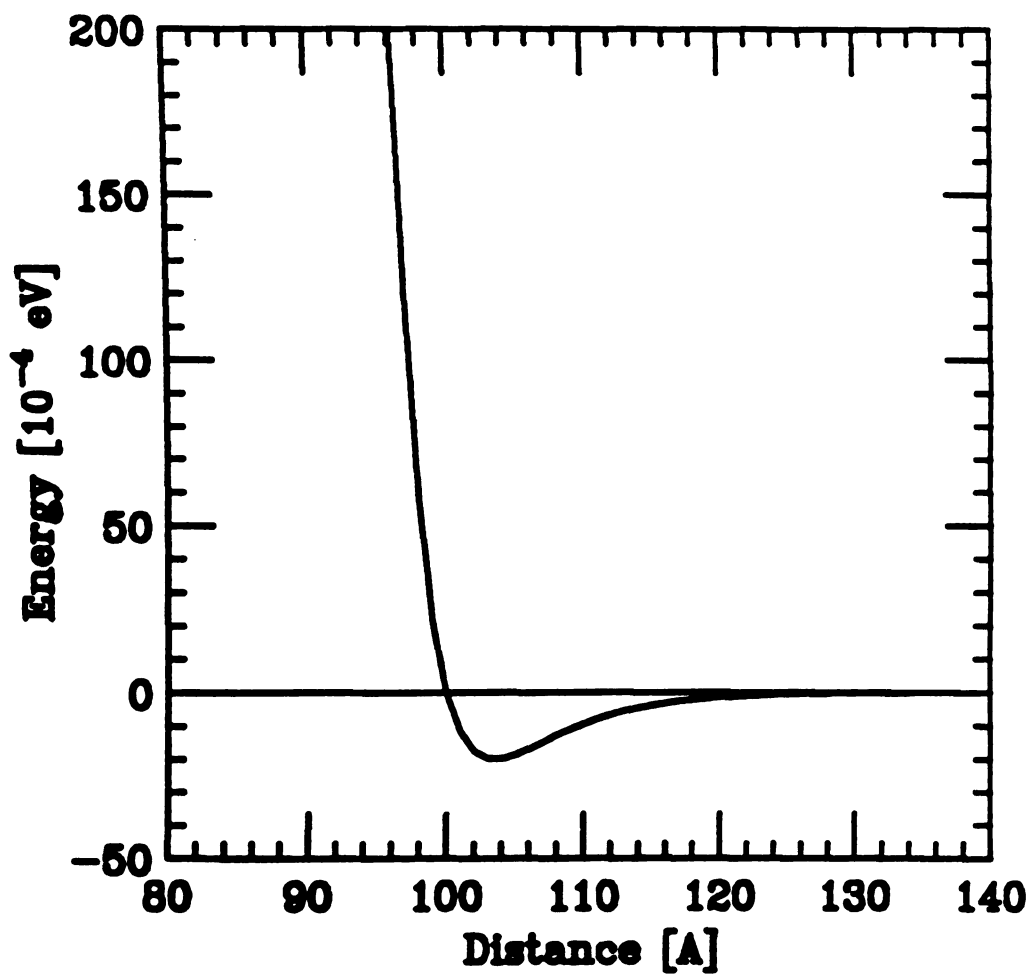
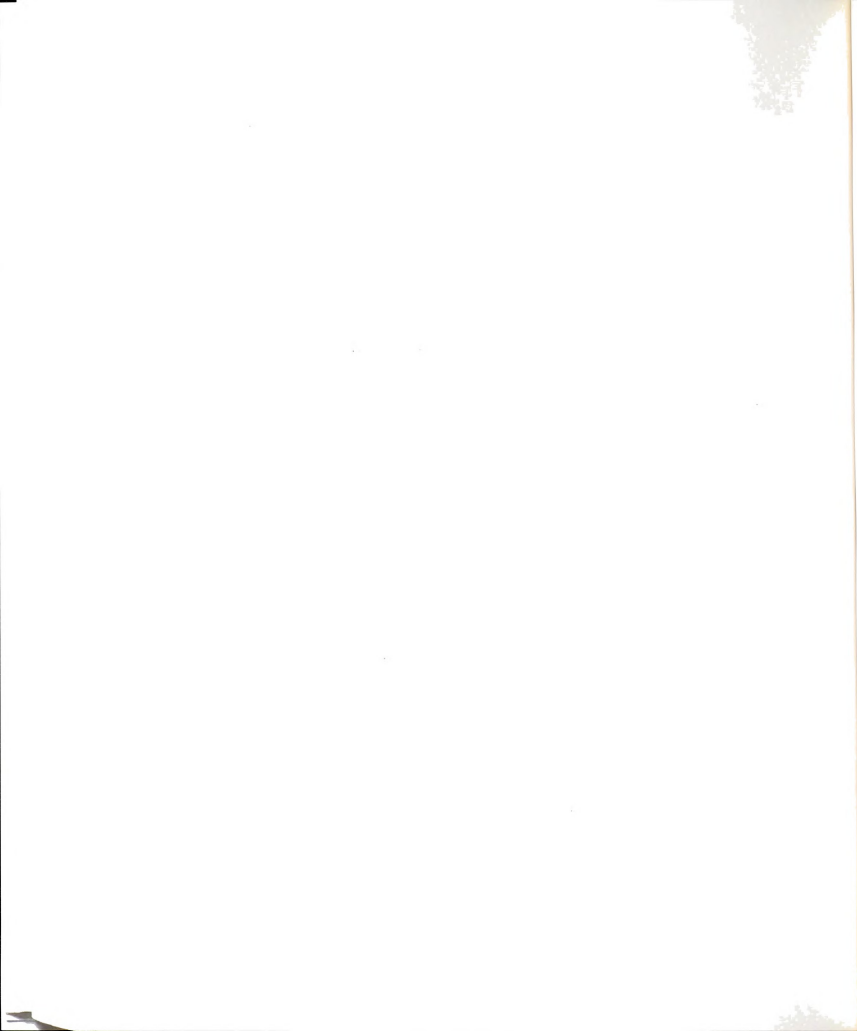


Figure 5.1: Soft-core potential for a ferrofluid particle,  $u_{sc}(r)$ , with  $\epsilon = 2.0 \times 10^{-3}$  eV,  $\rho_1 = 2.5$  Å and  $\rho_2 = 5.0$  Å.



For completeness, I summarize the units and conversion factors between these units in Table 5.1. All the units with tilde are the units used in our numerical calculations. In Table 5.2, the actual physical quantities used and the typical values we need to deal with in this study are listed.

The dipole-dipole interaction in Eq. (5.4) has two terms competing each other. The first term,  $\hat{\mu}_i \cdot \hat{\mu}_j$ , tends to make the dipoles anti-parallel each other and favors anti-ferromagnetic arrangement. On the contrary, the second term,  $-3(\hat{\mu}_i \cdot \hat{r}_{ij})(\hat{\mu}_j \cdot \hat{r}_{ij})$ , tends to make the dipoles align themselves and favors a head-to-tail “chain” structure. Since the second term has a three times bigger prefactor, it is easy to understand why the chain structure is most commonly observed in ferrofluids and other strongly interacting dipole fluids. Suppose we have two parallel dipoles whose positions are fixed along  $x$ -axis and make angle  $\theta$  with  $x$ -axis as in Fig. 5.2. The first term in Eq. (5.4) is fixed to unity while the second term changes as we vary the angle  $\theta$ . When  $\theta$  is small the dipole-dipole interaction is attractive, but above a certain angle,  $\theta_c$ , the interaction becomes repulsive. This angle satisfies

$$1 - 3 \cos^2 \theta_c = 0 \quad (5.12)$$

which yields  $\theta_c = \cos^{-1} \sqrt{1/3}$  or  $54.7^\circ$ . This effect will be seen again when we consider the breaking of the rings of these particles.

The formulation is exactly the same as for electrorheological fluids [TaoR94]. There the particles have electric dipole moments,  $\vec{p}_i$ , and are subject to an external electric field,  $\vec{E}$ . One simply needs to replace all  $\vec{\mu}_i$ 's with  $\vec{p}_i$ 's and  $\vec{B}$  with  $\vec{E}$ . But in this latter case, the electric dipole moments are not fixed, but rather induced by the applied field.

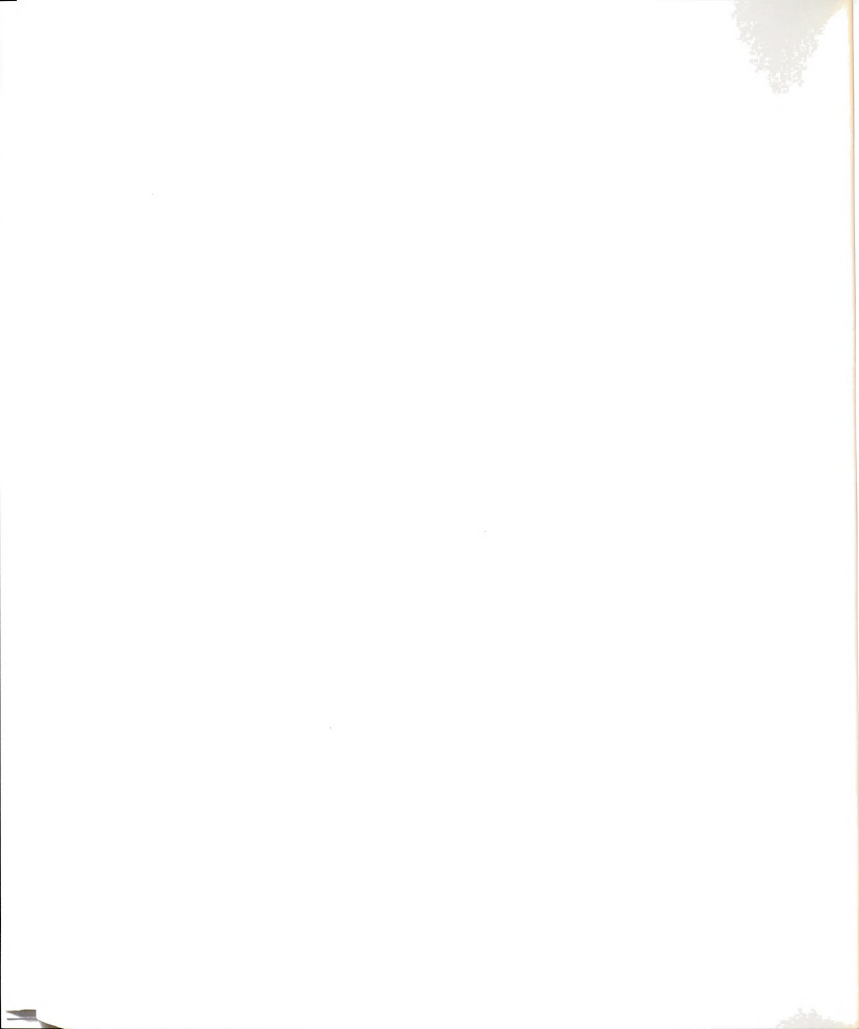
Table 5.1: Units and conversion factors of physical quantities related to the present model of ferrofluids.

Physical quantity	Symbol	Value
Length	$\tilde{\text{\AA}}$	100 $\text{\AA}$
Mass	$a\tilde{m}u$	$10^6$ amu
Energy	$e\tilde{V}$	$10^{-4}$ eV
Time	$\tilde{S} = \tilde{\text{\AA}}\sqrt{a\tilde{m}u/e\tilde{V}}$	$1.02 \times 10^{-7}$ S
Magnetic moment	$\tilde{\mu}_B$	$1.3647 \times 10^3 \mu_B$
Magnetic Field	$\tilde{G}$	12.6592 G
Temperature	$\tilde{K}$	1.16049 K
Dipole-dipole energy	$\tilde{\mu}_B^2/\tilde{\text{\AA}}^3$	$e\tilde{V}$
Dipole-field energy	$\tilde{\mu}_B\tilde{G}$	$e\tilde{V}$
Thermal energy	$k_B\tilde{K}$	$e\tilde{V}$



Table 5.2: Physical parameters and typical values of some quantities used in ferrofluid study.

Physical quantity	Symbol	Value
Length	$\sigma$	1.0 Å
Mass	$m$	1.64 a.m.u
Magnetic Field	B	10.0 G
Magnetic moment	$\mu_0$	15.388 $\mu_B$
Dipole-dipole energy	$\mu_0^2/\sigma^3$	236.8 eV
Dipole-field energy	$\mu_0 B$	153.88 eV
Soft-core energy	$\epsilon$	20.0 eV
Soft-core repulsion range	$\rho_1$	2.5 Å
Soft-core attractive range	$\rho_2$	5.0 Å



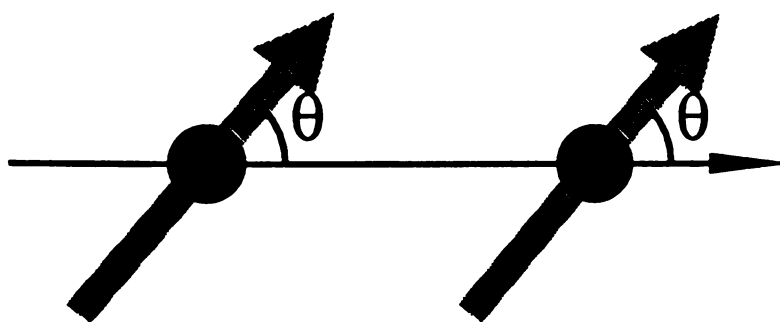


Figure 5.2: Two dipoles on  $x$ -axis.

### 5.3 Molecular dynamics of spherical tops

Since we are modeling ferrofluid particles by spheres carrying a dipole moment each particle has not only positional coordinates, but also orientational coordinates. The former set of coordinates is very common in any molecular dynamics simulation, but the latter requires some careful considerations[Alle90]. The orientation of a rigid body specifies the relation between an axis system fixed in space and one fixed in that body. Usually the ‘principal’ body-fixed system in which the inertia tensor is diagonal is chosen. In our case we choose the third axis along the dipole moment and the other two axes on the sphere’s equator plane. Any unit vector  $\vec{e}$  may be expressed in terms of its components in body-fixed or space-fixed frames: we thus use the notation  $\vec{e}^b$  and  $\vec{e}^s$ , respectively. The rotation matrix  $A$  relates these components by

$$\vec{e}^b = A \cdot \vec{e}^s. \quad (5.13)$$

The nine components of the rotation matrix are the direction cosines of the body-fixed axis vectors in the space-fixed frame, and they completely define the molecular orientation. In fact there is substantial redundancy in this formula: only three independent quantities (generalized coordinates) are needed to define  $A$ . These are generally taken to be the Euler angles  $\phi\theta\psi$  in a suitable convention (See Fig. 5.3 and [Gold80]). Then,

$$A = \begin{pmatrix} \cos \phi \cos \psi - \sin \phi \cos \theta \sin \psi & \sin \phi \cos \psi + \cos \phi \cos \theta \sin \psi & \sin \theta \sin \psi \\ -\cos \phi \sin \psi - \sin \phi \cos \theta \cos \psi & -\sin \phi \sin \psi + \cos \phi \cos \theta \cos \psi & \sin \theta \cos \psi \\ \sin \phi \sin \theta & -\cos \phi \sin \theta & \cos \theta \end{pmatrix} \quad (5.14)$$

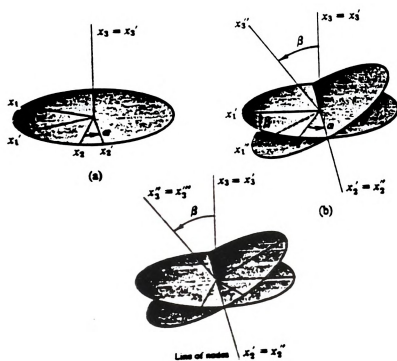
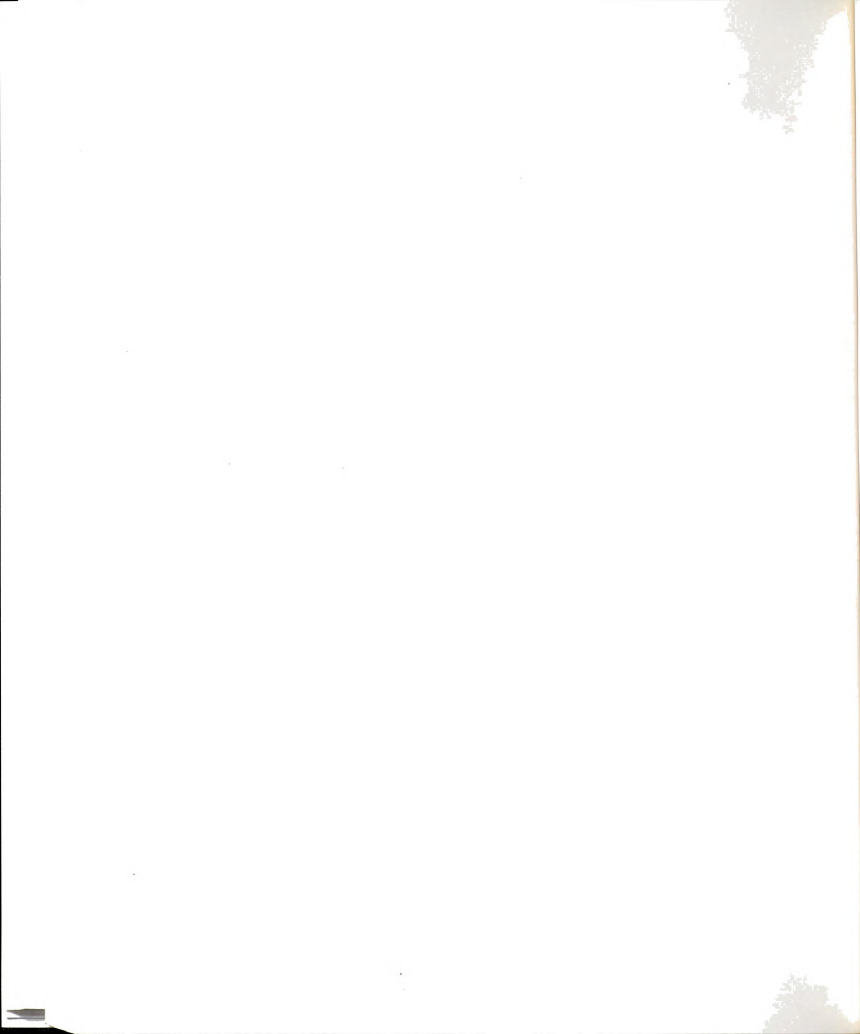


Figure 5.3: Definition of Euler angles.



Clearly, if  $\vec{e}$  is a vector fixed in the particle body-frame (such as the dipole moment vector), then  $\vec{e}^b$  will not change with time. In space-fixed coordinates, though, the components of  $\vec{e}^s$  will vary. This is a special case of the general equation linking time derivatives in the two coordinate systems[Gold80]

$$\dot{\vec{e}}^s = \dot{\vec{e}}^b + \vec{\omega}^s \times \vec{e}^s = \vec{\omega}^s \times \vec{e}^s. \quad (5.15)$$

The time derivative of the angular velocity vector  $\vec{\omega}$  is dictated by the torque  $\vec{n}$  acting on the dipole. Although the torque is most easily evaluated in space-fixed axes, it is most convenient to make the connection with  $\vec{\omega}$ , via the angular momentum  $\vec{l}$ . We use the Newtonian equation

$$\dot{\vec{l}}^s = \vec{n}^s \quad (5.16)$$

and obtain, after applying Eq. (5.15), the expression

$$\dot{\vec{l}}^s = \dot{\vec{l}}^b + \vec{\omega}^s \times \vec{l}^s \quad (5.17)$$

or

$$\dot{\vec{l}}^b + \vec{\omega}^b \times \vec{l}^b = \vec{n}^b. \quad (5.18)$$

Eq. (5.18) is thus the appropriate form of the Newtonian equation of motion relative to the body axes. The  $i$ th component of Eq. (5.18) can be written as

$$\dot{l}_i + \epsilon_{ijk} \omega_j l_k = n_i, \quad (5.19)$$

(Repeated indices imply summation.)

where the "body" superscript has been dropped. If now the body axes are taken

as the principal axes relative to the reference point, then the angular momentum components are  $l_i = I_i \omega_i$ . Equation (5.19) then takes the form

$$I_i \dot{\omega}_i + \epsilon_{ijk} \omega_j \omega_k I_k = n_i, \quad (5.20)$$

since the principal moments of inertia are, of course, time independent. For spherical tops, such as our spherical dipole moments, all three principal moments of inertia have same values  $I$  and the cross product term in Eq. (5.20) yields

$$\dot{\vec{\omega}}^b = \vec{n}^b / I. \quad (5.21)$$

Conversion between the space-fixed and the body-fixed system is handled by the analogues of Eq. (5.13), i.e.

$$\vec{n}^b = \mathbf{A} \cdot \vec{n}^s \quad (5.22)$$

$$\vec{\omega}^s = \mathbf{A}^{-1} \cdot \vec{\omega}^b = \mathbf{A}^T \cdot \vec{\omega}^b \quad (5.23)$$

since the inverse of  $\mathbf{A}$  is its transpose. To complete the picture, we need an equation of motion for the particle orientation itself, i.e. for its rotation matrix  $\mathbf{A}$ . We may write down the equations of motion of the Euler angles [Gold80]

$$\begin{aligned} \dot{\phi} &= -\omega_x^s \frac{\sin \phi \cos \theta}{\sin \theta} + \omega_y^s \frac{\cos \phi \cos \theta}{\sin \theta} + \omega_z^s \\ \dot{\theta} &= \omega_x^s \cos \phi + \omega_y^s \sin \phi \\ \dot{\psi} &= \omega_x^s \frac{\sin \phi}{\sin \theta} - \omega_y^s \frac{\cos \phi}{\sin \theta}. \end{aligned} \quad (5.24)$$

These equations would apply to each dipole separately to obtain its own new rotation matrix  $\mathbf{A}$ . In principle, Eqs. (5.14) with (5.21)–(5.24), may be solved in a step-by-step fashion, just as we deal with translational equations of motion. They, however, suffer from a serious drawback. The presence of the  $\sin \theta$  terms





in Eqs. (5.24) means that a divergence occurs whenever  $\theta$  approaches 0 or  $\pi$ . The molecular motion is of course, unaffected when this occurs but, because of our choice of axes, the angles  $\phi$  and  $\psi$  become degenerate. Thus the equations of motion are unsatisfactory when written in this form. One way to cope with this would be to reduce the time step, so as to deal with the more rapidly varying quantities, whenever any molecule approached the critical values  $\theta \approx 0$  or  $\pi$ . This would be very expensive and awkward. A slightly more satisfactory solution was employed by Barojas, Levesque, and Quentrec[Baro73]: two alternative sets of space-fixed axes for each molecule were used, and whenever the angle in one system approached 0 or  $\pi$ , a switch over to the other set was made.

In recent years, a much more elegant and straightforward solution to the problem of divergence in the orientational equations of motion has been proposed. Recognizing that singularity-free equations could not be obtained in terms of three independent variables, Evans [Evan77a] suggested the use of four quaternion parameters as generalized coordinates. Quaternions fulfil the requirements of having well-behaved equations of motion. The four quaternions are linked by one algebraic equation, so there is just one 'redundant' variable. The basic simulation algorithm has been described by Evans and Murad[Evan77b]. In the following section, I will briefly summarize the theory of quaternion parameters adapted in our molecular dynamics simulations.

## 5.4 Quaternion molecular dynamics

The procedures to utilize the quaternion parameters in molecular dynamics has been summarized beautifully by M.P. Allen [Alle84].

A quaternion  $Q$  is a set of four scalar quantities, or a combination of a scalar and a three-component vector

$$Q = (q_0, q_1, q_2, q_3) = (q_0, \vec{q}). \quad (5.25)$$

The "quaternion product" of two quaternions  $P$  and  $Q$  is defined via the combination of the usual scalar product  $\vec{p} \cdot \vec{q}$  and vector product  $\vec{p} \times \vec{q}$  as

$$P \star Q = (p_0 q_0 - \vec{p} \cdot \vec{q}, p_0 \vec{q} + q_0 \vec{p} + \vec{p} \times \vec{q}). \quad (5.26)$$

One thing to note is that there is a sign mistake in Allen's definition [ Eq. (B2) in [Alle84]] which could confuse many readers. As I verified in Eq. [Evan77a] (5.26) is correct. Of course, the scalar product of two quaternions is still defined in the usual way

$$P \cdot Q = p_0 q_0 + \vec{p} \cdot \vec{q}. \quad (5.27)$$

The quaternion product is associative

$$P \star Q \star R = P \star (Q \star R) = (P \star Q) \star R, \quad (5.28)$$

but not commutative

$$P \star Q \neq Q \star P. \quad (5.29)$$

The conjugate of  $Q$  is defined as

$$\bar{Q} = (q_0, -\vec{q}), \quad (5.30)$$

so that

$$\bar{Q} \star Q = Q \star \bar{Q} = (|Q|^2, \vec{0}), \quad (5.31)$$

CONFIDENTIAL

NO-3-2000-000

where  $|Q|^2 = Q \cdot Q$  is the norm of  $Q$ . The quaternions of interest here satisfy the constraint

$$|Q|^2 = q_0^2 + q_1^2 + q_2^2 + q_3^2 = 1. \quad (5.32)$$

Therefore  $\tilde{Q}$  is the same as  $Q^{-1}$ , the inverse of  $Q$ , since the quaternion  $(1, \vec{0})$  acts as an identity element in the quaternion product. The way in which a quaternion with unit norm may represent the orientation of a rigid body is discussed in Sec. 4-5 of [Gold80]. For example, the transformation between body-fixed vectors  $\vec{r}^b$  and space-fixed vectors  $\vec{r}^s$  may be expressed as

$$R^b = \tilde{Q} \star R^s \star Q, \quad (5.33)$$

where  $R^b = (0, \vec{r}^b)$  and  $R^s = (0, \vec{r}^s)$ .

The equations of rotational motion for each particle are advantageously expressed in quaternion form as

$$\dot{Q} = \frac{1}{2} Q \star \Omega^b = \frac{1}{2} \Omega^s \star Q, \quad (5.34)$$

where  $\Omega^b = (0, \vec{\omega}^b)$  and  $\Omega^s = (0, \vec{\omega}^s)$ . Here,  $\vec{\omega}^b$  is the body-fixed,  $\vec{\omega}^s$  the space-fixed, angular velocity. For a spherical top, following Eq. (5.21), the angular velocities evolve according to

$$\dot{\Omega}^b = N^b/I \quad \text{or} \quad \dot{\Omega}^s = N^s/I, \quad (5.35)$$

where  $I$  is the moment of inertia,  $N^b = (0, \vec{n}^b)$ ,  $N^s = (0, \vec{n}^s)$ , and  $\vec{n}^b$  and  $\vec{n}^s$  are respectively the torque in the body-fixed and space-fixed frame.

These first-order differential equations can be integrated in time by various standard methods[Alle90]. But calculating the torque directly from the molecular



orientations is not simple when many dipole moments are present. It would be nice if we could express the torques in terms of a "quaternion gradient" of the potential energy. At this point, we will eliminate the angular velocities from these equations. Differentiating Eq. (5.34) with respect to time we get

$$\dot{\bar{Q}} = \frac{1}{2}\dot{Q} \star \Omega^b + \frac{1}{2}Q \star \dot{\Omega}^b. \quad (5.36)$$

Using Eq. (5.34) we note

$$\frac{1}{2}\Omega^b = \bar{Q} \star \dot{Q}. \quad (5.37)$$

Taking derivatives of both side of Eq. (5.31) and applying the quaternion product of  $\dot{Q} \star$  from the left, we get

$$\dot{Q} \star \bar{Q} \star \dot{Q} = -|\dot{Q}|^2 Q. \quad (5.38)$$

Combining these results we arrive at the second order differential equation

$$\ddot{Q} = -|\dot{Q}|^2 Q + \frac{1}{4}N/I, \quad (5.39)$$

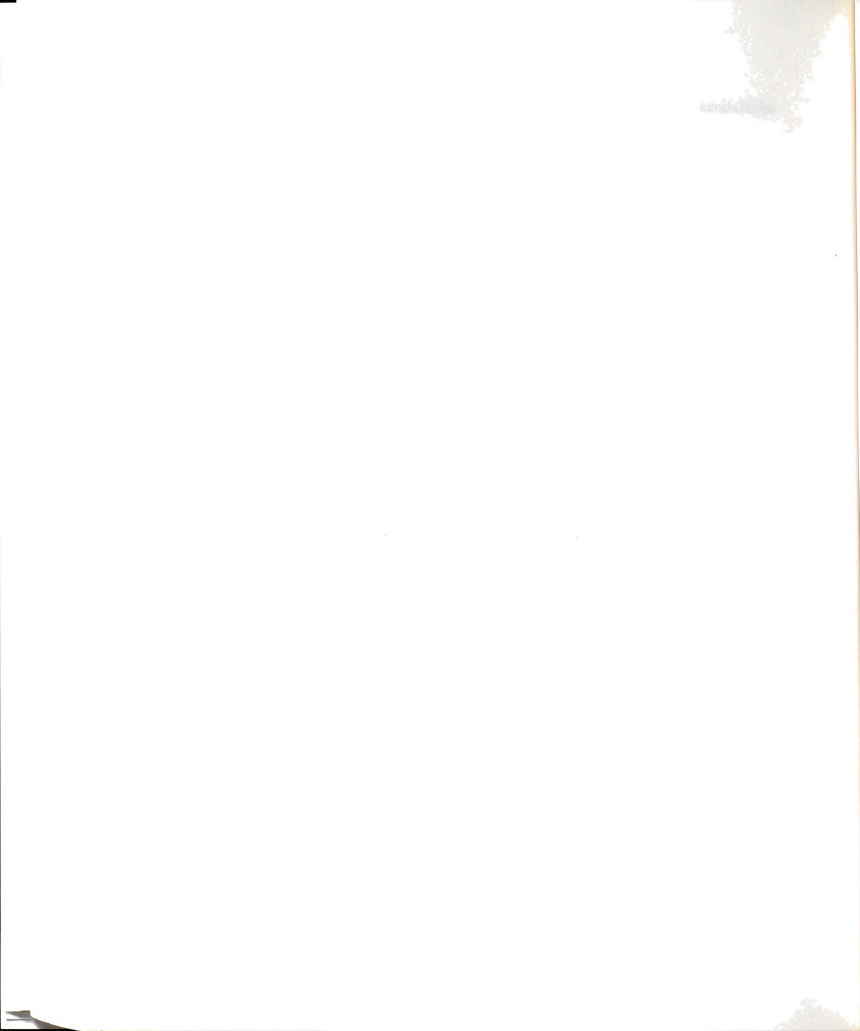
where

$$N = 2Q \star N^b = 2N' \star Q. \quad (5.40)$$

The elegant feature of this procedure is that  $N$  can be expressed directly in terms of quaternion parameters[Alle84]:

$$N = -(\partial U/\partial q_0, \partial U/\partial q_1, \partial U/\partial q_2, \partial U/\partial q_3). \quad (5.41)$$

Here  $U$  is the potential energy of the system as a function of the quaternion parameters of *all* the particles, and we differentiate with respect to the quaternions of the particle under consideration. These derivatives should really be taken





subject to the constraint, Eq. (5.32), but then it would be impractical to use Eq. (5.41) to solve the equation of motion. Fortunately, however, it is possible to treat the quaternions as independent parameters, and take unconstrained derivatives, if the consequent motion off the constant- $|Q|^2$  hypersurface is projected out. This correction should be performed at every step in the following procedure [Alle84]:

[Step 1] After calculating  $N$  from Eq. (5.41), we subtract the quantity  $(Q \cdot N)Q$ , which yields

$$N' = N - (Q \cdot N)Q. \quad (5.42)$$

[Step 2] Using  $N'$  obtained in [Step 1], calculate  $N^b$  or  $N^s$  from Eq. (5.40)

$$N^b = \frac{1}{2}\tilde{Q} \star N' \quad \text{or} \quad N^s = \frac{1}{2}N' \star \tilde{Q}. \quad (5.43)$$

These quantities are used in Eq. (5.35) to get new  $\dot{\Omega}^b$  or  $\dot{\Omega}^s$ .

[Step 3] Advance  $\Omega^b$  or  $\Omega^s$  one time step to get their new values, using the result of [Step 2].

[Step 4] After calculating  $\dot{Q}$  from Eq. (5.34), the quantity  $(Q \cdot \dot{Q})Q$  is subtracted, yielding

$$\dot{Q}' = \dot{Q} - (Q \cdot \dot{Q})Q. \quad (5.44)$$

[Step 5] Advance  $Q$  one time step using  $\dot{Q}'$  obtained in [Step 4] to get new quaternion parameters.

[Step 6] Renormalize this new  $Q$  to have unit norm.



Note that after these corrections  $N'$  and  $\dot{Q}'$  are perpendicular to  $Q$ , yielding

$$\begin{aligned} Q \cdot N' &= 0 \\ Q \cdot \dot{Q}' &= 0, \end{aligned} \tag{5.45}$$

so that

$$Q \cdot \ddot{Q}' = -|\dot{Q}'|^2. \tag{5.46}$$

In the above procedure, the [Step 1], [Step 4] and [Step 6] are the critical steps to keep our quaternion parameters on the constant- $|Q|^2$  hypersurface. We can understand this more clearly by expanding  $Q$  over the time domain. Suppose that we have normalized  $Q$  at time  $t$ ,

$$|Q(t)|^2 = 1. \tag{5.47}$$

At time  $t + \delta t$ ,

$$Q(t + \delta) = Q(t) + \dot{Q}'(t)\delta t + \frac{1}{2}\ddot{Q}'(t)\delta t^2 + \mathcal{O}(\delta t^3). \tag{5.48}$$

The the norm of  $Q$  becomes

$$\begin{aligned} |Q(t + \delta t)|^2 &= |Q(t)|^2 + 2Q(t) \cdot \dot{Q}'(t)\delta t + |\dot{Q}'(t)|^2\delta t^2 + Q \cdot \ddot{Q}'\delta t^2 + \mathcal{O}(\delta t^3) \\ &= 1 + \mathcal{O}(\delta t^3). \end{aligned} \tag{5.49}$$

Thus previous correction procedures guarantee us conservation of the norm of  $Q$  up to the second order in  $\delta t$  without renormalizing.

Another important reason to implement this correction comes from the self-consistency of the formalism. By definition, the 0-th (or "scalar") component [See



definition in Eq. (5.25)] of  $N^b$  or  $N^s$  should vanish. From Eqs. (5.42) and (5.43)

$$\begin{aligned} N^s &= \frac{1}{2}[N \star \tilde{Q} - (Q \cdot N)Q \star \tilde{Q}] \\ &= \frac{1}{2}[N \star \tilde{Q} - (Q \cdot N)(1, \vec{0})]. \end{aligned} \quad (5.50)$$

Recalling the definition of  $\tilde{Q}$ , we can easily show that the 0-th component of  $N^s$  vanishes. Furthermore we need to note that the correction [Step 1] not only eliminates the 0-th component of  $N^s$  but also it is the only modification it makes as far as  $N^s$  is concerned. Thus we could skip the correction [Step 1] and do the [Step 2] and simply discard the 0-th component of  $N^b$  or  $N^s$ . A similar argument can be used to show that the correction [Step 4] eliminates the 0-th component of  $\Omega^b$  or  $\Omega^s$  if we have to calculate them by inverting Eq. (5.34) to

$$\Omega^b = 2\tilde{Q} \star \dot{Q}' \quad \text{or} \quad \Omega^s = 2\dot{Q}' \star \tilde{Q}. \quad (5.51)$$

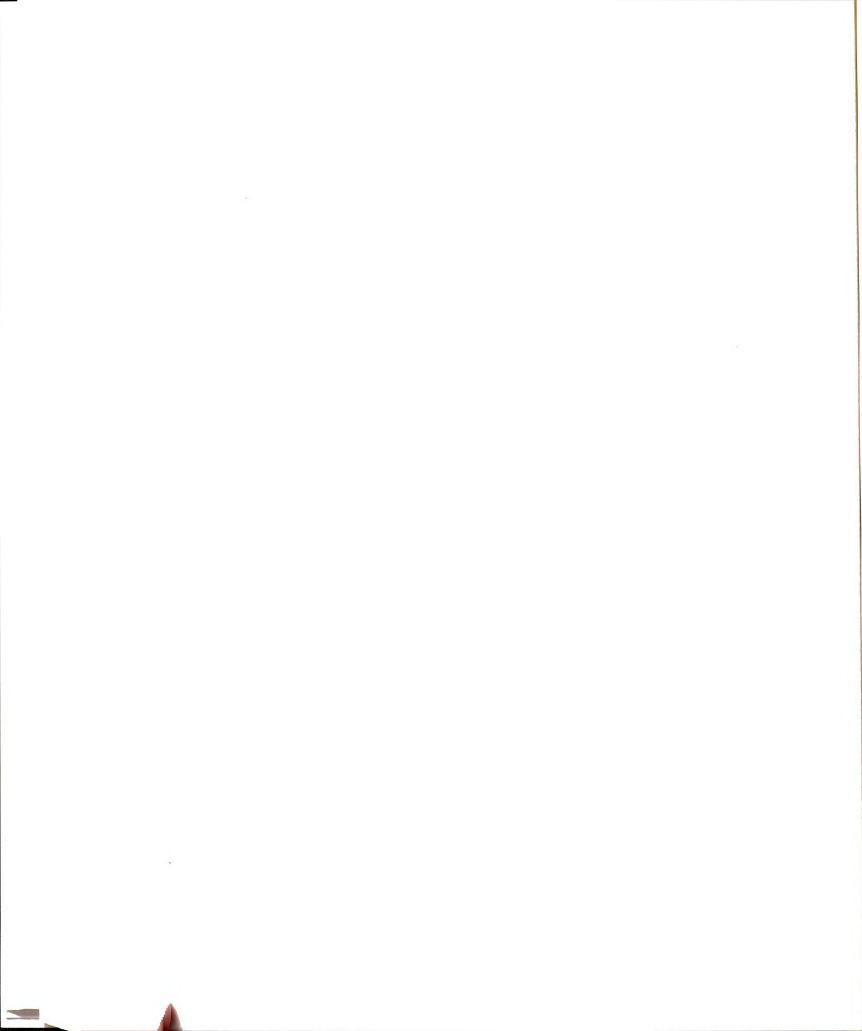
In the Euler angle convention of Fig. 5.3 and Eq. (5.14), it is most convenient to define

$$\begin{aligned} q_0 &= \cos \frac{1}{2}\theta \cos \frac{1}{2}(\phi + \psi) \\ q_1 &= \sin \frac{1}{2}\theta \cos \frac{1}{2}(\phi - \psi) \\ q_2 &= \sin \frac{1}{2}\theta \sin \frac{1}{2}(\phi - \psi) \\ q_3 &= \cos \frac{1}{2}\theta \sin \frac{1}{2}(\phi + \psi). \end{aligned} \quad (5.52)$$

Then the rotation matrix becomes

$$A = \begin{pmatrix} q_0^2 + q_1^2 - q_2^2 - q_3^2 & 2(q_1q_2 + q_0q_3) & 2(q_1q_3 - q_0q_2) \\ 2(q_1q_2 - q_0q_3) & q_0^2 - q_1^2 + q_2^2 - q_3^2 & 2(q_2q_3 + q_0q_1) \\ 2(q_1q_3 + q_0q_2) & 2(q_2q_3 - q_0q_1) & q_0^2 - q_1^2 - q_2^2 + q_3^2 \end{pmatrix}, \quad (5.53)$$

which is obtained by converting Eq. (5.33) into matrix equation. Similarly the



equation of motion for quaternions for each particle, Eq. (5.34), can also be converted to the simple matrix equation

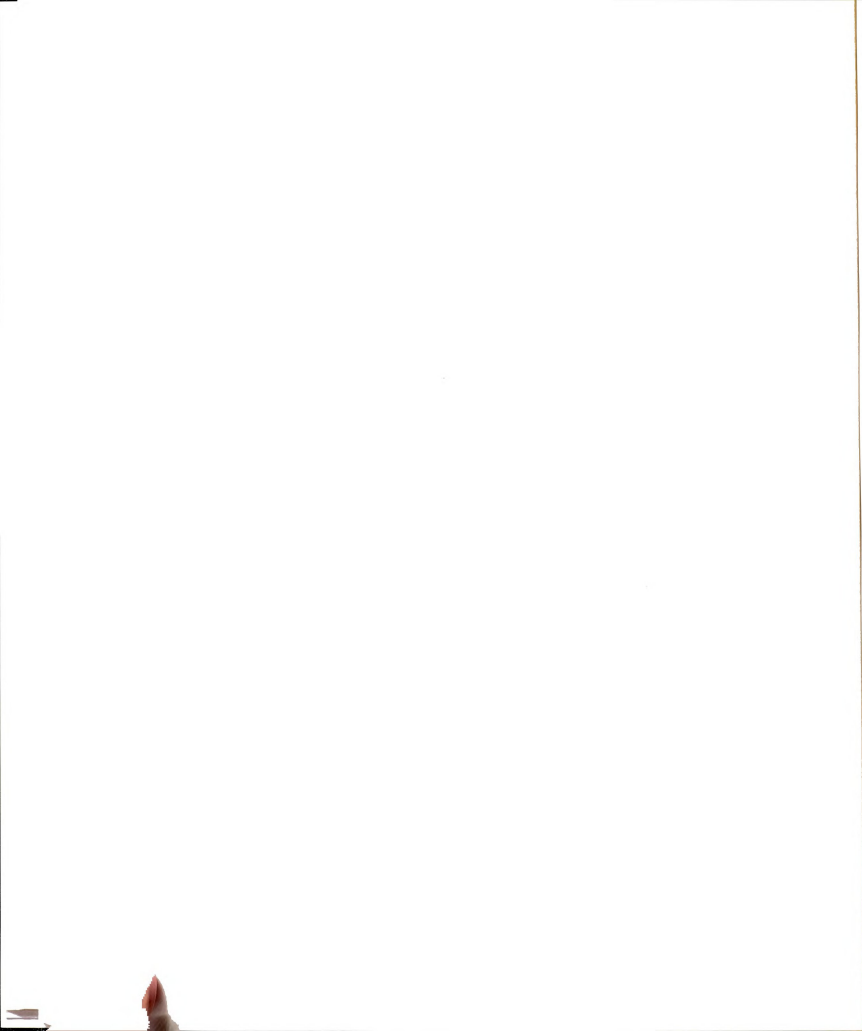
$$\begin{pmatrix} \dot{q}_0 \\ \dot{q}_1 \\ \dot{q}_2 \\ \dot{q}_3 \end{pmatrix} = \frac{1}{2} \begin{pmatrix} q_0 & -q_1 & -q_2 & -q_3 \\ q_1 & q_0 & -q_3 & q_2 \\ q_2 & q_3 & q_0 & -q_1 \\ q_3 & -q_2 & q_1 & q_0 \end{pmatrix} \begin{pmatrix} 0 \\ \omega_x^b \\ \omega_y^b \\ \omega_z^b \end{pmatrix}. \quad (5.54)$$

As we expected, the equations of motion, Eq. (5.54) with Eq. (5.21), contains no unpleasant singularities, if the transformation matrix (5.53) is used, to transform between space-fixed and body-fixed coordinates.

## 5.5 Rings and chains

Fig. 5.4 depicts the structure of a chain and ring of 10 magnetic dipoles. The directions of magnetic dipoles are represented by two hemispheres. Blue (dark) and orange (light) color represents the north and south pole of the dipoles, respectively.

Due to the dipole-dipole interaction, described in Eq. (5.4), the magnetic dipoles want to align. For a small number of dipoles in the absence of external field, a chain structure is the most stable configuration. As the number of dipoles increases, ring configurations become more favorable over chains, since the increase of the energy due to bending of the aligned dipoles will be more than compensated by joining two ends. The potential energy per particle for the chain (open diamond) and ring (solid square) configuration as a function of the number of the magnetic dipoles is plotted in Fig. 5.5. Each energy is obtained as a result of complete structure optimization using the conjugate gradient (CG) method [Pres86]. There is no external field applied. We note that for the number





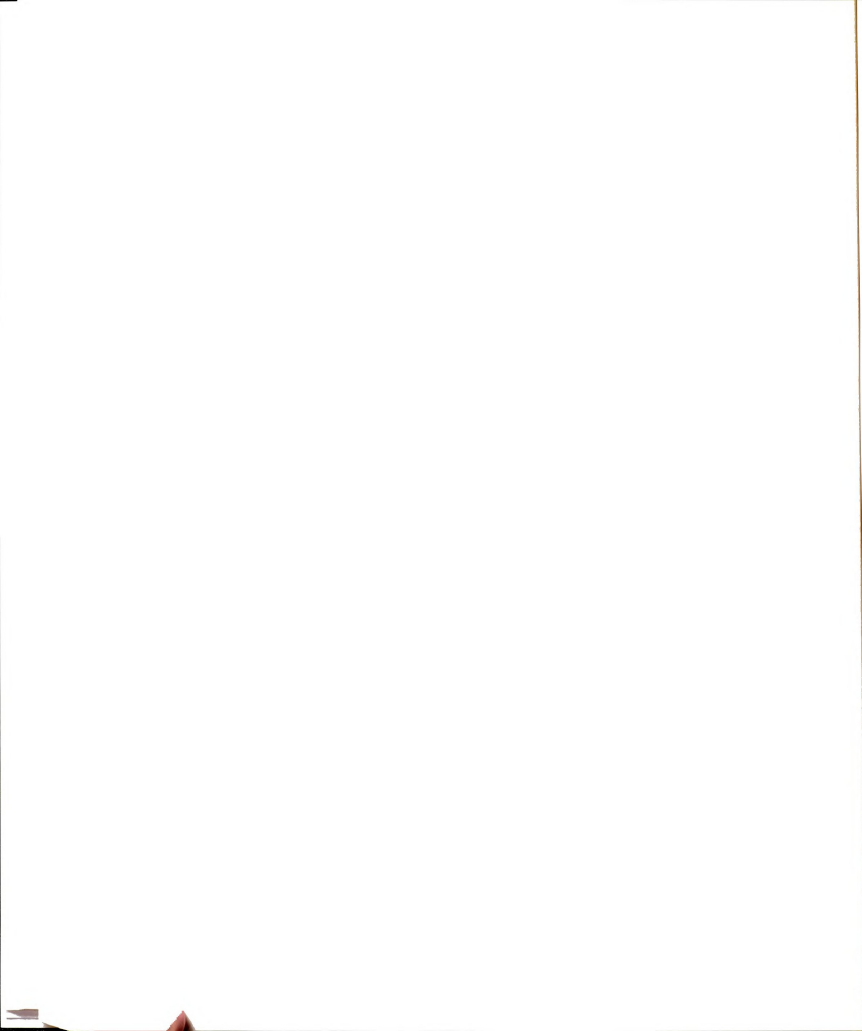
(a)



(b)



Figure 5.4: 10 ferromagnetic spheres in a (a) chain and (b) ring structure. The directions of magnetic dipoles are represented by two hemispheres. Blue (dark) and orange (light) color represents the north and south pole of the dipoles, respectively.



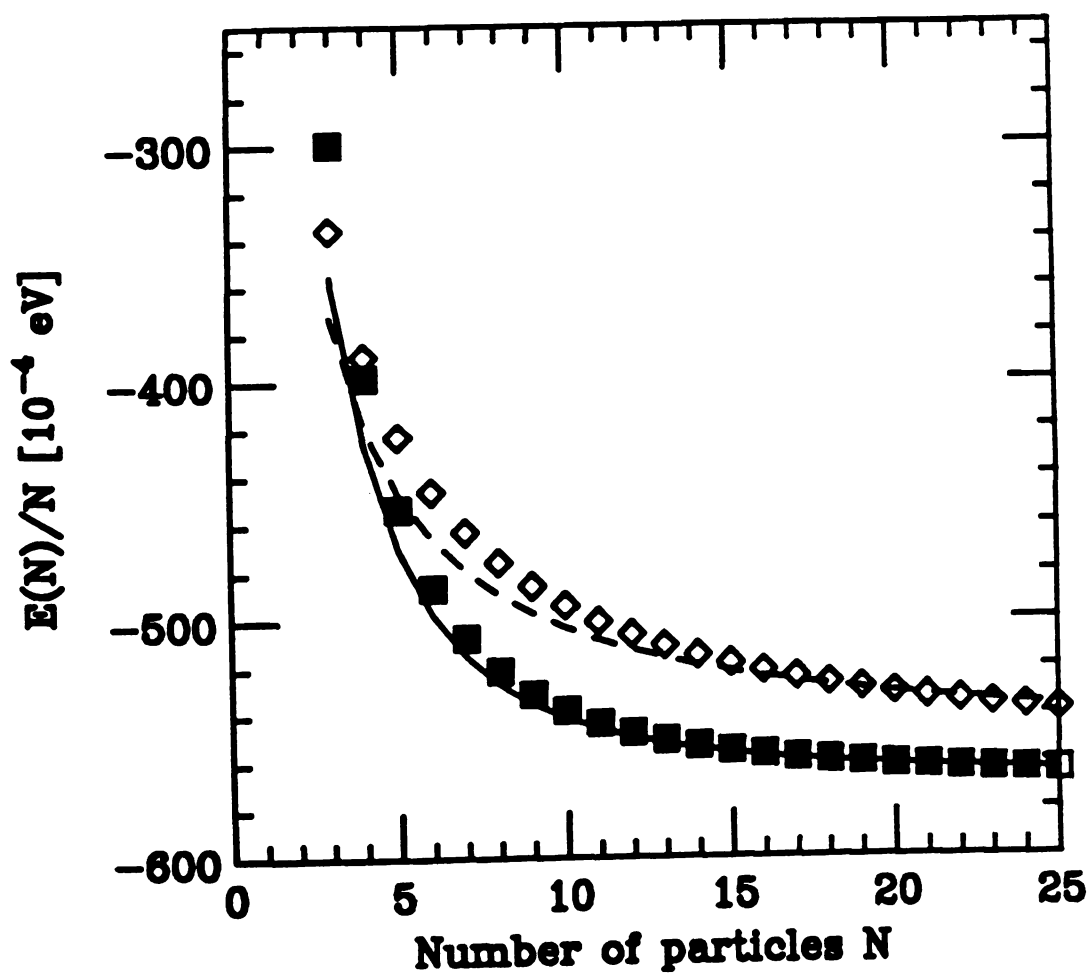


Figure 5.5: Energy per particle of a chain (open diamond) and a ring (solid square) of magnetic dipoles as a function of the number of particles in the absence of external field. The solid and dotted lines are the predictions from Eq. (5.61) and Eq. (5.62), respectively, with  $\alpha_r=1.20$  and  $\alpha_c=1.18$ .



of dipoles,  $N$  is bigger than 4, rings are always more stable than chains. The more dipoles are in the ring, the smaller is the bending angle and energy. It also should be noted that the difference in energy is maximum around  $N \simeq 9$  and is getting smaller as  $N$  increases. This behaviour can be understood easily with very simple arguments. Consider a  $N$  dipoles ring as in Fig. 5.6. Since we have  $N$  dipoles, the angle between two neighboring dipoles is

$$\theta = 2\pi/N \quad (5.55)$$

From the figure we can easily see that neighboring dipole 1 and 2

$$\begin{aligned} \hat{\mu}_1 \cdot \hat{\mu}_2 &= \cos \theta \\ \hat{\mu}_1 \cdot \hat{r}_{12} &= \cos \frac{1}{2}\theta \\ &= \hat{\mu}_2 \cdot \hat{r}_{12} \end{aligned} \quad (5.56)$$

and the dipole-dipole interaction between them is

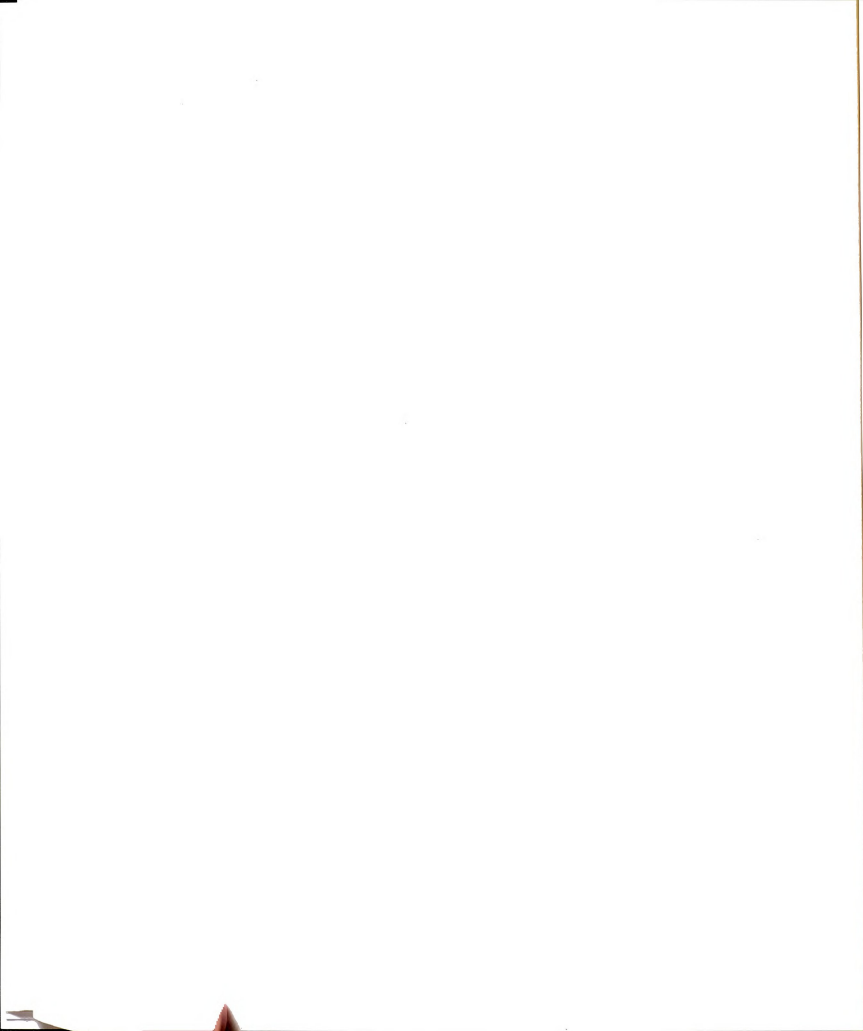
$$U_{12}(\theta) = -2 \frac{\mu_0^2}{d^3} \left( \frac{3 + \cos \theta}{4} \right) \quad (5.57)$$

We know that the distance between the dipoles  $d$  will change for each different  $N$  to minimize the energy. In our simple argument we assume that it is independent of particle number  $N$  and set to their diameter  $\sigma$ . Furthermore we will neglect the details of the higher-order neighbor interactions and simply say that the energy for  $N$  particle system is

$$U_{\text{ring}}(N) \simeq \alpha_r N U_{12}(\theta) \quad (5.58)$$

where  $\alpha_r$  is the constants to be determined and independent of  $N$  and contains the information on the soft-core potential. Thus the energy *per particle* becomes

$$\frac{U_{\text{ring}}(N)}{N} \simeq -2\alpha_r \frac{\mu_0^2}{\sigma^3} \left[ \frac{3 + \cos(2\pi/N)}{4} \right] \quad (5.59)$$



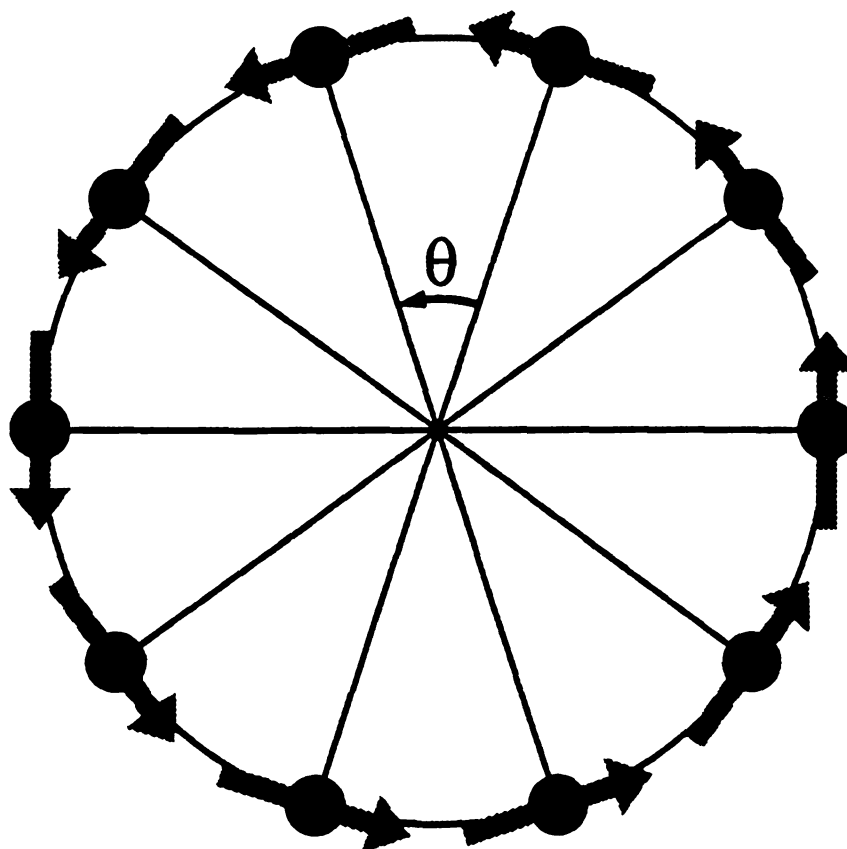
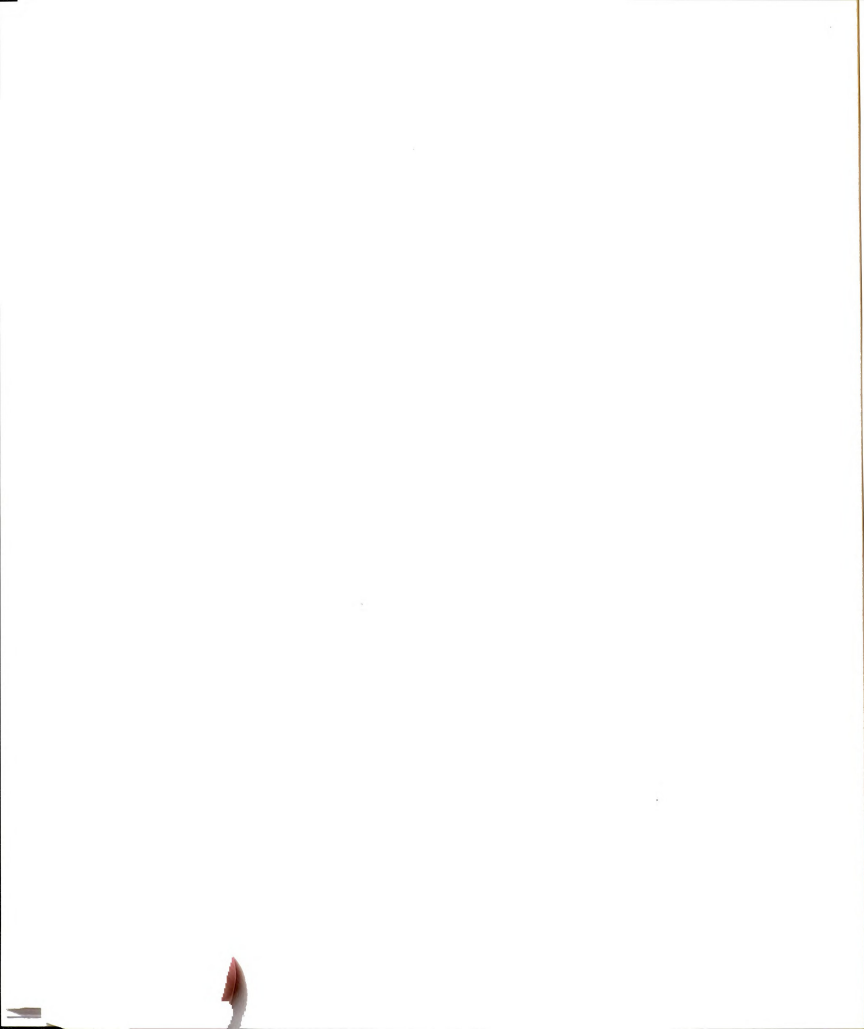


**Figure 5.6:** A vector representation of ring of 10 magnetic dipoles. The directions of magnetic dipoles are represented by the arrows.





and with similar arguments for linear chain

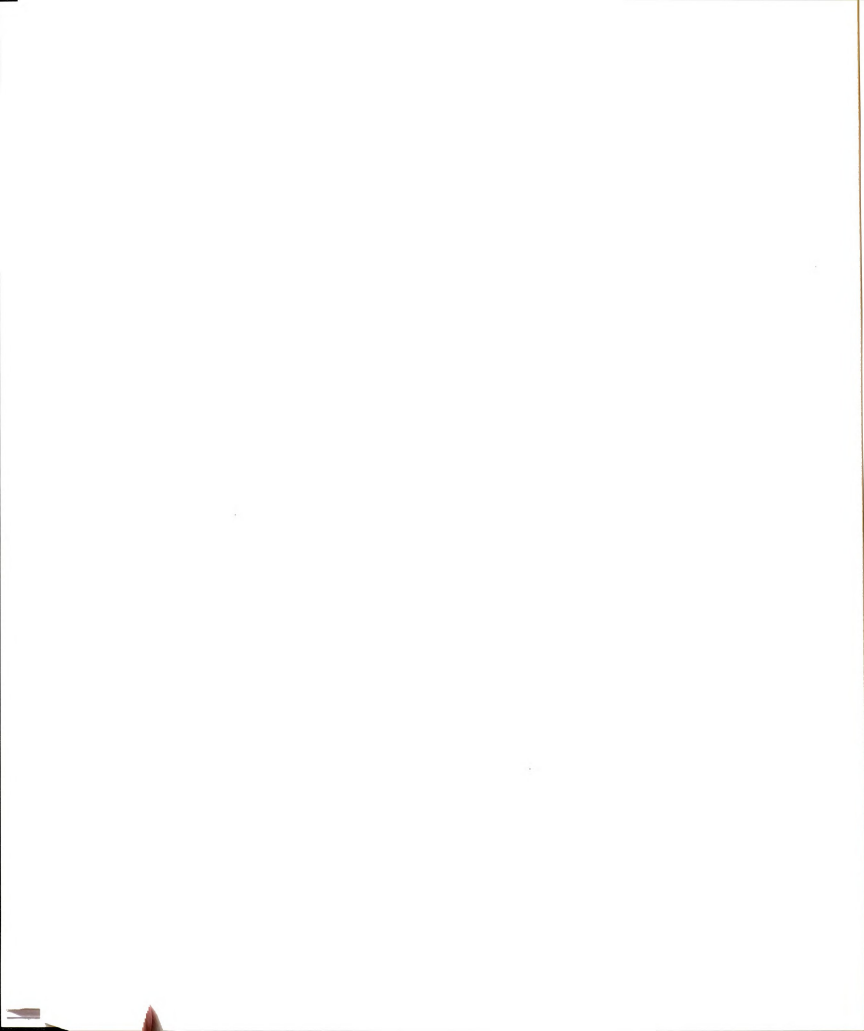
$$\begin{aligned}\frac{U_{\text{chain}}(N)}{N} &\simeq -2\alpha_c \frac{\mu_0^2}{\sigma^3} \frac{N-1}{N} \\ &= -2\alpha_c \frac{\mu_0^2}{\sigma^3} \left(1 - \frac{1}{N}\right)\end{aligned}\quad (5.60)$$

By matching the values from Eq. (5.59) and Eq. (5.60) to the ones obtained from full energy-optimized calculation at large  $N$ , say 25, we can set the values of  $\alpha_r$  and  $\alpha_c$ . The solid and dotted lines in Fig. 5.5 are the plots of Eq. (5.59) and Eq. (5.60) with  $\alpha_r=1.20$  and  $\alpha_c=1.18$ . The analytic curves represent the numerical data very well except a little deviation in small  $N$  region. This is a remarkable agreement, considering how simple and crude our arguments are. We may also notice that it even predicts correct  $N$  value to make the ring more stable, which is 4. Also from these analytic expression, we can get the scaling behaviour for large  $N$

$$\frac{U_{\text{ring}}(N)}{N} \simeq -2\alpha_r \frac{\mu_0^2}{\sigma^3} \left(1 - \frac{\pi^2}{2} \frac{1}{N^2} + \dots\right). \quad (5.61)$$

Thus the energy per particle for the ring decays as  $1/N^2$  while the energy per particle for the chain decays as  $1/N$ .

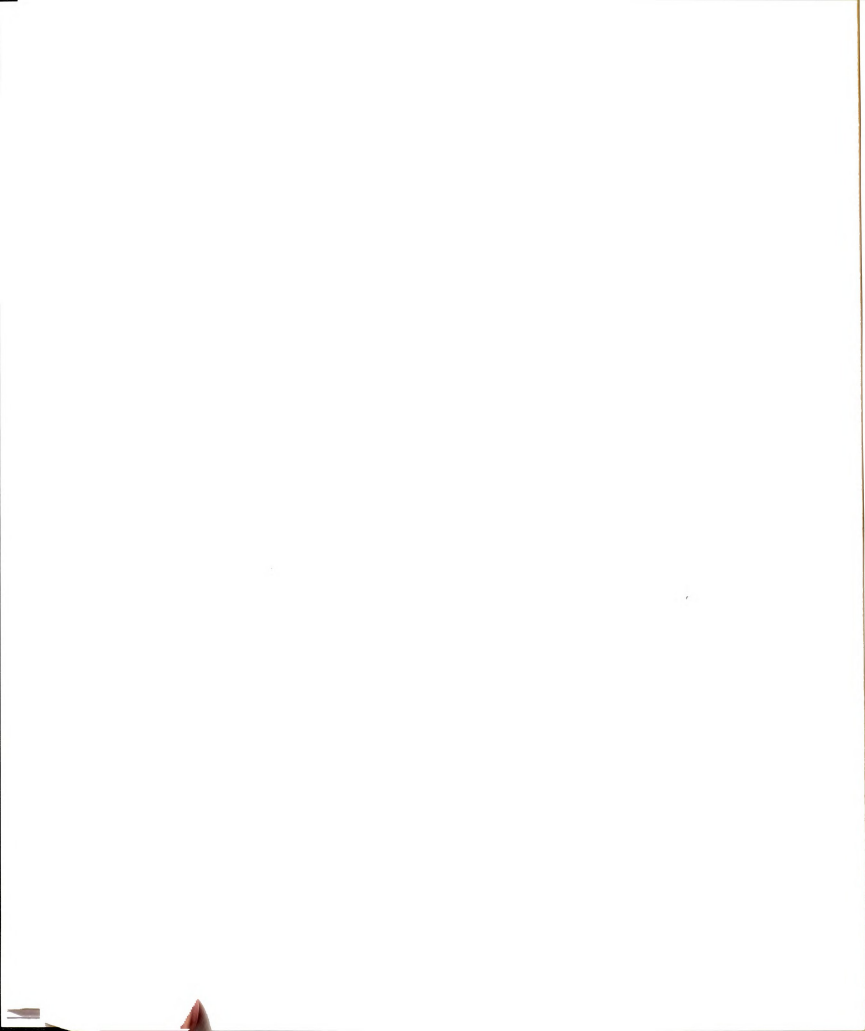
Now let us apply an external magnetic field to these systems. The chains will obviously align with the external field to minimize the energy. The behaviour of the ring is not very trivial when subject to an external field. They would like to align with the field but then half of them have to be “anti-parallel” to the field. This increases the total energy, resulting no net energy gain if they remain a perfect circle. The rings can gain energy slightly by distorting their structure from the perfect circle. Fig. 5.7(a) is a 20 particle ring forced to remain parallel to the field. The external field is applied horizontally and is represented by an arrow in the figure. We used the same coloring convention for the dipoles and the



field. The dipoles in Fig. 5.7(a) are allowed to adjust their positions in the plane of the ring. The ring makes an "egg-shape" which has a flatter side and a pointed tip. Having the flatter side makes the ring accommodate "more" dipoles parallel to the field. The pointed tip, however, costs a lot of energy because of the sharp turn of the dipole direction and becomes very vulnerable as the field increases. Above a certain critical magnetic field, this tip becomes too sharp and the ring can not support the stress any more. The ring breaks at this tip and becomes a chain or fragments to little pieces, depending on the surrounding medium.

It turned out, however, that the rings can stand much higher fields without breaking by being perpendicular to the field, as shown in Fig. 5.7(b). In the figure the field is pointing out of the paper, as represented by the head of the cylindrical arrow. It should be noted that their positions remain on a perfect circle, yet the dipoles show a tendency to align with the field. In figure, you see more blue (dark) colors for each sphere meaning that they are facing toward you. The decreasing dipole-dipole interaction within the ring is compensated by the field-dipole interactions. Above a certain critical field, these dipoles rotate sufficiently out of the ring plane to become nearly parallel to each other, and their mutual interaction vanishes. At this moment the ring flies apart into individual particles.

Therefore in the following discussions I will focus only on the chains parallel to the external field and rings perpendicular to the external field. The energies per particle of a chain and a ring of 10 dipoles are plotted in Fig. 5.8. As seen in Fig. 5.5, at zero field, the ring structure has the lower energy. As the field increases, the energy per dipole of the chain decreases linearly in the external field. In contrast to this, the energy per dipole of the ring structure remains almost



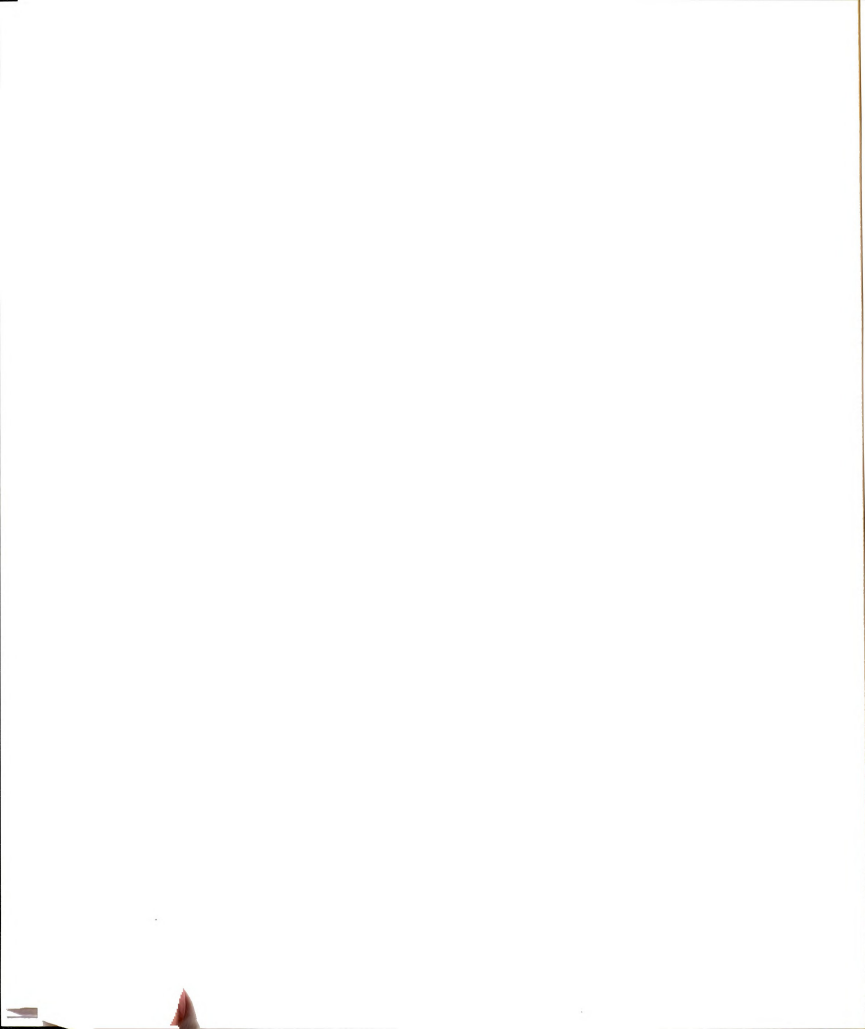
(a)



(b)



Figure 5.7: Rings of 20 magnetic dipoles in an external field which is (a) parallel (300 G) and (b) perpendicular (500 G) to the ring plane. The external field is represented by the arrows, and has the same coloring convention as the magnetic dipoles, used in Fig. 5.4.



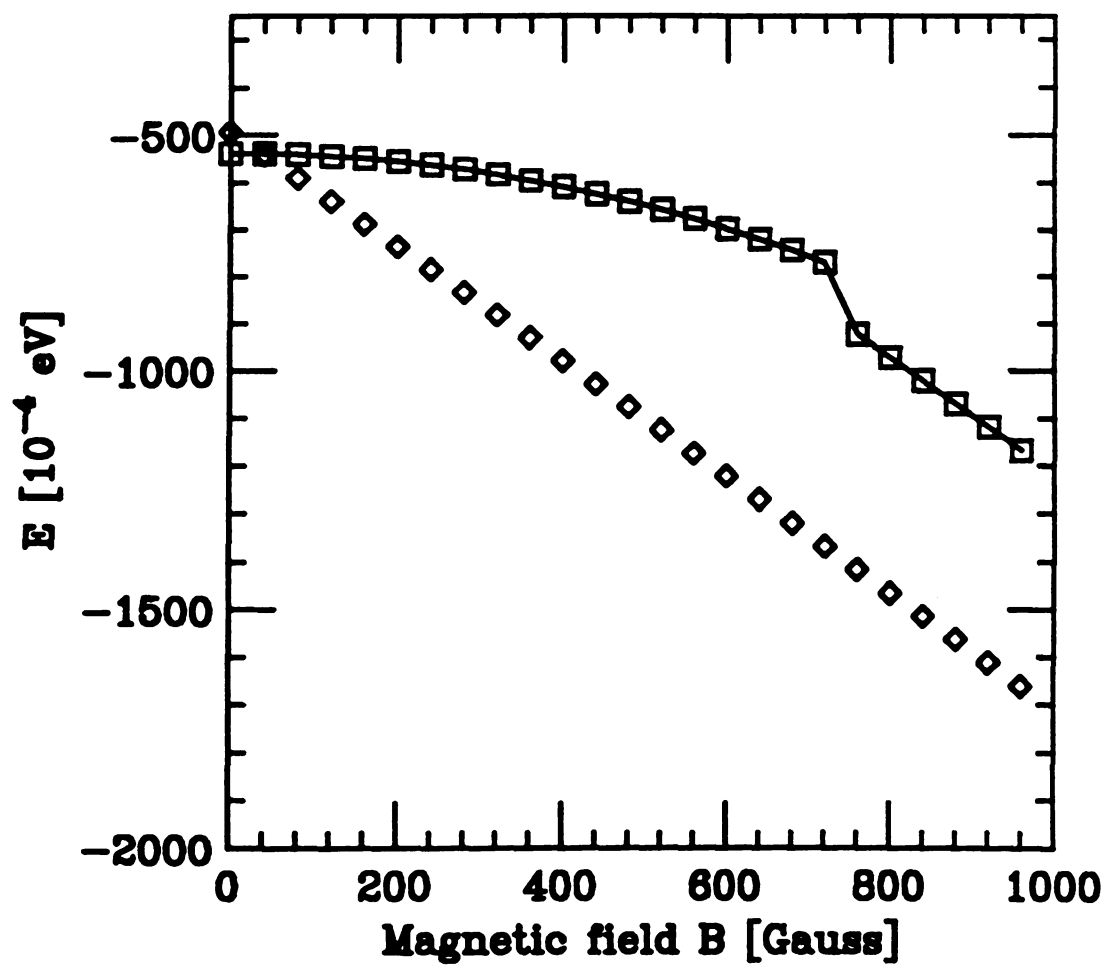


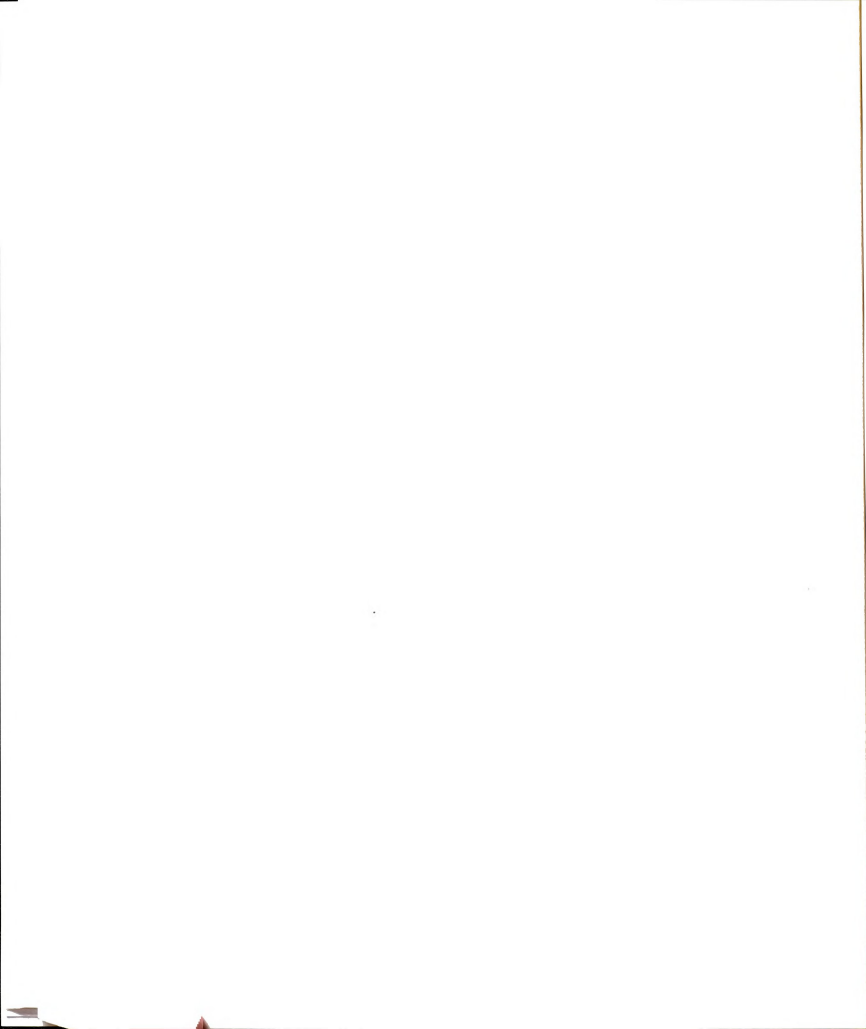
Figure 5.8: Energy per particle of a chain (open diamonds) and a ring (solid squares) of 10 magnetic dipoles as a function of the external field.





constant at low fields and decreases very slowly at higher fields. At a relatively low field value, about 37 G for  $N = 10$ , these two curves cross and the chain structure becomes energetically more favorable. Once the ring structure is formed, however, the ring does not break into a chain at this external field. The ring is in a local energy minimum in the multi-dimensional coordinates space and there is an activation barrier to overcome. We can go over this barrier dynamically by pumping energy into the system and increase the kinetic energies of the particles. When the added total energy added exceeds the height of the barrier, the system will find the saddle point in phase space and move into the lower minimum. This is the subject I discuss in following sections using the molecular dynamics study. The alternative way of finding the lower (local) energy minimum is to lower the barrier by changing the external field. When we increase the external field, we are changing the contour of the energy surface in multi-dimensional coordinates space. Increasing the magnetic field will lower the energy barrier for a certain geometry, which will result in a saddle point pathway leading from the higher local energy minimum of ring structure to the lower energy minimum of chain structure. For 10 dipoles ring, this energy barrier is removed at external fields exceeding 750 G, as shown in Fig. 5.8.

Therefore, from Fig. 5.8 and the preceeding arguments we can define two critical fields for the rings of a given number of dipoles. The lower critical field,  $B_{c1}$ , is the field above which a chain becomes energetically more favorable. The upper critical field,  $B_{c2}$ , is the field at which the energy barrier between the chain and ring structure disappears. Fig. 5.9 is the plot of  $B_{c1}$  for a given magnetic field. The results obtained from conjugate gradient method (squares) are compared with



the analytic predictions (curve) using Eq. (5.59) and Eq. (5.60)

$$\begin{aligned}\mu_0 B_{c1} &= \frac{U_{\text{chain}}(N)}{N} - \frac{U_{\text{ring}}(N)}{N} \\ &\simeq 2 \frac{\mu_0^2}{\sigma^3} \left[ (\alpha_r - \alpha_c) + \frac{\alpha_c}{N} + \alpha_r \frac{\cos(2\pi/N) - 1}{4} \right].\end{aligned}\quad (5.62)$$

And for large  $N$

$$\mu_0 B_{c1} \simeq 2 \frac{\mu_0^2}{\sigma^3} \left[ (\alpha_r - \alpha_c) + \frac{\alpha_c}{N} - \frac{\alpha_r \pi^2}{2N^2} + \dots \right]. \quad (5.63)$$

This analytic expression predicts correct  $1/N$  scaling behaviour for large  $N$  and even predicts correct  $N$  to have maximum  $B_{c1}$ , which is 9. Fig. 5.10 is the plot of  $B_{c2}$  for a given magnetic field obtained from conjugate-gradient energy optimization.  $B_{c2}$  is related to the height  $E^*$  of the barrier between the minimum energy configuration for the ring and that of chain. We can estimate  $E^*$  using

$$E^* \sim \mu_0 B_{c2}, \quad (5.64)$$

as the amount of energy needed to break a ring into a chain or another lower symmetry structure in the absence of the external field. One thing to note is that these estimates are the result of straight energy minimization calculations with absolutely no dynamics. In next Section we will consider the stability of dipole rings with the full dynamics.

## 5.6 Molecular dynamics study

We studied the stability of the magnetic dipoles by considering the ground state energies of ring and chain structure. This study, however, only gives the estimation of the energy barrier in zero field. If we want to know the stability of the ring for



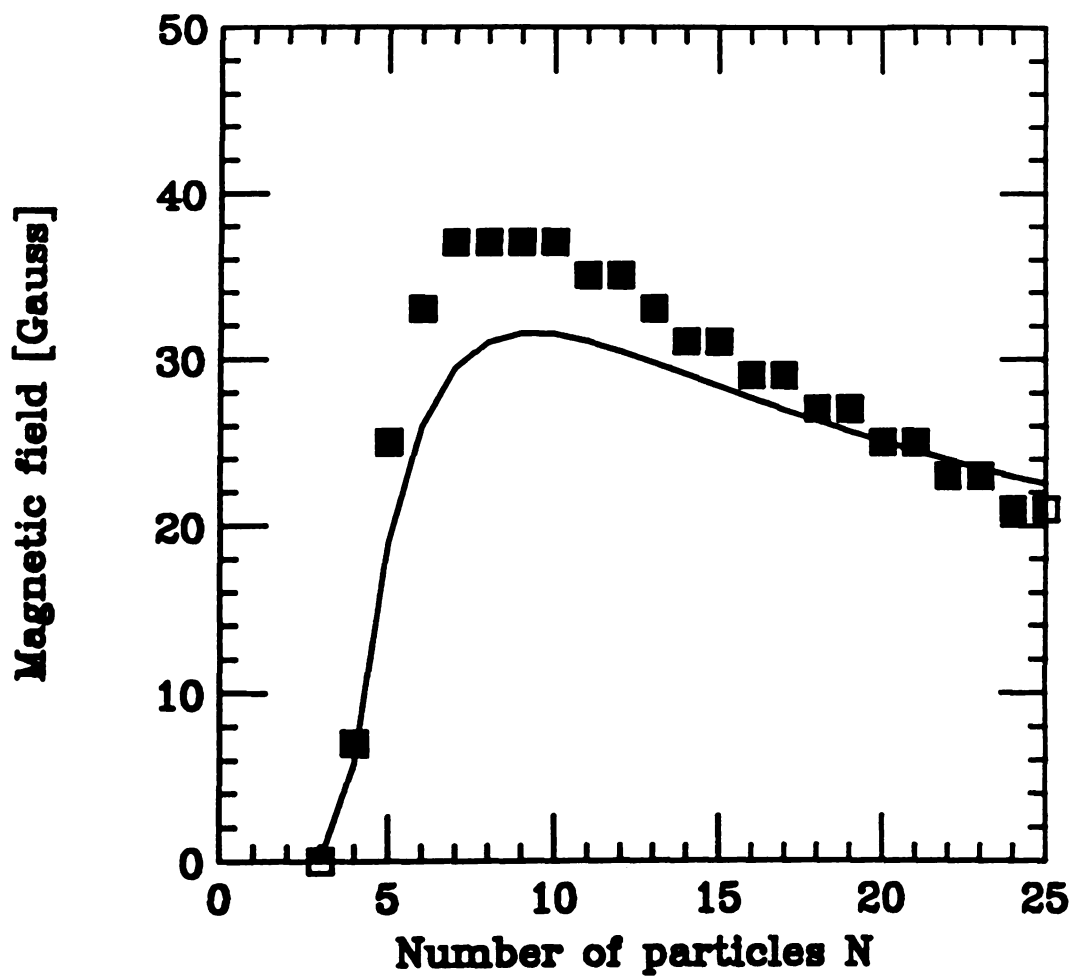
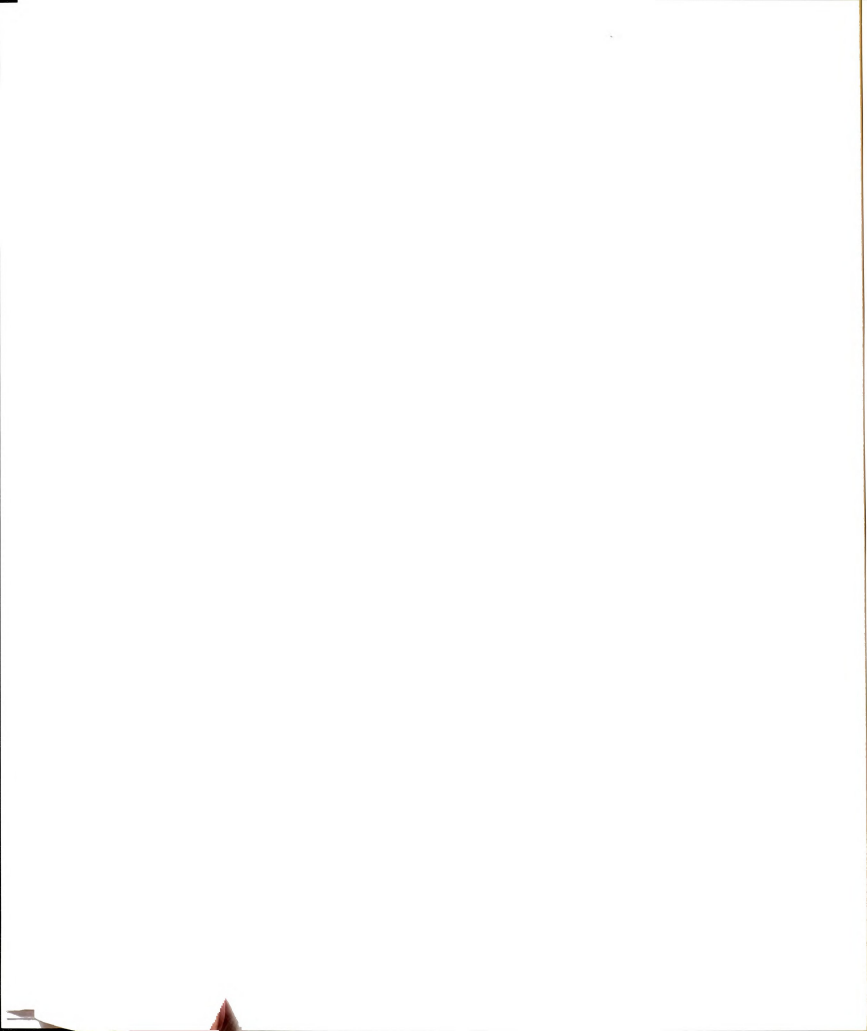


Figure 5.9: Lower ( $B_{c1}$ ) critical field for magnetic dipole rings as a function of the number of particles. Results from energy minimization (squares) are compared to analytic expression (curve) from Eq. (5.62).



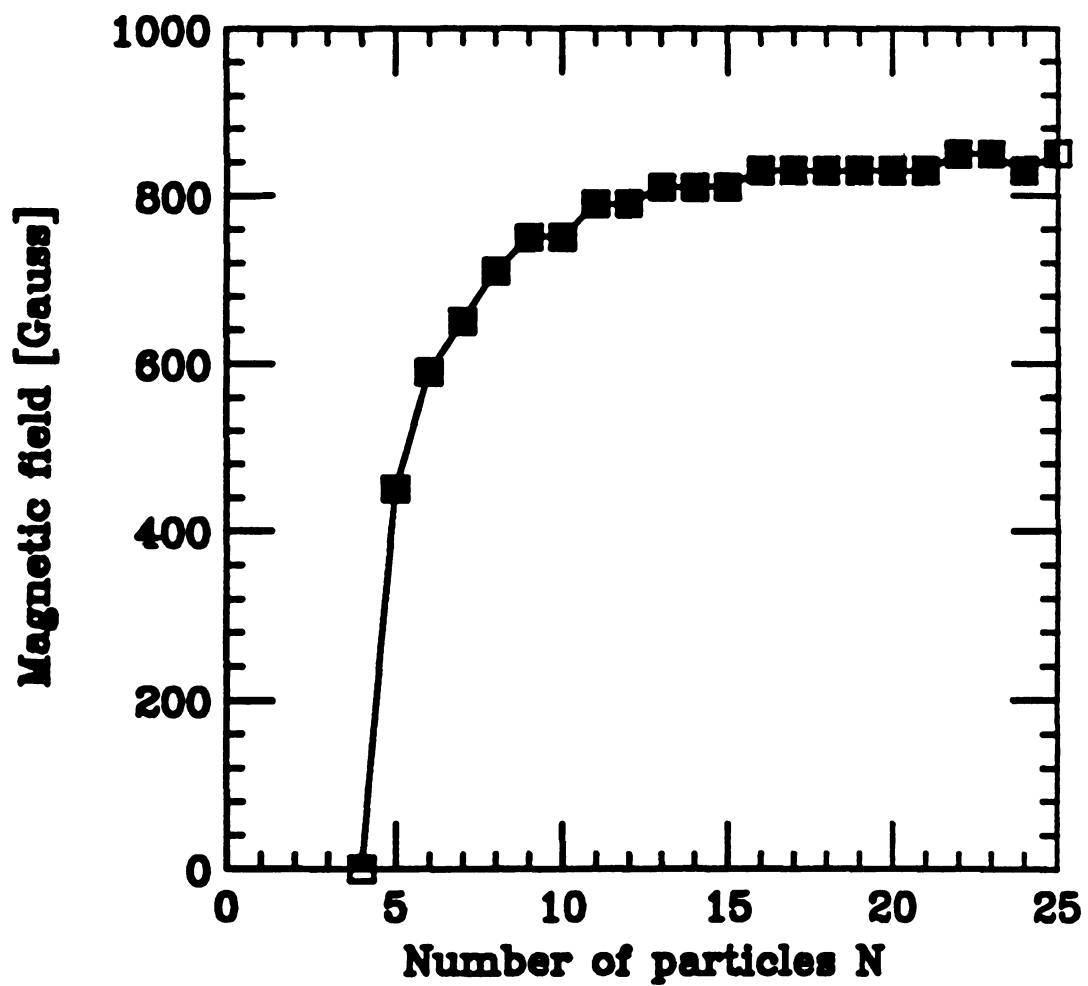
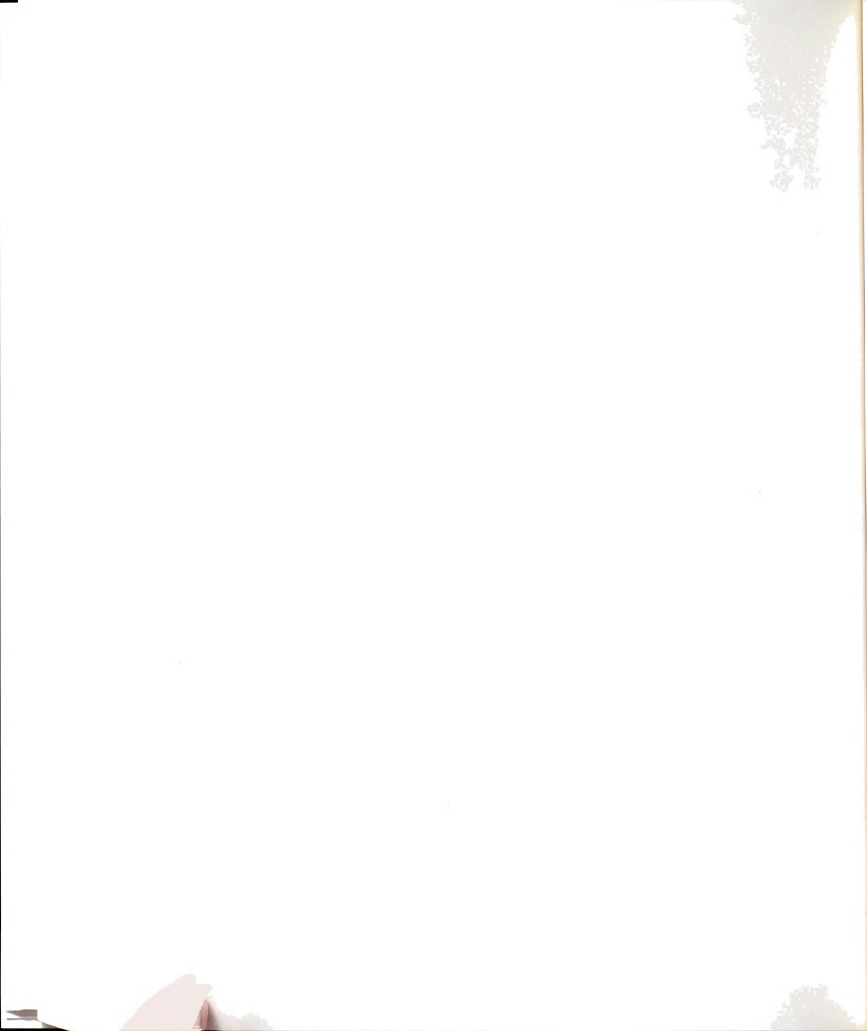


Figure 5.10: Upper critical field ( $B_{c2}$ ) for magnetic dipole rings as a function of the number of particles.





a given field, we need to do the dynamics study. For MD simulation we integrate the equations of motion, such as Eq. 4.29, with fourth-order Runge-Kutta method [Pres86]. The equations of motion include the quaternion parameters to represent the rotation of the dipoles. We use an adaptive step-size control in which the time step  $\delta t$  varies according to the moves of particles. Two criteria,  $\delta r_{c1}$  and  $\delta r_{c2}$  are specified. If the largest position change among all particles,  $\delta r_{\max}$ , is smaller than  $\delta r_{c1}$ , the time step  $\delta t$  in the subsequent integration will be increased. When  $\delta r_{\max}$  is bigger than  $\delta r_{c2}$ , the time step  $\delta t$  decreases. Otherwise we keep the current time step  $\delta t$ . All of the MD results in this chapter are generated with the initial time step  $\delta t = 5.0 \times 10^{-11}$  S,  $\delta r_{c1} = 0.8$  Å and  $\delta r_{c2} = 1.2$  Å.

For a given field, we first obtain the optimized configuration using the conjugate-gradient method. We then give a small kinetic energy corresponding to a temperature of 1 K. The velocities and angular velocities are generated randomly according to the Maxwell-Boltzmann velocity distribution of given temperature. We use the step-wise microcanonical MD simulation meaning that we pump energy into the system at one time and keep the system isolated for a sufficiently long time. The system will explore the multi-dimensional phase space available within that given total energy. If the barrier is lower than the total energy the system will eventually find the pathway leading to other local minimum. After a sufficiently long time, if ring is still intact, it usually means that the barrier is higher than the total amount of energy pumped in. After then we increase the total energy of the system by heating up the particles (scaling of velocities) and repeat above simulation steps until we have a broken ring. The amount of energy we pump in at each step will determine the resolution of energy scale of our study. In Fig. 5.11, we plot the variation of the energy barrier,  $E^*$ , as a function of the

1000  
1000  
1000

applied field,  $B$ . To generate the data we run MD simulations for an isolated system (microcanonically) at each given total energy for  $1.0 \times 10^{-6}$  S. We add  $3.0 \times 10^{-3}$  eV of energy into kinetic energy if the ring is not broken until that time.

$E^*$  is the amount of total energy you need to put in to break a ring of ferrofluid particles at given magnetic field. In the region below this curve, once you have a ring of ferrofluid particles, you will have a stable ring. When the total energy difference from the optimized configuration is more than this value, the ring will disintegrate into chains or smaller pieces. According to the "equipartition theorem" [Reif65a], the average kinetic energy,  $\bar{K}$  of a ferrofluid system which has 6 degrees of freedom per particle (3 translational and 3 rotational) is

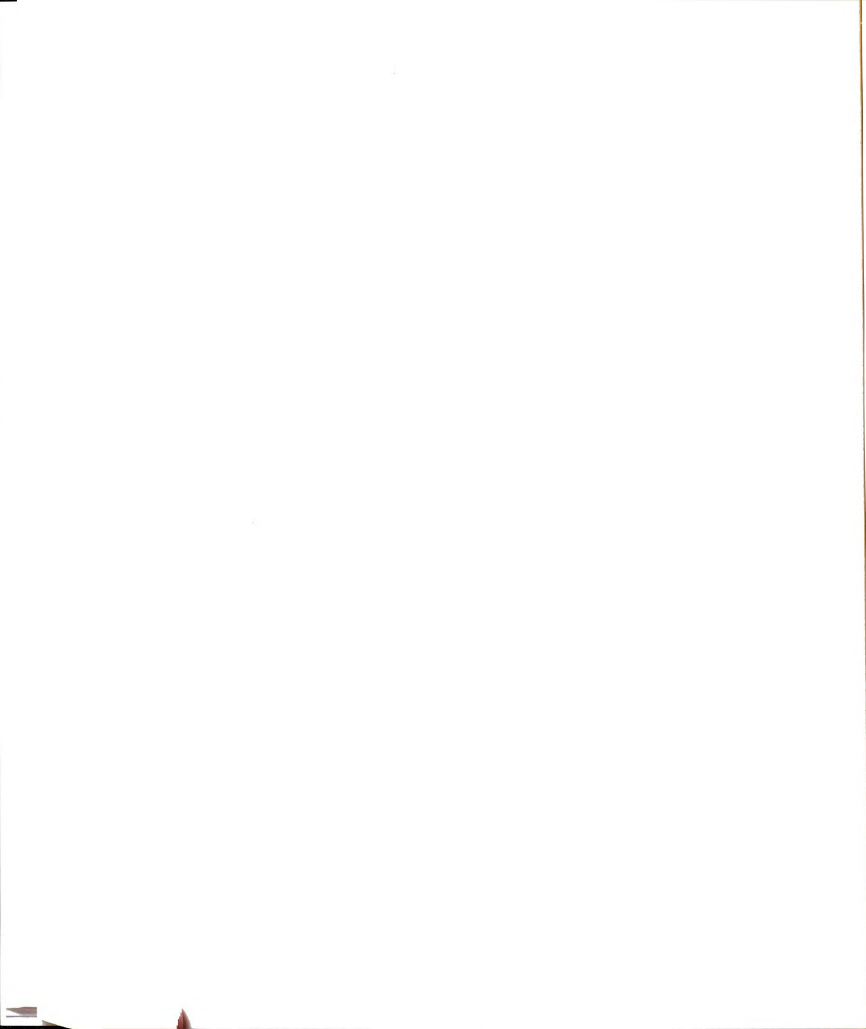
$$\bar{K} = 6 \cdot \frac{1}{2} k_B T = 3 k_B T. \quad (5.65)$$

Fig. 5.12 is the plot of the estimation of melting temperature  $T_M^*$  as a function of magnetic field.  $T_M^*$  is calculated from Eq. (5.65) using the average kinetic energy of the system when the ring breaks.

## 5.7 Ongoing work

The ferrofluid as well as an electrorheological fluid is a system of dipole particles immersed in a viscous fluid. It is well known that these sufficiently small macroscopic particles exhibit a random type of motion, so-called "Brownian motion" [Reif65b]. If we consider the effect of this Brownian motion, the governing equation of motion becomes the "Langevin equation"

$$m \frac{dv}{dt} = \mathcal{F} - \gamma v + F'(t). \quad (5.66)$$



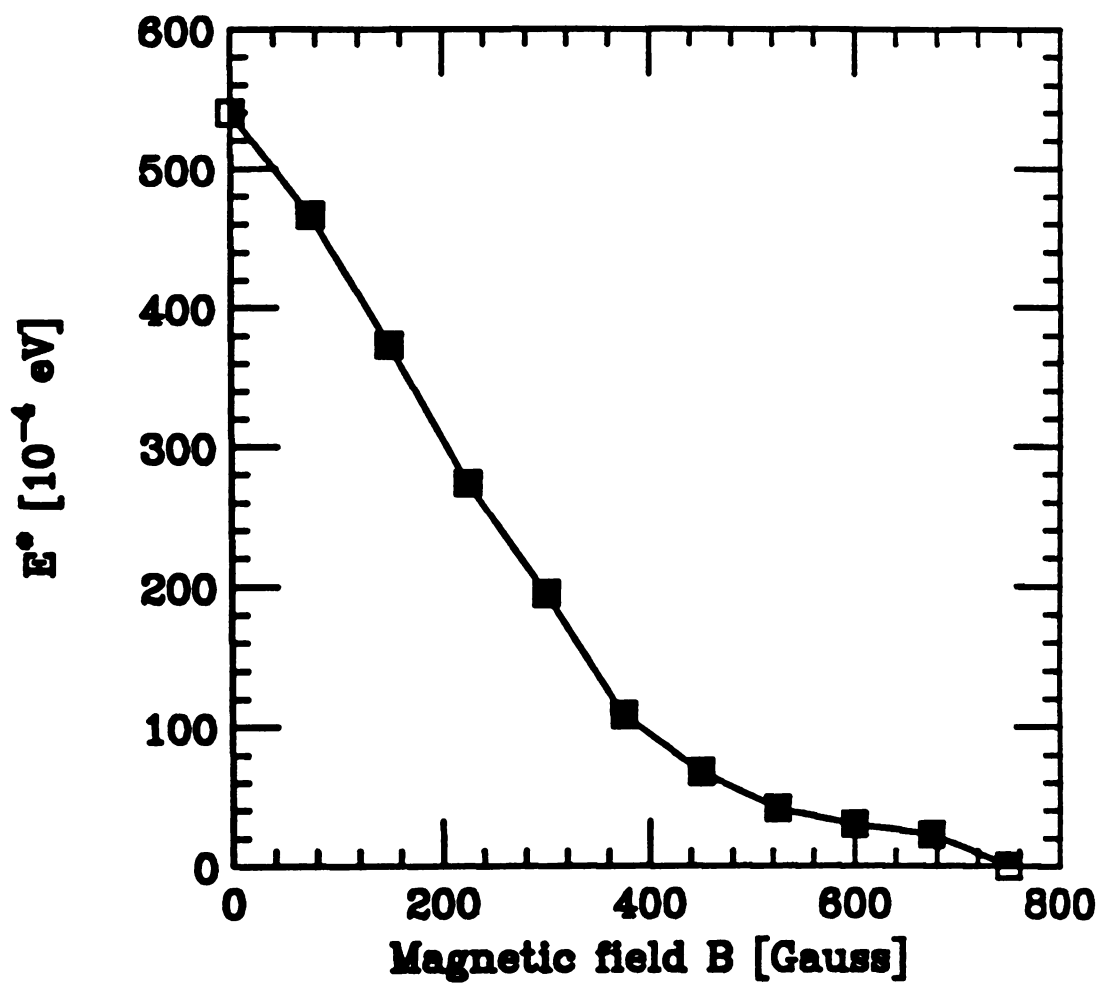


Figure 5.11: Energy barrier  $E^*$  of ferrofluid rings as a function of applied field  $B$ .



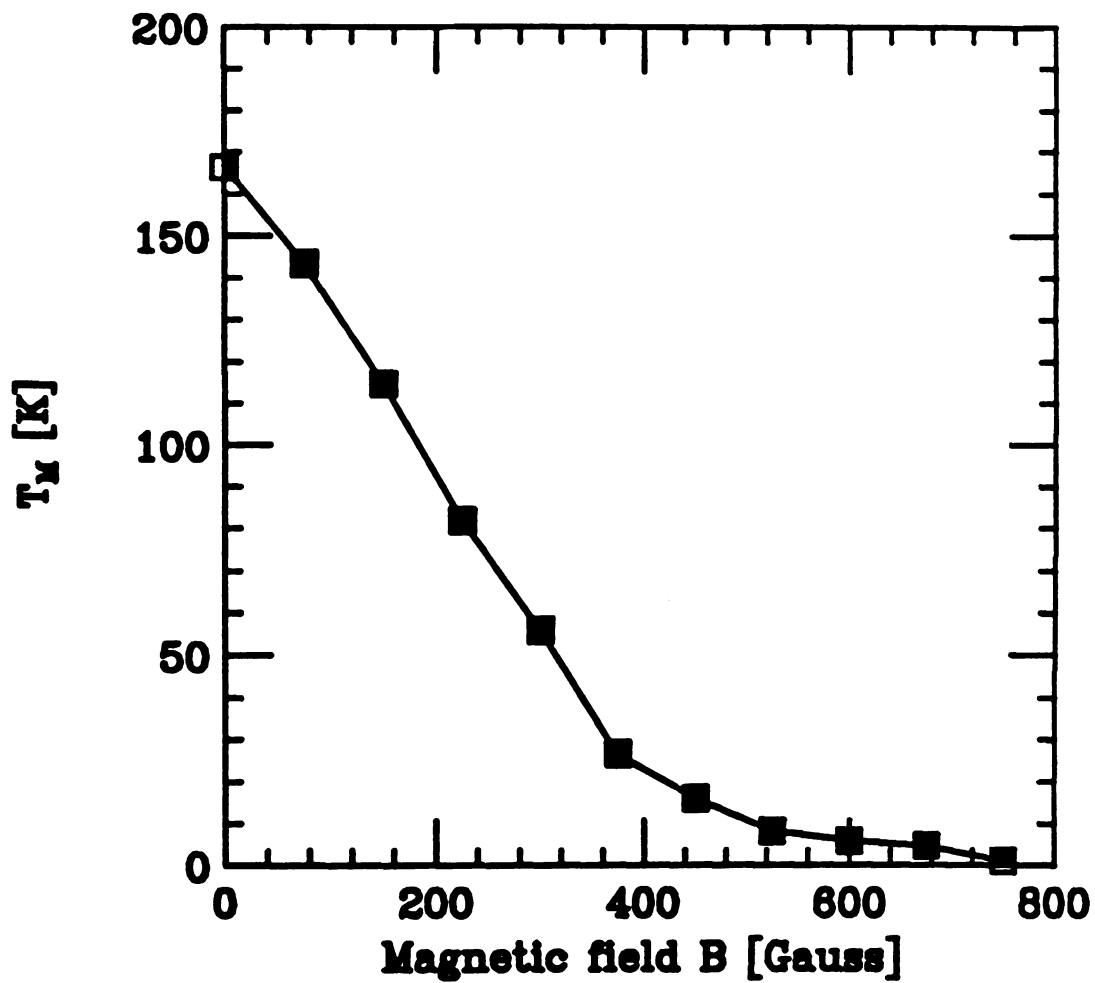
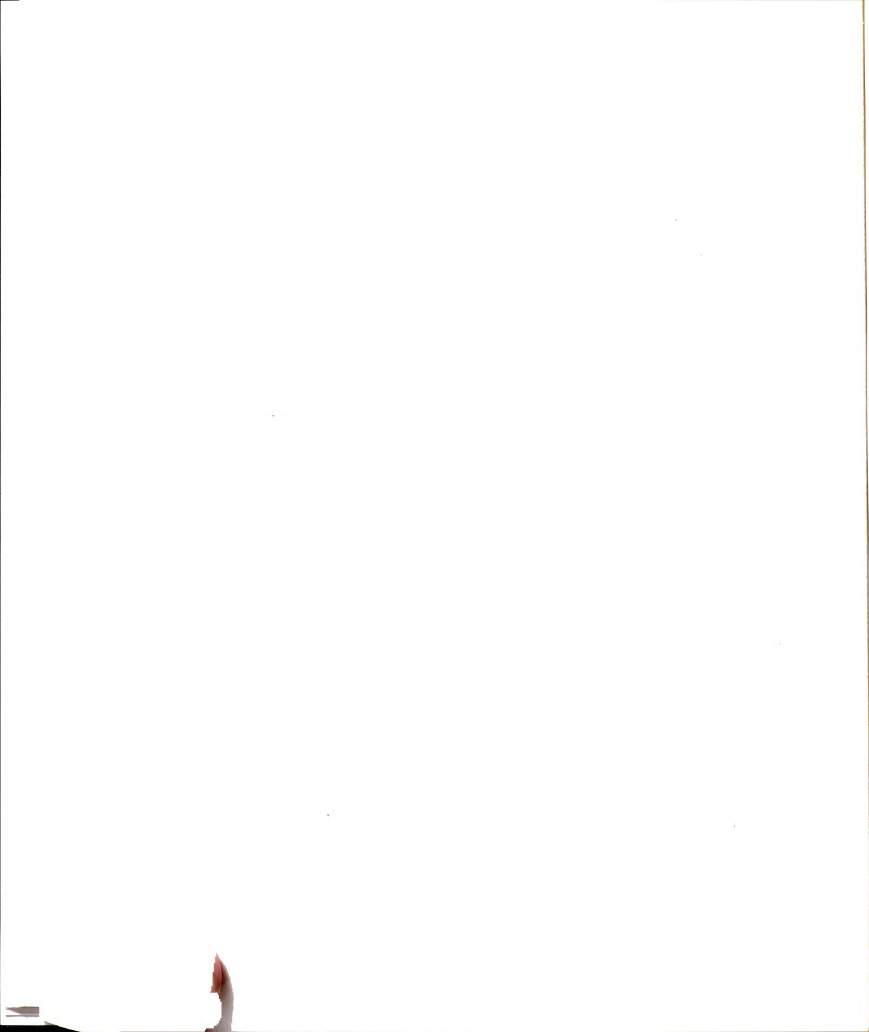


Figure 5.12: Estimation of melting temperature  $T_M^*$  of ferrofluid rings as a function of applied field  $B$ .





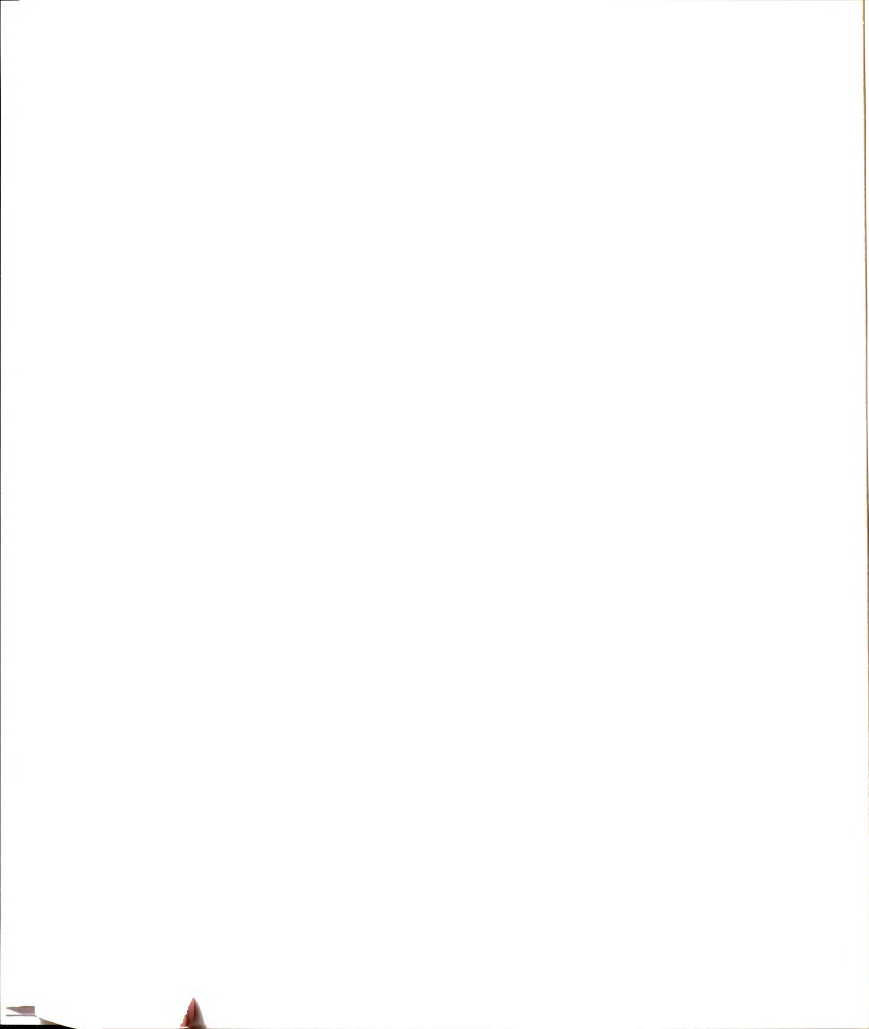
$\mathcal{F}$  is the force that we have without the Brownian motion, such as the one from the dipole-dipole interaction. The frictional coefficient  $\gamma$  is given by “Stoke’s law” [Page52, Joos58]

$$\gamma = 3\pi\eta\sigma \quad (5.67)$$

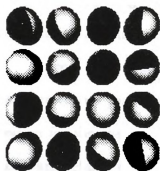
where  $\eta$  is the viscosity of the surrounding fluid and  $\sigma$  is the diameter of the particles. The magnitude of the Brownian force depends on the temperature  $T$  and the viscosity  $\eta$  of the fluid. To simulate the effect of Brownian motion we generate the random force  $F'(t)$  which has the Gaussian distribution with zero-mean and the width

$$\Omega = \sqrt{6\pi k_B T \sigma \eta / \tau} \quad (5.68)$$

where  $\tau$  is an adjustable parameter and has the dimension of a time [TaoR94]. With given values of the state parameters, we can tune  $\tau$  so that it generates ensemble of systems with the average temperature matching the heat bath or fluid temperature. We have very preliminary MD simulation results with this model of Brownian motion and it will be part of our next paper. Also, we are simulating the aggregation of many of these ferrofluid particles into chains and branched structures. Fig. 5.13 shows one of our preliminary results on the aggregation of 64 magnetic dipoles in the absence of the field. At the start of the simulation, 64 magnetic dipoles are perturbed randomly by 10% of the lattice constant, 173 Å, from their  $4 \times 4 \times 4$  cubic lattice structure and only the top layer is seen clearly. After about  $1.0 \times 10^{-8}$  S, the particles aggregate into two rings and one giant “snake”. One exciting fact is that this aggregation was done in zero-field. Many simulations and experiments have been performed in rather high-field and



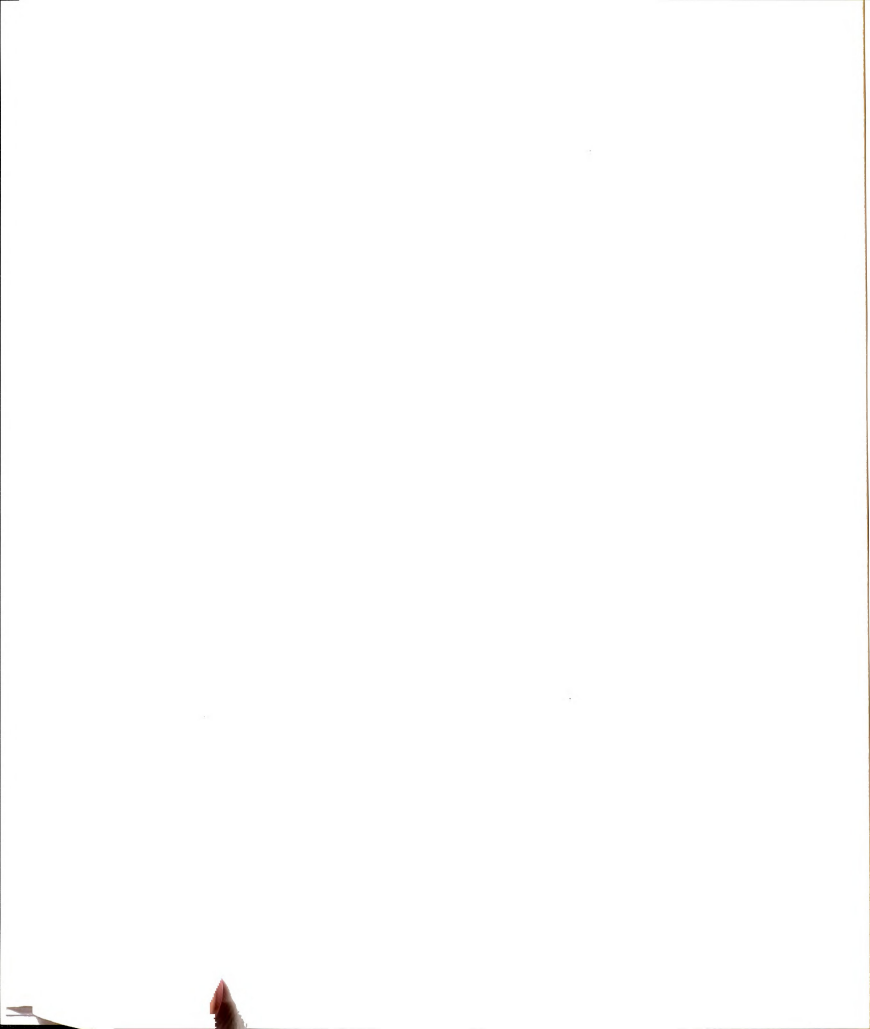
(a)



(b)



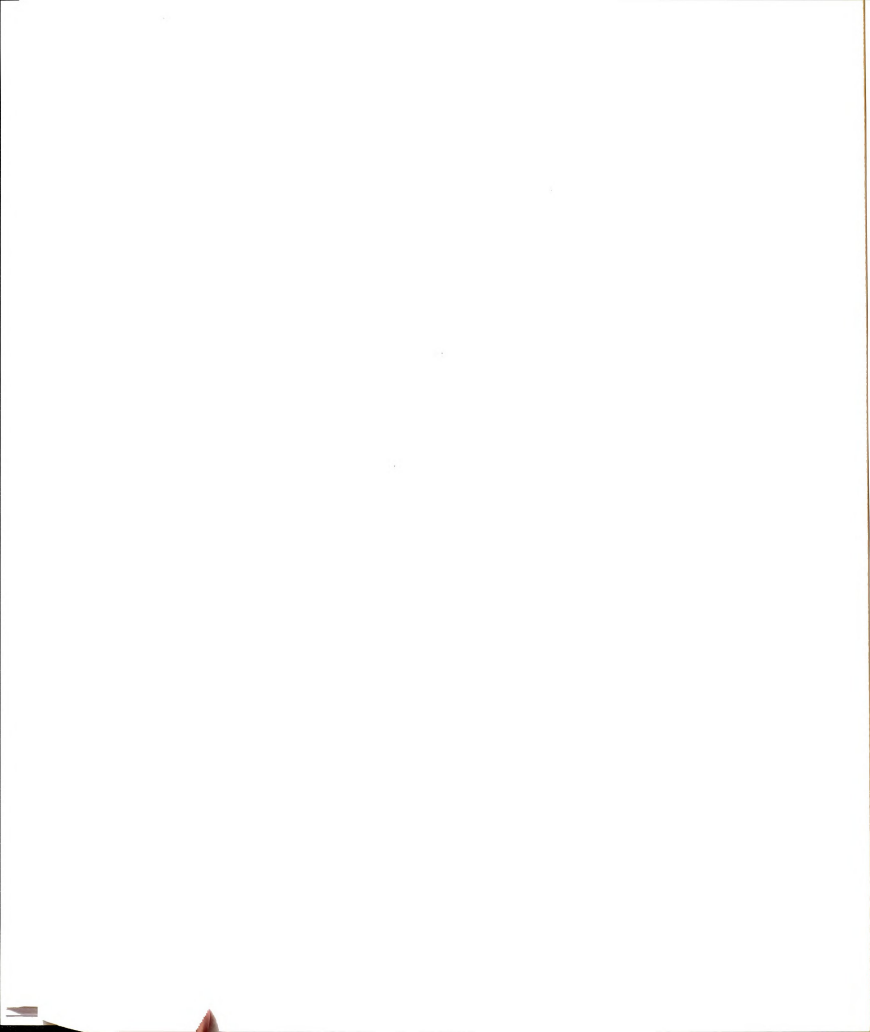
Figure 5.13: Aggregation of 64 magnetic dipoles. (a) Initial configuration and (b) final configuration. In (a) 64 magnetic dipoles are perturbed randomly by 10% of the lattice constant, 173 Å, from their  $4 \times 4 \times 4$  cubic lattice structure and only the top layer is seen clearly.



that might explain why almost no literature discusses about the ring structure in ferrofluids.

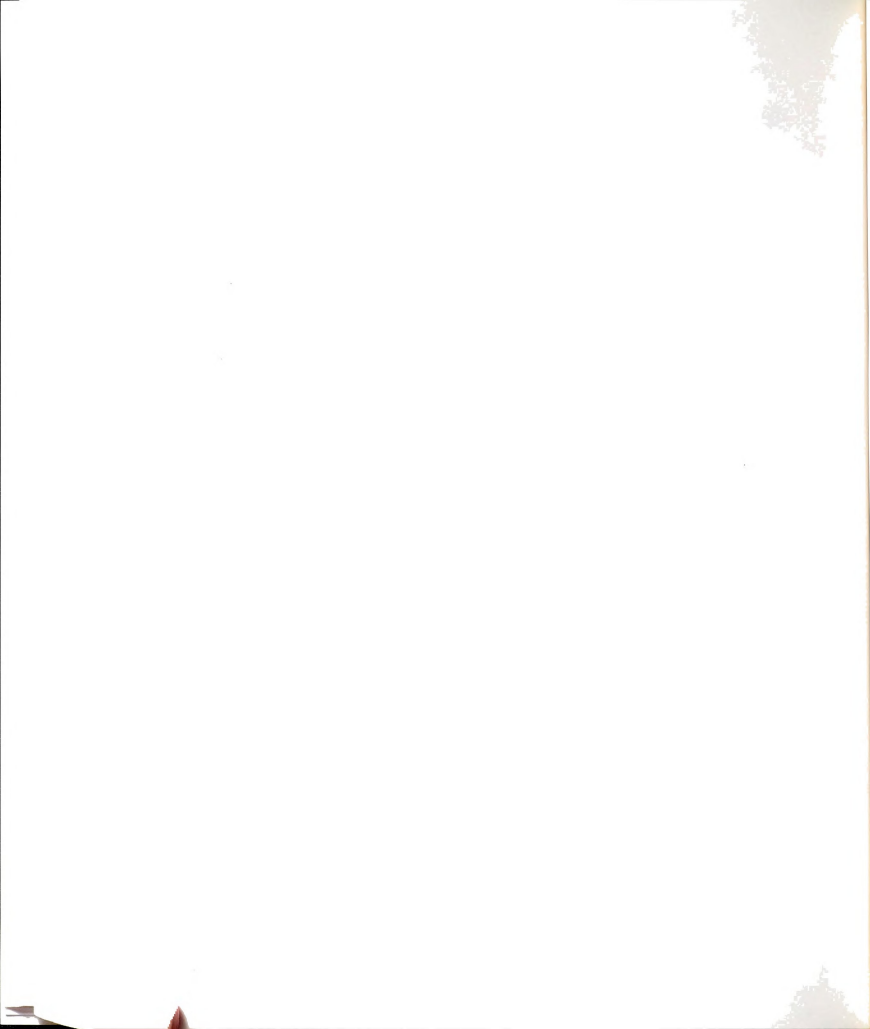
## 5.8 Conclusions

In this work we tried to study the early stages of the colloidal aggregation in ferrofluid and the stability of the ring structure of these particles. We found that the ring is the most stable structure for ferrofluid particles in low field and low temperature as long as it has more than 4 particles. Based on simple arguments, we derived an analytic expression for the energy of the ring and chain structure. Two critical fields,  $B_{c1}$  and  $B_{c2}$ , are defined and their values from the conjugate-gradient method was obtained. Performing the molecular dynamics simulation including the quaternion parameters to represent the rotation of the dipoles, we found the energy barriers,  $E^*$ , and the estimation of melting temperature  $T_M^*$  to break a ring structure into lower symmetry ones as a function of applied field. Our result indicates that in zero-field the ring structure should be observed in carefully controlled experiments.



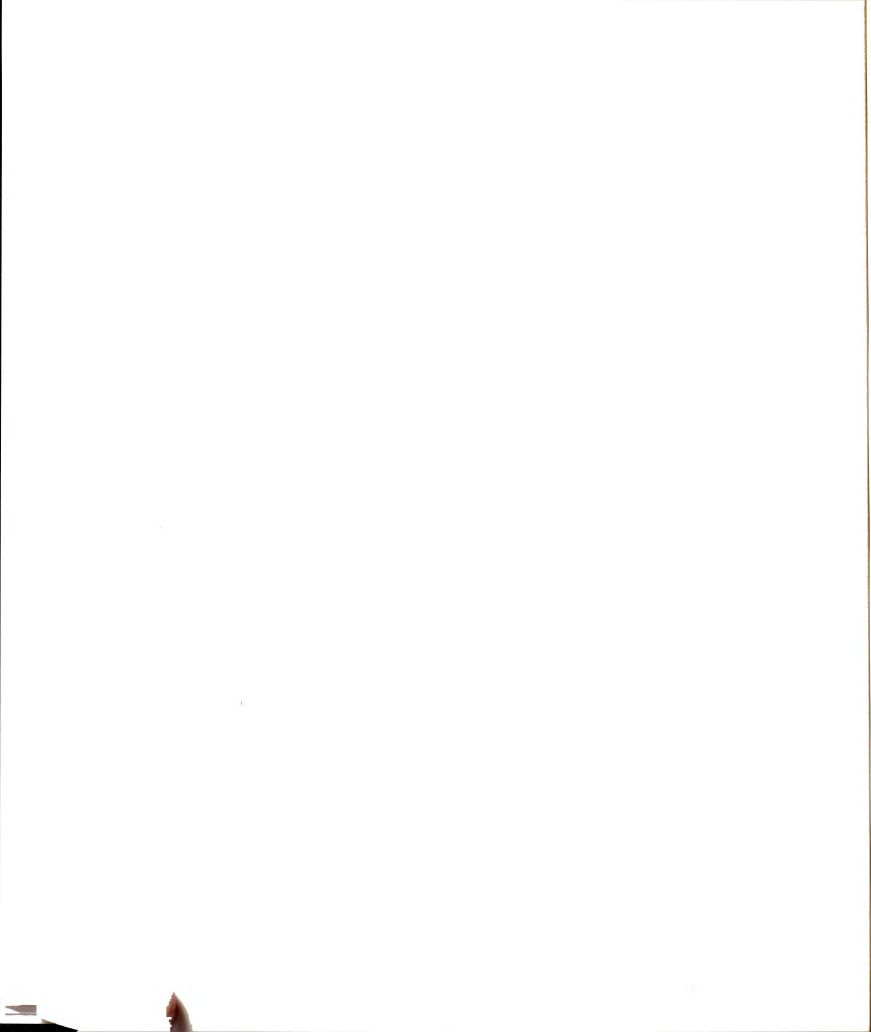
# Bibliography

- [Abro72] Milton Abromowitz and Irene A. Stegun, *Handbook of Mathematical Functions*, Dover Publications Inc., New York (1972).
- [Alle84] Michael P. Allen, *A molecular dynamics simulation study of octopoles in the field of a planar surface*, Mol. Phys. **52**, 717 (1984).
- [Alle90] M.P. Allen and D.J. Tildesley, *Computer Simulations of Liquids*, Oxford University Press, New York (1990).
- [Ande62] P.W. Anderson, *Theory of flux creep in hard superconductors*, Phys. Rev. Lett. **9**, 309 (1962).
- [Ande84] H.C. Anderson, M.P. Allen, A. Bellemans, J. Board, J.H.R. Clarke, M. Ferrario, J.M. Hail, S. Nosé, J.V. Opheusden and J.P. Ryckaert, *New molecular dynamics methods for various ensembles*, Rapport d'activité scientifique du CECAM, pp. 82-115 (1984)
- [Arba90] S. Arbabi and M. Sahimi, *Test of universality for three-dimensional models of mechanical breakdown of disordered solids*, Phys. Rev. B **41**, 772 (1990).
- [Arca85] L. de Arcangelis, S. Redner and H.J Herrmann, *A Random fuse model for breaking process*, J. de Physique Lett. **46**, L585 (1985).

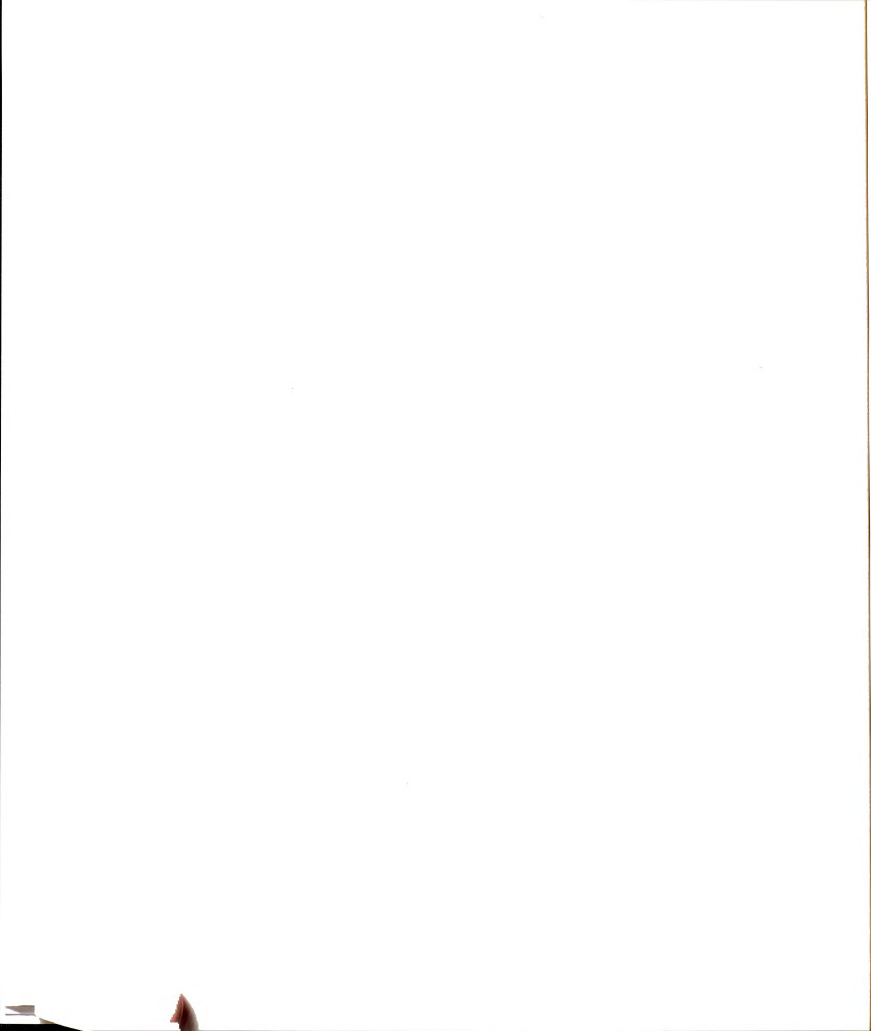




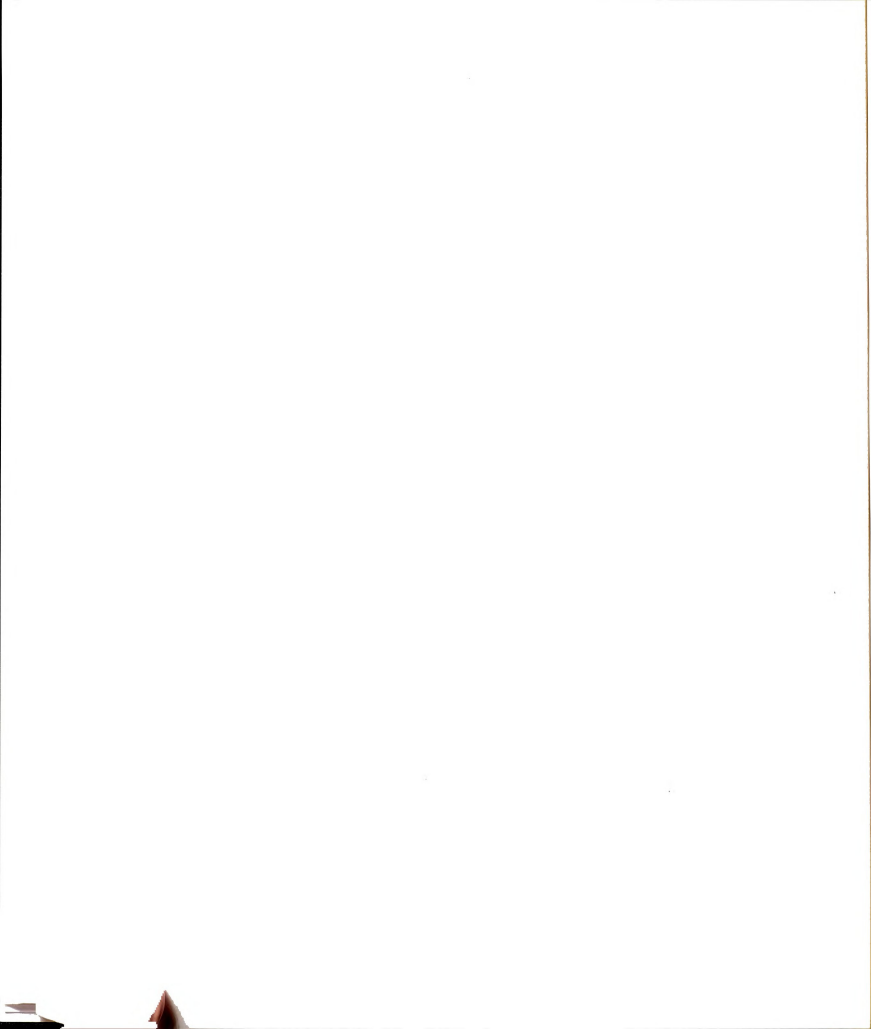
- [Ball90] Pietro Ballone and Paolo Milani, Phys. Rev. B **42**, 3201 (1990).
- [Baro73] J. Barojas, D. Levesque and B. Quentrec, *Simulation of diatomic homonuclear liquids*, Phys. Rev. A **7**, 1092 (1973).
- [Beal88] P.D. Beal and D.J. Srolovitz, *Elastic fracture in random materials*, Phys. Rev. B **37**, 5500 (1988).
- [Bean62] C.P. Bean, *Magnetization of hard superconductors*, Phys. Rev. Lett. **8**, 250 (1962).
- [Bean64] C.P. Bean, Rev. Mod. Phys. **36**, 31 (1964).
- [Beer82] N. Beer and D.G. Pettifor, Proc. NATO adv. study Inst. (Gent), Plenum, New York (1982).
- [Beng87] L. Benguigui, P. Ron and D.J. Bergman, *Strain and Stress at the fracture of percolative media*, J. de Physique **48**, 1547 (1987).
- [Bill93] W.E. Billups and M.A. Ciufolini editors, *Buckminsterfullerenes*, VCH Publishers, New York (1993).
- [Bloc29] F. Bloch, Z. Phys. **52**, 555 (1929).
- [Bloc87] H. Bloch and J.P. Kelly, U.S. Patent No. 4687589 (1987).
- [Bonn92] R.T. Bonnecaze and J.F. Brady, *Dynamic simulation of an electrorheological fluid*, J. Chem. Phys. **96**, 2183 (1992).
- [Born91] I.C. van den Born, H.D. Hoekstra and J.Th. de Hosson, Phys. Rev. B **43**, 3794 (1991).



- [Bowm87] J.J. Bowman, T.B.A. Senior and P.L.E. Uslenghi, *Electromagnetic and Acoustic Scattering by Simple Shapes*, Hemisphere Publishing Corp., New York (1987).
- [Busm92] H.G. Busmann, T. Lill, B. Reif and I.V. Hertel, *Surf. Sci.* **272**, 146 (1992).
- [Cald94] F. Leal Calderon, T. Stora, O. Mondain Monval, P. Poulin and J. Biette, *Direct Measurement of Colloidal Forces*, *Phys. Rev. Lett.* **72**, 2959 (1994).
- [Camp92] E.E.B. Campbell, A. Hielscher, R. Ehlich, V. Schyja and I.V. Hertel, *Nuclear Physics Concepts in the Study Atomic Cluster Physics*, edited by R. Schmidt, H.O. Lutz and R. Dreizler, *Lecture Notes in Physics*, Vol. 404, p. 185, Springer, Berlin (1992).
- [Camp93] E.E.B. Campbell, V. Schyja, R. Ehlich and I.V. Hertel, *Phys. Rev. Lett.* **70**, 263 (1993).
- [Cast88] E. Castillo, *Extreme Value theory in Engineering*, Academic Press, San Diego, CA (1988).
- [Chan91] S.K. Chan, S.G. Kim and P.M. Duxbury, *Elasticity and fracture of tubular honeycombs containing random vacancies*, *Proc. CASME II* (1991).
- [Chau88] P. Chaudhari *et al.*, *Phys. Rev. Lett.* **60**, 1653 (1988).
- [Chen92] T.J. Chen, R.N. Zitter and R. Tao, *Phys. Rev. Lett.* **68**, 2555 (1992).
- [Clar00] David Clarke, private communication.



- [Chel91] James R. Chelikowsky, Phys. Rev. Lett. **67**, 2970 (1991).
- [Clem87] J.R. Clem *et al.*, Phys. Rev. B **35**, 6637 (1987).
- [Copp89] R.W. Coppard, L.A. Dissado, S.M. Rowland and R. Rakowski, *Dielectric breakdown of metal-loaded polyethylene*, J. Phys.: Condens. Matter **1**, 3041 (1989).
- [Croc94] John C. Crocker and David G. Grier, *Microscopic Measurement of the Pair Interaction Potential of Charge-Stabilized Colloid*, Phys. Rev. Lett. **73**, 352 (1994).
- [Cryo89] Proceedings of the International Conference on "Critical Currents in High  $T_c$  Superconductors", Cryogenics, (**29**, 225-408 March 1989 supplement).
- [Curl88] Robert F. Curl and Richard E. Smalley, Science **242**, 1017 (1988).
- [Curl91] Robert F. Curl and Richard E. Smalley, Scientific American, October 1991, p. 54.
- [Curt90] W.A. Curtin and H. Scher, *Brittle fracture of disordered materials*, J. Mater. Res. **5**, 535 (1990).
- [Curt91] W.A. Curtin and H. Scher, Phys. Rev. Lett. **67**, 2457 (1980).
- [Curt92] W.A. Curtin and H. Scher, Phys. Rev. B **45**, 2620 (1992).
- [Dick93] Akiva J. Dickstein, Shyamsunder Erramilli, Raymond E. Goldstein, David P. Jackson and Stephen A. Langer, *Labyrinthine Pattern Formation in Magnetic Fluids*, Science. **261**, 1012 (1993).

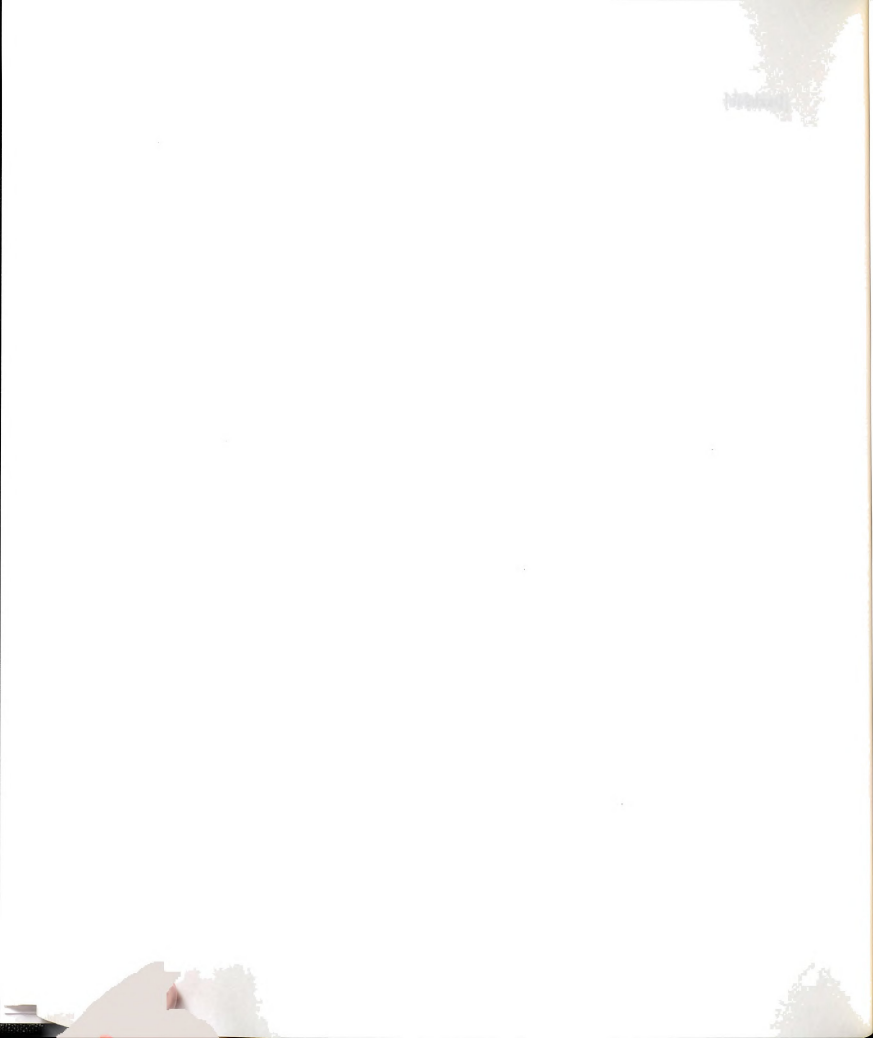


- [Dimo88] D. Dimos *et al.*, Phys. Rev. Lett. **61**, 219 (1988).
- [Donn90] J.B. Donnet and R.C. Bansal, *Carbon Fibers*, Marcel Dekker Inc., 2nd ed. (1990)
- [Dres88] M.S. Dresslhaus, G. Dresslhaus and K. Sugihara, I.L. Spain and H.A. Goldberg, *Graphite fibers and filaments*, Springer Verlag, NY (1988)
- [Duxb86] P.M. Duxbury, P.D. Beale and P.L. Leath, Phys. Rev. Lett. **57**, 1052 (1986).
- [Duxb87a] P.M. Duxbury, P.L. Leath and P.D. Beale, *Breakdown properties of quenched random system - the random fuse network*, Phys. Rev. B **36**, 369 (1987).
- [Duxb87b] P.M. Duxbury and P.L. Leath, J. Phys. A. **20**, L411 (1987).
- [Duxb90a] P.M. Duxbury and S.G. Kim, *Scaling theory and simulations of fracture in disordered media*, Proc. CASME II (1990).
- [Duxb90b] P.M. Duxbury, P.D. Beale, H. Bak and P.A. Schroeder, *Capacitance and dielectric breakdown of metal loaded dielectrics*, J. Phys. D. **23**, 1546 (1990).
- [Duxb91] P.M. Duxbury and S.G. Kim, *Scaling theory of elasticity and fracture in disordered networks*, Mat. Res. Symp. Proc. **207**, 179 (1991).
- [Duxb94a] P.M. Duxbury and P.L. Leath, *Failure Probability and Average Strength of Disordered Systems*, Phys. Rev. Lett. **72**, 2805 (1994).

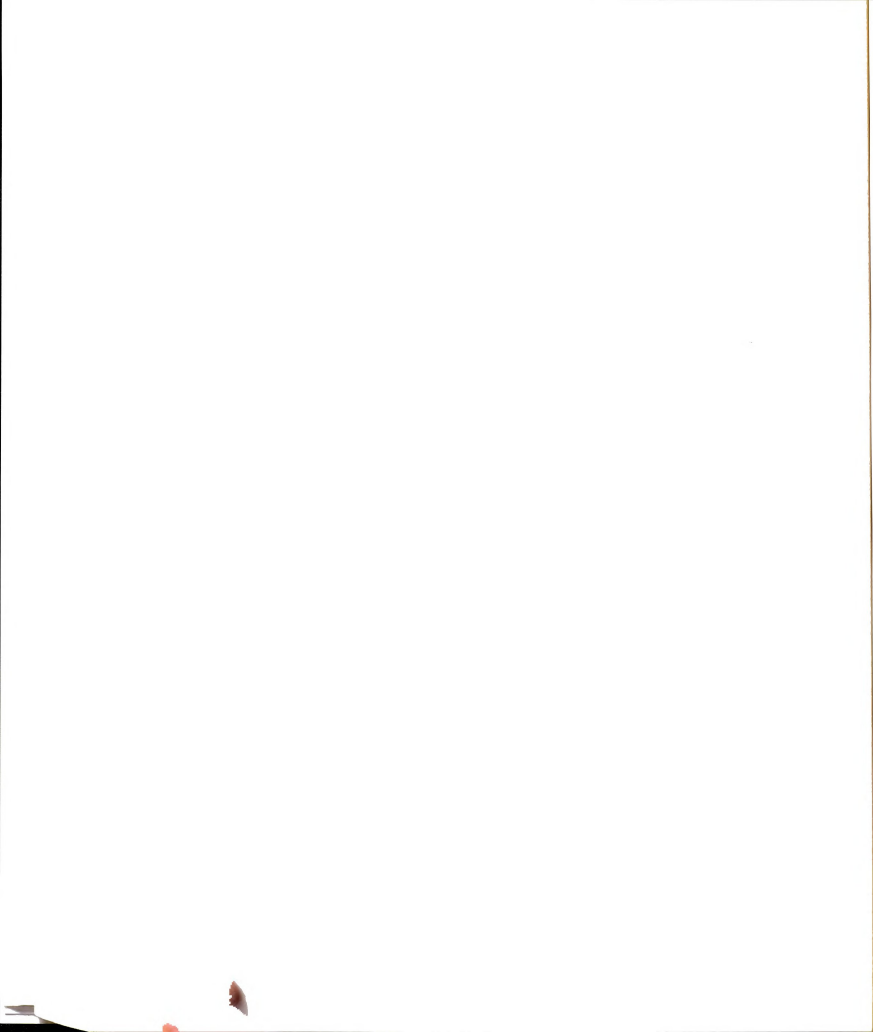




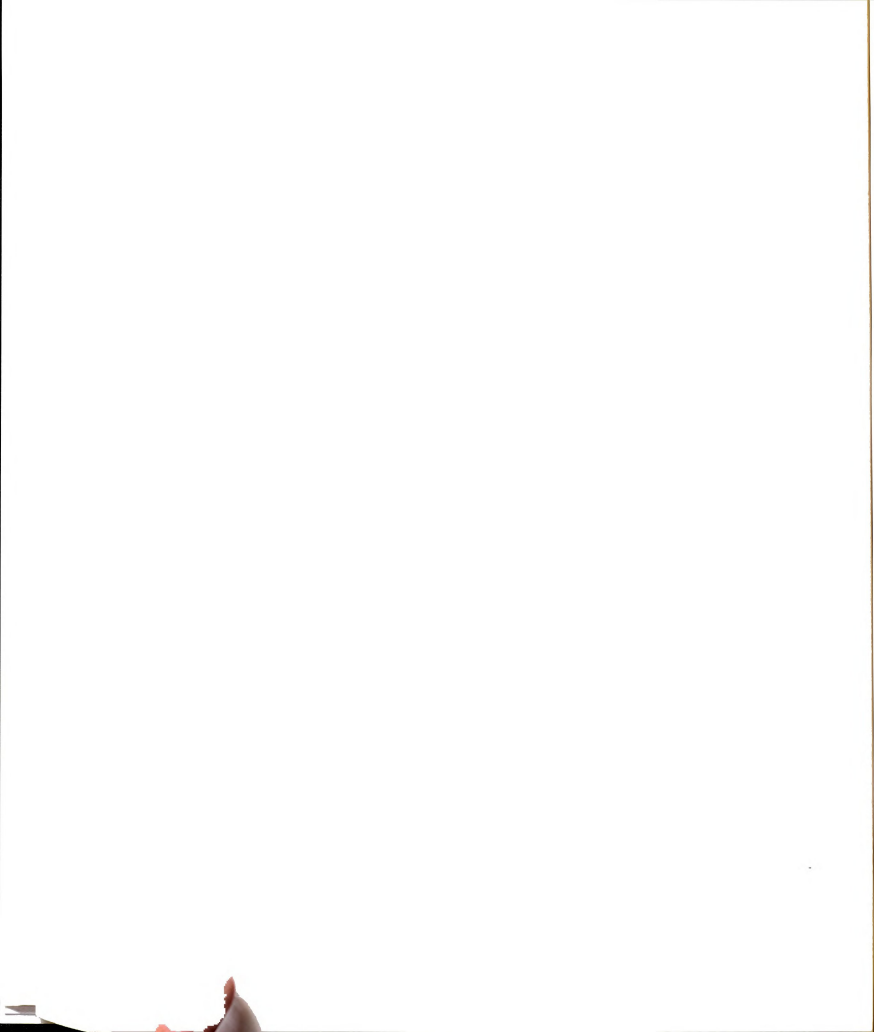
- [Duxb94b] P.M. Duxbury, S.G. Kim and P.L. Leath, *Size effect and statistics of fracture in random materials*, Mat. Sci. and Eng. A176, 25 (1994).
- [Duze81] T. Van Duzer and C.W. Turner, *Principles of Superconductive Devices and Circuits*, Elsevier, New York (1981)
- [Ebbe92] T.W. Ebbesen, J. Tabuchi, K. Tanigaki, *The mechanistics of fullerene formation*, Chem. Phys. Lett. 191, 336 (1992).
- [Evan77a] D.J. Evans, *On the representation of orientation space*, Mol. Phys. 34, 317 (1977).
- [Evan77b] D.J. Evans and S. Murad, *Singularity-free algorithm for molecular dynamics simulation of rigid polyatomics*, Mol. Phys. 34, 327 (1977).
- [Feng85] S. Feng, M.F. Thorpe and E. Garboczi, *Effective-medium theory of percolation on central-force elastic networks*, Phys. Rev. B 31, 276 (1985).
- [Feng87] S. Feng, B.I. Halperin and P.N. Sen, *Transport properties of continuum systems near the percolation threshold*, Phys. Rev. 35, 197 (1987).
- [Fili88] F.E. Filisko and W.E. Armstrong, U.S. Patent No. 4744914 (1988).
- [Foul89] W.M.C. Foulers and R. Haydock, Phys. Rev. B 39, 12520 (1989).
- [Gala78] J. Galambos, *The Asymptotic Theory of Extreme Order Statistics*, Wiley, New York (1978).
- [Gall89a] G. Galli, R.M. Martin, R. Car and M. Parrinello, Phys. Rev. Lett. 62, 555 (1989).



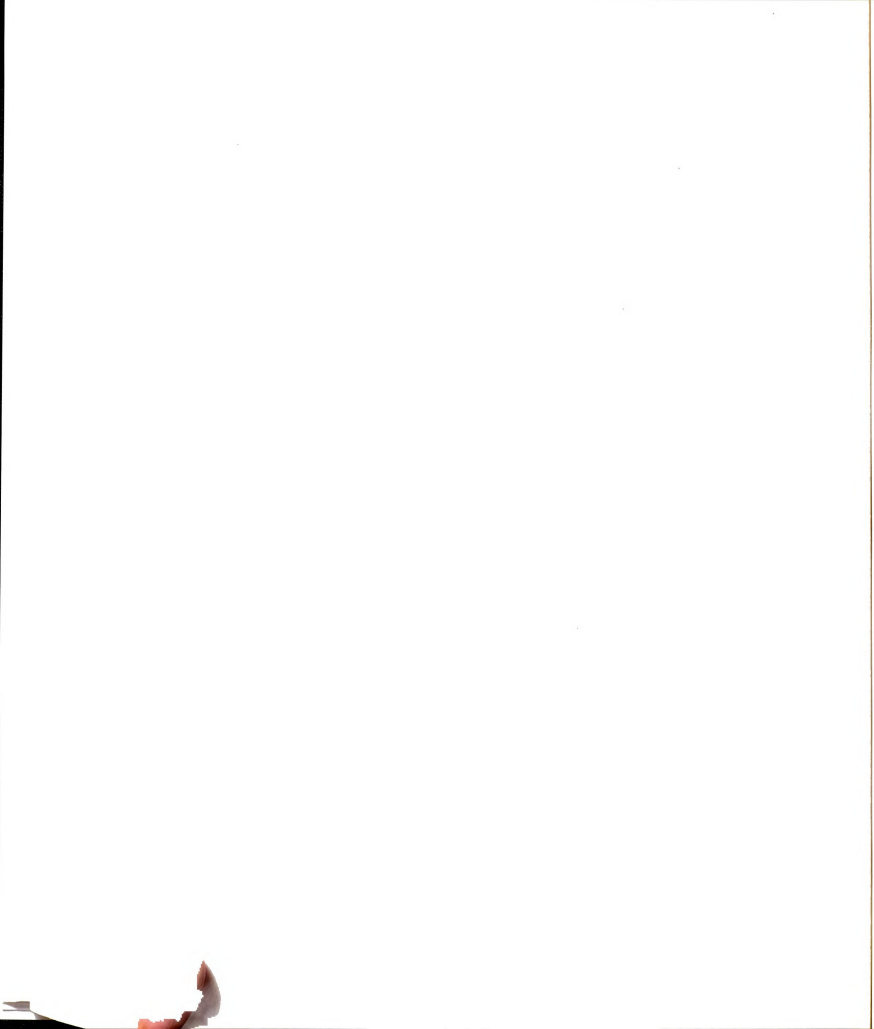
- [Gall89b] G. Galli, R.M. Martin, R. Car and M. Parrinello, *Phys. Rev. Lett.* **63**, 988 (1989).
- [Garb88] E.J. Garboczi, *Effective force constant for central force random network*, *Phys. Rev. B* **37**, 318 (1988).
- [Gear71] C.W. Gear, *Numerical Initial Value Problems in Ordinary Differential Equations*, Prentice-Hall, Englewood Cliffs, NJ (1971).
- [Gibs88] L.J. Gibson and M.F. Ashby, *Cellular Solids*, Pergamon Press, NY (1988).
- [Gind92] J.M. Ginder and L.D. Elie, Page 23, *Electrorheological Fluids*, edited by R. Tao, World Scientific, Singapore (1992)
- [Gold80] Herbert Goldstein, *Classical Mechanics*, 2nd Ed., Addison-Wesley, Reading MA (1980).
- [Good89] L. Goodwin, A.J. Skinner and D.G. Pettifor, *Europhys. Lett.* **9**, 701 (1989).
- [Grad80] I.S. Gradshteyn and I.M. Ryzhik, *Table of integrals, series, and products*, Academic Press, New York (1980).
- [Gumb58] E.J. Gumbel, *Statistics of Extremes*, Columbia Univ. Press, NY (1958).
- [Guyo87] E. Guyon, S. Roux and D.J. Bergman, *Critical Behavior of Elastic failure thresholds in Percolation*, *J. de Physique* **48**, 903 (1987).
- [Hals90] T.C. Halsey and W. Toor, *Phys. Rev. Lett.* **65**, 2820 (1990).



- [Hans89] A. Hansen, S. Roux and H.J. Herrmann, *Rupture of central-force lattices*, J. Phys. Paris **50**, 733 (1989).
- [Harl91] D.G. Harlow and S.L. Phoenix, J. Mech. Phys. Solids **39**, 173 (1991).
- [Hart77] H.L. Hart, *A Survey of the Literature on the size Effect on Material Strength*, Tech. Rep. AFFDL-TR-77-11 (Air force Light Dynamics Laboratory, Wright Patterson AFB, OH 45433), 1977.
- [Hash83] Z. Hashin, *Analysis of Composite Materials - A Survey*, J. Appl. Mech. **50**, 481 (1983).
- [Hass89] G.N. Hassold and D.J. Srolovitz, *Brittle fracture in materials with random defects* Phys. Rev. B **39**, 9273 (1989).
- [Hayd80] Roger Haydock, *The Recursive Solution of the Schrödinger Equation*, Solid State Phys. **35**, 215 (1980).
- [Hein80] Volker Heine, *Electronic Structure from the Point of View of the Local Atomic Environment*, Solid State Phys. **35**, 1 (1980).
- [Held93] G. von Helden, N.G. Gotts and M.T. Bowers, Nature **363**, 60 (1993).
- [Herr89] H.J. Herrmann, A. Hansen and S. Roux, *Fracture of disordered elastic lattices in two dimensions*, Phys. Rev. B **39**, 637 (1989).
- [Herr90] H.J. Herrmann and S. Roux editors, *Statistical Models for the Fracture of disordered Materials*, Elsevier Science Publishers, NY (1990)
- [Hinr89] E.L. Hinrichsen, A. Hansen and S. Roux, *A fracture growth model*, Europhys. Lett. **8**, 1 (1989).

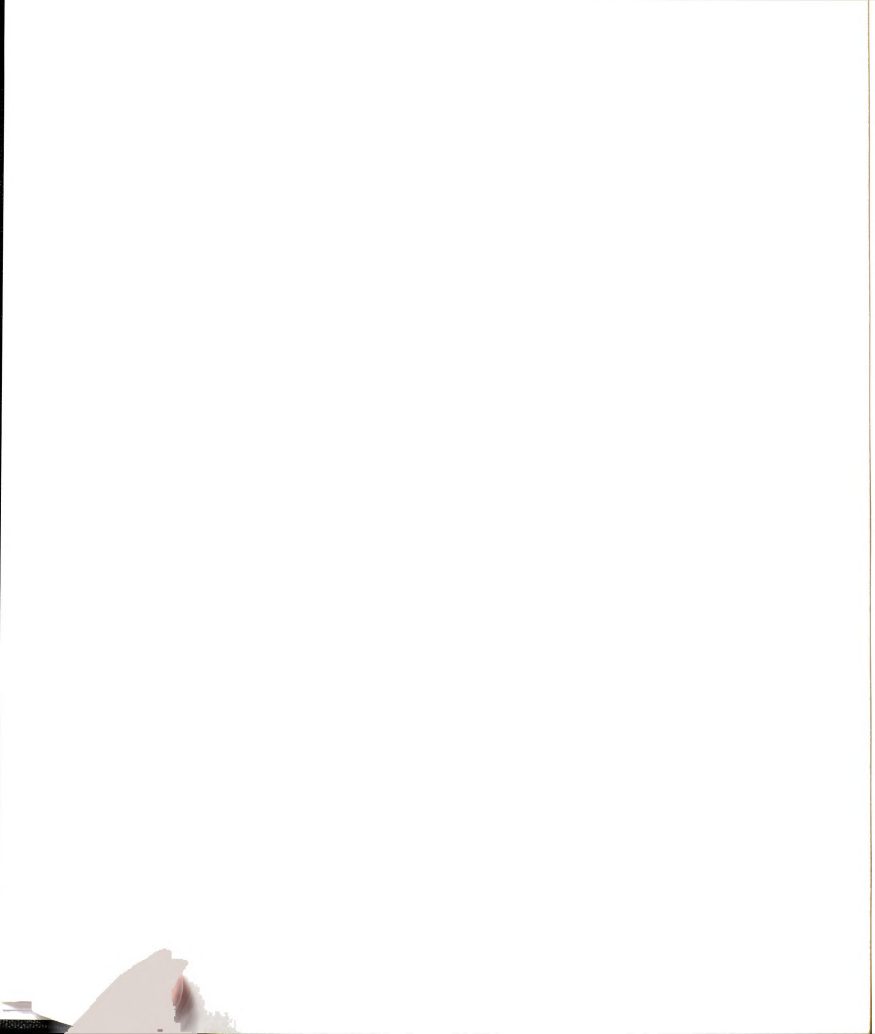


- [Hohe64] P. Hohenberg and W. Kohn, *Phys. Rev.* **136**, B864 (1964).
- [Hoov85] W.G. Hoover, *Canonical dynamics: Equilibrium phase-space distributions*, *Phys. Rev. A* **31**, 1695 (1985).
- [Hunt94] Joanna M. Hunter, James L. Fye, Eric J. Roskamp, and Martin F. Jarrold, *J. Phys. Chem.* **98**, 1810 (1994).
- [Iji91] Sumio Iijima, *Nature* **354**, 56 (1991).
- [Jack75] J.D. Jackson, *Classical Electrodynamics*, Second ed. Wiley, New York (1975).
- [Jaya79] A. de S. Jayatilaka, *Fracture of Engineering Brittle Materials*, Applied Science, London (1979).
- [Joan74] J. Joannopoulos and F. Yndurain, *Phys. Rev. B* **10**, 5164 (1974).
- [John90] Robert Johnson, Gerard Meijer and Donald S. Bethune, *C<sub>60</sub> Has Icosahedral Symmetry*, *J. Am. Ceram. Soc.* **112**, 8983 (1990).
- [Joos58] G. Joos, *Theoretical Physics*, 3rd ed., p. 218, Haffner Publishing Company, New York, N.Y. (1958).
- [Jund94] P. Jund, S.G. Kim, D. Tománek and J. Hetherington, *Stability of Magnetic Dipole Structures in Ferrofluids*, preprint (1994).
- [Kahn88] B. Kahng, G.G. Bartrouni, S. Redner, L. de Arcangelis and H.J. Herrmann, *Electric breakdown in a fuse network with continuously distributed breaking strengths*, *Phys. Rev. B* **37**, 7625 (1988).
- [Keat66] P.N. Keating, *Phys. Rev.* **145**, 637 (1966).

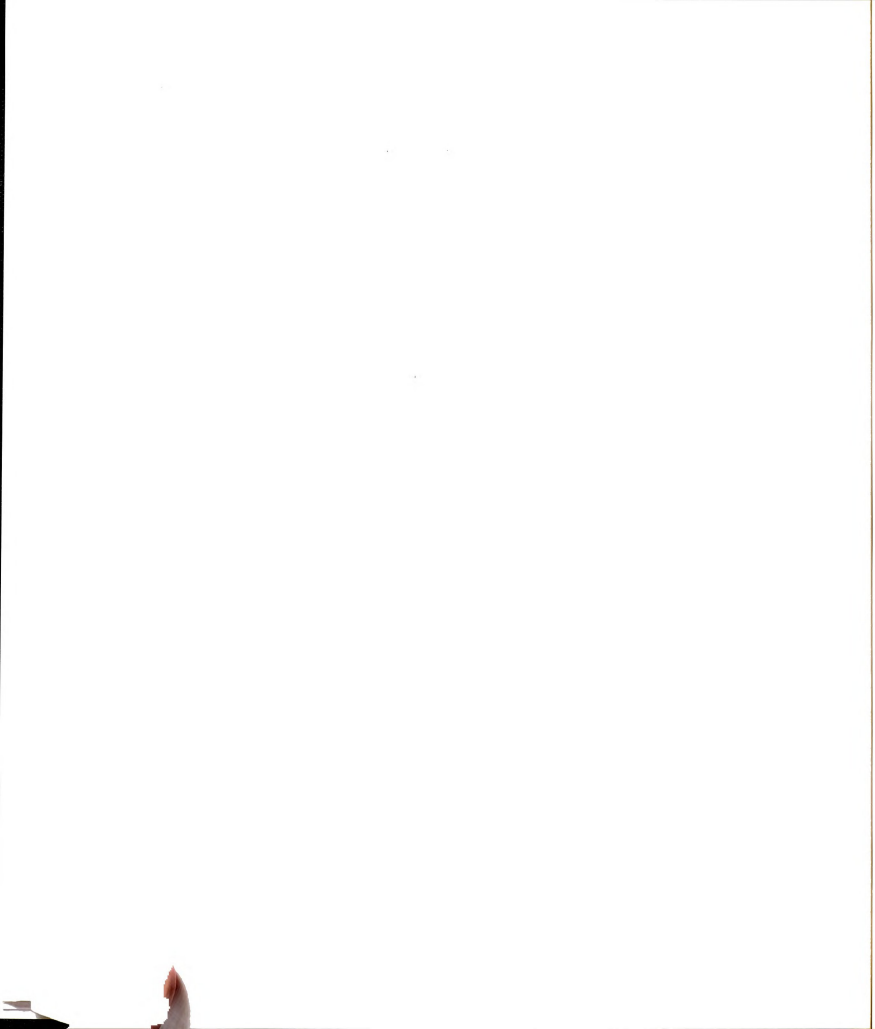




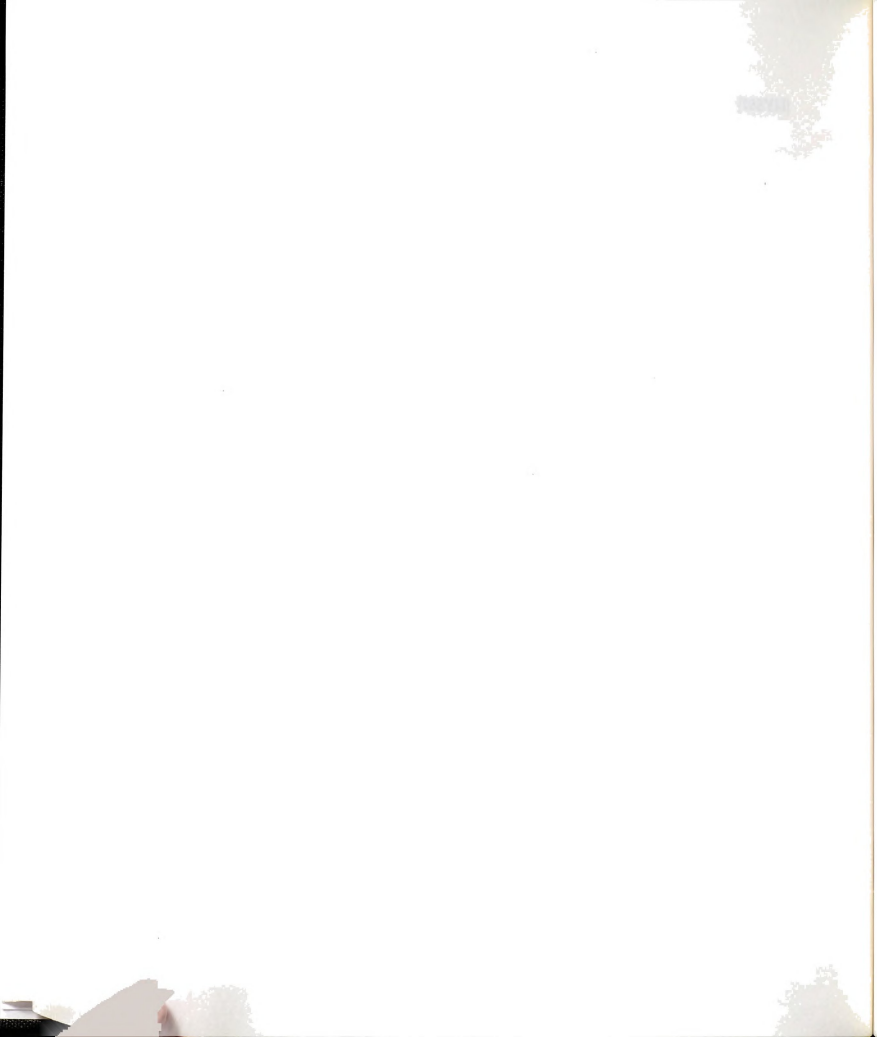
- [Kell80] M.J. Kelly, *Application of the Recursion Method to the Electronic Structure from an Atomic Point of View*, Solid State Phys. **35**, 295 (1980).
- [Kell81] B.T. Kelly, *Physics of Graphite*, Applied Science Publishers (1982).
- [Kell86] A. Kelly and N.H. McMillan, *Strong Solids*, Clarendon Press, Oxford (1986).
- [Kern92] R. Kerner, K.A. Penson and K.H. Bennemann, Europhys. Lett. **19**, 363 (1992).
- [KimE93] Eunja Kim, Young Hee Lee and Jae Young Lee, *Fragmentation of  $C_{60}$  and  $C_{70}$  clusters*, Phys. Rev. B **48**, 18230 (1993).
- [KimS91] S.G. Kim and P.M. Duxbury, *Cracks and critical current*, J. Appl. Phys. **70**, 3164 (1991).
- [KimS94a] Seong Gon Kim and David Tománek, *Melting the fullerenes: A molecular dynamics study*, Phys. Rev. Lett. **72**, 2418 (1994).
- [KimS94b] S.G. Kim, W. Zhong and D. Tománek, *Synthesizing Carbon Fullerenes*, preprint (1994).
- [KimS94c] S.G. Kim, P. Jund, D. Tománek and J. Hetherington, *Structure Formation in Ferrofluids*, in preparation (1994).
- [KimY62] Y.B. Kim, C.F. Hempstead and A. Strnad, Phys. Rev. Lett. **9**, 306 (1962).
- [Kirk39] J.G. Kirkwood, J. Chem. Phys. **7**, 506 (1939).



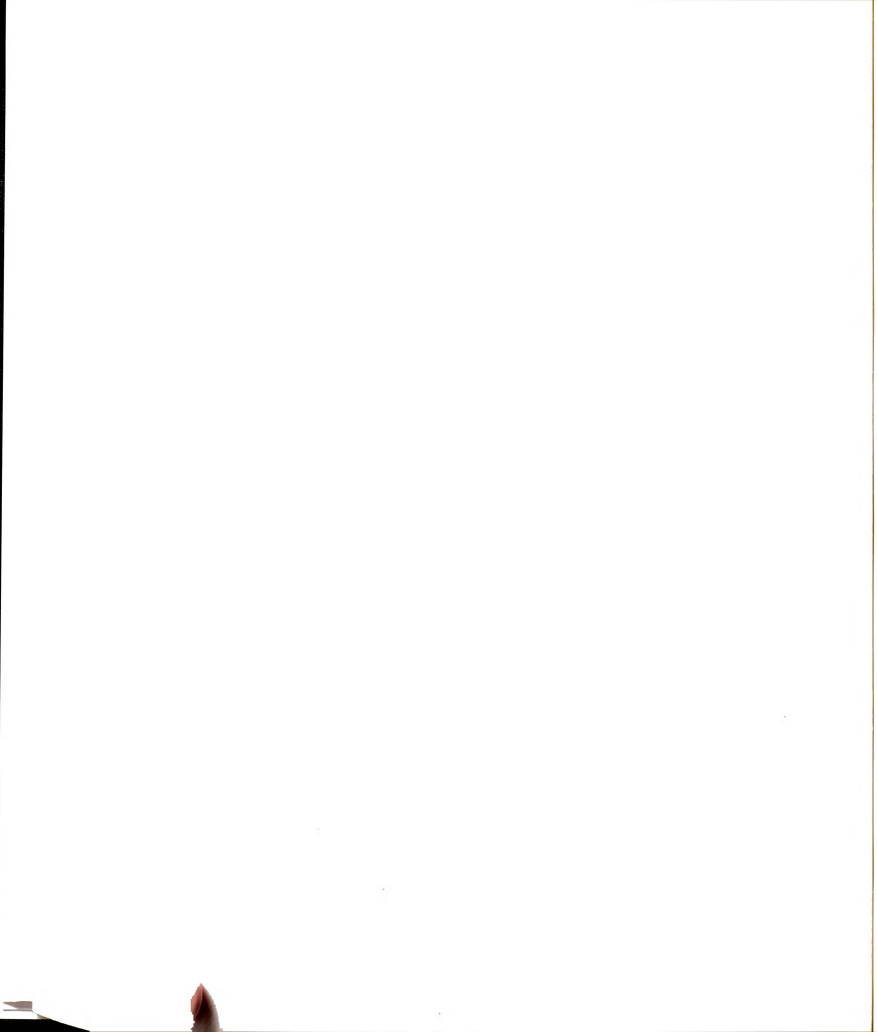
- [Kitt86] C. Kittel, *Introduction to Solid State Physics*, sixth edition, John Wiley, New York (1986).
- [Klin89] D.J. Klingenberg, Frank van Swol and C.F. Zukoski, *Dynamic simulation of electrorheological suspensions*, J. Chem. Phys. **91**, 7888 (1989).
- [Kohn65] W. Kohn and L.J. Sham, Phys. Rev. **140**, A1133 (1965).
- [Kraj82] D. Krajcinovic and M.A.G. Silva, *Statistical Aspects of the Continuous Damage Theory*, Int. J. Solids Structures **18**, 551 (1982).
- [Krat90] W. Krätschmer, L.D. Lamb, K. Fostiropoulos, and D.R. Huffman, Nature **347**, 354 (1990).
- [Krot85] H.W. Kroto, J.R. Heath, S.C. O'Brien, R.F. Curl, and R.E. Smalley, Nature **318**, 162 (1958).
- [Kusa90] P.G. Kusalik, *Computer simulation results for the dielectric properties of a highly polar fluid*, J. Chem. Phys. **95**, 3520 (1990).
- [Lang92] Stephen A. Langer, Raymond E. Goldstein and David P. Jackson, *Dynamics of labyrinthine pattern formation in Magnetic Fluids*, Phys. Rev. A **46**, 4894 (1992).
- [Leat94] P.L. Leath and P.M. Duxbury, preprint.
- [Leno92] Thomas Lenosky, Xavier Gonze, Michael Teter and Veit Elser, Nature **355**, 333 (1992).
- [Lill93] T. Lill, F. Lacher, H.-G. Busmann and I.V. Hertel, Phys. Rev. Lett. **70**, 3383 (1993).



- [LiYS87] Y.S. Li and P.M. Duxbury, *Size and location of the largest current in a random resistor network*, Phys. Rev. B **36**, 5411 (1987).
- [LiYS88] Y.S. Li and P.M. Duxbury, *Crack arrest by residual bonding in spring and resistor networks*, Phys. Rev. B **38**, 9257 (1988).
- [LiYS89] Y.S. Li and P.M. Duxbury, Phys. Rev. B **40**, 4889 (1989).
- [LiXP93] X.-P. Li, R.W. Nunes and D. Vanderbilt, Phys. Rev. B **47**, 10891 (1993).
- [Loui87] E. Louis and F. Guinea, *The fractal nature of fracture*, Europhys. Lett. **3**, 871 (1987).
- [Luch87] M.U. Luchini and C.M.M. Nex, *A new procedure for appending terminators in the recursion method*, J. Phys. C: Solid State Phys. **20**, 3125 (1987).
- [Lund83] S. Lundqvist and N.H. March, *Theory of the Inhomogeneous Electron Gas*, Plenum (1983).
- [Mann88] J. Mannhart *et al.*, Phys. Rev. Lett. **61**, 2476 (1988).
- [Mann89] J. Mannhart *et al.* Science. **245**, 839 (1989).
- [Mand84] B.B. Mandelbrot, D.E. Passoja and A.J. Paullay, *Fractal character of fracture surfaces of metals*, Nature **308**, 721 (1984).
- [Mart92] J.E. Martin, J. Odinek and T.C. Halsey, Phys. Rev. Lett. **69**, 1524 (1992).

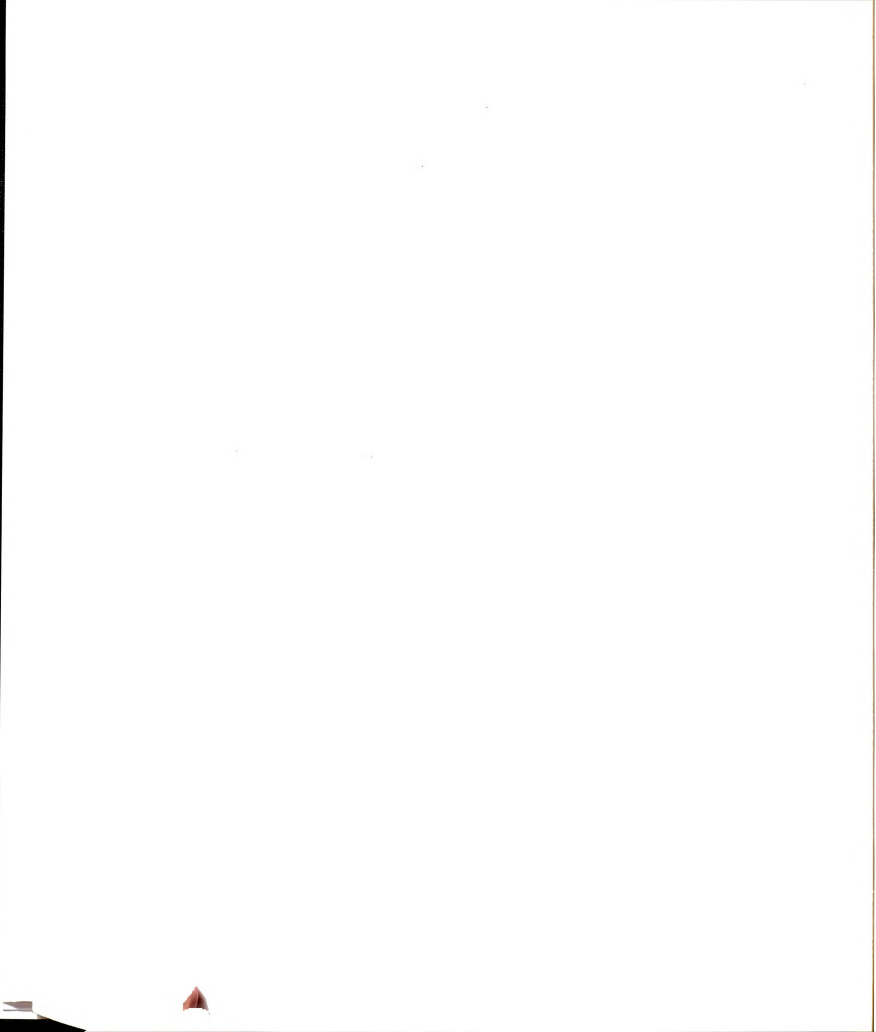


- [McLa46] N.W. McLachlan, *Mathieu functions and their classification*, J. Math. Phys. **25**, 209 (1946).
- [McLa47] N.W. McLachlan, *Theory and Application of Mathieu Functions*, Clarendon Press, Oxford, England (1947).
- [Meak88] P. Meakin, *Simple models for crack growth*, Crystal prop. and prep. **17** and **18**, 1, (1988).
- [Meak91] P. Meakin, Science **252**, 226, (1991).
- [Mech89] J.J. Mecholsky, D.E. Passoja and K.S. Feinberg-Ringel, *Quantitative analysis of brittle fracture surfaces using fractals geometry*, J. Am. Ceram. Soc. **72**, 60 (1989).
- [Mors53] Philip M. Morse and Herman Feshbach, *Methods of Theoretical Physics*, Part I and Part II, McGraw-Hill Book Company, Inc., New York (1953).
- [Mull49a] R.S. Mulliken, J. Chem. Phys. **46**, 467 (1949).
- [Mull49b] R.S. Mulliken, J. Chem. Phys. **46**, 675 (1949).
- [Nels78] David R. Nelson, *Study of melting in two dimensions*, Phys. Rev. B **18**, 2318 (1978).
- [Nels88] D.R. Nelson, Phys. Rev. Lett. **60**, 1973 (1988).
- [Nick88] G.A. Nicklasson, A. Torebring, C. Larsson, C.G. Granqvist and T. Farestam, *Fractal Dimension of Gas-Evaporated Co Aggregates: Role of Magnetic Coupling*, Phys. Rev. Lett. **60**, 1735 (1988).





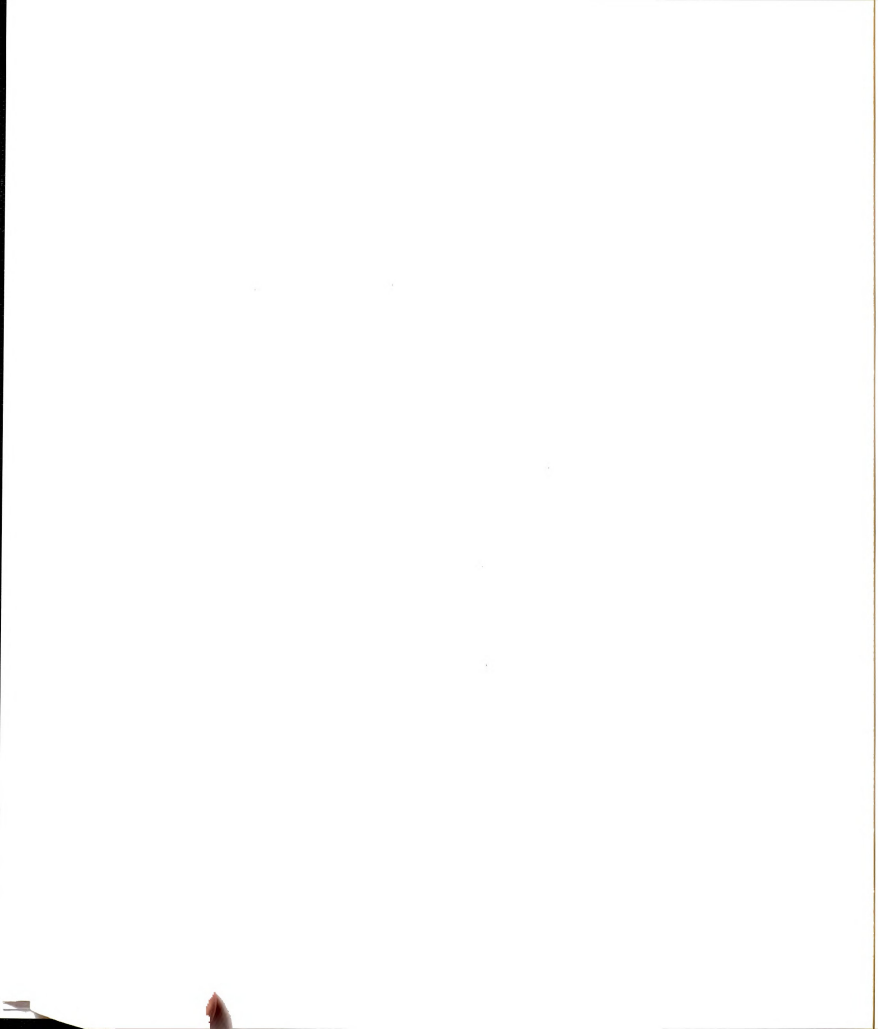
- [Nose84] S. Nosé, *Mol. Phys.* **52**, 255 (1984).
- [Orla91] Terry P. Orlando and Kevin A. Delin, *Foundation of Applied Superconductivity*, Addison Wesley, Reading MA (1991).
- [Page52] L. Page, *Introduction to Theoretical Physics*, 3rd ed., p. 286, D. Van Nostrand Company, Princeton, N.J. (1952).
- [Phoe83] S.L. Phoenix and L.J. Tierney, *Eng. Frac. Mech.* **18**, 193 (1983).
- [Phoe92] S.L. Phoenix and R.L. Smith, preprint (1988).
- [Pigg80] M.R. Piggot, *Load Bearing Composites*, Pergamon Press, Oxford (1980).
- [Pres86] William H. Press, Brian P. Flannery, Saul A. Teukolsky and William T. Vetterling, *Numerical Recipes: The Art of Scientific Computing*, Cambridge University Press, Cambridge (1986).
- [RayP85] P. Ray and B.K.Chakrabarti, *A microscopic approach to the statistical fracture analysis of disordered brittle solids*, *Solid State Communications* **53**, 477 (1985).
- [Reif65a] Federick Reif, *Fundamentals of Statistical and Thermal Physics*, Page 248, McGraw-Hill, New York, NY (1965).
- [Reif65b] Federick Reif, *Fundamentals of Statistical and Thermal Physics*, Page 560, McGraw-Hill, New York, NY (1965).
- [Rose85] R.E. Rosensweig, *Ferrohydrodynamics*, Cambridge University Press, Cambridge (1985).



- [Root51] C.C.J. Roothaan, Rev. Mod. Phys. **23**, 69 (1951).
- [Root60] C.C.J. Roothaan, Rev. Mod. Phys. **32**, 179 (1960).
- [Roux88] S. Roux, A. Hansen, H.J. Herrmann and E. Guyon, *Rupture of Heterogeneous Media in the limit of infinite disorder*, J. Stat. Phys. **52**, 237 (1988).
- [Sahi86] M. Sahimi and J.D. Goddard, *Elastic percolation models for cohesive failure in heterogeneous systems*, Phys. Rev. B **33**, 7848 (1986).
- [Sahi91] M. Sahimi and S. Arbabi, Mat. Res. Symp. Proc. **207**, 201 (1991).
- [Sahi93] M. Sahimi and S. Arbabi, Phys. Rev. B **47**, 713 (1993).
- [Seif92] G. Seifert and R. Schmidt, p. 261, *Clusters and Fullerenes*, edited by V. Kumar, T.P. Martin and E. Tosatti, World Scientific, Singapore (1992).
- [Sier00] K. Sieradzki, private communication.
- [Sier86] K. Sieradzki and R. Li, *Fracture behavior of a solid with random porosity*, Phys. Rev. Lett. **56**, 2509 (1986).
- [SihG73] G.C. Sih, *Handbook of Stress Intensity Factors*, Institute of Fracture and Solid Mechanics, Lehigh University, Bethlehem, PA (1973).
- [Slat54] J.C. Slater and G.F. Koster, *Simplified LCAO Method for the Periodic Potential Problem*, Phys. Rev. **94**, 1498 (1954).
- [Smit80] R.L. Smith, Proc. R. Soc. London A **372**, 539 (1980).
- [Srol88] D.J. Srolovitz and P.D. Beale, J. Am. Ceram. Soc., **71**, 362 (1988).



- [Stev94] Mark J. Stevens and Gary S. Grest, *Coexistence in Dipolar Fluids in a Field*, Phys. Rev. Lett. **72**, 3686 (1994).
- [Tada73] H. Tada, P.C. Paris and G.R. Irwin, *The Stress Analysis of Cracks Handbook*, Del Research Corp., Hellertown, PA (1973).
- [Taka86] H. Takayasu, *Pattern formation of dendritic fractals in fracture and electric breakdown*, Proceedings of the symposium on fractals in physics, 181 (1986).
- [TaoR92] R. Tao, editor, *Electrorheological Fluids*, World Scientific, Singapore (1992)
- [TaoR94] R. Tao and Qi Jiang, *Simulation of Structure Formation in an Electrorheological Fluid*, Phys. Rev. Lett. **73**, 205 (1994).
- [Teje94] C.F. Tejero, a. Daanoun, H.N.W.Lekkerkerker and M. Baus, *Phase Diagrams of "Simple" Fluids with Extreme Pair Potentials*, Phys. Rev. Lett. **73**, 752 (1994).
- [Term86] Y. Termonia and P. Meakin, *Formation of fractal cracks in a kinetic fracture model*, Nature **320**, 429 (1986).
- [Term87a] Y. Termonia and P. Smith, *Macromolecules*, **20**, 835 (1987).
- [Term87b] Y. Termonia, *J. Mater. Sci.* **22**, 1733 (1987).
- [Term88] Y. Termonia and P. Smith, in A.E. Zachariades and R.S. Porter (editors), *"High Modulus Polymers Approaches to Design and Development"*, Dekker, New York (1988).



- [Ters88] J. Tersoff, Phys. Rev. Lett. **61**, 2879 (1988).
- [Thor83] M.F. Thorpe, J. Non-Cryst. Solids **57**, 355 (1983)
- [Thor87] M.F. Thorpe, *Rigidity Percolation in Glassy Structures*, J. Non-Cryst. Solids **76**, 109 (1987)
- [Till86] D.R. Tilley and J. Tilley, *Superfluidity and Superconductivity*, Adam Hilger Ltd., Boston (1986).
- [Tink65] M. Tinkham, *Superconductivity*, Gordon and Breach, New York (1965)
- [Toma86] David Tománek and Michael A. Schluter, *Calculation of Magic Numbers and the Stability of Small Si Clusters*, Phys. Rev. Lett. **56**, 1055 (1986).
- [Toma91] David Tománek and Michael A. Schluter, *Growth Regimes of Carbon Clusters*, Phys. Rev. Lett. **67**, 2331 (1991).
- [Turc85] D.L. Turcotte, R.F. Smalley Jr. and Sara A. Solla, *Collapse of loaded fractal trees*, Nature **313**, 671 (1985).
- [Unde86] E.E. Underwood and K. Banerji, *Fractals in fractography*, Mat. Sci. and Eng. **80**, 1 (1986).
- [Vand92] David Vanderbilt and J. Tersoff, Phys. Rev. Lett. **61**, 2879 (1988).
- [Waka92] T. Wakabayashi and Y. Achiba, *A model for the  $C_{60}$  and  $C_{70}$  growth mechanism*, Chem. Phys. Lett. **190**, 465 (1992).

- [Waka93] T. Wakabayashi, H. Shiromaru, K. Kikuchi and Y. Achiba, *A selective isomer growth of fullerenes*, Chem. Phys. Lett. **201**, 470 (1993).
- [Wang94] Hao Wang, Yun Zhu, C. Boyd, Weili Luo, A. Cebers and R.E. Rosensweig, *Periodic Branched structures in a Phase-Separated Magnetic Colloid*, Phys. Rev. Lett. **72**, 1929 (1994).
- [Weas90] Robert C. Weast, editor in-chief, *CRC Handbook of Chemistry and Physics*, Page B-10, 62th edition, CRC Press, Boca Raton, Florida (1990).
- [Weib51] W. Weibull, J. Appl. Mech. **18**, 293 (1951).
- [WeiD92a] Dongquing Wei and G.N. Patey, Phys. Rev. Lett. **68**, 2043 (1992).
- [WeiD92b] Dongquing Wei and G.N. Patey, *Ferroelectric liquid-crystal and solid phases formed by strongly interacting dipolar soft spheres*, Phys. Rev. A **46**, 7783 (1992).
- [Weis93] J.J. Weis and D. Levesque, *Chain Formation in Low Density Dipolar Hard Spheres: A Monte Carlo Study*, Phys. Rev. Lett. **71**, 2729 (1993).
- [Welt89] William Weltner, Jr. and Richard J. Van, Chem. Rev. **89**, 1713 (1989).
- [XiaW89] W. Xia and P.L. Leath, Phys. Rev. Lett. **63**, 1428 (1989).
- [XuCH92] C. H. Xu, C. Z. Wang, C. T. Chan and K. M. Ho, *A transferable tight-binding potential for carbon*, J. Phys.: Condens. Matter **4**, 6047 (1992).



- [XuCH94] Chunhui Xu and Gustavo E. Scuseria, *Tight-Binding Molecular Dynamics Simulations of Fullerene Annealing and Fragmentation*, Phys. Rev. Lett. **72**, 669 (1994).
- [Yann91] C.S. Yannoni, P.P. Bernier, D.S. Bethune, G. Meijer and J.R. Salem, J. Am. Ceram. Soc. **113**, 3190 (1991).
- [Zabo86] J.G. Zabolotzky, D.J. Bergman and D. Stauffer, J. Stat. Phys. **44**, 211 (1986).
- [Zhon93] W. Zhong, D. Tománek and George F. Bertsch, *Total energy calculations for extremely large clusters: The recursive approach*, Solid State Communications **86**, 607 (1993).



MICHIGAN STATE UNIV. LIBRARIES



31293010206088